University of Pennsylvania
ScholarlyCommons

Publicly Accessible Penn Dissertations

2019

Designing Colloidal Nanomaterials For Electronic And Optoelectronic Devices Through Surface Modification

Tianshuo Zhao
University of Pennsylvania, zhaotianshuo@gmail.com

Follow this and additional works at: https://repository.upenn.edu/edissertations

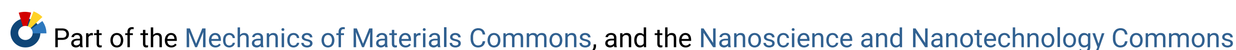
Part of the Mechanics of Materials Commons, and the Nanoscience and Nanotechnology Commons

Recommended Citation

Zhao, Tianshuo, "Designing Colloidal Nanomaterials For Electronic And Optoelectronic Devices Through Surface Modification" (2019). *Publicly Accessible Penn Dissertations*. 3228.
https://repository.upenn.edu/edissertations/3228

This paper is posted at ScholarlyCommons. https://repository.upenn.edu/edissertations/3228
For more information, please contact repository@pobox.upenn.edu.

Designing Colloidal Nanomaterials For Electronic And Optoelectronic Devices Through Surface Modification

Abstract

Colloidal quantum dots (QDs) are nanometer-sized semiconductors synthesized by wet chemical methods and stabilized by surface ligands in solvents. They are prized for the size-dependent electronic band structures, giving rise to tunable optical properties. Their solution form is also suitable for large-area and low-cost fabrication processes. These unique characteristics make this class of materials promising as building blocks for next-generation thin-film electronic and optoelectronic devices. However, the construction of QD based devices requires precise control of their material properties, including carrier mobility, lifetime, doping concentration and energy positions of the conduction and valence band edges. The large surface-to-volume ratio allows these properties to be manipulated through surface modification of QDs. In this thesis, we systematically study the effect of surface treatments, such as ligand exchange, surface passivation, remote doping, on the chemical and physical properties of QD dispersions and thin films. We design surface modified QDs with desirable characteristics and integrate them into QD based devices, including field-effect transistors (FETs), solar cells and photodetectors to enhance device performance.

We design QD thin films with specific surface treatments to improve two important interfaces in PbS QD solar cells. By introducing a CdI_2-treated CdSe QD buffer layer at the ZnO nanoparticle/PbS QD junction interface and improving the p-type doping of the ethanedithiol-PbS QD layer via sulfur enrichment at the back-contact interface, we aim at suppressing interface recombination and facilitating carrier extraction.

The ionization of dopants added on the surface of nanostructures during remote doping is inefficient. Both experimentally and theoretically, we study the effect of dielectric confinement on the doping efficiency in PbSe nanowires. On the FET platform, we show improved doping efficiency by encapsulating the nanowires with high-dielectric media to reduce dielectric mismatch between them.

We further study the synthesis and surface chemistry of III-V QDs. We develop a general route to prepare InP, InAs, InSb and $InAs_xSb_{1-x}$ QDs based on the co-reduction of indium and pnictogen halide precursors. This simplifies the preparation and enhances the stability of V precursors compared to existing approaches. We develop ligand exchange and doping strategies for III-V QD thin films to fabricate high performance devices.

Degree Type

Dissertation

Degree Name

Doctor of Philosophy (PhD)

Graduate Group

Materials Science & Engineering

First Advisor

Cherie R. Kagan

Keywords

devices, electronics, III-V quantum dots, optoelectronics, quantum dots, surface modification

Subject Categories

Mechanics of Materials | Nanoscience and Nanotechnology

This dissertation is available at ScholarlyCommons: https://repository.upenn.edu/edissertations/3228

DESIGNING COLLOIDAL NANOMATERIALS FOR ELECTRONIC AND OPTOELECTRONIC DEVICES THROUGH SURFACE MODIFICATION

Tianshuo Zhao

A DISSERTATION

in

Materials Science and Engineering

Presented to the Faculties of the University of Pennsylvania

in

Partial Fulfillment of the Requirements for the

Degree of Doctor of Philosophy

2019

Supervisor of Dissertation

____

Cherie R. Kagan, Stephen J. Angello Professor, Materials Science and Engineering

Graduate Group Chairperson

____

Shu Yang, Professor, Materials Science and Engineering

Dissertation Committee

Christopher B. Murray, Richard Perry University Professor, Materials Science and Engineering

Vivek B. Shenoy, Eduardo D. Glandt President's Distinguished Professor, Materials Science and Engineering

Shu Yang, Professor, Materials Science and Engineering

DESIGNING COLLOIDAL NANOMATERIALS FOR ELECTRONIC AND OPTOELECTRONIC

DEVICES THROUGH SURFACE MODIFICATION

COPYRIGHT

2019

Tianshuo Zhao

This work is licensed under the

Creative Commons Attribution-

NonCommercial-ShareAlike 3.0

License

To view a copy of this license, visit

https://creativecommons.org/licenses/by-nc-sa/3.0/us/

To my family

ACKNOWLEDGMENT

Looking back on my five-and-a-half-year PhD career, I would like to express my great gratitude to many people who have helped and influenced me and my research. First of all, I sincerely thank my advisor Prof. Cherie Kagan. Thank her for allowing me to join the lab and unveiling a beautiful world of nanocrystals to me. Thank her for all the patient guidance and kind helps she has been giving me from the first day we met. Thank her, together with her spouse Prof. Chris Murray, for setting such good role models for me as scientists, researchers and mentors. It would not be possible for me to complete this dissertation without her support and advise. I would also like to thank Prof. Chris Murray. As a mentor and also my committee member, he has given me a lot of constructive suggestions regarding my projects as well as the encouragement to finish them. It is my great pleasure to have Prof. Shu Yang and Prof. Vivek Shenoy on my committee since my qualifying exam. I appreciate the questions, discussions and suggestions they had for my research projects.

I am grateful to my colleges in both the Kagan group and Murray group, including alumni and current group members: Aaron Fafarman, Ji-Hyuk Choi, Taejong Paik, Young Jae Shin, Pil Sung Jo, Nuri Oh, David Kim, Wenting Li, Marjan Saboktakin, Soong Ju Oh, Yuming Lai, Ed Goodwin, Nicholas Greybush, Wenxiang Chen, F. Scott Stinner, Eric Wong, Daniel Straus, Guannan Liu, Ming-Yuan Chuang, Jingsong Meng, Chawit Uswachoke, Mingliang Zhang, Chenjie Zeng, Hak-Jong Choi, Han Wang, Jiacen Guo, Qinghua Zhao, Steven Neuhaus, Austin Keller, Henry Shulevitz, Sarah Thompson, Jaeyoung Lee, Martin Sarott, Matteo Cargnello, Benjamin Diroll, E. Ashley Gaulding, Davit Jishkariani, Stan Najmr, Yaoting Wu, Haoran Yang, Xingchen Ye, Sen Zhang, Guillaume Gouget, Natalie Gogotsi, Katherine Elbert, Jennifer D Lee, Shengsong Yang. I really enjoy working with and learning from them. Without the effective collaboration among us and a variety of instruments well-maintained by them, I won’t be able to finish any part

of my projects or thesis. Of course, all the temporary frustration and following happiness we have had together working in lab become my unforgettable memory at Penn.

Last but not least, I would like to give my special thanks to my family. It couldn't be luckier for me to marry my dearest wife Victoria Ran Tian in the first year of my PhD. I am grateful that we found each other lifelong companions. I thank her for always being so supportive to my career and helping me pursuing my dreams. My son Benjamin Lanyuan Zhao was born during the 4th year of my PhD, adding another bright color to my life. Seeing my wife and my son when I return home from work has become one of my greatest comforts every day. I also want to thank my parents, parents in law and sister in law, who have lived with us and helped us taking care of the baby.

ABSTRACT

DESIGNING COLLOIDAL NANOMATERIALS FOR ELECTRONIC AND OPTOELECTRONIC DEVICES THROUGH SURFACE MODIFICATION

Tianshuo Zhao

Prof. Cherie R. Kagan

Colloidal quantum dots (QDs) are nanometer-sized semiconductors synthesized by wet chemical methods and stabilized by surface ligands in solvents. They are prized for the size-dependent electronic band structures, giving rise to tunable optical properties. Their solution form is also suitable for large-area and low-cost fabrication processes. These unique characteristics make this class of materials promising as building blocks for next-generation thin-film electronic and optoelectronic devices. However, the construction of QD based devices requires precise control of their material properties, including carrier mobility, lifetime, doping concentration and energy positions of the conduction and valence band edges. The large surface-to-volume ratio allows these properties to be manipulated through surface modification of QDs. In this thesis, we systematically study the effect of surface treatments, such as ligand exchange, surface passivation, remote doping, on the chemical and physical properties of QD dispersions and thin films. We design surface modified QDs with desirable characteristics and integrate them into QD based devices, including field-effect transistors (FETs), solar cells and photodetectors to enhance device performance.

We design QD thin films with specific surface treatments to improve two important interfaces in PbS QD solar cells. By introducing a CdI_2-treated CdSe QD buffer layer at the ZnO nanoparticle/PbS QD junction interface and improving the p-type doping of the ethanedithiol-PbS

QD layer via sulfur enrichment at the back-contact interface, we aim at suppressing interface recombination and facilitating carrier extraction.

The ionization of dopants added on the surface of nanostructures during remote doping is inefficient. Both experimentally and theoretically, we study the effect of dielectric confinement on the doping efficiency in PbSe nanowires. On the FET platform, we show improved doping efficiency by encapsulating the nanowires with high-dielectric media to reduce dielectric mismatch between them.

We further study the synthesis and surface chemistry of III-V QDs. We develop a general route to prepare InP, InAs, InSb and $InAs_xSb_{1-x}$ QDs based on the co-reduction of indium and pnictogen halide precursors. This simplifies the preparation and enhances the stability of V precursors compared to existing approaches. We develop ligand exchange and doping strategies for III-V QD thin films to fabricate high performance devices.

TABLE OF CONTENTS

ACKNOWLEDGMENT .... **IV**

ABSTRACT .... **VI**

LIST OF TABLES .... **XIII**

LIST OF ILLUSTRATIONS .... **XV**

CHAPTER 1 INTRODUCTION **1**

1.1 From Bulk Semiconductors to Quantum Dots (QDs) **1**

1.2 Colloidal Synthesis of QDs **7**

1.2.1 Hot-injection Synthesis of Colloidal QDs 9

1.2.2 Heat-up Synthesis of Colloidal QDs 11

1.2.3 Purification and Size Selection of Colloidal QDs 14

1.3 Surface Modification of QDs **15**

1.3.1 Ligand Exchange of QDs 15

1.3.2 Remote Doping of Nanostructures 21

1.4 Colloidal QD Based Electronic and Optoelectronic Devices **23**

1.4.1 QD Based Field-Effect Transistors 23

1.4.2 QD Based Solar Cells 27

1.4.3 QD Based Photodetectors 29

1.5 Thesis Overview **31**

1.6 References 33

CHAPTER 2 ADVANCED ARCHITECTURE FOR PBS COLLOIDAL QUANTUM DOT (CQD) SOLAR CELLS EXPLOITING A CDSE QUANTUM DOT (QD) BUFFER LAYER 43

2.1 Fabrication and Characteristics of PbS QD Solar Cells with the CdSe QD Buffer Layer 44

2.2 Optical and Electrical Characterization of the CdI2-capped CdSe QD layer 48

2.3 The Effect of the QD Buffer Layer Properties on Carrier Transport 51

2.4 The Mechanism of the CdSe QD Buffer Layer Enhancement 60

2.5 Quantitative Device J-V analysis 63

2.6 Conclusions 65

2.7 References 66

CHAPTER 3 THE EFFECT OF SURFACE CHALCOGEN ENRICHMENT ON PBS COLLOIDAL QUANTUM DOTS 70

3.1 Sulfur-Enriched PbS QDs by Colloidal Atomic Layer Deposition 71

3.2 Facet-dependent Deposition of Sulfur Atoms 76

3.3 Charge Transport and Doping of PbS/S QD Films 80

3.4 Chemical Origin of Surface Sulfur Doping in PbS QDs 83

3.5 Conclusions 86

3.6 References 87

CHAPTER 4 THE EFFECT OF DIELECTRIC ENVIRONMENT ON DOPING EFFICIENCY IN COLLOIDAL PBSE NANOSTRUCTURES 90

4.1 Fabrication and Doping of PbSe Nanowire (NW) Array Field-Effect Transistors (FETs) 92

4.2 Encapsulation of PbSe NW Array FETs with Different Dielectric Overlayer 97

4.3 Theorical Model for Ionization Energy and Doping Efficiency of Dopants in PbSe NWs Embedded in Different Dielectric Environment 101

4.4 Fabrication and Doping Efficiency of PbSe single NW FETs 105

4.5 Ionization Energy Measured from PbSe single NW FET devices 112

4.6 Conclusions 116

4.7 References 117

CHAPTER 5 GENERAL SYNTHESIS ROUTE TO HIGH QUALITY COLLOIDAL III-V SEMICONDUCTOR QUANTUM DOTS BASED ON PNICTOGEN CHLORIDES 121

5.1 Synthesis of III-V Colloidal Quantum Dots (QDs) via Co-reduction 122

5.2 Pnictogen Chloride ($PnCl_3$)-Oleylamine Precursors 126

5.3 Optical, Structural and Electrical Characterization of III-V QDs 129

5.3.1 InAs QD Characterization, Ligand Exchange and Devices 129

5.3.2 Surface Oxidation of InSb NCs 133

5.4 Synthesis and Characterization of $InAs_xSb_{1-x}$ Alloy NCs 137

5.5 Conclusions 143

5.6 References 144

CHAPTER 6 III-V COLLOIDAL QUANTUM DOTS BASED ELECTRONIC AND OPTOELECTRONIC DEVICES 146

6.1 Synthesis of Tetrahedral InP QDs 147

6.2 Solid-State and Solution Ligand Exchange of InP QDs 153

6.3 Doping of InP QD Films for FETs 157

6.4 Surface Modification and Optoelectronic Properties of InSb and $InAs_xSb_{1-x}$ QD films 162

6.5 Conclusions 168

6.6 References 169

CHAPTER 7 CONCLUSIONS 171

7.1 Future Work 171

7.1.1 Correlation Between Defects and Physical Properties of InSb QDs 171

7.1.2 Encapsulation and Passivation of III-V QD Devices 173

7.1.3 Designing All III-V QD Based Solar Cells 175

7.2 Concluding Remarks ... 177

7.3 References ... 180

LIST OF TABLES

Table 1.1 Performance metrics of photoconductors 31

Table 2.1 Device parameter statistics 47

Table 2.2 Element analysis of 8 nm CdSe QD thin films 50

Table 2.3 Material Parameters 55

Table 2.4 Device parameter statistics with and without the CdI2-treated PbS QD interface layers 58

Table 2.5 Device parameters based on the dark characteristics 64

Table 3.1 Stoichiometry of 3 nm PbS QDs after different Na_2S cALD treatments 74

Table 3.2 Stoichiometry of PbS QDs after different cALD treatments 75

Table 3.3 Simulated Pb:S ratios for 3 nm and 4 nm PbS QDs as each facet group is covered by S 80

Table 3.4 Atomic percentage of components detected in XPS measurement 86

Table 4.1 Theoreticacl Prediction of Ionization Energy 102

Table 4.2 Trap Density in PbSe NW 111

Table 5.1 Elemental composition and lattice constant of $InAs_xSb_{1-x}$ NCs 139

Table 6.1 EDS result of InP QDs as synthesized, with Na_2S treatment in the solid-state or solution phase 156

Table 6.2 Electron mobility and on/off ratio of the FET devices operated in the saturation regime
....157

LIST OF ILLUSTRATIONS

Figure 1.1 (a) Linear combination of atomic s and p orbitals giving rise to valence and conduction bands in a semiconductor.[1] Valence band states formed by s and p bonding orbitals are filled by electrons, and conduction band states formed by s and p antibonding orbitals are empty. The Fermi level E_F lies in the bandgap between valence and conduction band. (b) Fermi function f(E) at increasingly higher temperatures from left to right.[5] f(E)=0 when $E>>E_F$, f(E)=1/2 when $E=E_F$ and f(E)=1 when $E<<E_F$. f(E)=1 in the valence band (grey) and f(E) is non-zero at the bottom of conduction band (pink) when the temperature is raised. 3

Figure 1.2 (a) E vs. k diagram showing the first energy state is shifted to higher k and energy spacing is increased due to stronger quantum confinement as QD size decreases.[8] UV-Vis spectra of (b) CdSe[8] and (c) PbS[8] colloidal QDs with increasing size. 5

Figure 1.3 Schematics of charge carriers and electric field lines between them in (a) bulk semiconductors and (b) nanostructures. ϵ_s and ϵ_{out} are the dielectric constant of semiconductor and surrounding environment, respectively. 7

Figure 1.4 (a) A single PbS QD composed of Pb (grey) and sulfur (yellow) atoms with a shell of oleic acid ligands.[15] Schematics of nucleation and growth processes for (b) hot-injection[16] and (c) heat-up[17] synthetic routes to colloidal QDs. 8

Figure 1.5 (a) LaMer model describing the nucleation and growth stages of colloidal synthesis for a faster (orange) and a slower (green) nucleation process that results in different polydispersity.[30] (b) Three-neck flask setup for hot-injection synthesis.[8] 11

Figure 1.6 (a) Initial, intermediate, and final chemical species at different stages of the heat-up synthesis. (b) Schematics to describe the nucleation and growth processes during the heat-up reaction.[31] 12

Figure 1.7 (a) Schematics of three categories of ligand binding to the surface of CdSe.[47] (b) Solid-state ligand exchange process, QD film formation and ligand exchange treatment (top) and TEM images of PbSe QD films before and after NH_4SCN ligand exchange (bottom). (c) Solution-ligand exchange steps begin with the ligand exchange treatment and then QD film fabrication (top) and SEM images of a film of SCN-exchanged CdSe QDs.[48] 18

Figure 1.8 (a) Schematics of the electronic states of QD arrays with short ligands (left) and long ligands (right).[48] (b) Density functional theory (DFT) simulated density of states for PbS QDs without (top) and with (bottom) trap states due to uncoordinated surface bonds. Schematic showing halides can passivate surface defects of PbS QDs (right).[56] (c) Carrier type and concentration in PbS QD films after different ligand exchange treatments in inert or air environments.[59] (d) Energy levels of PbS QD films after ligand treatments measured by ultraviolet photoelectron spectroscopy.[61] 20

Figure 1.9 (a) Stoichiometry control of PbSe QD films to yield n-type or p-type devices by Pb or Se enrichment through thermal evaporation, respectively (left). The Fermi level is tuned by the number of Pb or Se added.[62] (b) Time-resolved microwave conductivity measurements to show carrier lifetime (left) and mobility quantum yield product (right) of CdSe QD films as a function of indium film thickness.[66] 22

Figure 1.10 (a) A typical configuration for QD thin-film FET devices. Bottom gate electrode is typically heavily doped Si and the gate dielectric layer is thermally grown SiO_2. On top of the QD layer, metal electrodes are usually deposited through evaporation as the source and drain contacts. I_D-V_G characteristics of (b) CdSe QD FETs with SCN ligand exchange and In doping at different source-drain voltages.[25] (c) PbSe QD FETs as fabricated with SCN ligand exchange (black), after deposition of 1 Å of Pb (red) or after 0.1 Å of Se (blue),[62] and (d) PbSe NW array FETs with 0 (black),3 (red), 6 (green),10 (blue) and 15 (cyan) Å of Pb deposited and (inset) Δn calculated from the shift in V_T as a function of the thickness of deposited Pb.[68] 26

Figure 1.11 Band diagram schematics of (a) Schottky junction (b) heterojunction and (c) p-i-n junction PbS QD solar cells. 29

Figure 1.12 Spectral coverage of QD photodetectors compared to other solution processible photodetectors.[76] 30

Figure 2.1 (a) SEM cross-sectional image and schematic of a ZnO NP/PbS QD solar cell with the CdSe QD buffer layer. (b) Current density–voltage (J–V) characteristics of representative solar cells without (black) and with (red) a CdSe QD buffer layer under AM 1.5 illumination. (c) Histogram of the device PCE without (black) and with (red) the CdSe QD buffer. 46

Figure 2.2 Characterization of the 8 nm CdSe QD buffer layer. (a) Absorption spectra of CdSe QD films as-deposited with organic ligands (grey), after treatment with CdI_2 (black) and upon annealing at 250 °C (red). Inset: corresponding IR absorption spectra of the CdSe QD films normalization by their absorption. (b) I_D–V_G (red) and *C-V* (blue) characteristics of CdI_2-treated CdSe QD FETs. (c) I_D-V_G (blue) and *C-V* (green) characteristics of ZnO NP FETs..................... 49

Figure 2.3 (a) Cyclic voltammograms of PbS QD (brown), 8 nm CdSe QD (red), 4 nm CdSe QD (pink) and ZnO NP (blue) thin films. UV-Vis absorption spectra of (b) ZnO NP films and (c) 4 nm CdI_2-treated CdSe QD (pink) and MPA treated PbS QD (brown) films. (d) Corresponding band energy positions of PbS QD, CdSe QD and ZnO NP films. 54

Figure 2.4 Band alignment of the ZnO NP/CdSe QD/PbS QD heterojunction with (a) a 8 nm CdSe QD buffer layer and (b) a 4 nm CdSe QD buffer layer. (c) *J*–*V* characteristics of devices constructed with (c) a 8 nm CdSe QD buffer and (d) a 4 nm CdSe QD buffer layer in the dark (black), under red light illumination (red), upon AM 1.5 white light illumination (dash, purple) and after 15 min of white light soaking (blue). 56

Figure 2.5 *J-V* characteristics of PbS QD solar cells with no (black), 20 nm (red), 40 nm (green) and 60 nm (blue) thick CdSe QD buffer layers. 57

Figure 2.6. *J-V* characteristics of representative solar cells without (black) and with (blue) a CdI_2-treated PbS QD interface layer under AM 1.5G illumination. 59

Figure 2.7 (a) EQE of PbS QD solar cells without the CdSe QD buffer layer (black) and with the CdSe QD buffer layer (red). Change of EQE (blue), $\Delta EQE = EQE\ (red) - EQE\ (black)$. (b) UV-Vis absorption spectra of the reference ZnO NP/PbS QD (black) and optimized ZnO NP/CdSe QD/PbS QD (red) device stacks on glass substrates. 61

Figure 2.8 TRMC measurements of (a) the product of the carrier quantum yield (Φ) and the sum of the carrier mobilities in ZnO NP/PbS QD (black) and ZnO NP/CdSe QD/PbS QD (red) films and (b) photoconductance decay lifetime of the ZnO NP/PbS QD (black) and ZnO NP/CdSe QD/PbS QD (red) stacks. 62

Figure 2.9. *J-V* analysis on representative PbS QD solar cells without (black) and with (red) the CdSe QD buffer layer. (a) *J-V* characteristics of PbS QD solar cells in the dark (dash lines) and under AM 1.5 illumination (solid lines). (b) The plot of d*J*/d*V* versus *V* to extrapolate *G*. (c) The plot of d*V*/d*J* versus *J-GV* with linear fit to extrapolate R and n. (d) The semilog plot of *J-GV* versus *V-RJ* with linear fit to extrapolate J_0. 64

Figure 3.1 (a) Schematic of the cALD process. PbS QDs dispersed in octane are phase separated from the Na_2S solution in FA (left). Sulfur atoms are added to the PbS QD surface during mixing of the two phases (middle). The PbS/S QD dispersion is purified twice with fresh FA (right). UV-Vis absorption spectra of (b) 3 nm and (c) 4 nm PbS QD solution as made (black), treated by 1 (red), 3 (green), 10 (blue), and 30 (cyan) μL of Na_2S solution. TEM images of 3 nm PbS QDs (d) as synthesized and treated by (e) 10 and (f) 30 μL of Na_2S solution during the cALD process. 73

Figure 3.2 Absorption spectra of PbS QD solutions as synthesized (black), with (a) only FA (red) and FA and OLAM (blue) and (b) 10 μL of Na_2S and 0.5 (red), 1 (blue) and 2 (green) μL of OLAM. 75

Figure 3.3 XRD patterns of films of (a) 3 nm PbS QDs (black) and 4 nm PbS QDs (red), (b) 4 nm PbS QDs (black) treated by only OLAM (red), and OLAM mixed with 1 (green), 3 (blue), 10 (cyan) μL of Na_2S solution, and (c) Intensity of (220) (black) and (200) (red) relative to that of (111) and Scherrer grain size calculated from (220) (blue) for 4 nm PbS QD films as synthesized, with OLAM treated only and with increasing amount of Na_2S enrichment. (d) XRD patterns of 3 nm PbS QDs (black) treated by only OLAM (red) and OLAM mixed with 1 μL of Na2S solution (green). Note: the sharp features at 44 and 56 ° are from the Si substrate. (e) Schematics of the surface ligands changed from OA to OLAM and S^{2-} during the cALD process. (f) Simulated crystal structures of PbS QDs terminated by (100) (111) and (110) facets with 3 nm and 4 nm in size, respectively. 79

Figure 3.4 (a) I_D-V_G characteristics of EDT capped PbS QD thin-film FETs (black), after 1(red), 3 (green), 10 (blue) and 30 (cyan) μL of Na_2S treatments. (b) Hole mobility and threshold voltage extracted from the FET characteristics as a function of QD stoichiometry. 82

Figure 3.5 Photoconductivity measurements on (a) day 1 and (b) day 10 of EDT capped PbS QD films (black), with 1 (red) and 3 (green) μL of Na_2S cALD treatments. (c) Corresponding absorption spectra of the three samples on day 1 (solid) and 10 (dashed). 83

Figure 3.6 Pb 4f and S 2s XPS spectra of EDT-PbS QD films (a) (b) without cALD and (c) (d) after 1 μL Na_2S cALD treatment. 85

Figure 4.1 (A) Top-view SEM image of a NW array FET and inset, schematic of the device geometry. (B) Cross-sectional SEM image of a NW array FET encapsulated by HfO_2 at low and (inset) high magnification. Representative I_D—V_G characteristics at (C) V_{DS}=0.25 V and (D)

V_{DS}=20 V of a NW array FET with 0 Å (black), 3 Å (red), 6 Å (green), 10 Å (blue), and 15 Å (cyan) of thermally-deposited Pb. (E) Representative I_D—V_G characteristics of PbSe NW array FETs doped by 0 Å (black), 3 Å (red), 6 Å (green), 10 Å (blue) of indium deposited by thermal evaporation in the linear regime (V_{DS}=0.25 V). Inset C and E: calculated change in carrier concentration as a function of the amount of thermally-deposited Pb or In. 95

Figure 4.2 I_D—V_G characteristics of PbSe NW array FETs as made (black), doped by 10 Å of Se (red), and encapsulated by PMMA (blue) at V_{DS}=-20 V. 96

Figure 4.3 Representative I_D—V_G characteristics of (A) Pb-doped and (B) In-doped NW array FETs as aligned (black), with 3 Å of Pb or with 5 Å of In deposited (red), and further covered by PVDF (blue). (C) Change in carrier concentration (Δn) in the NW arrays created by either 3 Å of Pb (black) or 5 Å of In (purple) before ($\frac{\epsilon_{out}}{\epsilon_0} = 1$) and after encapsulation by PMMA ($\frac{\epsilon_{out}}{\epsilon_0} = 3$) , PVDF ($\frac{\epsilon_{out}}{\epsilon_0} = 9$) and HfO_2 ($\frac{\epsilon_{out}}{\epsilon_0} = 20$) , respectively. 99

Figure 4.4 I_D—V_G characteristics of PbSe NW array FETs as made (black), doped by 3 Å of Pb (red), and embedded in (a) PMMA (blue) and (b) HfO_2 (blue) and after air exposure overnight (magenta). I_D—V_G characteristics of PbSe NW array FETs as made (black), doped by 5 Å of In (red), and embedded in (c) PMMA (blue) and (d) HfO_2 (blue). 100

Figure 4.5 (A) Schematics showing the larger ionization energy ($E_I = E_C - E_D$) and therefore lower probability of promoting electrons from the donor state to conduction band at room temperature (low doping efficiency) in a low (red) dielectric constant medium in comparison to that for a high (blue) dielectric medium. (B) Coulomb interactions, depicted by the density of electric field lines, are not as readily screened between the ionized dopant and free electrons in a

low, relative to a high-ϵ medium. (C) Theoretical doping efficiency (yellow) and measured doping efficiency (normalized Δn) of Pb (black squares) or In (green circles) in PbSe NWs as a function of the dielectric constant of the surrounding medium. From bright yellow to light yellow, the E_I^0 used in theoretical calculation change from 0.01 to 0.07 eV. 104

Figure 4.6 (A) Representative I_D—V_G characteristics of a single PbSe NW FET as made (black) and with 1 Å (red), 2 Å (green), and 3 Å (blue) of evaporated Pb. (B) Representative I_D—V_G characteristics of a single PbSe NW FET as made (black), with 5 Å of Pb (red), and PVDF encapsulation (blue). Inset: normalized doping efficiency and electron concentration change calculated based on theoretical model (dash line) and single PbSe NW FET data (dots). 107

Figure 4.7 I_D—V_G characteristics of individual PbSe single NW FETs as made (black), doped by 3 Å of Pb (red), and embedded in (a)-(c) PMMA, (d)-(f) PVDF, and (g) –(i) HfO_2 (blue)................109

Figure 4.8 (a) Electron mobility extracted from PbSe single NW FETs in Figure S4 as made (black), with 3 Å of Pb (red), and embedded in left: PMMA, middle: PVDF, right: HfO_2 (blue). (b) Mobility enhancement of samples in (a) after doped by Pb (red) and encapsulated by the corresponding dielectric matrix (blue). 110

Figure 4.9 (A) I_D—V_G characteristics of a HfO_2-covered, 5 Å Pb-doped single NW FET at V_D=2 V at 230 K (black), 250 K (red), 270 K (green), 300 K (blue), and 320 K (cyan). (B) Calculated free electron concentration (black symbols) as a function of temperature (T) and (red line) fit to ln(n) *versus* T. (c) $\ln(I_D) - 1000/T$ plots at different V_{DS} and the electron barrier at metal semiconductor interface as a function of $V_{DS}^{1/2}$. ϕ'_{MS} represents $\frac{q\phi_{MS}-\left(\frac{qE}{4\pi\epsilon_{PbSe}}\right)^{0.5}}{q}$. The extrapolation of the inset plot gives the SB height (0.196 eV) 114

Figure 4.10 (A) I_D—V_G characteristics of a HfO_2-covered, 5 Å Pb-doped single NW FET at V_D=2 V from 80 K to 300 K. (B) Calculated free electron concentration (black symbols) as a function of temperature (T) and fit to ln(n) *versus* T over a lower T range (80 – 240 K, purple), a higher T range (155 -300 K, pink) and over the whole range (80-300 K, dashed grey line). The E_I calculated from fitted slopes are labeled with corresponding colors. The errors of *n* and E_I are measurement uncertainty. 115

Figure 5.1 (a) to (f) low magnification TEM images, selected area electron diffraction pattern (b to c insets) and high resolution TEM images (d to f insets) and (g) UV-Vis-NIR absorption spectra of different-sized InP, InAs and InSb QDs. 125

Figure 5.2 UV-Vis-NIR absorption spectra of InAs NCs synthesized at a reaction temperature of 320 °C for 15, 30, 45 and 60 min (from left to right). 126

Figure 5.3 Photos of (a) PCl_3-, $AsCl_3$- and $SbCl_3$-oleylamine solutions (from left to right) at 50 °C, and (b) $PnCl_3$-OLAM solution with addition of hexane, acetone, chloroform, methanol, isopropanol, or ethanol from left to right. (c) H-NMR spectra of OLAM (red), OLAM mixed with $InCl_3$ (light green), OLAM mixed with $InCl_3$ then $PnCl_3$ ($AsCl_3$, $SbCl_3$ and PCl_3) (dark green) and OLAM mixed with $PnCl_3$ (blue), OLAM mixed with PnCl3 then $InCl_3$ (purple). 129

Figure 5.4 (a) Low-resolution and (inset) high-resolution TEM images of InAs QDs synthesized at 320 °C for 15 min. (b) Absorption (black) and photoluminescence spectra of InAs QDs as-synthesized (dark blue) and upon treatment with 1 mg/mL (light blue) and 2 mg/mL (cyan) $NOBF_4$ in acetonitrile. 130

Figure 5.5 (a) Schematics of solution and solid hybrid ligand exchange process. (b) UV-Vis absorption and (c) FTIR spectra of InAs QD films before (black) and after only solution exchange (red), with hybrid exchange (green), and with hybrid exchange and annealing at 300 °C for 5 min (blue). I_D-V_G characteristics (saturation regime, V_D=50 V) of InAs QD FETs (d) with Na_2S solution

exchange only (black) and hybrid ligand exchange with Na_2S (red), and (e) with Na_2S solution exchange and NaN_3 solid-state ligand exchange in linear (black) and log (red) scale. 132

Figure 5.6 XPS spectra of (a) In 3d and (b) Sb 3d lines. Experiment data (black) and fitting of InSb (black), In_2O_3 (blue), and Sb_2O_5 (green). 134

Figure 5.7 XPS spectra of (a) In 3d and (b) Sb 3d lines. Experimental data (black) and fitting (red, blue, green). From top to bottom rows: InSb QDs as synthesized, stored in glovebox for one week and exposed to air for 10 min. 136

Figure 5.8 (a) Absorption spectra and (b) Powder XRD patterns of InAs, $InAs_xSb_{1-x}$ and InSb QD dispersions and films with an As:Sb precursor ratio from 1:0 to 0.9:0.1, 0.5:0.5, 0.1:0.9 and 0:1, respectively. (c) High resolution TEM images of $InAs_xSb_{1-x}$ QDs with x=0, 0.9, 0.5 and 0.1. (d) PL spectra of InAs (black), $InAs_{0.5}Sb_{0.5}$ (red), and InSb (green) synthesized at 300 °C for 15 min. . 138

Figure 5.9 TEM images of $InAs_xSb_{1-x}$ QDs with As:Sb precursor ratio of (a) 10:0, (b) 9:1, (c) 5:5, (d) 1:9 and (e) 0:10. 140

Figure 5.10 Bandgap energies of InAs (black squares), $InAs_xSb_{1-x}$ (blue triangles) and InSb (red dots) as a function of NC diameter square d^2. 141

Figure 5.11 I_D-V_G FET device characteristics of $InAs_xSb_{1-x}$ alloy QDs (saturation regime, V_D=50 V) (a) as fabricated with Na_2S solid-state ligand exchange and (b) after being annealed at 200 °C for 10 min. 142

Figure 6.1 (a) Reaction scheme of InP QD synthesis. TEM images of (b) branched (c) tetrahedral and (d) spherical InP QDs achieved at 190 °C, 200 °C and 210 °C, respectively. 149

Figure 6.2 (a) to (d) TEM images and (e) absorption spectra of InP QDs made with 130 (black), 140 (red), 150 (green), and 160 µL (blue) of $(TMS)_3P$, respectively. (f) UV-Vis absorption of InP

QDs synthesized at 200 °C with 160 μL of $(TMS)_3P$, but different growth times ranging from 10 (black) to 20 (red), 30 (green) and 60 (blue) min. 150

Figure 6.3 Absorption (black) and PL (blue) spectra of tetrahedral InP QD dispersions with (a) MA, (b) OA and (c) TOP as ligands. Dashed line: same sample remeasured after air exposure for 30 min........ 152

Figure 6.4 Solid-state ligand exchange of InP QDs. (a) I_D-V_G characteristics (V_D=50 V) of InP QD FETs with Na_2S (black), NaHS (red), NH_4SCN (green), TBAI (blue), NH_4Cl (cyan), NaN_3 (purple) and MPA (yellow) solid-state ligand exchange. (b) FTIR spectra of InP QDs with Na_2S (black), NaN_3 (red) and NH_4Cl (green) treatment normalized to the film thickness. The area under C-H stretch is integrated for every treatment. (c) UV-Vis absorption spectra of InP QD film as made (black), after Na_2S ligand exchange (red) and after Na_2S ligand exchange and being annealed at 300 °C for 10 min (green). (d) TEM images of InP QDs before (left) and after (right) the solid-state Na_2S ligand exchange........ 155

Figure 6.5 I_D-V_G characteristics of InP QD FETs (V_D=50 V) (a) with Na_2S solid-state (black) and solution (red) ligand exchange, (b) with Na_2S solution exchange only (black), and solution and solid-state Na_2S (red), NaN_3 (blue) and NH_4Cl (green) ligand treatment. 157

Figure 6.6 I_D-V_G characteristics of InP QD FETs (V_D=50 V) (a) with Au (black), Al (red), Ag (green) and In/Au (blue) top contacts, (b) without (black) and with (red) 5 Å of Sn deposited and annealed at 150 °C for 10 min (green), (c) with Au (d) with In/Au electrodes before (black) and after (red) 2-nm Se doping and annealing at 300 °C for 10 min. 160

Figure 6.7 (a) Statistics and champion performance of InP QD FETs with Na_2S solution exchange and Na_2S or NaN_3 solid-state ligand treatments. (b) I_D-V_G characteristics (V_D=50 V) of champion FETs with Na_2S solution exchange and Na_2S (black) or NaN_3 (red) solid-state treatment. 161

Figure 6.8 I_D-V_G characteristics of InSb QD FETs (a) with Na_2S (black), MPA (red), TBAI (green) and NH_4SCN (blue) solid-state ligand exchange, (b) with InI_3 (dark blue), InI_3-EDT (light blue), Na_2S-InI_3 (light purple) and Na_2S-TOP:$InCl_3$ (dark purple). (c) Electron mobility and V_T of InSb QD FET devices after different solid-state treatments with p-type to n-type doping from left to right. (d) Photos and schematics and (e) photoconductivity measurements (V=10 V) of InSb QD photoconductors with varying ligands. 164

Figure 6.9 Schematics of (a) device structure and (b) I-V measurement setup for InSb and $InAs_xSb_{1-x}$ QD photodiodes. (c) Photoresponse at 1550 nm illumination of InSb and $InAs_xSb_{1-x}$ QD photodiodes with different ligand treatments at 0 V. (d) Representative I-V characteristics of Na_2S treated $InAs_xSb_{1-x}$ QD photodiodes in the dark (black) and under 1550 nm illumination (red). Inset: responsivity calculated based on the photocurrent. 167

Figure 7.1 Room and low temperature PL spectra of InSb QDs. 173

Figure 7.2 I_D-V_G characteristics of representative InAs QD FETs (a) as fabricated (black), stored in a glovebox for 4 dyas (red), with air exposure for 5 min (green) and after being re-annealed at 300 °C for 5 min in a glovebox, and (b) before (black) and after (red) ALD encapsulation and further being annealed at 300 °C for 2 min in inert glovebox atmosphere (green). 175

Figure 7.3 The proposed device structure for all III-V QD based solar cells. 177

CHAPTER 1 Introduction

1.1 From Bulk Semiconductors to Quantum Dots (QDs)

Semiconductors are solid-state materials with electrical conductivity that's "just right" between that of insulators and that of most of metals, tunable through the introduction of impurities ("doping") and the application of external stimuli.[1] Owing to their electric-field controllable conductivity, semiconductors, specifically silicon, have been extensively used to build circuits, forming the material foundation for the modern electronics industry. Semiconductors are also responsive to photoexcitation, essential for light detection and energy conversion, and therefore have been widely exploited in optoelectronic devices.[2]

These exceptional properties of semiconductors originate from their moderate bandgap energies between that of metals (0 eV) and insulators (>4 eV), which is the energetic difference between their conduction and valence bands. The formation of the conduction band, valence band and bandgap are elaborated as follows.[1] For every atom, a nucleus is surrounded by electrons in atomic orbitals with quantized energies. Only the outmost orbital is not fully filled by electrons, and these electrons in the outer shell are called valence electrons. When the distance of two atoms approaches the lattice constant, the wavefunctions of the valence electrons overlap. Through this orbital interaction, two new orbitals are generated, namely bonding and anti-bonding orbitals with reduced and augmented orbital energies, respectively. As a result, the bonding orbital is filled with electrons while the anti-bonding orbital is empty at 0 K. Applying this theory to semiconductor crystals containing numerous atoms, the bonding orbitals will develop into a continuous energy band called the valence band and will be filled by electrons. Likewise, the empty antibonding orbitals will broaden into a conduction band. Only electrons excited into the conduction band and missing electrons, or "holes" in the valence band move freely and contribute to electrical conductivity. For intrinsic semiconductors, there is no available state for electrons to reside between the two bands, therefore the size of this bandgap determines the energy required

to generate free electrons in the conduction band and holes in the valence band. This linear combination of atomic orbital is illustrated in Figure 1.1 for a typical semiconductor with valence electrons originating from atomic s and p orbitals.[1]

Electrons follow the Pauli exclusion principle and fill up the valence band beginning from the lowest energy state. At thermodynamic equilibrium, the energy level with exactly 50% probability of being occupied is defined as Fermi level, E_F [Figure 1.1b].[3] In general, the probability that a state with energy E is occupied by an electron is given by the Fermi function f(E) derived from the Fermi-Dirac distribution:[3]

$$f(E) = \frac{1}{e^{(E-E_F)/k_B T} + 1}$$

where k_B is Boltzmann's constant and T is absolute temperature. The temperature dependence of f(E) is illustrated in Figure 1.1b. The probability of having high-energy electrons increases with temperature.

The conductivity of the semiconductor is directly proportional to the number of free carriers including electrons in the conduction band and holes in the valence band. Electrons can only reside at energies with existing electronic states, and the number of electronic energy states per unit volume per unit energy is termed the density of states g(E). Considering the probability for electrons to occupy available states at energy E given by f(E), the concentration of electrons in the conduction band n_0:

$$n_0 = \int_{E_c}^{E_{top}} g_c(E) \cdot f(E) dE$$

where E_c and E_{top} is the bottom and top of conduction band, respectively. To calculate the hole concentration in the valence band p_0, [1-f(E)] is used instead to present the probability of hole occupation. g(E) is derived by solving Schrödinger's equation using geometric boundary

conditions.[4] For ideal bulk semiconductors, g(E)=0 when $E_C<E<E_V$, and $g(E)\sim E^{1/2}$ when E is above the bottom of the conduction band or below the top of the valence band. For undoped semiconductors, the intrinsic carrier concentration $n_i=n_0=p_0$. Through temperature, doping, photoexcitation or external field, we can control the concentration of free carriers and manipulate the electronic properties of semiconductor materials.

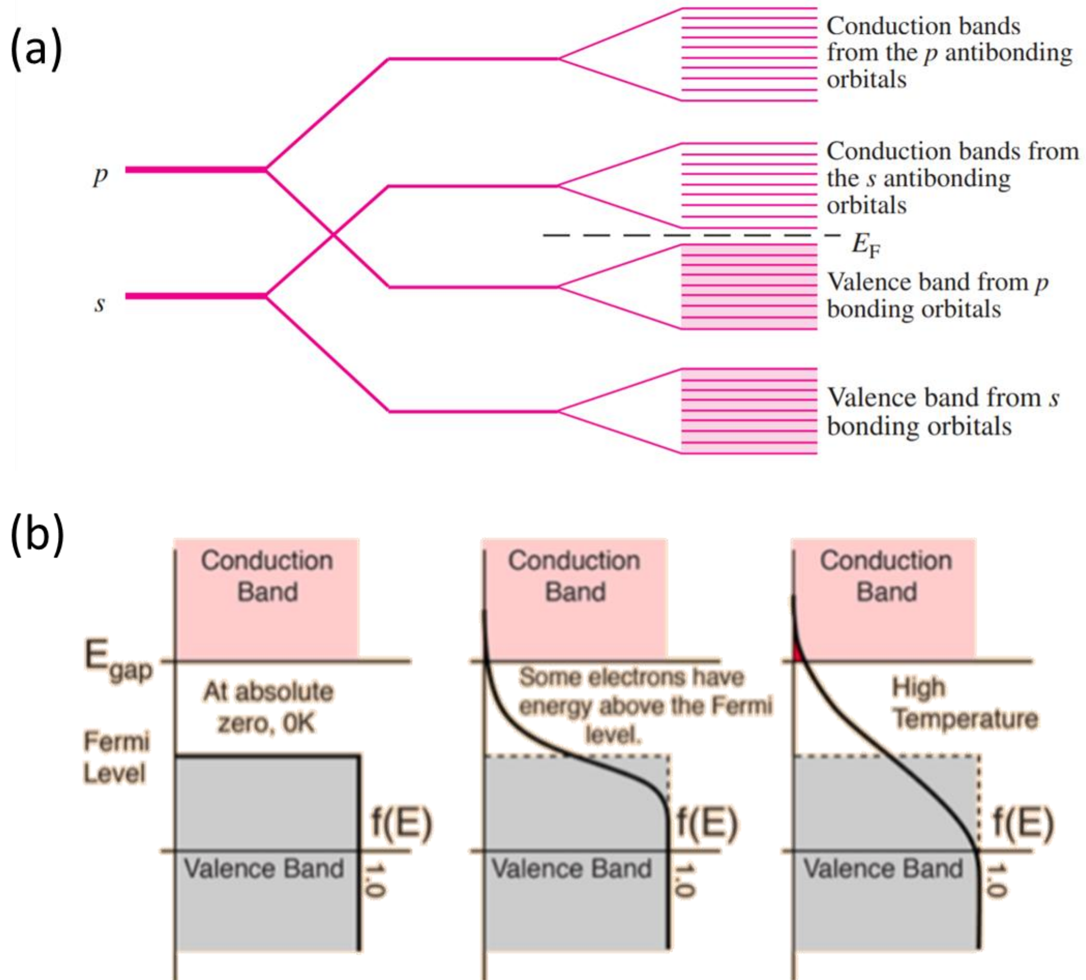

Figure 1.1 (a) Linear combination of atomic s and p orbitals giving rise to valence and conduction bands in a semiconductor.[1] Valence band states formed by s and p bonding orbitals are filled by electrons, and conduction band states formed by s and p antibonding orbitals are empty. The Fermi level E_F lies in the

bandgap between valence and conduction band. (b) Fermi function f(E) at increasingly higher temperatures from left to right.[5] f(E)=0 when $E>>E_F$, f(E)=1/2 when $E=E_F$ and f(E)=1 when $E<<E_F$. f(E)=1 in the valence band (grey) and f(E) is non-zero at the bottom of conduction band (pink) when the temperature is raised.

When the size of semiconductor crystals are reduced to the nanoscale, typically in the range of 1-20 nm, the semiconductor is only composed of hundreds to thousands of atoms. Both theoretically and experimentally,[6,7] these nanosized semiconductor crystals are proven to exhibit discrete energy levels that are intermediate between discrete states of atoms and continuous bands of bulk. The energy gaps between the states, including the bandgap, increase as the crystal size decreases. These size-dependent properties arise from quantum confinement effects, and these semiconductor nanocrystals are often coined quantum dots (QDs). The size-dependent band structure of QDs is well described by the "particle in a box" model in quantum physics, where carriers are confined within the QD diameter 2r by potential walls at the QD surface. Based on the effective mass approximation, assuming infinite potential barriers, parabolic bands, and the bulk effective masses of carriers, the energy states of carriers are found upon solving the Schrödinger equation and take on discrete values $E = \frac{\hbar^2\pi^2 n^2}{2m_0 r^2}$, where m_0 is effective mass, n=1,2,3… Thus, the energy gap between these states are inversely proportional to the QD radius r.[7] In the strong confinement regime when r is small, the confinement energy (~$1/r^2$) is dominant over the Coulomb attraction (~1/r) between charge carriers. It is appropriate to treat carriers, or electrons and holes, independently. Therefore, the effective bandgap energy of QDs becomes:[7]

$$E_{g,effective} = E_g + \frac{\hbar^2\pi^2}{2r^2}\left(\frac{1}{m_{eff}^c} + \frac{1}{m_{eff}^v}\right) - E_{coulomb}$$

where E_g is the bulk bandgap, m^c_{eff} and m^v_{eff} are the effective masses of electrons and holes, respectively, and $E_{Coulomb}$ is the Coulombic attraction energy and is a small correction. A

representative E vs. k diagram is shown in Figure 1.2a to demonstrate this size-dependent bandgap and discrete energy levels of QDs.[8] Optically, the first excitonic peak of QDs shifts to shorter wavelengths, corresponding to a growing of the bandgap energy, and the energy separation between states increases as the particle size decreases from the bulk. As examples, UV-Vis absorption spectra of CdSe and PbS QDs of various sizes are shown in Figure 1.2b and c.

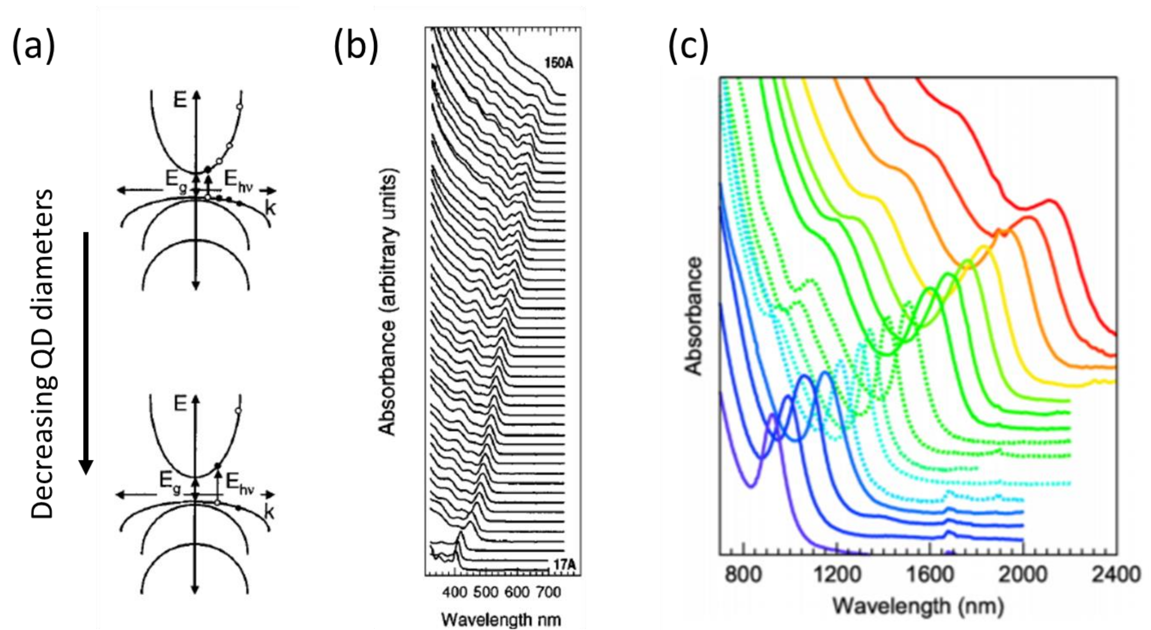

Figure 1.2 (a) E vs. k diagram showing the first energy state is shifted to higher k and energy spacing is increased due to stronger quantum confinement as QD size decreases.[8] UV-Vis spectra of (b) CdSe[8] and (c) PbS[8] colloidal QDs with increasing size.

In addition to quantum confinement effects, there is another non-negligible effect prevailing in low-dimensional materials, known as dielectric confinement.[9] Semiconductor having dielectric constant ϵ_s are often embedded in media with relatively low dielectric constant ϵ_{out},

forming a dielectric mismatch. In bulk, due to the screening effect, the interaction between charge carriers are hardly affected by the dielectric environment [Figure 1.3a]. However, in nanostructures, when one or more of the dimensions are greatly reduced, the electric field lines between charge carriers tend to penetrate into the surrounding dielectric material [Figure 1.3b]. Since ϵ_{out} is low, the Coulomb interaction between carriers will be enhanced, leading to increased exciton binding energy and exciton oscillator strength in nanoscale systems.[10] For QD systems with strong quantum confinement, i.e., for QD sizes equal to or smaller than the exciton Bohr radius, excitons feel the dielectric boundary and the electrical force lines more easily leak out, giving rise to more significant dielectric confinement effects. Additionally, QDs with high dielectric constants, like lead chalcogenides, often have a large dielectric mismatch with their surrounding environment, and are expected to experience more significant dielectric confinement effects.[10] The enhanced Coulomb interactions within QDs from dielectric confinement effects causes electrons to bind more strongly to the impurity dopant atoms, increasing the ionization energy of dopants and therefore limiting the doping efficiency in 0D system. It is of both scientific and technological importance to address the inefficient doping caused by dielectric confinement in low dimensional material systems.

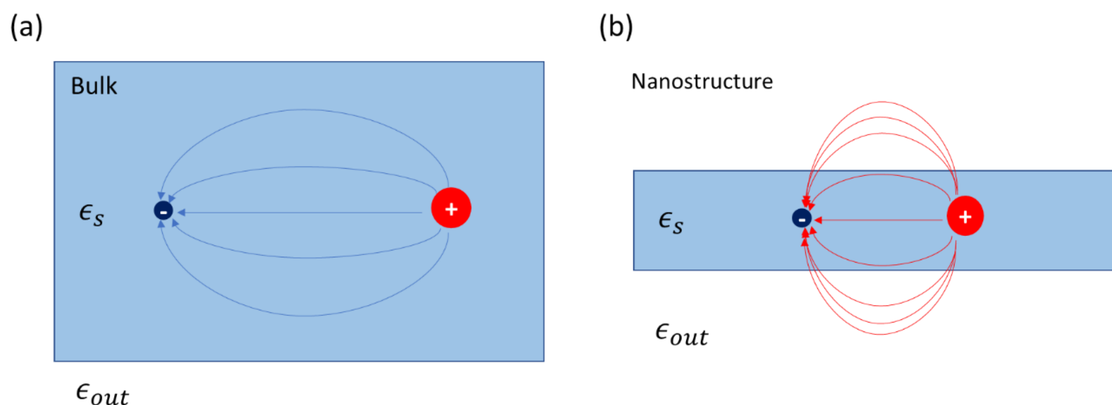

Figure 1.3 Schematics of charge carriers and electric field lines between them in (a) bulk semiconductors and (b) nanostructures. ϵ_s and ϵ_{out} are the dielectric constant of semiconductor and surrounding environment, respectively.

1.2 Colloidal Synthesis of QDs

The unique physical properties, such as the size-dependent bandgap, unveiled in these nanoscale semiconductor crystals, have generated broad interest in QD materials as a platform to study fundamental photophysics[10] as well as to be used as building blocks for next-generation devices, including transistors,[11] solar cells,[12] photodetectors[13] and LEDs.[14] Colloidal synthesis is a wet-chemical approach to prepare inorganic QD cores stabilized by long-chain surface ligands [Figure 1.4a]. Advances in these methods allow the preparation of QD samples uniform and tailorable in size, shape, structure and surface chemistry.[8] The chemical synthetic approach also enables large-scale research and application of QD materials with reduced cost.

A typical synthesis of colloidal QDs involves precursor reagents and stabilizing organic molecules, also referred to as ligands. If one or more precursors are injected at elevated temperatures to initiate QD nucleation and growth, the synthesis approach is named as hot-injection. Whereas, the “heat-up” method, another common way to prepare QDs, includes mixing

all precursors at room temperature and increasing the temperature of the mixture. During the formation of QDs, precursors are firstly transferred into monomers. When the monomer concentration is above the threshold value, they begin to form nuclei followed by particle growth which both consume monomers. The length of the nucleation process depends on how rapid the monomer concentration and/or temperature drops below the threshold. And the reaction is typically quenched once desired particle size is reached. As shown in Figure 1.4b and c, the nucleation and growth processes exist in both the hot-injection and heat-up method, however the two stage are more distinguished in the hot-injection synthesis, while they usually happen more simultaneously during the heat-up approach. Further detailed description of each of these processes will be given in the following sections, respectively. Standard Schlenk line techniques are typically employed to make air-sensitive QDs, such as CdSe, PbSe, InP, etc. Precursor reagents are degassed, reactions are kept in an inert environment and the products are transferred into a nitrogen- or argon- filled glovebox using air free techniques.

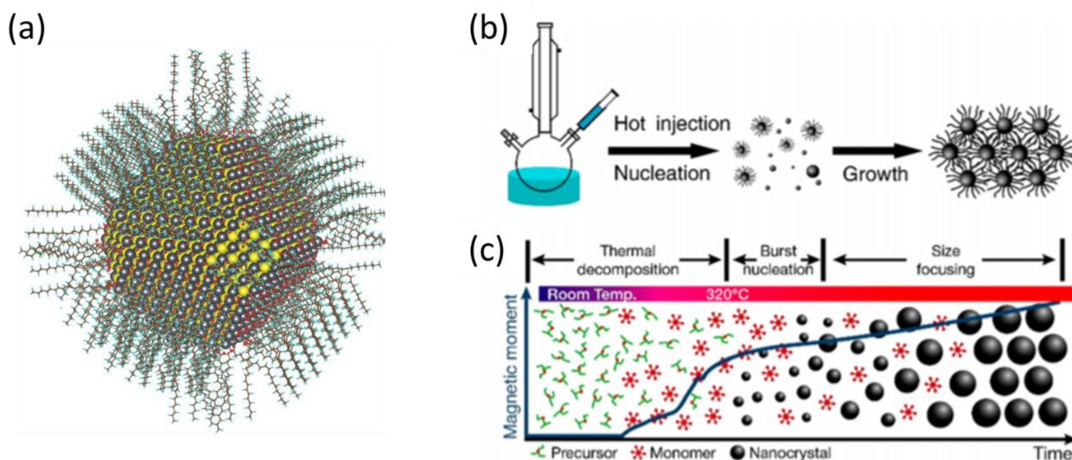

Figure 1.4 (a) A single PbS QD composed of Pb (grey) and sulfur (yellow) atoms with a shell of oleic acid ligands.[15] Schematics of nucleation and growth processes for (b) hot-injection[16] and (c) heat-up[17] synthetic routes to colloidal QDs.

1.2.1 Hot-injection Synthesis of Colloidal QDs

To ensure the monodispersity of colloidal systems, LaMer et. al. described the requirement to separate nucleation and growth processes during synthesis [Figure 1.5a]. Applying this model to QD synthesis, above the nucleation temperature, the monomer concentration must increase rapidly above the saturation limit to initiate nucleation. When the monomers are consumed and the concentration drops below the threshold for nucleation, the nucleation process is ceased and particle growth becomes dominant.[18] If the time scale of the nucleation stage is fast, there will be little particle growth during nucleation, giving rise to a more uniform size distribution [Figure 1.5a, orange].[18] It is often realized by careful selection of precursor reactivity and the rapid decrease of temperature after the injection.[19] Compared to the nucleation stage, particle growth should be at a slower rate in consuming the monomers to ensure the uniformity of QD size. As the reaction time extends, the QD keeps growing by consuming free monomers in the solution. At certain stage, however, reduced size uniformity is commonly observed, as the big QDs grow bigger at the expense of smaller QDs. This Ostwald ripening process happens because decomposition of small QDs with high surface energies is thermodynamically favorable.[19] Therefore, using prolonged reaction times to increase QD particle size should be used with caution if a uniform size distribution is also desired.

The hot-injection synthesis of colloidal QDs is commonly carried out in a three-neck flask setup [Figure 1.5b]. Rapid injection of one precursor into a reaction mixture containing other precursors at elevated temperatures, suddenly boosts the monomer concentration above the threshold concentration descried by the La Mer model to drive a “short burst of nucleation”.[20] Upon injection, the temperature drops and monomer concentration decreases, so the nucleation process is stopped. It is followed by subsequent growth on existing nuclei and the Ostwald ripening stages. Once reaching the desired particle size, the heat source is removed and the

reaction is quenched immediately by a water or ice bath. Experimentally, different QD particle size and shape can be achieved by tailoring the reaction temperature, reactivity and concentration of precursors, and selection of ligands, etc. For example, higher reaction temperature at injection and/or during QD growth and longer reaction time yields larger particles. Higher reactivity or concentrations of precursors promote nuclei formation, shortening the growth period and rendering smaller particles.[21] The concentration and type of ligands also alter the reactivity of precursors resulting in different QD sizes. The shape evolution of QDs is governed by thermodynamic or kinetic driving forces.[22] Facets having high surface energies are less favorable to terminate the QD surface. For example, low-energy {100} surfaces outgrow high-energy {111} surfaces in larger lead chalcogenide QDs, giving rise to size-dependent shape evolution from truncated octahedra to cubes.[23] Preferential growth occurs when the thermodynamic energy provided by the reaction temperature is only sufficient to activate the atom adsorption/ligand desorption on specific facets, leading to growth of these facets at a faster rate and QDs terminated by other facets with slower growth rate. At low temperature, the QD growth is dominated by kinetics, along certain directions that have less steric hindrance.[24] To minimize overall surface energy, QDs fuse into nanowires through oriental attachment.[23]

Pioneered by Murray et al in the early 1990s, the colloidal synthesis of CdE (E=S, Se, Te) QDs are developed and showcased based on the hot-injection method, where dimethylcadmium, TOPSe and trioctylphosphine oxide (TOPO)/ trioctylphosphine (TOP) are used as Cd, Se source and surface ligands, respectively.[20] In a more recent adaptation, cadmium stearate is chosen as the Cd precursor, dissolved in octadecylamine with TOPO as ligands. At a high temperature, e.g. 320 °C, Se in tributylphosphine solution is swiftly injection to form CdSe QDs.[25] Likewise, IV-VI QDs, such as PbS QDs, are synthesized by injecting bis(trimethylsilyl) sulfide (TMS) into a mixture of PbO, oleic acid and octadecene (ODE) at elevated temperatures.[26] A representative synthesis of InP QDs, as an example of the III-V family, includes a solution of indium acetate and myristic acid in ODE and injection of tris(trimethylsilyl)phosphine.[27]

Additionally, derivatives of the simplest single-injection reaction are developed for preparing core/shell structures,[28] seeded growth of large and heterostructured QDs,[29] nanowires,[23] etc.

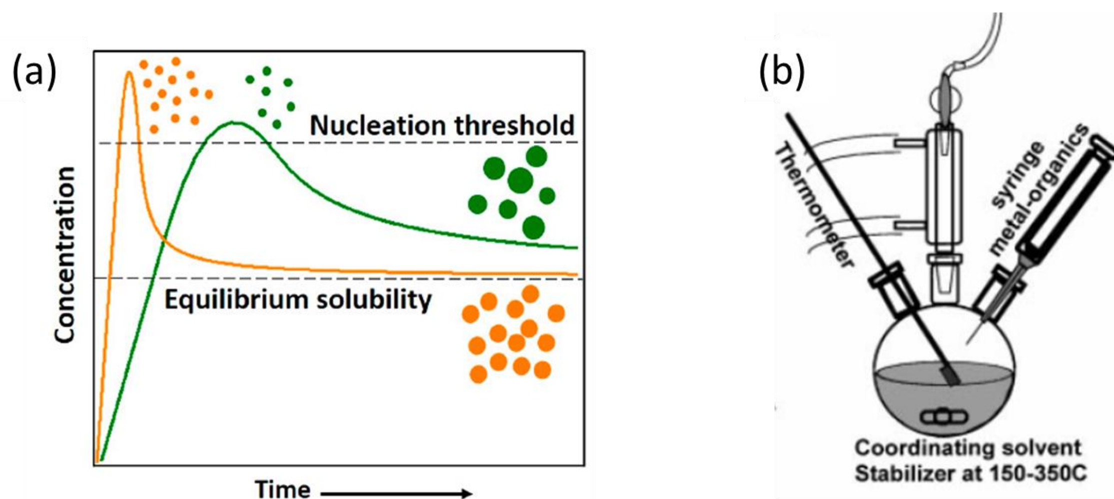

Figure 1.5 (a) LaMer model describing the nucleation and growth stages of colloidal synthesis for a faster (orange) and a slower (green) nucleation process that results in different polydispersity.[30] (b) Three-neck flask setup for hot-injection synthesis.[8]

1.2.2 Heat-up Synthesis of Colloidal QDs

Although the hot-injection method has been well established to build up a library of colloidal QDs, there are several drawbacks potentially detrimental for it to be further scaled up for large area application and high throughput industrial production. For example, as the volume of injection as well as the total reaction increases, the injection rate, cooling time upon injection and reagent mixing time after injection become more difficult to control, introducing additional variation from batch to batch.[31] An alternative route to synthesize QDs is based on the heat-up approach, where all precursors and reagents are mixed at room temperature and heated up to induce

nucleation and growth of QDs. Figure 1.6a shows the chemical reactions and intermediate species formed during the transition from precursors to QDs. As the reaction solution is heated, the original precursors thermally decompose or “crack” to yield monomers needed to form the final QD lattice. Then nuclei are formed and grow into QD crystals. The nucleation and growth stages are depicted in more detail in Figure 1.6b. The rate constant of precursors conversion to monomers and monomer conversion to nuclei transitions are described by k_f and $k_{1,p}$, respectively. Once the concentration of monomers is above a threshold value, new nuclei are formed and eventually grow through the addition of monomers diffused from the solution to the QD surface at a diffusivity D. At the QD surface, the growth and dissolution happen simultaneously at a rate k_g and k_d, respectively.

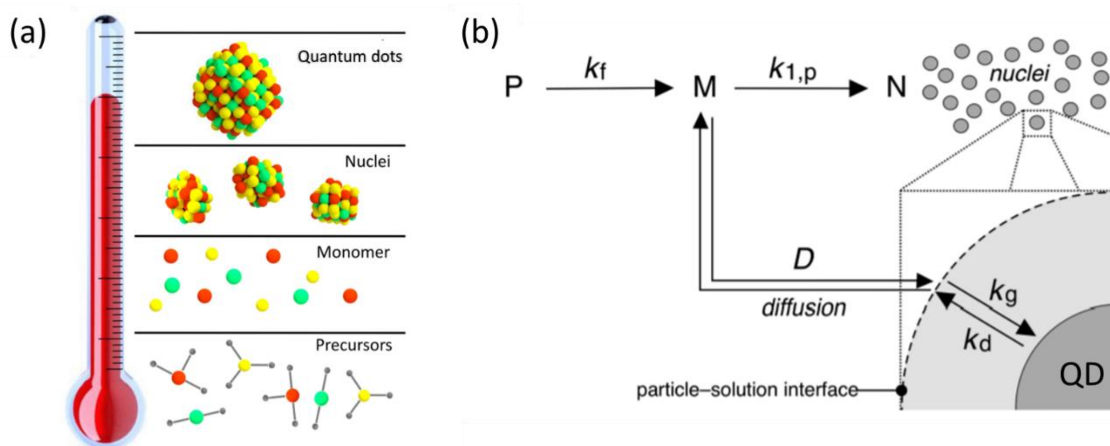

Figure 1.6 (a) Initial, intermediate, and final chemical species at different stages of the heat-up synthesis. (b) Schematics to describe the nucleation and growth processes during the heat-up reaction.[31]

In contrast to the separate nucleation and growth events during the hot-injection reaction, the two stages overlap strongly in the heat-up synthesis process [Figure 1.4b and c], because of

the extended nucleation stage. During the heat up, the production rate of monomers increases with temperature, keeping the monomer concentration above the nucleation threshold. Meanwhile, the growth of nuclei consumes monomers and reduce their concentration. The comingled nucleation and growth events of the heat-up method requires a balance between the nucleation and growth rates to yield monodisperse QDs.[31] Experimentally, the heating rate and choice of precursors and ligands are two major knobs to tune the nucleation and growth rates, and hence affect the QD particle size and size distribution.[31] Under fast heating rates, the formation of monomers from precursors is much faster than the consumption of monomers needed by the nuclei growth. Therefore, the majority of monomers form nuclei, while the rest are distributed among these nuclei for further particle growth. This results in a smaller particle size but improved size distribution and higher production yield.[31] The choice of precursor reagents and ligands together determines the reactivity of the precursor. If the precursor is highly reactive, monomers may form even at room temperature. At high temperatures, both generation and consumption rates of monomers are high, so that the nucleation is rapidly terminated by the growth process, giving rise to a broad size distribution. On the other hand, low precursor reactivity delays the beginning of nucleation and inhibits particle growth. The resulting longer growth time is usually accompanied by the Ostwald ripening process that further deteriorates the size uniformity. The role of the ligand here is to modify the nucleation and growth via binding to precursors. Weaker binding energy between ligands and monomers is favorable for nucleation, but stabilization of the colloidal system requires sufficiently strong chemical bonds between ligands and the QD surface.[31] By selecting appropriate precursors and ligands, we can achieve moderate precursor reactivity to balance the nucleation and growth rates and narrow the QD size distribution, while providing enough stability to the colloidal system.

Successful examples of heat-up synthesis include II-VI (CdS,[32] CdSe,[33] CdTe,[34] CdS_xSe_{1-x},[35] $CdSe_xTe_{1-x}$,[36] ZnS,[37] etc.), IV-VI (PbS,[38] PbSe,[39] PbTe,[40] etc), III-V (InP,[41] InAs,[30] InSb[42]), and other metal chalcogenides (Ag_2S,[43] Cu_2S,[37] etc.) QDs. A wider range of QD

synthesis based on the heat-up method is still under construction to expand the QD library by exploring more precursor-ligand chemistries.

1.2.3 Purification and Size Selection of Colloidal QDs

After either hot-injection or heat-up synthesis, the crude reaction needs to be further purified to remove excess organic reagents and other by-products and yield the final QD product. Depending on the air stability, QDs can be washed in open air or in a glovebox circulating an inert atmosphere. The purification usually includes sequential precipitation and redispersion of QDs by adding nonsolvents and solvents.[20] Typically as synthesized, the QDs are sterically stabilized by long organic ligands in non-polar solvents. The addition of nonsolvents, such as methanol, acetone, etc., increases the polarity of the solvent and causes the organic ligands to contract and minimize their interaction with the environment, destabilizing QD dispersions by reducing the interdot repulsive forces provided by the organic ligands. The QDs then aggregate and are precipitated through centrifugation, while precursor residues and by-products of the reaction are separated and removed along with the supernatant. The isolated QD solids are re-dispersible in non-polar solvents, including hexane, octane, toluene, etc., if there is still a sufficient amount of surface ligands bound. Repetition of such steps are usually required to completely purify the QD materials. Recent studies have shown that protic solvents, like alcohols, strip ligands as well as metal atoms off the QD surface more effectively than aprotic solvents, e.g. acetone and acetonitrile.[44] Therefore, the selection of nonsolvents and number of washing cycles affect the colloidal stability, as well as the optical and electronic properties of the QDs.

An important process derived from the differential dispersability of QDs in solvents is to size-select QDs by titration of a nonsolvent.[20,45] In the distribution of QDs, bigger QDs tend to aggregate before smaller ones due to the larger van der Waals forces between bigger QDs when the nonsolvent is added to the QD dispersion. By centrifuging or filtering the partially flocculated

suspension, bigger QDs are collected while the small particles are still dispersed in the supernatant. As such gentle precipitation is repeated, step by step, a series of QDs can be obtained with different sizes. Reducing the titration step size or slowing down the destabilization process helps further narrow the size distribution.[16]

1.3 Surface Modification of QDs

QDs are promising building blocks for next-generation thin film technologies. Owing to their nanoscale dimensions, QDs have a large surface-to-volume ratio, a geometric feature commonly shared by all nanomaterials. Consequently, surface composition and structure play an influential role in determining the electronic properties of QD solids, including carrier mobility, carrier lifetime, doping concentration and energy levels. Through surface modification, such as ligand exchange and remote doping, we can design and engineer the surface chemistry, stoichiometry and composition to tailor material properties of QD thin films and build functional devices. In the rest of this section, surface modification strategies and their effects on QD thin films are further discussed.

1.3.1 Ligand Exchange of QDs

As introduced in section 1.2, surface ligands are molecules that bind to QD surface atoms. Ligands are necessary during chemical synthesis to control the kinetics of QD nucleation and growth, to passivate surface dangling bonds, and to sterically stabilize QDs in solvents to form colloidal dispersions. Based on the bonds between metal atoms and ligand headgroups, there are three types of ligands commonly encountered in the QD systems.[46] L-type ligands are charge neutral with a lone electron pair coordinating surface metal atoms. Examples include amines (RNH_2), phosphines (R_3P), and phosphine oxides (R_3PO). X-type ligands generally bind

to charged surface sites in the form of opposite ionic species, such as carboxylates ($RCOO^-$), thiolates (RS^-), phosphonates ($RPO(OH)O^-$) and inorganic ions (halides, chalcogenides, pseudohalides, etc.). For some chalcogenide QDs, neutral molecules can also attach to electron-rich sites through their metal atoms as electron acceptors, classified as Z-type ligands. For example, $Pb(OOCR)_2$ and $CdCl_2$ on PbS or CdSe QD surface. Figure 1.7a schematically shows the interaction between three types of ligands and the CdSe QD surface.

Organic molecules with an anchoring headgroup and long hydrocarbon tails, such as L-type trioctylphosphine (TOP), trioctylphosphine oxide (TOPO), oleylamine (OLAM), and X-type oleic acid (OA), typically introduced during chemical synthesis form shells to sterically stabilize the colloidal QD system.[47] However, when assembled into solids, QDs capped by these bulky ligands are poorly conductive due to the lack of electronic communication between semiconductor cores as the organic ligands act as energy barriers, isolating electron wavefunctions within each individual QD.[48] To improve electronic transport, more compact ligands are employed to replace the long organic ligands and reduce interdot distance. This process is referred to as ligand exchange and the choice of new ligands ranges from smaller organic molecules (ethanedithiol, benzenedithiol, mercaptopropionic acid, ethylenediamine, etc.) to inorganic molecules and atomic ions (hydrazine, chalcogenidometallates, halometallates, chalcogenides, hydroxides, halides and pseudohalides).[49] Some solvents (dimethylformamide, alcohols) and reagents (Meerwin's salt) also aid to increase QD assembly conductivity by stripping organic ligands from the QD surface.[47] The ligand exchange reaction is driven by different metal-ligand affinities and the relative abundance of incoming and outgoing ligands. Stronger binding energies and excess concentration make newly introduced ligands more favorable to replace the original ones and attach to the QD surface.[49]

There are two major approaches to implement the ligand exchange process, namely solid-state ligand exchange and solution-ligand exchange, depending on the form of QDs during

the process. Solid-state ligand exchange is performed by applying a solution containing the compact ligands onto a pre-deposited QD solid with long organic surface ligands or immersing the QD film in the solution of new ligands [Figure 1.7b, top].[50] In seconds to tens of seconds, the newly introduced shorter ligands replace the original ligands on the QD surface, leading to a reduction in interparticle distance. The ligand exchange in some cases can also induce a structural rearrangement of the QDs in arrays [Figure 1.7b, bottom]. If the volume change is significant, cracks and voids may form in single-layer ligand-exchanged QD films. Multiple cycles of film deposition followed by solid-state ligand exchange are therefore preferred for device applications to fill in cracks and build up the desired thickness in a layer-upon-layer fashion.[51]

Dispersity of QDs is a crucial requirement for the solution-ligand exchange. In general, QDs capped by long organic ligands are dispersed in non-polar solvents, but aggregate in polar solvents, because it's energetically favorable for the hydrocarbon chains to minimize their contact with polar solvents, leading to ligand contraction and loss of steric stabilization.[49] However, the solubility of compact ligands, typically short anions, is higher in polar solvents than in non-polar solvents. Therefore, the polarity of the QD surface and the dispersing solvent of QDs are typically switched from non-polar to polar after ligand exchange. Taking advantages of this surface chemistry, solution-ligand exchange has proven successful for II-VI, IV-VI and III-V QDs with at least one of the following ligand families, such as chalcogenides[52], halides[53], pseudohalides[54], chalcogenidometallates[55] etc. as ligand reagents. The key to maintaining QD dispersity in polar solvents after solution-ligand exchange is the electrostatic stabilization associated with the new ligands. The charged QD surface is surrounded by oppositely charged counterions to achieve charge balance. In polar solvents with high dielectric constants, such as N,N-dimethylformamide (DMF) and formamide (FA), the electrostatic attraction between oppositely charged ions is screened, thus the QDs are stabilized by a diffuse double layer consisting of counterions.[49] Experimentally, the effective solution-ligand exchange is indicated by the transition of QDs from the non-polar phase into the polar phase [Figure 1.7c, top]. Its advantage over the solid-state

ligand exchange is that the film fabricated after the solution exchange has few to no cracks. Films consist of closely packed QDs, although only short-range ordering has been achieved [Figure 1.7c, bottom].[48] The development of solution-ligand exchange further facilitates the high throughput production of QD thin-film devices by simplifying the film deposition step and reducing material waste.

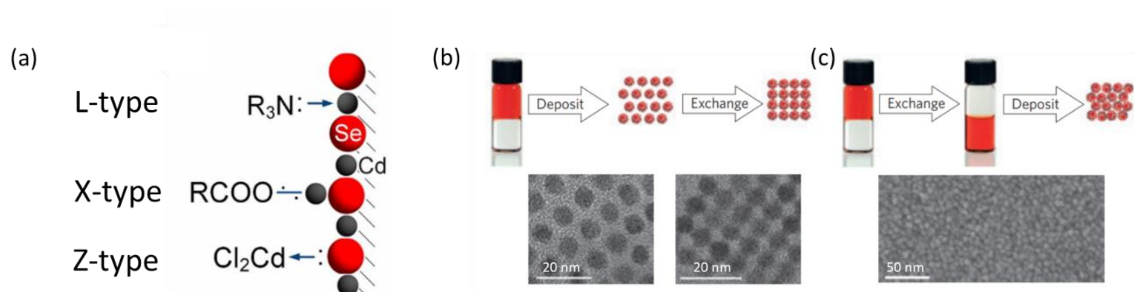

Figure 1.7 (a) Schematics of three categories of ligand binding to the surface of CdSe.[47] (b) Solid-state ligand exchange process, QD film formation and ligand exchange treatment (top) and TEM images of PbSe QD films before and after NH_4SCN ligand exchange (bottom). (c) Solution-ligand exchange steps begin with the ligand exchange treatment and then QD film fabrication (top) and SEM images of a film of SCN-exchanged CdSe QDs.[48]

Besides stabilization, surface ligands influence other physical properties of QD films as well. The size of the ligand molecules determines interdot distance and electronic coupling in QD solids. As the spacing between adjacent QDs decreases, if the energetic and structural disorder is not taken into consideration, the wavefunctions of carriers extend and overlap, transforming the discrete energy levels into a continuous mini-band [Figure 1.8a].[48] The electronic coupling between QDs is enhanced, giving rise to higher carrier mobility and a transition from hopping to band-like transport.[25] Surface ligands passivate dangling bonds and defects. The most widely

studied QD systems, namely CdSe and PbS, are terminated by metal-rich surfaces. The uncoordinated surface atoms and surface vacancies both result in intragap states that can act as trap states if located near mid-gap, reducing carrier lifetime and quenching the photoluminescence of QDs [Figure 1.8b, left].[49] It has been reported that metal halides both introduced at the end of chemical synthesis[56] and used as reagents during solid-state ligand exchange[57] can passivate surface defects and reduce trap-assisted carrier recombination [Figure 1.8b, right]. Through ligand treatments, we can improve carrier mobility and lifetime and hence diffusion lengths within QD films,[58] which are important material properties for electronic and optoelectronic device applications.

Surface ligands alter the carrier concentration within QD films. X-type ligands bring charges to the QD system. A charge-orbital balance model is established to predict doping induced by ligands.[59] If the total charge of positive ions, typically metal ions, is more than that of the negative ions including both the anions in the QD core and X-type ligands, then the QD solids become more n-type (and vice versa p-type). Figure 1.8c shows a correlation between carrier concentration and ligand treatment condition of PbS QD films, providing a convenient guide to designing the doping profile of QD layers within devices. Chalcogenidometallates ligands,[60] such as $[Cd_2Se_3]^{2-}$, $Cu_7S_4^{-}$, etc., can also provide metal ions during thermal decomposition, so that the doping mechanism is different from that of anionic ligands and will be discussed in the next section.

Finally, the absolute energy levels of QD films can be shifted by varying surface ligands. Charged ligands induce additional surface dipoles to the QD system; the dipole between QD surface atoms and ligand headgroups as well as the intrinsic dipole of the ligand molecule itself. Depending on the direction and magnitude of the overall surface dipole, all the energy levels, including the conduction band edge, valence band edge and Fermi level, are shifted towards or away from the vacuum.[61] This shifting of energy levels by a variety of ligands is summarized in

Figure 1.8d. Both carrier concentration and energy level positions are essential to be calibrated before building effective devices.

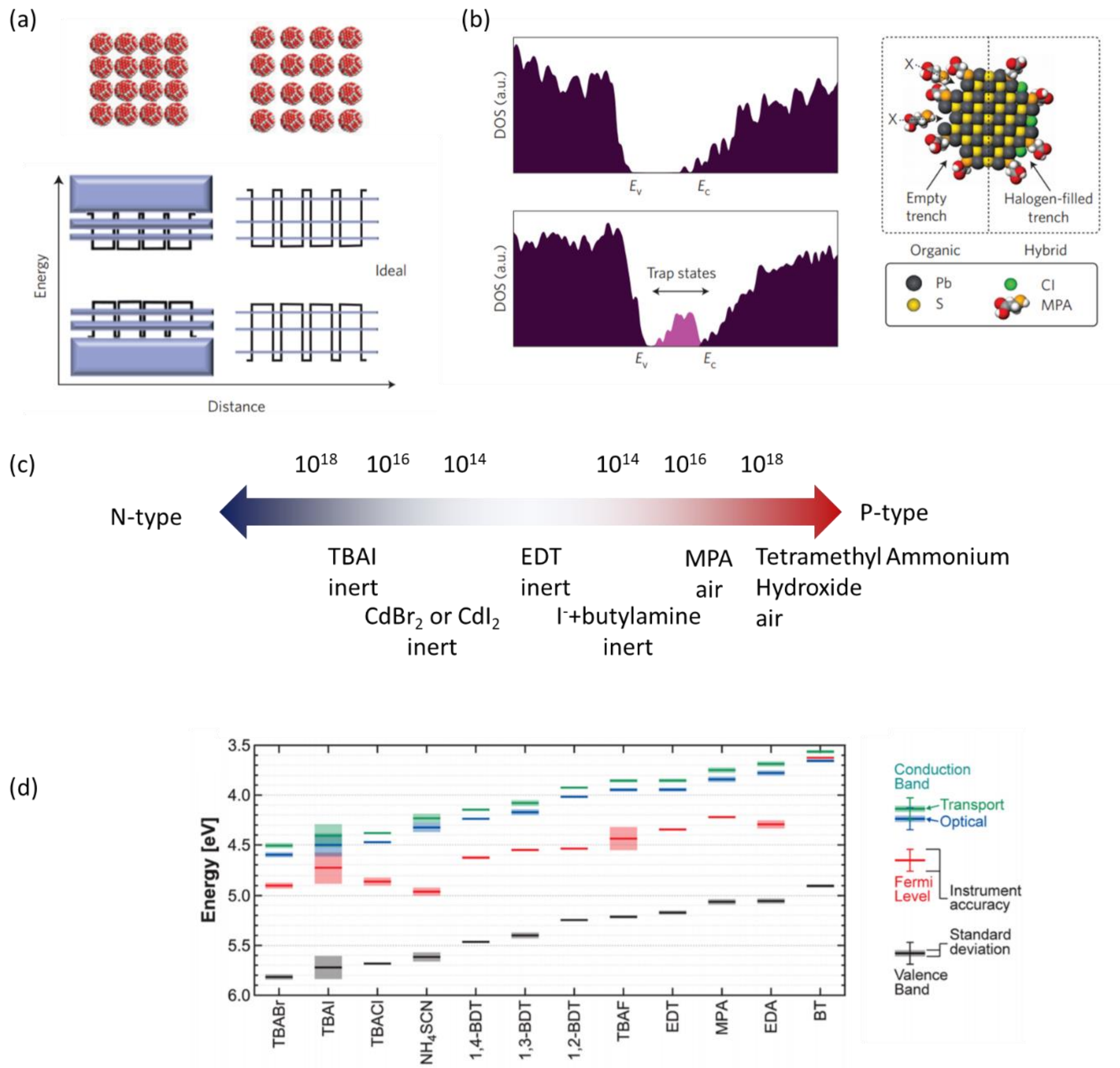

Figure 1.8 (a) Schematics of the electronic states of QD arrays with short ligands (left) and long ligands (right).[48] (b) Density functional theory (DFT) simulated density of states for PbS QDs without (top) and with (bottom) trap states due to uncoordinated surface bonds. Schematic showing halides can passivate surface defects of PbS QDs (right).[56] (c) Carrier type and concentration in PbS QD films after different ligand

exchange treatments in inert or air environments.[59] (d) Energy levels of PbS QD films after ligand treatments measured by ultraviolet photoelectron spectroscopy.[61]

1.3.2 Remote Doping of Nanostructures

Doping is used to tailor carrier statistics and the electrical properties of semiconductors, which further affects device design and performance. Unlike substitutional doping common in bulk semiconductors, doping in QDs can be realized "remotely" by adding dopant atoms on their surface.[48] More specifically, it can be categorized into two groups. One way of changing carrier concentration as well as the Fermi levels in QD films is through the control of surface stoichiometry. In lead chalcogenide QDs, by enriching the QD system with Pb or S(Se), the QD film becomes more n- or p-type and the Fermi level shifts toward conduction or valence band [Figure 1.9a].[62] Similar effect has been reported for CdSe nanowires (NWs).[63] Consistent with the experimental observations, DFT simulation indicates that excess surface Pb induces shallow energy states close to the conduction band, while states introduced by an excess of S atoms lie closely above the valance band.[64] The doping concentration is so sensitive to stoichiometry that QD systems are easily unintentionally doped by any process that alters the stoichiometry. For example, as synthesized QDs tend to form n-type films because they have metal-rich surfaces to satisfy the charge balance between the QDs and X-type ligands. Also, certain solvents, e.g. alcohols, and ligands are known to remove surface metal atoms and change surface stoichiometry.[44]

The other approach developed to dope QD films is by introduction of impurity atoms onto the QD surface. They can be added through post-synthesis chemical treatments,[65] diffusion of atoms from thermally evaporated films,[25] and generated during the decomposition of a complex ligand.[55] The impurity atoms, either isovalent or aliovalent to the host atoms, not only change the Fermi level of the QD ensemble, but also increase carrier lifetime and mobility by passivating

surface trap states. For example, CdSe QD thin films have demonstrated outstanding transport properties with carrier mobility >25 cm²/Vs after being annealed with In contacts.[25] Time-resolved microwave conductivity measurements unveil that the thermally diffused In improves the carrier lifetime and the product of quantum yield Φ and carrier mobility μ in the CdSe QD films by passivating surface traps and doping [Figure 1.9b].[65,66]

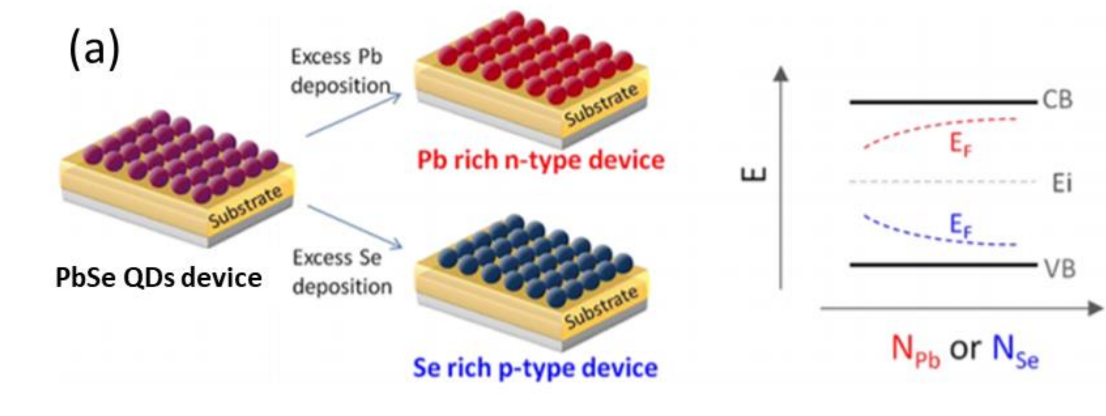

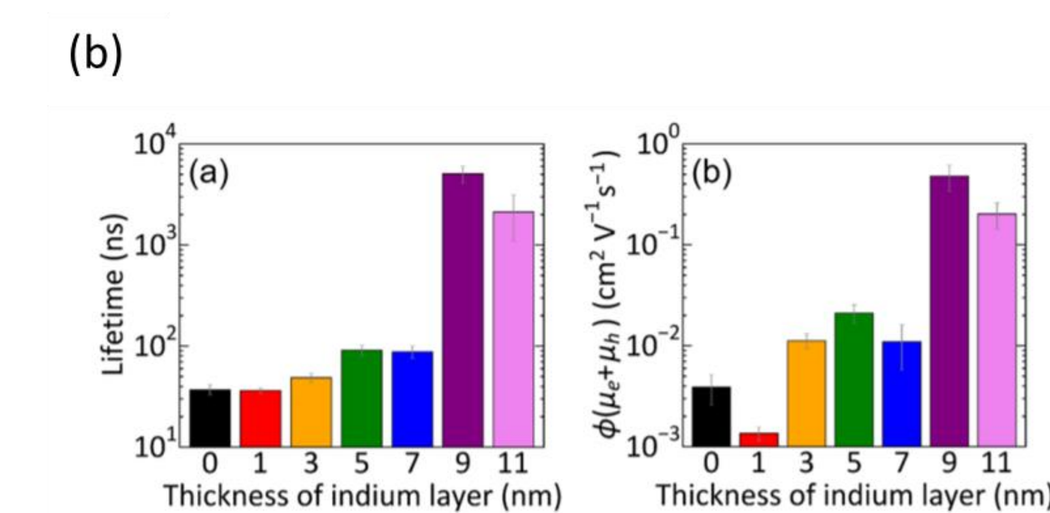

Figure 1.9 (a) Stoichiometry control of PbSe QD films to yield n-type or p-type devices by Pb or Se enrichment through thermal evaporation, respectively (left). The Fermi level is tuned by the number of Pb or

Se added.[62] (b) Time-resolved microwave conductivity measurements to show carrier lifetime (left) and mobility quantum yield product (right) of CdSe QD films as a function of indium film thickness.[66]

1.4 Colloidal QD Based Electronic and Optoelectronic Devices

Owing to the size- and surface-dependent material properties, QDs hold high promise in serving as the active materials in novel electronic and optoelectronic devices.[47] As colloids, QD dispersions can be easily fabricated into large-area thin films through common solution-based coating and printing techniques such as spin-coating, dip-coating, spray-coating, doctor blade coating, inkjet printing, 3D printing, etc.[67] Their low-temperature, vacuum-free and non-epitaxial processes not only reduce fabrication cost, but also are compatible with fabrication on unconventional substrates, such as flexible plastics, to enable the fabrication of QD based flexible circuitry. In the following section, we will review the fundamentals of QD based field-effect transistors, solar cells and photodetectors.

1.4.1 QD Based Field-Effect Transistors

Transistors are the most fundamental device units for modern analog and digital circuitry. Colloidal QDs have been integrated into thin-film field-effect transistors (FETs). The standard bottom gate/top contact FET structure is shown in the schematic in Figure 1.10a, but other configurations of these components, such as top gate/bottom contact, also exist without loss of generality. On top of a gate electrode and dielectric layer stack, typically heavily-doped Si and thermally grown SiO_2 respectively, the QD thin film is fabricated as the channel layer. The film can be deposited first and treated by solid-state ligand exchange, or QDs are solution-ligand exchanged prior to film deposition. Top contacts, namely source and drain electrodes, define the dimension of the FET channel. The Fermi level, carrier concentration and therefore conductivity

of the channel layer is modulated through the gate bias. Typically, the channel material has poor conductivity when zero or insufficient gate bias is applied, and the FET device has low output currents in the off-state. At high gate voltage, a sufficient carrier concentration is accumulated within the Debye length of the QD layer close to the dielectric interface, forming a conductive channel between the source and drain electrodes. This voltage is referred to as the threshold voltage (V_T), and the device operates in the on-state with gate bias higher than V_T. By analyzing the FET characteristics, we can extract their device parameters, including carrier mobility, current modulation (on-off ratio), threshold voltage, hysteresis and subthreshold swing, and use these metrics to probe carrier transport, doping, trap state density, etc. within the QD film and/or at the dielectric interface.

High mobility and on-off ratios of FETs are prerequisite for real device applications. The former can be realized by developing effective ligand exchange strategies to reduce interdot distance, and relatively wider bandgap (II-V and III-V) and low doping concentrations are beneficial for maintaining low off-current. Figure 1.10b shows I_D-V_G characteristics of a representative CdSe QD FET with SCN ligand exchange and In doping.[25] By fitting I_D-V_G in the linear regime ($V_D << V_G - V_T$) and $I_D^{1/2}$ -V_G in the saturation regime ($V_D > V_G - V_T$), linear and saturation mobility can be extracted and found to be ~27 cm^2/Vs in this case. SCN solution-ligand exchange effectively removes long organic ligands and thermal diffusion of In n-dopes CdSe QD films and passivates their surface traps. Recently, chalcogenidometallates ligands have been used as molecular solders to sinter and dope QD films and achieve >200 cm^2/Vs in CdSe[60] and ~15 cm^2/Vs in InAs[55] QD FETs. However, the off-currents in these cases are typically increased and the on-off ratios are reduced possibly due to over-doping by the chalcogenidometallate ligands.

The FET geometry is used as a platform to study the carrier type and change in carrier concentration within the QD layer. As introduced in section 1.3 above, the doping concentration of PbSe QDs is tunable via stoichiometry control. Due to the Pb-rich stoichiometry, PbSe QDs are

unintentionally n-doped as synthesized, giving rise to predominately n-type ambipolar FET characteristics [Figure 1.10c, black]. It becomes more n-type with higher electron currents and lower threshold voltage after Pb deposition [Figure 1.10c, red]. However, when Se is deposited on the FET channel, the device has higher currents at more negative gate voltages [Figure 1.9c, blue], indicating the switch of majority carriers from electrons to holes within the QD channel, induced at negative gate voltages.[62] More quantitatively, the change of carrier concentration (Δn) is linearly proportional to the change in threshold voltage (V_T). Figure 1.10d shows V_T monotonically decreases as PbSe NW FETs are doped by addition of more thermally evaporated Pb, consistent with Fermi level moving closer to the conduction band edge so that lower gate voltages are needed to turn on the device.[68] Based on the change of threshold voltage ΔV_T, Δn is calculated and plotted in the inset of Figure 1.10d.

Although QD based FETs have demonstrated promising properties, such as low-cost fabrication, high carrier mobility, decent on-off ratios and relative air-stability, there are still important scientific and engineering challenges for this technology to be further developed. For example, stable and reliable p-type QD devices with performance comparable to that of the n-type QD devices are absent, impeding the fabrication of QD based complex circuitry such as CMOS.[47]

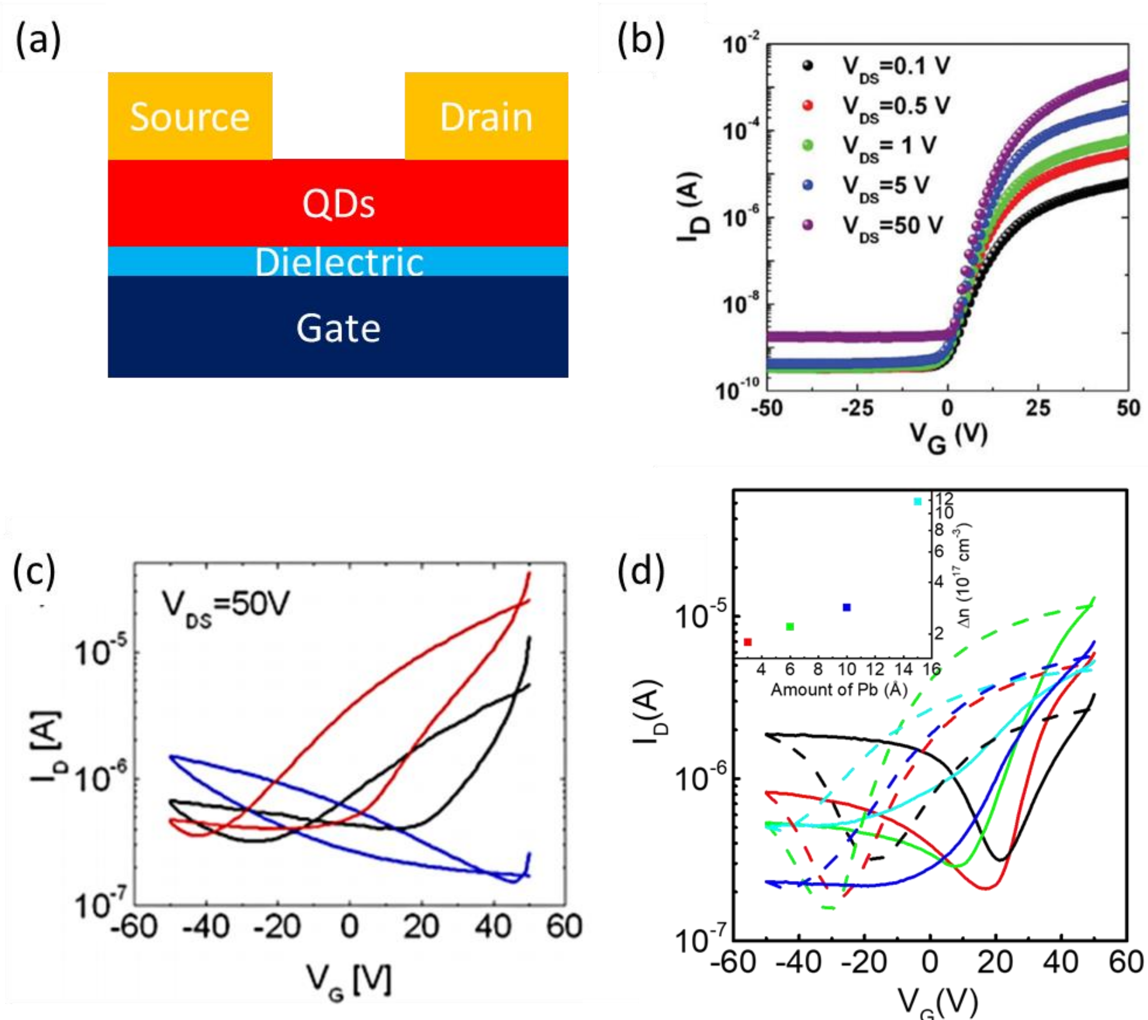

Figure 1.10 (a) A typical configuration for QD thin-film FET devices. Bottom gate electrode is typically heavily doped Si and the gate dielectric layer is thermally grown SiO_2. On top of the QD layer, metal electrodes are usually deposited through evaporation as the source and drain contacts. I_D-V_G characteristics of (b) CdSe QD FETs with SCN ligand exchange and In doping at different source-drain voltages.[25] (c) PbSe QD FETs as fabricated with SCN ligand exchange (black), after deposition of 1 Å of Pb (red) or after 0.1 Å of Se (blue),[62] and (d) PbSe NW array FETs with 0 (black),3 (red), 6 (green),10 (blue) and 15 (cyan) Å of Pb deposited and (inset) Δn calculated from the shift in V_T as a function of the thickness of deposited Pb.[68]

1.4.2 QD Based Solar Cells

Strongly quantum-confined PbS QDs can have bandgap energies between 1.1-1.3 eV, matching their absorption to the region of highest irradiance in the solar spectrum and close to the optimal bandgap described by Shockley and Quiesser, making them promising candidate materials for photovoltaics.[12] Since the first report of PbS QD based solar cells in 2005,[69] there have been extensive studies in this field and significant progress achieved, such that the power conversion efficiency (PCE) of PbS QD solar cells has been improved from <4% to >12%.[70] This advance stems from continuous efforts in both understanding the material science of PbS QDs and improving solar cell device design.

Efficient solar energy conversion relies on successful separation and collection of photogenerated carriers within the thickness of the minority carrier diffusion length L_D and depletion region x_d of a solar cell. Film thickness less than L_D+x_d limits light absorption, but devices with absorbers that are too thick suffer from carrier recombination in the quasi-neutral region, leading to lower fill factor, higher series resistance and lower PCE. L_D is directly proportional to the square root of the mobility and lifetime product of the minority carriers. Through progressive improvements in the passivation of PbS QDs, the minority carrier diffusion length has increased from <80 nm[56] to 230 nm[58] and recently to 300 nm.[70] As a result, the optimal device thickness has been doubled, reaching 600 nm, to achieve more light absorption and higher short-circuit currents without degrading other device parameters.

A depletion region is formed at the metal/semiconductor or p/n semiconductor interface. Photogenerated carriers drift under the built in potential V_{bi}. The width of depletion region x_d for a homojunction is:[71]

$$x_d = \sqrt{\frac{2\epsilon_s}{q}(\frac{1}{N_a}+\frac{1}{N_d})(V_{bi}-V_a)}$$

where ϵ_s is the permittivity of the semiconductor, N_a and N_d are the concentrations of acceptors in the p-type material and donors in the n-type material, respectively, and V_a is applied bias. If one side of the junction is much more highly doped than the other side, for example $N_d >> N_a$, then the depletion region will lie mostly within the p-side of the junction and the depletion width is inversely proportional to N_a. To elongate the depletion width, the PbS QD device structure employed has evolved from that of a Schottky junction to that of a heterojunction and to a p-i-n junction [Figure 1.11]. Schottky junction PbS QD solar cells are the most straightforward and earliest reported device structure [Figure 1.11a].[69] With optimized device fabrication process, the PCE reaches 5%,[72] but is limited by the need to illuminate the QD thin film through a transparent electrode away from metal-semiconductor junction. The heterojunction structure is adopted to overcome this problem. A wide bandgap oxide e.g. ZnO in Figure 1.11b is used to replace the opaque metal of the Schottky junction. ZnO creates a highly n-doped region at the junction that is mostly transparent to visible and infrared light. When it's illuminated from the ZnO side, light with energy lower than the bandgap of ZnO can reach the PbS QD layer and generate carriers at the junction interface,[73] and a depletion region that extends into the p-type PbS QD layer. The incorporation of hole transport layers, such as MoO_3, creates favorable band bending for carrier extraction.[74] Combined with advanced ligand passivation methods, the PbS QD heterojunction solar cell boosted PCE >7%.[56] In 2014, the development of a p-i-n structure marked another breakthrough for PbS QD solar cells.[75] In this device design, the depletion width is further extended by introducing on top of an intrinsic TBAI-treated PbS QD layer, a more heavily p-doped EDT-capped PbS QD layer [Figure 1.11c]. The EDT-PbS QD film serves as a hole transport layer and improves air-stability of the device as well. Recent progress in reducing structural and energetic disorder in the intrinsic PbS QD layer by exploiting a 2D matrix of PbI_2 raises the PCE above 12%, making it competitive with other emerging thin-film photovoltaic technologies, up until recently, with the introduction of metal halide perovskite solar cells.[70]

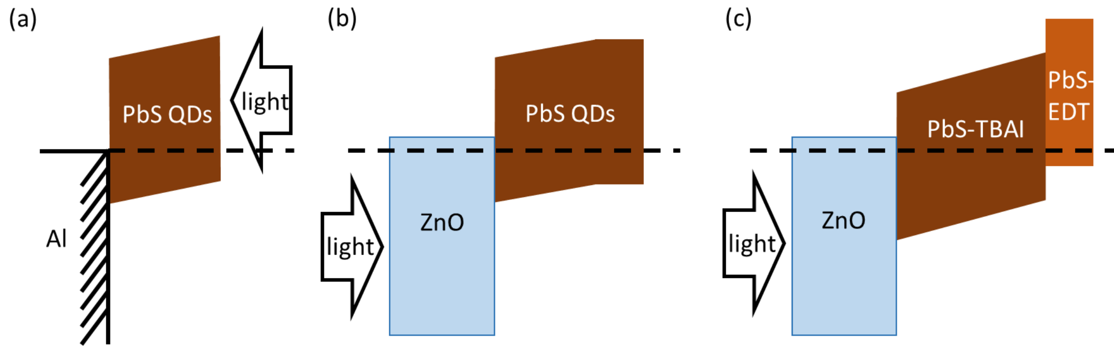

Figure 1.11 Band diagram schematics of (a) Schottky junction (b) heterojunction and (c) p-i-n junction PbS QD solar cells.

1.4.3 QD Based Photodetectors

Photodetectors are a class of devices with photo-responsivities as photogenerated carriers are conducted out of the semiconductor and received by a read-out integrated circuit (ROIC).[47] Photodiodes are one kind of photodetectors. Additionally, two terminal photoconductors and three terminal phototransistors are also typical photodetector structures. The most significant difference during the operation of these three structures is that both photoconductors and phototransistors are majority carrier devices with lateral carrier transport, while photodiodes rely on minority carriers moving vertically.

Similar to other device applications, QDs have advantages over bulk materials when making photodetectors such as the easy, low-cost and large area fabrication and compatibility with flexible substrates.[76] Moreover, based on the quantum confinement effect, the tunable bandgap energy of QDs allow a wider spectral range for applications compared to other solution processable systems [Figure 1.12]. QD photodetectors also show broadband spectral sensitivity, especially in the IR region that is not cover by Si.[13] Table 1.1 lists the general performance metrics for photodetectors, where external quantum efficiency quantifies the conversion efficiency

of optical signals to electrical signals, 3dB bandwidth presents the working frequency range of the device, and specific detectivity is a normalized metric that can be used to compare the sensitivity of different photodetector technologies regardless of their geometry and design.

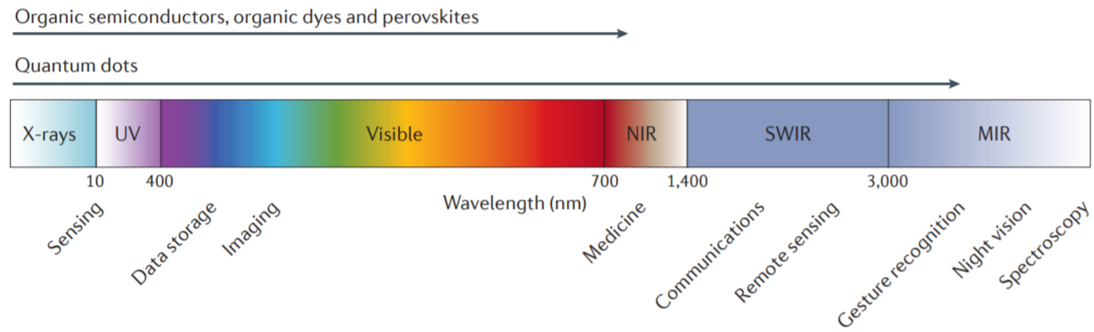

Figure 1.12 Spectral coverage of QD photodetectors compared to other solution processible photodetectors.[76]

Table 1.1 Performance metrics of photoconductors[76]

Metric	Unit	Definition
Photocurrent (I_{ph})	A	Current flowing through a device owing to illumination
Dark current (I_d)	A	Current flowing in the absence of illumination
Responsivity (R)	A W^{-1}	R =I_{ph}/P, P incident optical power
External quantum efficiency (EQE)	%	Number of carriers circulating divided by the number of incident photons
Gain (G)	Unitless	Number of collected carriers divided by the number of photons absorbed
−3dB bandwidth (BW)	Hz	Modulation frequency at which the responsivity of the device is half of that at steady state conditions
Linear dynamic range (LDR)	dB	Range of incident optical powers for which the detector responds linearly
Noise current (I_N)	A $Hz^{-1/2}$	Root mean square of current fluctuation
Noise-equivalent power (NEP)	W $Hz^{-1/2}$	Optical power that would be required to generate the given noise current spectral density $I_N/B^{1/2}$. It is a measure of the sensitivity of the device ($NEP=(I_N/B^{1/2})/R$)
Specific detectivity (D*)	cm $Hz^{1/2}$ W^{-1} (Jones)	NEP normalized to the area of the device (A) and to the electrical bandwidth of the noise measurement (B): $D^*=A^{1/2}/NEP=R(AB)^{1/2}/I_N$
Spectral selectivity (FWHM)	nm	Full width at half maximum resonance width

1.5 Thesis Overview

Through this thesis, we systematically study the effect of surface modification on the physical properties of II-VI, IV-VI and III-V QD systems and exploit surface-modified QDs in the fabrication of thin-film electronic and optoelectronic devices, including FETs, solar cells and photodetectors. By engineering the QD materials and improving device design, we enhance device performance.

Chapter 2 and 3 focus on two important interfaces in PbS QD solar cells, namely the ZnO nanoparticle/PbS QD junction interface and the PbS QD/Au back contact interface, respectively. In Chapter 2, a thin CdSe QD buffer layer is designed with CdI_2 ligand exchange to suppress interface recombination and provide additional photogenerated carriers to the PbS QD heterojunction solar cell. In Chapter 3, we develop a solution phase colloidal atomic layer deposition method to controllably enrich the surface of 3 nm PbS QDs with sulfur. The motivation of this study is to increase carrier concentration in the p-type EDT-PbS QD layer to reduce observed Schottky barriers at the Au back contact and create a band alignment that facilitates hole extraction.

Chapter 4 studies the effect of dielectric confinement on the doping efficiency in PbSe nanowires by altering the surrounding dielectric environment. It unveils the reason for low doping efficiency in these low dimensional nanostructures and provides facile approaches to improve it.

In Chapter 5 and 6, we extend our studies to III-V QDs. We firstly develop a general route to synthesize InP, InAs, InSb and $InAs_xSb_{1-x}$ QDs based on the co-reduction of indium and pnictogen halides in Chapter 5. In Chapter 6, III-V QD based FETs and photodetectors are fabricated with newly developed ligand exchange strategies.

Chapter 7 proposes future works to further investigate III-V QDs and design their electronic and optoelectronic devices, and concludes this thesis.

1.6 References

(1) Yu, P. Y.; Cardona, M. *Fundamentals of Semiconductors : Physics and Materials Properties*; Springer, 2010.

(2) Rudan, M. *Physics of Semiconductor Devices*; Springer International Publishing: Cham, 2018.

(3) Kittel, C. *Introduction to Solid State Physics*; Wiley, 2005.

(4) Alivisatos, A. P. Semiconductor Clusters, Nanocrystals, and Quantum Dots. *Science.* **1996**, *271* (5251), 933–937.

(5) Hyperphysics. Fermi level and Fermi function[online] http://hyperphysics.phy-astr.gsu.edu/hbase/Solids/Fermi.html.

(6) Ekimov, A. I.; Efros, A. L.; Onushchenko, A. A. Quantum Size Effect in Semiconductor Microcrystals. *Solid State Commun.* **1985**, *56* (11), 921–924.

(7) Brus, L. E. Electron–electron and Electron-hole Interactions in Small Semiconductor Crystallites: The Size Dependence of the Lowest Excited Electronic State. *J. Chem. Phys.* **1984**, *80* (9), 4403–4409.

(8) Murray, C. B.; Kagan, C. R.; Bawendi, M. G. Synthesis and Characterization of Monodisperse Nanocrystals and Close-Packed Nanocrystal Assemblies. *Annu. Rev. Mater. Sci.* **2000**, *30* (1), 545–610.

(9) Pereira, R. N.; Stegner, A. R.; Andlauer, T.; Klein, K.; Wiggers, H.; Brandt, M. S.; Stutzmann, M. Dielectric Screening versus Quantum Confinement of Phosphorus Donors in Silicon Nanocrystals Investigated by Magnetic Resonance. *Phys. Rev. B* **2009**, *79* (16),

161304.

(10) Takagahara, T. Effects of Dielectric Confinement and Electron-Hole Exchange Interaction on Excitonic States in Semiconductor Quantum Dots. *Phys. Rev. B* **1993**, *47* (8), 4569–4584.

(11) Hetsch, F.; Zhao, N.; Kershaw, S. V.; Rogach, A. L. Quantum Dot Field Effect Transistors. *Mater. Today* **2013**, *16* (9), 312–325.

(12) Carey, G. H.; Abdelhady, A. L.; Ning, Z.; Thon, S. M.; Bakr, O. M.; Sargent, E. H. Colloidal Quantum Dot Solar Cells. *Chem. Rev.* **2015**, *115* (23), 12732–12763.

(13) Saran, R.; Curry, R. J. Lead Sulphide Nanocrystal Photodetector Technologies. *Nat. Photonics* **2016**, *10* (2), 81–92.

(14) Choi, M. K.; Yang, J.; Hyeon, T.; Kim, D.-H. Flexible Quantum Dot Light-Emitting Diodes for next-Generation Displays. *npj Flex. Electron.* **2018**, *2* (1), 10.

(15) Zherebetskyy, D.; Scheele, M.; Zhang, Y.; Bronstein, N.; Thompson, C.; Britt, D.; Salmeron, M.; Alivisatos, P.; Wang, L.-W. Hydroxylation of the Surface of PbS Nanocrystals Passivated with Oleic Acid. *Science* **2014**, *344* (6190), 1380–1384.

(16) Park, J.; Joo, J.; Kwon, S. G.; Jang, Y.; Hyeon, T. Synthesis of Monodisperse Spherical Nanocrystals. *Angew. Chemie Int. Ed.* **2007**, *46* (25), 4630–4660.

(17) Kwon, S. G.; Piao, Y.; Park, J.; Angappane, S.; Jo, Y.; Hwang, N.-M.; Je-Geun Park, A.; Hyeon, T. Kinetics of Monodisperse Iron Oxide Nanocrystal Formation by “Heating-Up” Process. *J. Am. Chem. Soc.* **2007**, *129* (41), 12571–12584.

(18) LaMer, V. K.; Dinegar, R. H. Theory, Production and Mechanism of Formation of

Monodispersed Hydrosols. *J. Am. Chem. Soc.* **1950**, *72* (11), 4847–4854.

(19) Srivastava, V.; Dunietz, E.; Kamysbayev, V.; Anderson, J. S.; Talapin, D. V. Monodisperse InAs Quantum Dots from Aminoarsine Precursors: Understanding the Role of Reducing Agent. *Chem. Mater.* **2018**, *30* (11), 3623–3627.

(20) Murray, C. B.; Norris, D. J.; Bawendi, M. G. Synthesis and Characterization of Nearly Monodisperse CdE (E = Sulfur, Selenium, Tellurium) Semiconductor Nanocrystallites. *J. Am. Chem. Soc.* **1993**, *115* (19), 8706–8715.

(21) Harris, D. K.; Bawendi, M. G. Improved Precursor Chemistry for the Synthesis of III–V Quantum Dots. *J. Am. Chem. Soc.* **2012**, *134* (50), 20211–20213.

(22) Peng, X. Mechanisms for the Shape-Control and Shape-Evolution of Colloidal Semiconductor Nanocrystals. *Adv. Mater.* **2003**, *15* (5), 459–463.

(23) Cho, K.-S.; Talapin, D. V; Gaschler, W.; Murray, C. B. Designing PbSe Nanowires and Nanorings through Oriented Attachment of Nanoparticles. *J. Am. Chem. Soc.* **2005**, *127* (19), 7140–7147.

(24) Liu, L.; Zhuang, Z.; Xie, T.; Wang, Y.-G.; Li, J.; Peng, Q.; Li, Y. Shape Control of CdSe Nanocrystals with Zinc Blende Structure. *J. Am. Chem. Soc.* **2009**, *131* (45), 16423–16429.

(25) Choi, J.-H.; Fafarman, A. T.; Oh, S. J.; Ko, D.-K.; Kim, D. K.; Diroll, B. T.; Muramoto, S.; Gillen, J. G.; Murray, C. B.; Kagan, C. R. Bandlike Transport in Strongly Coupled and Doped Quantum Dot Solids: A Route to High-Performance Thin-Film Electronics. *Nano Lett.* **2012**, *12* (5), 2631–2638.

(26) Hines, M. A.; Scholes, G. D. Colloidal PbS Nanocrystals with Size-Tunable Near-Infrared

Emission: Observation of Post-Synthesis Self-Narrowing of the Particle Size Distribution. *Adv. Mater.* **2003**, *15* (21), 1844–1849.

(27) Battaglia, D.; Peng, X. Formation of High Quality InP and InAs Nanocrystals in a Noncoordinating Solvent. *Nano Lett.* **2002**, *2* (9), 1027–1030.

(28) Reiss, P.; Protière, M.; Li, L. Core/Shell Semiconductor Nanocrystals. *Small* **2009**, *5* (2), 154–168.

(29) Talapin, D. V.; Nelson, J. H.; Shevchenko, E. V.; Aloni, S.; Bryce Sadtler; Alivisatos, A. P. Seeded Growth of Highly Luminescent CdSe/CdS Nanoheterostructures with Rod and Tetrapod Morphologies. *Nano Lett.* **2007**, *7* (10), 2951–2959.

(30) Grigel, V.; Dupont, D.; De Nolf, K.; Hens, Z.; Tessier, M. D. InAs Colloidal Quantum Dots Synthesis via Aminopnictogen Precursor Chemistry. *J. Am. Chem. Soc.* **2016**, *138* (41), 13485–13488.

(31) van Embden, J.; Chesman, A. S. R.; Jasieniak, J. J. The Heat-Up Synthesis of Colloidal Nanocrystals. *Chem. Mater.* **2015**, *27* (7), 2246–2285.

(32) Narayan Pradhan; Beni Katz; Efrima, S. Synthesis of High-Quality Metal Sulfide Nanoparticles from Alkyl Xanthate Single Precursors in Alkylamine Solvents. *J. Phys. Chem.* **2003**, *107* (50), 13843–13854.

(33) Brennan, J. G.; Siegrist, T.; Carroll, P. J.; Stuczynski, S. M.; Brus, L. E.; Steigerwald, M. L. The Preparation of Large Semiconductor Clusters via the Pyrolysis of a Molecular Precursor. *J. Am. Chem. Soc.* **1989**, *111* (11), 4141–4143.

(34) Brennan, J. G.; Siegrist, T.; Carroll, P. J.; Stuczynski, S. M.; Reynders, P.; Brus, L. E.; Steigerwald, M. L. Bulk and Nanostructure Group II-VI Compounds from Molecular

Organometallic Precursors. *Chem. Mater.* **1990**, *2* (4), 403–409.

(35) Ouyang, J.; Vincent, M.; Kingston, D.; Descours, P.; Boivineau, T.; Zaman, M. B.; Wu, X.; Yu, K. Noninjection, One-Pot Synthesis of Photoluminescent Colloidal Homogeneously Alloyed CdSeS Quantum Dots. *J. Phys. Chem. C* **2009**, *113* (13), 5193–5200.

(36) Wang, R.; Calvignanello, O.; Ratcliffe, C. I.; Wu, X.; Leek, D. M.; Zaman, M. B.; Kingston, D.; Ripmeester, J. A.; Yu, K. Homogeneously-Alloyed CdTeSe Single-Sized Nanocrystals with Bandgap Photoluminescence. *J. Phys. Chem. C* **2009**, *113* (9), 3402–3408.

(37) Choi, S.-H.; An, K.; Kim, E.-G.; Yu, J. H.; Kim, J. H.; Hyeon, T. Simple and Generalized Synthesis of Semiconducting Metal Sulfide Nanocrystals. *Adv. Funct. Mater.* **2009**, *19* (10), 1645–1649.

(38) Zhang, J.; Gao, J.; Miller, E. M.; Luther, J. M.; Beard, M. C. Diffusion-Controlled Synthesis of PbS and PbSe Quantum Dots with *in Situ* Halide Passivation for Quantum Dot Solar Cells. *ACS Nano* **2014**, *8* (1), 614–622.

(39) Yu, K.; Ouyang, J.; Leek, D. M. In-Situ Observation of Nucleation and Growth of PbSe Magic-Sized Nanoclusters and Regular Nanocrystals. *Small* **2011**, *7* (15), 2250–2262.

(40) Shen, H.; Jiang, X.-D.; Wang, S.; Fu, Y.; Zhou, C.; Li, L. S. Facile Preparation of Metal Telluride Nanocrystals Using Di-n-Octylphosphine Oxide (DOPO) as an Air-Stable and Less Toxic Alternative to the Common Tri-Alkylphosphines. *J. Mater. Chem.* **2012**, *22* (48), 25050.

(41) Li, L.; Reiss, P. One-Pot Synthesis of Highly Luminescent InP/ZnS Nanocrystals without Precursor Injection. *J. Am. Chem. Soc.* **2008**, *130* (35), 11588–11589.

(42) Liu, W.; Chang, A. Y.; Schaller, R. D.; Talapin, D. V. Colloidal InSb Nanocrystals. *J. Am.*

Chem. Soc. **2012**, *134* (50), 20258–20261.

(43) Du, Y.; Xu, B.; Fu, T.; Cai, M.; Li, F.; Zhang, Y.; Wang, Q. Near-Infrared Photoluminescent Ag_2S Quantum Dots from a Single Source Precursor. *J. Am. Chem. Soc.* **2010**, *132* (5), 1470–1471.

(44) Goodwin, E. D.; Diroll, B. T.; Oh, S. J.; Paik, T.; Murray, C. B.; Kagan, C. R. Effects of Post-Synthesis Processing on CdSe Nanocrystals and Their Solids: Correlation between Surface Chemistry and Optoelectronic Properties. *J. Phys. Chem. C* **2014**, *118* (46), 27097–27105.

(45) Vossmeyer, T.; Katsikas, L.; Giersig, M.; Popovic, I. G.; Diesner, K.; Chemseddine, A.; Eychmueller, A.; Weller, H. CdS Nanoclusters: Synthesis, Characterization, Size Dependent Oscillator Strength, Temperature Shift of the Excitonic Transition Energy, and Reversible Absorbance Shift. *J. Phys. Chem.* **1994**, *98* (31), 7665–7673.

(46) Green, M. L. H. A New Approach to the Formal Classification of Covalent Compounds of the Elements. *J. Organomet. Chem.* **1995**, *500* (1–2), 127–148.

(47) Kagan, C. R.; Lifshitz, E.; Sargent, E. H.; Talapin, D. V. Building Devices from Colloidal Quantum Dots. *Science (80-.).* **2016**, *353* (6302), 5523.

(48) Kagan, C. R.; Murray, C. B. Charge Transport in Strongly Coupled Quantum Dot Solids. *Nat. Nanotechnol.* **2015**, *10* (12), 1013–1026.

(49) Boles, M. A.; Ling, D.; Hyeon, T.; Talapin, D. V. The Surface Science of Nanocrystals. *Nat. Mater.* **2016**, *15*, 141–154.

(50) Poirier, G. E.; Pylant, E. D.; Henderson, J. I.; Janes, D. B.; Kolagunta, V. R.; Kubiak, C. P.; Mahoney, W. J.; Osifchin, R. G. The Self-Assembly Mechanism of Alkanethiols on

Au(111). *Science.* **1996**, *272* (5265), 1145–1148.

(51) Koleilat, G. I.; Levina, L.; Shukla, H.; Myrskog, S. H.; Hinds, S.; Pattantyus-Abraham, A. G.; Sargent, E. H. Efficient, Stable Infrared Photovoltaics Based on Solution-Cast Colloidal Quantum Dots. *ACS Nano* **2008**, *2* (5), 833–840.

(52) Nag, A.; Kovalenko, M. V.; Lee, J. S.; Liu, W.; Spokoyny, B.; Talapin, D. V. Metal-Free Inorganic Ligands for Colloidal Nanocrystals: S^{2-}, HS^{-}, Se^{2-}, HSe^{-}, Te^{2-}, HTe^{-}, $TeS^{3\backslash n2-}$, OH^{-}, and $NH^{2\backslash n-}$ as Surface Ligands. *J. Am. Chem. Soc.* **2011**, *133* (27), 10612–10620.

(53) Liu, M.; Voznyy, O.; Sabatini, R.; García de Arquer, F. P.; Munir, R.; Balawi, A. H.; Lan, X.; Fan, F.; Walters, G.; Kirmani, A. R.; et al. Hybrid Organic–inorganic Inks Flatten the Energy Landscape in Colloidal Quantum Dot Solids. *Nat. Mater.* **2017**, *16* (2), 258–263.

(54) Fafarman, A. T.; Koh, W.; Diroll, B. T.; Kim, D. K.; Ko, D.-K.; Oh, S. J.; Ye, X.; Doan-Nguyen, V.; Crump, M. R.; Reifsnyder, D. C.; et al. Thiocyanate-Capped Nanocrystal Colloids: Vibrational Reporter of Surface Chemistry and Solution-Based Route to Enhanced Coupling in Nanocrystal Solids. *J. Am. Chem. Soc.* **2011**, *133* (39), 15753–15761.

(55) Liu, W.; Lee, J.-S.; Talapin, D. V. III–V Nanocrystals Capped with Molecular Metal Chalcogenide Ligands: High Electron Mobility and Ambipolar Photoresponse. *J. Am. Chem. Soc.* **2013**, *135* (4), 1349–1357.

(56) Ip, A. H.; Thon, S. M.; Hoogland, S.; Voznyy, O.; Zhitomirsky, D.; Debnath, R.; Levina, L.; Rollny, L. R.; Carey, G. H.; Fischer, A.; et al. Hybrid Passivated Colloidal Quantum Dot Solids. *Nat. Nanotechnol.* **2012**, *7* (9), 577–582.

(57) Crisp, R. W.; Kroupa, D. M.; Marshall, A. R.; Miller, E. M.; Zhang, J.; Beard, M. C.; Luther, J. M. Metal Halide Solid-State Surface Treatment for High Efficiency PbS and PbSe QD

Solar Cells. *Sci. Rep.* **2015**, *5*, 9945.

(58) Carey, G. H.; Levina, L.; Comin, R.; Voznyy, O.; Sargent, E. H. Record Charge Carrier Diffusion Length in Colloidal Quantum Dot Solids via Mutual Dot-To-Dot Surface Passivation. *Adv. Mater.* **2015**, *27* (21), 3325–3330.

(59) Voznyy, O.; Zhitomirsky, D.; Stadler, P.; Ning, Z.; Hoogland, S.; Sargent, E. H. A Charge-Orbital Balance Picture of Doping in Colloidal Quantum Dot Solids. *ACS Nano* **2012**, *6* (9), 8448–8455.

(60) Dolzhnikov, D. S.; Zhang, H.; Jang, J.; Son, J. S.; Panthani, M. G.; Shibata, T.; Chattopadhyay, S.; Talapin, D. V. Materials Chemistry. Composition-Matched Molecular "Solders" for Semiconductors. *Science* **2015**, *347* (6220), 425–428.

(61) Brown, P. R.; Kim, D.; Lunt, R. R.; Zhao, N.; Bawendi, M. G.; Grossman, J. C.; Bulovi, V. Energy Level Modification in Leadsulfide Quantum Dot Thin Films through Ligand Exchange. *ACS Nano* **2014**, *8*, 5863–5872.

(62) Oh, S. J.; Berry, N. E.; Choi, J.-H.; Gaulding, E. A.; Paik, T.; Hong, S.-H.; Murray, C. B.; Kagan, C. R. Stoichiometric Control of Lead Chalcogenide Nanocrystal Solids to Enhance Their Electronic and Optoelectronic Device Performance. *ACS Nano* **2013**, *7* (3), 2413–2421.

(63) Kim, D. K.; Fafarman, A. T.; Diroll, B. T.; Chan, S. H.; Gordon, T. R.; Murray, C. B.; Kagan, C. R. Solution-Based Stoichiometric Control over Charge Transport in Nanocrystalline CdSe Devices. *ACS Nano* **2013**, *7* (10), 8760–8770.

(64) Kim, D.; Kim, D.-H.; Lee, J.-H.; Grossman, J. C. Impact of Stoichiometry on the Electronic Structure of PbS Quantum Dots. *Phys. Rev. Lett.* **2013**, *110* (19), 196802.

(65) Thon, S. M.; Ip, A. H.; Voznyy, O.; Levina, L.; Kemp, K. W.; Carey, G. H.; Masala, S.; Sargent, E. H. Role of Bond Adaptability in the Passivation of Colloidal Quantum Dot Solids. *ACS Nano* **2013**, *7* (9), 7680–7688.

(66) Straus, D. B.; Goodwin, E. D.; Gaulding, E. A.; Muramoto, S.; Murray, C. B.; Kagan, C. R. Increased Carrier Mobility and Lifetime in CdSe Quantum Dot Thin Films through Surface Trap Passivation and Doping. *J. Phys. Chem. Lett.* **2015**, *6* (22), 4605–4609.

(67) Kagan, C. R. Flexible Colloidal Nanocrystal Electronics. *Chem. Soc. Rev.* **2018**, Advance Article.

(68) Zhao, Q.; Zhao, T.; Guo, J.; Chen, W.; Zhang, M.; Kagan, C. R. The Effect of Dielectric Environment on Doping Efficiency in Colloidal PbSe Nanostructures. *ACS Nano* **2018**, *12* (2), 1313–1320.

(69) McDonald, S. A.; Konstantatos, G.; Zhang, S.; Cyr, P. W.; Klem, E. J. D.; Levina, L.; Sargent, E. H. Solution-Processed PbS Quantum Dot Infrared Photodetectors and Photovoltaics. *Nat. Mater.* **2005**, *4* (2), 138–142.

(70) Xu, J.; Voznyy, O.; Liu, M.; Kirmani, A. R.; Walters, G.; Munir, R.; Abdelsamie, M.; Proppe, A. H.; Sarkar, A.; García de Arquer, F. P.; et al. 2D Matrix Engineering for Homogeneous Quantum Dot Coupling in Photovoltaic Solids. *Nat. Nanotechnol.* **2018**, *13* (6), 456–462.

(71) Sze, S. M.; Ng, K. K. *Physics of Semiconductor Devices*, 3rd ed.; Wiley-Interscience: Hoboken, N.J, 2007.

(72) Piliego, C.; Protesescu, L.; Bisri, S. Z.; Kovalenko, M. V.; Loi, M. A. 5.2% Efficient PbS Nanocrystal Schottky Solar Cells. *Energy Environ. Sci.* **2013**, *6* (10), 3054.

(73) Luther, J. M.; Gao, J.; Lloyd, M. T.; Semonin, O. E.; Beard, M. C.; Nozik, A. J. Stability

Assessment on a 3% Bilayer PbS/ZnO Quantum Dot Heterojunction Solar Cell. *Adv. Mater.* **2010**, *22* (33), 3704–3707.

(74) Brown, P. R.; Lunt, R. R.; Zhao, N.; Osedach, T. P.; Wanger, D. D.; Chang, L. Y.; Bawendi, M. G.; Bulović, V. Improved Current Extraction from ZnO/PbS Quantum Dot Heterojunction Photovoltaics Using a MoO3 Interfacial Layer. *Nano Lett.* **2011**, *11* (7), 2955–2961.

(75) Chuang, C.-H. M.; Brown, P. R.; Bulović, V.; Bawendi, M. G. Improved Performance and Stability in Quantum Dot Solar Cells through Band Alignment Engineering. *Nat. Mater.* **2014**, *13* (8), 796–801.

(76) García de Arquer, F. P.; Armin, A.; Meredith, P.; Sargent, E. H. Solution-Processed Semiconductors for next-Generation Photodetectors. *Nat. Rev. Mater.* **2017**, *2* (3), 16100.

CHAPTER 2 Advanced Architecture for PbS Colloidal Quantum Dot (CQD) Solar Cells Exploiting a CdSe Quantum Dot (QD) Buffer Layer

This work has been published as Zhao, T., Goodwin, E. D., Guo, J., Wang, H., Diroll, B. T., Murray, C. B., and Kagan, C. R. Advanced architecture for colloidal PbS quantum dot solar cells exploiting a CdSe quantum dot buffer layer. *ACS Nano*, 2016, 10(10), 9267-9273.

PbS QDs have tunable bandgap energies across the near-infrared region of the electromagnetic spectrum which makes them appealing for solar cell applications.[1] Over the past decade, progress made in improving the mobility-lifetime product of minority carriers in the QD thin films,[2,3] passivating the QD surface,[4–6] and designing the device structure,[7] has boosted the power conversion efficiency (PCE) of PbS QD solar cells to as high as 10%[8] and has improved their air stability.[7,9] The device architecture of the most widely studied PbS QD solar cells consists of a heterojunction with a wide-band-gap oxide, typically ZnO or TiO_2. The junction interface is tailored to reduce carrier recombination and engineer energy levels, for example, by inserting an additional window layer by atomic layer deposition[10] or electrophoretic deposition,[11] passivating the junction with doped polymers[12] or modifying the interface with self-assembled monolayers.[8]

Akin to copper indium gallium selenide (CIGS) thin film solar cells where thin film CdS is often introduced at the CIGS/oxide junction,[13] here we fabricate ZnO nanoparticle (NP)/PbS QD solar cells with a buffer layer of CdSe QDs at the heterojunction interface. In contrast to the wide-bandgap and high-resistivity CdS buffer material used in the CIGS system, we n-dope the CdSe QD layer through treatment with the metal salt CdI_2, as confirmed by current-voltage and capacitance-voltage measurements. We optimize the band alignment by exploiting the size-dependent electronic structure of CdSe QDs and study the resulting carrier transport across the junction under different illumination conditions. Using external quantum efficiency (EQE) and time-resolved microwave conductivity (TRMC) measurements, we show that the CdSe QD buffer layer reduces interface recombination and provides additional photogenerated carriers, resulting

in significantly higher open circuit voltage (V_{OC}) and short circuit current density (J_{SC}) and therefore a 25% enhancement in power conversion efficiency (PCE) for ZnO NP/CdSe QD/PbS QD solar cells in comparison to reference cells without the CdSe QD layer.

2.1 Fabrication and Characteristics of PbS QD Solar Cells with the CdSe QD Buffer Layer

The PbS QD solar cell device structure developed in this work is imaged in cross-section under a scanning electron microscopy (SEM) and depicted schematically [Figure 2.1a]. Compared to the commonly explored depleted heterojunction PbS QD solar cells, we introduce an extra buffer layer made of CdSe QDs at the interface between the ZnO NP and PbS QD layers.

From the bottom up, pre-patterned ITO/glass substrates are cleaned by sonication in 5% Hellmanex in DI water, pure DI water and ethanol consecutively, followed by UV–Ozone treatment for 30 minutes and MPTS (5% in toluene) soaking for 10 hours before use.[14] The substrates are rinsed with toluene and sonicated in ethanol to remove excess unbound MPTS molecules. Then the ZnO NPs (5 nm in diameter), synthesized according to the literature procedure,[15] are deposited by spin-coating in air to form a 100 nm thick layer. Using a robotic dip-coater mounted in a nitrogen glovebox, we fabricate CdSe QD (4 nm or 8 nm in diameter) layers by sequentially dipping samples into CdSe QD dispersions in hexane (10 mg/mL), methanolic CdI_2 solutions (24 mg/mL) and pristine methanol, during which the substrate is held for 60 s in the CdI_2 ligand solution and 30 s in the methanol rinse. Between each step, there is enough waiting time to allow the solvent to evaporate. Multiple dip-coating cycles build up the CdSe QD layer to controlled thicknesses ranging from 20 to 60 nm. Once the CdSe QD film is deposited, it is annealed at 250 °C for 10 min before being transferred out of the glove box. The PbS QD (3 nm in diameter) thin films are fabricated by sequentially building up multiple layers to realize an

optimal thickness of 250 nm. Each PbS QD layer is deposited by spin-coating a PbS QD dispersion in octane and hexane mixture (50 mg/mL) and immersing the samples in a methanolic solution of 3-mercaptopropionic acid (MPA) as previously reported.[4] The fabrication of the PbS QD layers is done in a fume hood with humidity below 30% at 25 °C. 12 nm of molybdenum trioxide (MoO_3) and 65 nm of Au are deposited by thermal evaporation through shadow masks, to create an electron blocking layer and to form the anode, respectively, completing the device and defining active device areas of 2 mm by 2 mm.

Current density-voltage (*J–V*) characteristics of representative solar cells without and with the CdSe QD buffer layer are measured under AM 1.5G illumination using a solar simulator (Oriel instruments model 96000, Newport Co.) mounted inside a N_2 glovebox and shown in Figure 2.1b. The device incorporating a 20 nm thick, CdSe QD buffer layer constructed from 8 nm QDs has both a larger V_{OC} and J_{SC}. The statistics and a histogram describing device performance for 20 independent devices fabricated on different substrates is reported in Table 2.1 and in Figure 2.1c. Devices with the CdSe QD buffer layer show a 25% improvement in the PCE of the solar cells from 6.0% (±0.5) to 7.5% (±0.4). The enhanced PCE is attributed to the significantly increased J_{SC} and an improved average V_{OC} and fill factor (FF). We perform a two-sample, two-tail unpaired t-test on each of the statistical results and the resulting p values are all much smaller than 0.05, indicating the difference in device performance is statistically significant.

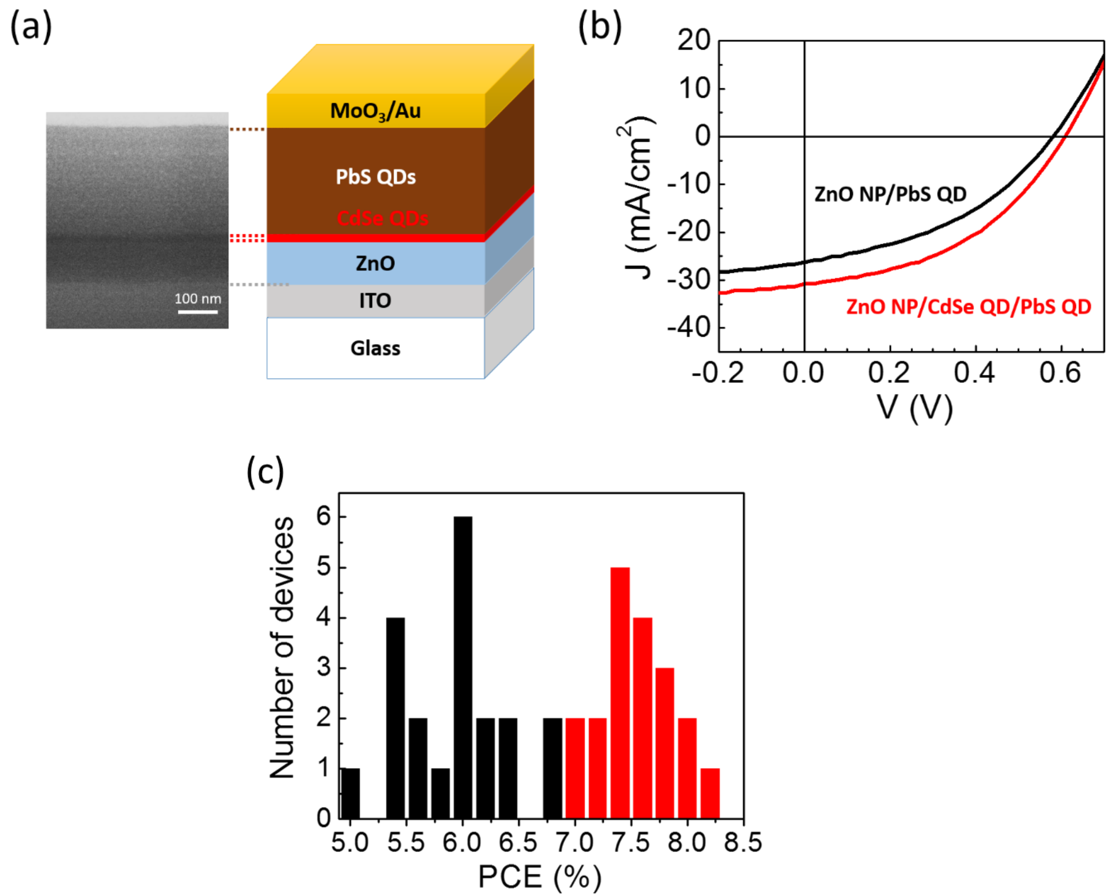

Figure 2.1 (a) SEM cross-sectional image and schematic of a ZnO NP/PbS QD solar cell with the CdSe QD buffer layer. (b) Current density–voltage (J–V) characteristics of representative solar cells without (black) and with (red) a CdSe QD buffer layer under AM 1.5 illumination. (c) Histogram of the device PCE without (black) and with (red) the CdSe QD buffer.

Table 2.1 Device parameter statistics

N=20	Voc (V)	Jsc (mA/cm^2)	FF	PCE (%)
ZnO NP/PbS QD	0.586±0.017	25.0±1.8	0.41±0.03	6.0±0.5
ZnO NP/CdSe QD/PbS QD	0.600±0.017	29.5±2.0	0.43±0.02	7.5±0.4

2.2 Optical and Electrical Characterization of the CdI2-capped CdSe QD layer

To understand the role of the CdSe QD buffer layer in enhancing the PbS QD solar cell performance, we characterize the thin film constructed with 8 nm CdSe QDs optically and electronically. UV–Vis absorption and Fourier transform infrared spectroscopy (FTIR) measurements show that the CdI_2 treatment successfully displaces 82% of the long organic ligands introduced in synthesis and leads to a red shift and broadening of the first excitonic resonance [Figure 2.2a], consistent with an increase in electronic coupling. Further annealing of the film gives rise to a negligible change in absorption both in the UV–Vis and IR spectra. The elemental composition of the CdSe QD film determined by energy-dispersive X-ray (EDX) spectroscopy shows that CdI_2 treatment enriches the CdSe QD surface in Cd and iodine [Table 2.2], which passivate the QD surface and reduce recombination as previously reported for II-VI and IV-VI QD thin films treated with metal halide salts. [5,16]

Figure 2.2b shows the current–voltage and capacitance–voltage (*C*–*V*) characteristics of a representative 8 nm CdSe QD thin film probed in the platform of the field-effect transistor (FET) to characterize the doping achieved by the CdI_2 treatment. Both the drain current *versus* gate voltage (I_D–V_G) and *C*–*V* characteristics are consistent with n-doped CdSe QD films. We calculate the total concentration of accumulated charges in the FET channel by integrating the capacitance from the extrapolated threshold voltage V_{TH} of V_G= -18 V to V_G= 0 V and divide it by the volume defined by the channel area and the Debye length to obtain the electron concentration in the CdSe QD thin film.[17] We find an electron concentration of ~4×10^{18} /cm^3 and therefore estimate the Fermi level to be 0.8 eV above midgap. The high electron concentration in the CdI_2-treated CdSe QD film is consistent with previous reports of Cd and iodine serving as donors.[18,19] We apply the same analysis to the ZnO NP film [Figure 2.2c] and find a higher electron concentration of ~1×10^{20} /cm^3.

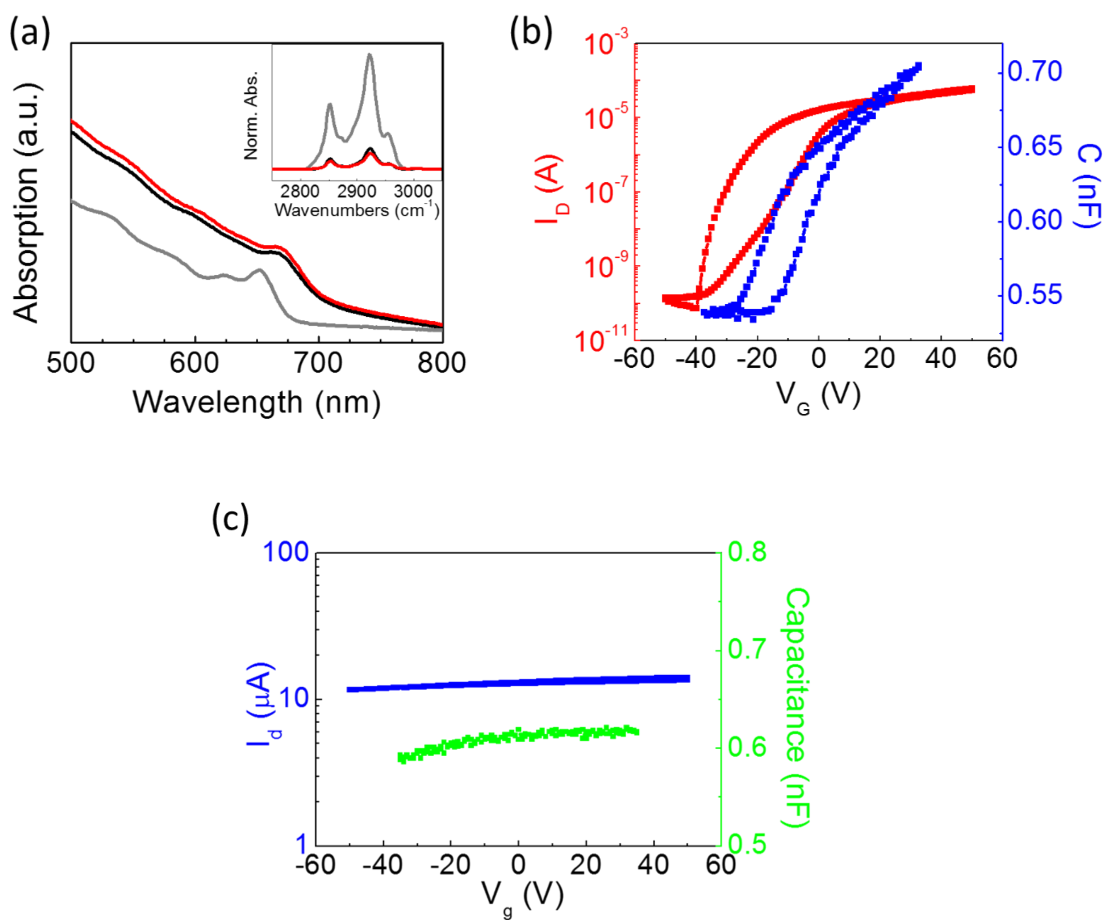

Figure 2.2 Characterization of the 8 nm CdSe QD buffer layer. (a) Absorption spectra of CdSe QD films as-deposited with organic ligands (grey), after treatment with CdI_2 (black) and upon annealing at 250 °C (red). Inset: corresponding IR absorption spectra of the CdSe QD films normalization by their absorption. (b) I_D–V_G (red) and *C*-*V* (blue) characteristics of CdI_2-treated CdSe QD FETs. (c) I_D-V_G (blue) and *C*-*V* (green) characteristics of ZnO NP FETs

Table 2.2 Element analysis of 8 nm CdSe QD thin films

Atomic %	Cd	Se	I	Cd:Se
CdSe-OA drop cast	58.7±1.4	41.3±0.2	N/A	1.42±0.01
$CdSe-CdI_2$	54.1±0.7	35.7±1.3	10.19±0.7	1.52±0.07

2.3 The Effect of the QD Buffer Layer Properties on Carrier Transport

To study and correlate the effect of inserting the CdSe QD buffer layer on the band alignment and device performance, we exploit the size-dependent electronic structure of CdSe QDs and fabricate solar cells with smaller (4 nm in diameter) and larger (8 nm in diameter) CdSe QD buffer layers. We construct equilibrium band diagrams for heterojunctions with 8 nm and 4 nm CdSe QD buffer layers. To find the band energies, we combine UV–Vis absorption and cyclic voltammetry measurements [Figure 2.3]. To identify the length scales of band bending at each of the device heterointerfaces, we use dielectric constants[20,21] and carrier concentrations found in literature[22] and from *C-V* measurements [Table 2.3]. For the 8 nm CdSe QD interface layer, at the CdSe QD/ZnO NP isotype interface, electrons will accumulate within the Debye length L_{Dn} of the CdSe QD layer, given by:[23]

$$L_{Dn} = \sqrt{\frac{\varepsilon_n \cdot kT}{q^2 \cdot N_d}} = 2\,nm$$

Electrons are depleted right at the ZnO NP surface, with L_{Dn}=0.2 nm, given its 100 times larger carrier concentration and similar dielectric constant to that of the CdSe QD layer. At the PbS QD/CdSe QD anisotype interface, the total depletion width X_d is calculated by:[23]

$$X_d = \sqrt{\frac{2\epsilon_n\epsilon_p}{q} \cdot \frac{(N_a+N_d)^2 \cdot V_{bi}}{N_a \cdot N_d(N_a \cdot \varepsilon_p + N_d\varepsilon_n)}}$$

Where the built-in potential V_{bi} is determined by

$$qV_{bi} = \frac{\Delta E_c - \Delta E_V}{2} + kT \cdot \ln\left(\frac{N_d N_a}{n_{i,n} n_{i,p}}\right)$$

And the depletion width in the CdSe QD layer is calculated as:

$$X_n = \frac{N_a}{N_a + N_d} \cdot X_d$$

For a carrier concentration of $5x10^{16}$ cm^{-3} in the PbS QD layer, V_{bi}=0.76 V and X_d is 170 nm. Given the 20 times larger carrier concentration in the CdSe QD layer, the depletion region in the n-type CdSe QD layer is X_n ~8 nm and the depletion region in the p-type PbS QD layer is X_p=162 nm. Therefore, there is a ~10 nm quasi-neutral region remains in the CdSe QD layer away from the device interfaces. Since the conduction band of the 8 nm CdSe QD layer lies below that of the PbS QD layer relative to the vacuum level, *i.e.* the conduction band offset between the CdSe and PbS QD layer is negative (ΔE_C <0), once the junction is formed, band bending provides a smooth transition in the conduction band across the heterointerface [Figure 2.4a]. In contrast, wider bandgap, 4 nm CdSe QDs introduce a larger and positive band offset (ΔE_C >0) that creates two barriers in the conduction band, one at the ZnO NP/CdSe QD interface and one at the CdSe QD/PbS QD interface of the junction [Figure 2.4b].

We investigate the influence of the band alignment introduced by the CdSe QD buffer layer on carrier transport. We measure the *J–V* characteristics of the ZnO NP/CdSe QD/PbS QD junctions in the dark and then under "red" light and standard AM 1.5G white light illumination. The "red" light is obtained from AM 1.5G solar simulated light that is additionally filtered by an 800 nm long pass filter, such that the red light can be selectively absorbed by the PbS QD layer and not by the CdSe QD layer. Figure 2.4c shows representative *J–V* characteristics of a PbS QD solar cell with the 8 nm CdSe QD buffer layer. The device exhibits well-behaved, rectifying characteristics of a diode in the dark and under both red and white light illumination conditions, consistent with the smooth transition in the conduction band of the junction shown in Figure 3a. The device with the 4 nm CdSe QD buffer layer has lower current densities both in dark and under illumination [Figure 2.4d], consistent with barriers to electron transport in the conduction band [Figure 2.4b]. Under red light illumination, the *J–V* curve has an "s-shape", which is similar

to that seen and commonly referred to in CIGS solar cells as a "red kink".[24] The distorted *J*–*V* characteristics in CIGS solar cells is attributed to the secondary barrier created by the conduction band offset between the CdS buffer layer and the CIGS active material, akin to the conduction band offset in the PbS QD solar cell with the 4 nm CdSe QD buffer layer reported here. Red photons have insufficient energy to generate carriers within the wide-bandgap buffer layer, and, at small forward bias, the interfacial barriers are too high for photo-generated carriers to surmount the barrier and transit the junction; thus the total current density decreases leading to a kink.

Under AM 1.5G white light illumination, compared to the well-behaved *J*–*V* characteristics from the device with the 8 nm CdSe QD buffer layer, the one constructed with the 4 nm CdSe QD buffer layer stills show a kink. We study the *J*–*V* characteristics after white light soaking of the junction for 15 min. In CIGS cells the high-energy photons of white light are used to increase the carrier concentration in the buffer layer and reduce the barrier height. For devices fabricated with the 8 nm CdSe QD buffer layer, the *J*–*V* characteristics are unchanged after AM 1.5G white light soaking for 15 min. However for devices constructed with the 4 nm CdSe QD buffer layer, the kink in the *J*–*V* characteristics nearly disappears, similar to the behavior observed in CIGS solar cells.[25]

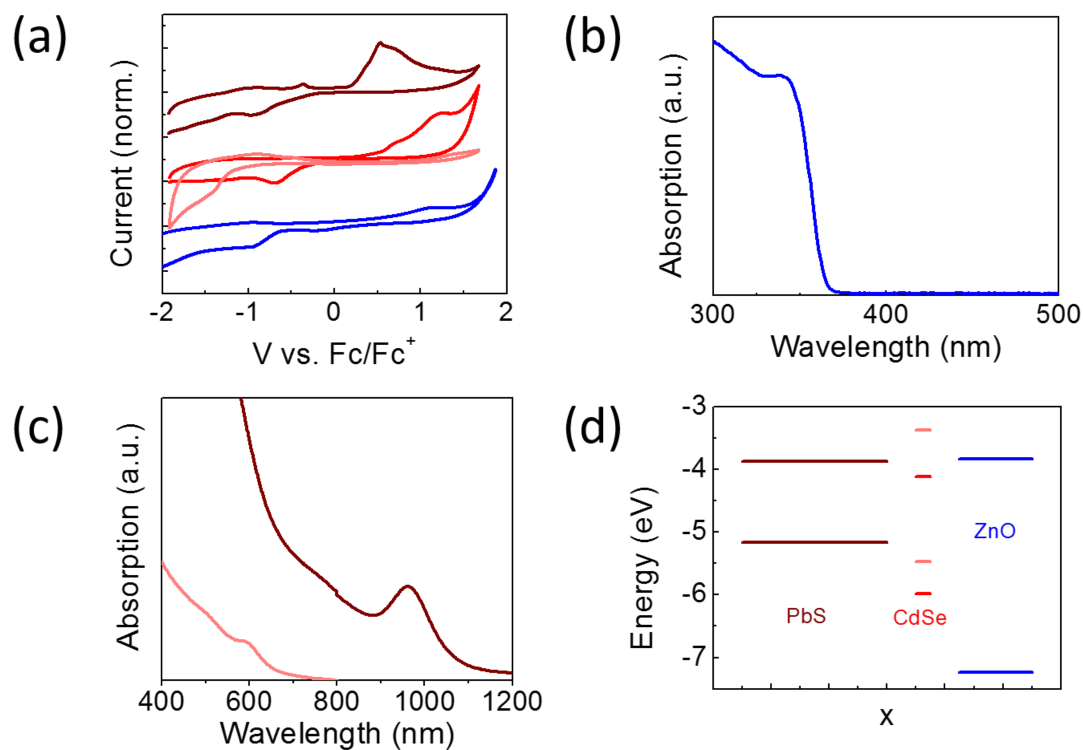

Figure 2.3 (a) Cyclic voltammograms of PbS QD (brown), 8 nm CdSe QD (red), 4 nm CdSe QD (pink) and ZnO NP (blue) thin films. UV-Vis absorption spectra of (b) ZnO NP films and (c) 4 nm CdI_2-treated CdSe QD (pink) and MPA treated PbS QD (brown) films. (d) Corresponding band energy positions of PbS QD, CdSe QD and ZnO NP films.

Table 2.3 Material Parameters

	Dielectric constant (ε_r)	Carrier concentration (N) (cm^{-3})	Intrinsic carrier concentration ($n_{i,n}$ or $n_{i,p}$)	Band discontinuity (ΔE) (eV)
ZnO NPs	3.7 (Ref. [26])	10^{20} (C-V)	Not used	Not used
CdSe QDs	4 (Ref. [20])	10^{18} (C-V)	10^{3} (Ref. [20])	ΔE_C=0.25 eV (cyclic voltammetry)
PbS QDs	20 (Ref. [21])	$5x10^{16}$ (Ref. [22])	10^{14} (Ref. [22])	ΔE_V=0.82 eV (cyclic voltammetry)

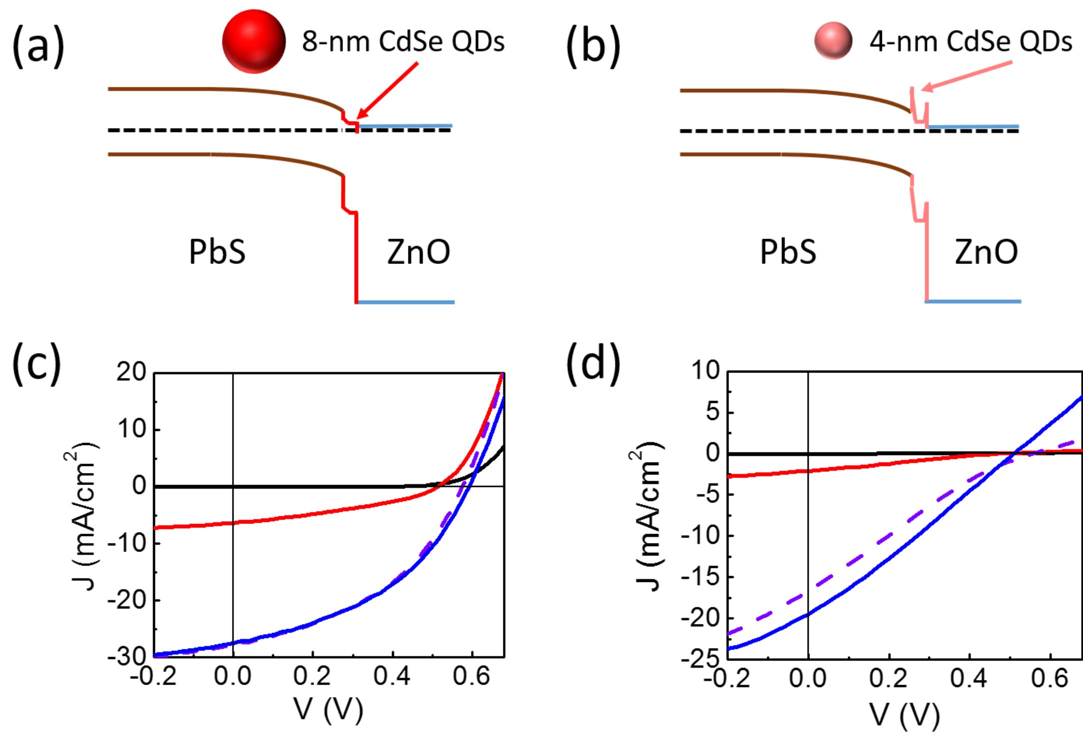

Figure 2.4 Band alignment of the ZnO NP/CdSe QD/PbS QD heterojunction with (a) a 8 nm CdSe QD buffer layer and (b) a 4 nm CdSe QD buffer layer. (c) *J–V* characteristics of devices constructed with (c) a 8 nm CdSe QD buffer and (d) a 4 nm CdSe QD buffer layer in the dark (black), under red light illumination (red), upon AM 1.5 white light illumination (dash, purple) and after 15 min of white light soaking (blue).

We optimize the thickness of the CdSe QD layer to maximize the device PCE. The *J–V* characteristics of solar cells with CdSe QD buffer layers of varying thickness are shown in Figure 2.5. As the thickness of the CdSe QD layer increases from 20 nm to 60 nm, the enhancement in the *J–V* characteristics weakens and ultimately degrades the device performance. This is consistent with 1) a smaller depletion region width in the CdSe QD layer compared to the PbS QD layer, as the CdSe QD layer has a higher carrier concentration and lower dielectric constant; 2) increased recombination in the neutral region of thicker CdSe QD layers and therefore lower V_{OC}, and 3) addition of device resistance with increasing semiconductor layer thickness. CdSe QD layers with thickness below 20 nm are not uniform and therefore thinner buffer layers are not included in this study.

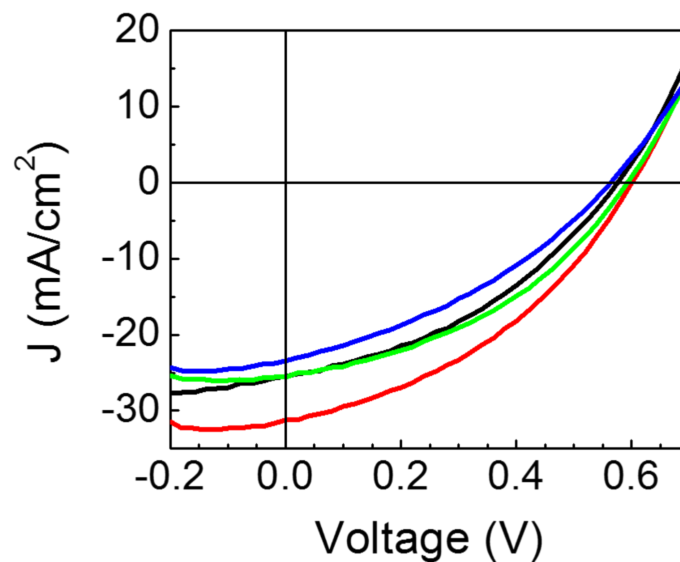

Figure 2.5 *J-V* characteristics of PbS QD solar cells with no (black), 20 nm (red), 40 nm (green) and 60 nm (blue) thick CdSe QD buffer layers.

To distinguish any effect of CdI_2 treatment at the PbS QD/ZnO NP interface from incorporating the CdI_2-treated CdSe QD interface layer, we fabricate devices in which we replace the CdSe QDs with the same PbS QDs as the rest of the active layer. All other parameters are identical during the processing. From the characterization of 12 different samples [Table 2.4], devices with CdI_2-treated PbS QD interface layers show a lower average V_{OC} and J_{SC} and therefore a lower average PCE. A representative *J-V* curve for a device with a CdI_2-treated PbS QD interface layer is shown in Figure 2.6 and compared to that of a ZnO NP/PbS QD reference device. The reduced device performance upon incorporating the CdI_2-treated PbS QD interface layer is consistent with literature reports of the influence of this metal halide treatment.[5]

Table 2.4 Device parameter statistics with and without the CdI_2-treated PbS QD interface layers

	Voc (V)	**Jsc (mA/cm^2)**	**FF**	**PCE (%)**
ZnO NP/PbS QD	0.586±0.017	25.0±1.8	0.41±0.03	6.0±0.5
ZnO NP/PbS QD-CdI_2/PbS QD	0.567±0.019	23.9±2.2	0.41±0.02	5.5±0.4

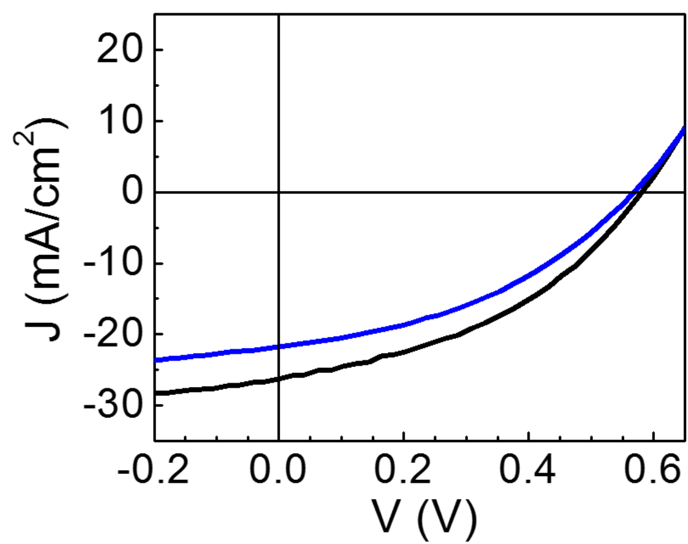

Figure 2.6. *J-V* characteristics of representative solar cells without (black) and with (blue) a CdI_2-treated PbS QD interface layer under AM 1.5G illumination.

2.4 The Mechanism of the CdSe QD Buffer Layer Enhancement

We study the underlying mechanism of the PCE enhancement by the CdSe QD buffer layer. Figure 2.7a shows that the device with the CdSe QD buffer layer has higher EQE over the entire measured wavelength range compared to an otherwise identical cell without the CdSe buffer layer. For photon energies smaller than the bandgap energy of the CdSe QD layer (1.85 eV, wavelengths >670 nm), the net EQE enhancement [Figure 2.7a, blue] is roughly constant, consistent with the CdSe QD buffer layer reducing interface recombination and facilitating carrier collection. For photon energies larger than the CdSe QD bandgap, with wavelengths <670 nm, the ΔEQE increases, consistent with higher absorbance in the device stack [Figure 2.7b] and generation and collection of carriers in the CdSe QD buffer layer. Unlike the loss that occurs in the highly resistive and wide-bandgap buffer layer in the analogous CIGS thin film devices,[13] the 8 nm CdSe QD layer in the PbS QD solar cells acts to contribute photogenerated carriers to the device efficiency.

We use time-resolved microwave conductivity (TRMC) measurements to characterize the product of the carrier quantum yield (QY) (Φ) and the sum of the carrier mobilities (∑μ) in the PbS QD heterojunction without and with the CdSe QD buffer layers. Figure 2.8a shows the QY–mobility product at various photoexcitation densities from 3 independent samples of ZnO NP/PbS QD and ZnO NP/CdSe QD/PbS QD stacks assembled on (3-mercaptopropyl)trimethoxysilane (MPTS)-treated float glass following the same fabrication procedure optimized for the solar cells. The ZnO NP/CdSe QD/PbS QD stacks show an increase in the QY–mobility product in comparison to those without the CdSe QD layer. Since the carriers being probed exist predominately in the PbS QD or ZnO NP layers, as the CdSe QD layer is relatively thin, we expect carrier mobility to remain unchanged and therefore the increase in the QY-mobility product to arise from an increase in QY. We hypothesize that the increase in QY with the additional CdSe QD layer is caused by a reduction in interfacial recombination and more efficient charge

extraction across the heterojunction. Noting that the photoexcitation is introduced by a 532-nm laser, we normalize the QY–mobility product to the film absorption, so the increase is also not caused by the added absorption from the CdSe QD layer. TRMC photoconductance lifetimes are shown for completeness in Figure 2.8b.

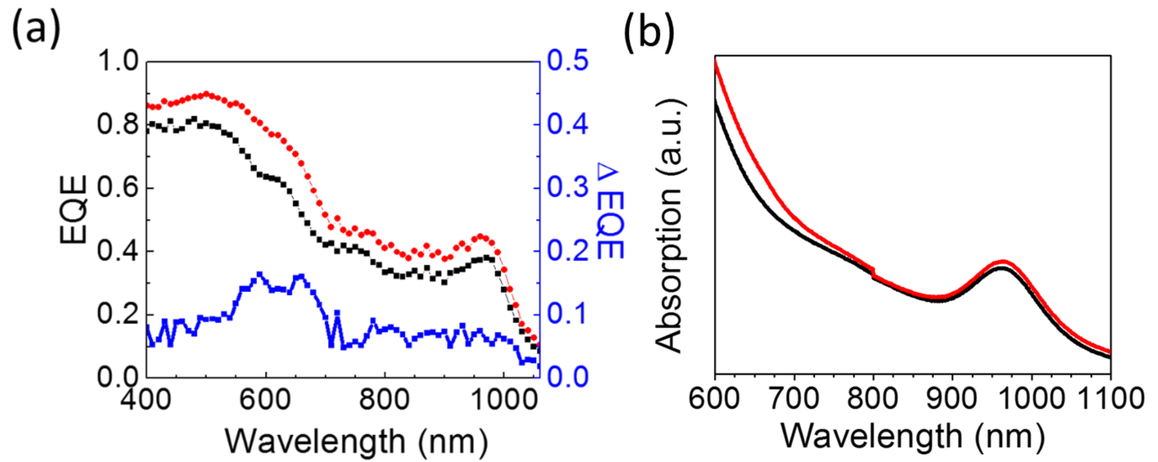

Figure 2.7 (a) EQE of PbS QD solar cells without the CdSe QD buffer layer (black) and with the CdSe QD buffer layer (red). Change of EQE (blue), $\Delta EQE = EQE\ (red) - EQE\ (black)$. (b) UV-Vis absorption spectra of the reference ZnO NP/PbS QD (black) and optimized ZnO NP/CdSe QD/PbS QD (red) device stacks on glass substrates.

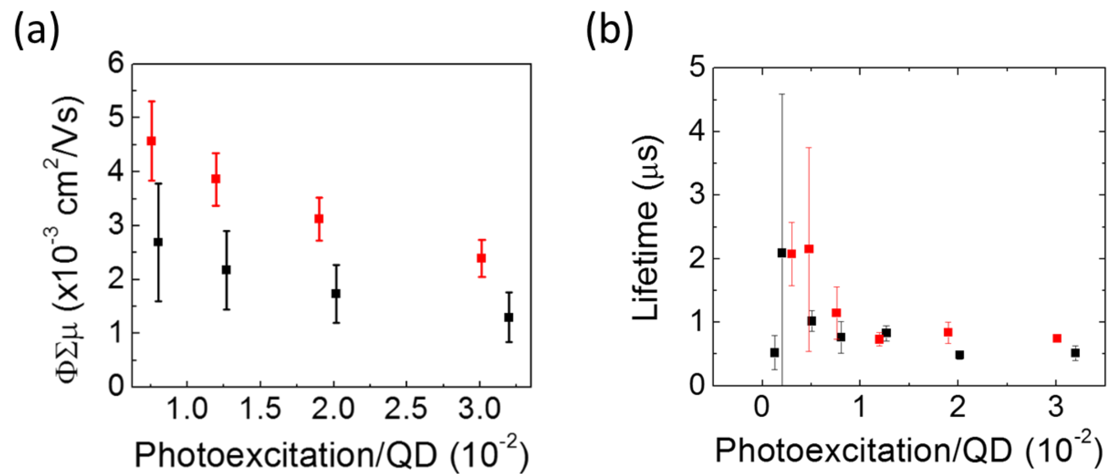

Figure 2.8 TRMC measurements of (a) the product of the carrier quantum yield (Φ) and the sum of the carrier mobilities in ZnO NP/PbS QD (black) and ZnO NP/CdSe QD/PbS QD (red) films and (b) photoconductance decay lifetime of the ZnO NP/PbS QD (black) and ZnO NP/CdSe QD/PbS QD (red) stacks.

2.5 Quantitative Device J-V analysis

To quantitatively study the role of the CdSe QD layer in changing device parameters, we analyze the *J–V* characteristics of the ZnO NP/PbS QD and ZnO NP/CdSe QD/PbS QD solar cells. Due to the relatively low fill factor of these devices, the uncertainty from analysis would be too large to make clear statements for *J–V* data under illumination.[27] As a result, all the following operations are only applied to the dark *J–V* characteristics. Simplified from the general diode equation, the total diode current in the dark is expressed as $J = J_0 \cdot exp\left[\frac{q}{nkT}(V - RJ)\right] + GV$, where J_0 is the saturation current density, q is elementary charge, n is the ideality factor, k is Boltzmann's constant, T is temperature, R is series resistance and G is shunt conductance. By plotting d*J*/d*V* against *V*, d*V*/d*J* against $(J - GV)^{-1}$ and *J* – G*V* against *V* – R*J* [Figure 2.9], we extract G, R, n, and J_0 respectively. Table 2.5 summarizes the device parameters obtained from the analysis of the dark *J–V* characteristics. With the CdSe QD buffer layer, G and J_0 are reduced, indicating the buffer layer prevents shunt leakage and suppresses recombination in dark operation. For the *J–V* characteristics under illumination, the open circuit voltage V_{OC} obeys the relation $V_{OC} = \frac{nkT}{q}\ln(\frac{J_{SC}}{J_0})$, when $J_{SC} \gg J_0$. Based on the V_{OC} from the *J–V* curve under illumination and the calculated J_0, we find n for the ZnO NP/PbS QD and ZnO NP/CdSe QD/PbS QD device under illumination to be 1.9±0.1 and 1.7±0.1 respectively. The smaller n is consistent with reduced recombination in the device with the buffer layer.

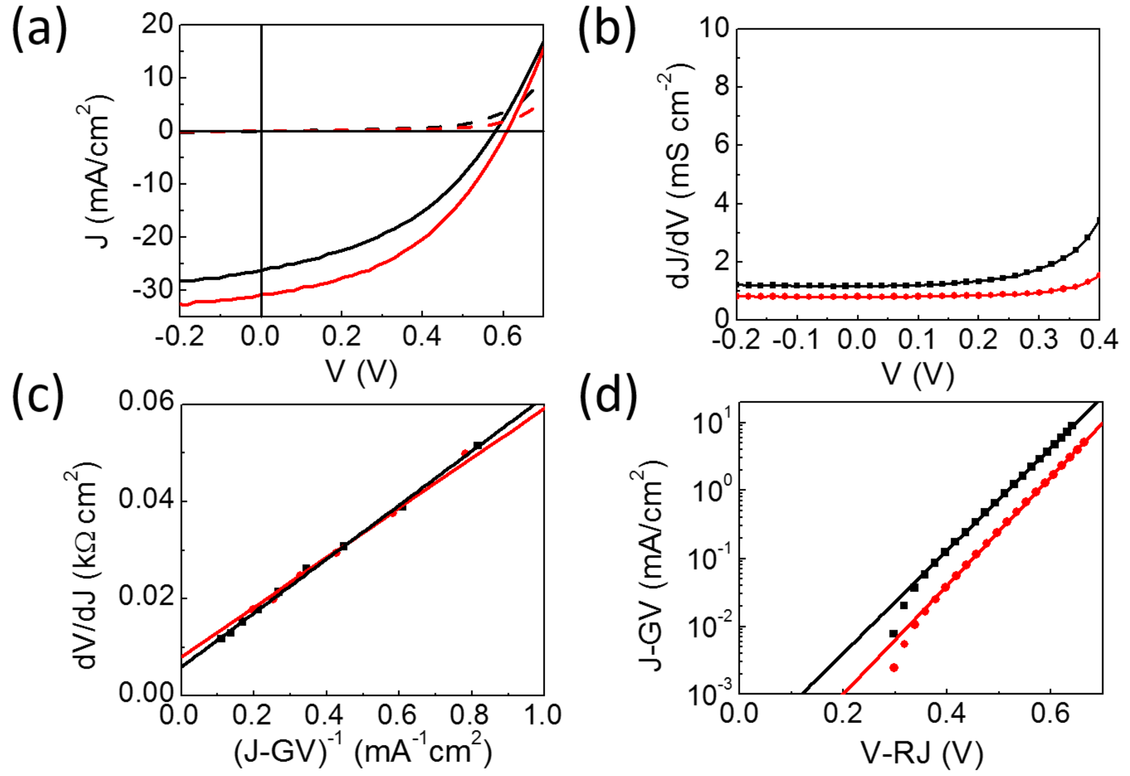

Figure 2.9. *J-V* analysis on representative PbS QD solar cells without (black) and with (red) the CdSe QD buffer layer. (a) *J-V* characteristics of PbS QD solar cells in the dark (dash lines) and under AM 1.5 illumination (solid lines). (b) The plot of d*J*/d*V* versus *V* to extrapolate *G*. (c) The plot of d*V*/d*J* versus *J-GV* with linear fit to extrapolate R and n. (d) The semilog plot of *J-GV* versus *V-RJ* with linear fit to extrapolate J_0.

Table 2.5 Device parameters based on the dark characteristics

	G (mS/cm^2)	R (Ωcm^2)	n	J_0 (mA/cm^{-2})
ZnO NP/PbS QD	1.2±0.2	6.1±2.2	2.4±0.4	$2.9±0.3×10^{-4}$
ZnO NP/CdSe QD/PbS QD	0.6±0.2	7.3±1.7	2.2±0.2	$1.0±0.1×10^{-4}$

2.6 Conclusions

In conclusion, we improve the performance of PbS QD solar cells by introducing a CdI_2-CdSe QD buffer layer at the ZnO NP/PbS QD heterojunction. The 8 nm CdSe QD buffer layer enhances the device J_{SC}, V_{OC} and FF. We attribute these improvements to the optimized band alignment across the junction, passivation of interface traps by the buffer layer and additional carriers photo-generated in the CdSe QD layer. We perform a complementary mathematical analysis of device J–V characteristics, and the improved device parameter is in agreement with our hypothesis based on our experimental observations. For future applications, the CdSe QD buffer layer can be applied to air-stable PbS/Se QD solar cells,[7,9,28] and to devices with structured, non-planar geometries.[29]

2.7 References

(1) Carey, G. H.; Abdelhady, A. L.; Ning, Z.; Thon, S. M.; Bakr, O. M.; Sargent, E. H. Colloidal Quantum Dot Solar Cells. *Chem. Rev.* **2015**, *115* (23), 12732–12763.

(2) Jeong, K. S.; Tang, J.; Liu, H.; Kim, J.; Schaefer, A. W.; Kemp, K.; Levina, L.; Wang, X.; Hoogland, S.; Debnath, R.; et al. Enhanced Mobility-Lifetime Products in PbS Colloidal Quantum Dot Photovoltaics. *ACS Nano* **2012**, *6* (1), 89–99.

(3) Carey, G. H.; Levina, L.; Comin, R.; Voznyy, O.; Sargent, E. H. Record Charge Carrier Diffusion Length in Colloidal Quantum Dot Solids via Mutual Dot-To-Dot Surface Passivation. *Adv. Mater.* **2015**, *27* (21), 3325–3330.

(4) Ip, A. H.; Thon, S. M.; Hoogland, S.; Voznyy, O.; Zhitomirsky, D.; Debnath, R.; Levina, L.; Rollny, L. R.; Carey, G. H.; Fischer, A.; et al. Hybrid Passivated Colloidal Quantum Dot Solids. *Nat. Nanotechnol.* **2012**, *7* (9), 577–582.

(5) Crisp, R. W.; Kroupa, D. M.; Marshall, A. R.; Miller, E. M.; Zhang, J.; Beard, M. C.; Luther, J. M. Metal Halide Solid-State Surface Treatment for High Efficiency PbS and PbSe QD Solar Cells. *Sci. Rep.* **2015**, *5*, 9945.

(6) Lan, X.; Voznyy, O.; Kiani, A.; García de Arquer, F. P.; Abbas, A. S.; Kim, G.-H.; Liu, M.; Yang, Z.; Walters, G.; Xu, J.; et al. Passivation Using Molecular Halides Increases Quantum Dot Solar Cell Performance. *Adv. Mater.* **2016**, *28* (2), 299–304.

(7) Chuang, C.-H. M.; Brown, P. R.; Bulović, V.; Bawendi, M. G. Improved Performance and Stability in Quantum Dot Solar Cells through Band Alignment Engineering. *Nat. Mater.* **2014**, *13* (8), 796–801.

(8) Kim, G.-H.; Garcia de Arquer, F. P.; Yoon, Y. J.; Lan, X.; Liu, M.; Voznyy, O.; Yang, Z.; Fan, F.; Ip, A. H.; Kanjanaboos, P.; et al. High Efficiency Colloidal Quantum Dot

Photovoltaics via Robust Self-Assembled Monolayers. *Nano Lett.* **2015**, *15* (11), 7691–7696.

(9) Zhang, J.; Gao, J.; Church, C. P.; Miller, E. M.; Luther, J. M.; Klimov, V. I.; Beard, M. C. PbSe Quantum Dot Solar Cells with More than 6% Efficiency Fabricated in Ambient Atmosphere. *Nano Lett.* **2014**, *14* (10), 6010–6015.

(10) Kemp, K. W.; Labelle, A. J.; Thon, S. M.; Ip, A. H.; Kramer, I. J.; Hoogland, S.; Sargent, E. H. Interface Recombination in Depleted Heterojunction Photovoltaics Based on Colloidal Quantum Dots. *Adv. Energy Mater.* **2013**, *3* (7), 917–922.

(11) Tan, F.; Wang, Z.; Qu, S.; Cao, D.; Liu, K.; Jiang, Q.; Yang, Y.; Pang, S.; Zhang, W.; Lei, Y.; et al. A CdSe Thin Film: A Versatile Buffer Layer for Improving the Performance of TiO 2 Nanorod Array:PbS Quantum Dot Solar Cells. *Nanoscale* **2016**, *8* (19), 10198–10204.

(12) Yuan, M.; Voznyy, O.; Zhitomirsky, D.; Kanjanaboos, P.; Sargent, E. H. Synergistic Doping of Fullerene Electron Transport Layer and Colloidal Quantum Dot Solids Enhances Solar Cell Performance. *Adv. Mater.* **2015**, *27* (5), 917–921.

(13) Jackson, P.; Hariskos, D.; Lotter, E.; Paetel, S.; Wuerz, R.; Menner, R.; Wischmann, W.; Powalla, M. New World Record Efficiency for Cu(In,Ga)Se2 Thin-Film Solar Cells beyond 20%. *Prog. Photovoltaics Res. Appl.* **2011**, *19* (7), 894–897.

(14) Katari, J. E. B.; Colvin, V. L.; Alivisatos, A. P. X-Ray Photoelectron Spectroscopy of CdSe Nanocrystals with Applications to Studies of the Nanocrystal Surface. *J. Phys. Chem.* **1994**, *98* (15), 4109–4117.

(15) Beek, W. J. E.; Wienk, M. M.; Kemerink, M.; Yang, X.; Janssen, R. a J. Hybrid Zinc Oxide Conjugated Polymer Bulk Heterojunction Solar Cells. *J. Phys. Chem. B* **2005**, *109* (19), 9505–9516.

(16) Goodwin, E. D.; Diroll, B. T.; Oh, S. J.; Paik, T.; Murray, C. B.; Kagan, C. R. Effects of Post-Synthesis Processing on CdSe Nanocrystals and Their Solids: Correlation between Surface Chemistry and Optoelectronic Properties. *J. Phys. Chem. C* **2014**, *118* (46), 27097–27105.

(17) Oh, S. J.; Berry, N. E.; Choi, J.-H.; Gaulding, E. A.; Paik, T.; Hong, S.-H.; Murray, C. B.; Kagan, C. R. Stoichiometric Control of Lead Chalcogenide Nanocrystal Solids to Enhance Their Electronic and Optoelectronic Device Performance. *ACS Nano* **2013**, *7* (3), 2413–2421.

(18) Kim, D. K.; Fafarman, A. T.; Diroll, B. T.; Chan, S. H.; Gordon, T. R.; Murray, C. B.; Kagan, C. R. Solution-Based Stoichiometric Control over Charge Transport in Nanocrystalline CdSe Devices. *ACS Nano* **2013**, *7* (10), 8760–8770.

(19) Zhitomirsky, D.; Furukawa, M.; Tang, J.; Stadler, P.; Hoogland, S.; Voznyy, O.; Liu, H.; Sargent, E. H. N-Type Colloidal-Quantum-Dot Solids for Photovoltaics. *Adv. Mater.* **2012**, *24* (46), 6181–6185.

(20) Straus, D. B.; Goodwin, E. D.; Gaulding, E. A.; Muramoto, S.; Murray, C. B.; Kagan, C. R. Increased Carrier Mobility and Lifetime in CdSe Quantum Dot Thin Films through Surface Trap Passivation and Doping. *J. Phys. Chem. Lett.* **2015**, *6* (22), 4605–4609.

(21) Grinolds, D. D. W.; Brown, P. R.; Harris, D. K.; Bulovic, V.; Bawendi, M. G. Quantum-Dot Size and Thin-Film Dielectric Constant: Precision Measurement and Disparity with Simple Models. *Nano Lett.* **2015**, *15* (1), 21–26.

(22) Voznyy, O.; Zhitomirsky, D.; Stadler, P.; Ning, Z.; Hoogland, S.; Sargent, E. H. A Charge-Orbital Balance Picture of Doping in Colloidal Quantum Dot Solids. *ACS Nano* **2012**, *6* (9), 8448–8455.

(23) Zeghbroeck, B. Van. Principles of Semiconductor Devices. *Colarado Univ.* **2004**.

(24) Kanevce, A.; Gloeckler, M.; Pudov, A. O.; Sites, J. R. Conduction-Band-Offset Rule Governing J-V Distortion in CdS/CI(G)S Solar Cells. *MRS Proc.* **2011**, *865*, F5.32.

(25) Pudov, A. O.; Kanevce, A.; Al-Thani, H. A.; Sites, J. R.; Hasoon, F. S. Secondary Barriers in CdS–CuIn[Sub 1−x]Ga[Sub x]Se[Sub 2] Solar Cells. *J. Appl. Phys.* **2005**, *97* (6), 064901.

(26) Monticone, S.; Tufeu, R. Complex Nature of the UV and Visible Fluorescence of Colloidal ZnO Nanoparticles. *J. Phys. Chem. B* **1998**, *102* (16), 2854–2862.

(27) Hegedus, S. S.; Shafarman, W. N. Thin-Film Solar Cells: Device Measurements and Analysis. *Prog. Photovoltaics Res. Appl.* **2004**, *12* (23), 155–176.

(28) Cao, Y.; Stavrinadis, A.; Lasanta, T.; So, D.; Konstantatos, G. The Role of Surface Passivation for Efficient and Photostable PbS Quantum Dot Solar Cells. *Nat. Energy* **2016**, *1* (4), 16035.

(29) Labelle, A. J.; Thon, S. M.; Masala, S.; Adachi, M. M.; Dong, H.; Farahani, M.; Ip, A. H.; Fratalocchi, A.; Sargent, E. H. Colloidal Quantum Dot Solar Cells Exploiting Hierarchical Structuring. *Nano Lett.* **2015**, *15* (2), 1101–1108.

CHAPTER 3 The Effect of Surface Chalcogen Enrichment on PbS Colloidal Quantum Dots

PbS colloidal quantum dot (QD) solar cells have been extensively studied over decades with significant improvement in device power conversion efficiency (PCE).[1] A milestone was reached in 2014 by Bawendi et al., demonstrating an n-i-p device structure by tailoring the doping concentration and energy levels of PbS QD films by layering films with different capping ligands, namely tetrabutylammonium iodide (TBAI) and ethanedithiol (EDT).[2] The EDT treated QD layer has favorable energy level positions, higher p-type doping and greater relative air-stability, promoting hole transport, increasing the depletion width and providing longer-lasting device performance.

In spite of the improved device PCE and air-stability, the ZnO/TBAI-PbS QDs/EDT-PbS QDs device design still suffers from a substantial open-circuit voltage (V_{OC}) deficit, which is attributed to trap-assisted carrier recombination within the device stack.[3,4] In addition to continuous improvements in passivating the intrinsic PbS QD layer,[5,6] effort has also been spent to suppress carrier recombination in other equally important components of the device, including the heterojunction interface and the transport layer at the device back contact.[7–10] In Chapter 2, a CdSe QD buffer is designed for the ZnO/PbS interface, while in this chapter we present our study to improve the p-type EDT-PbS QD back contact layer.

Recent studies indicate insufficient p-doping in the EDT-PbS QD layer creates Schottky barriers at the PbS QD/Au interface that hinders hole extraction.[11,12] In contrast to the many reports exploring halide and metal-halide treatments to prepare intrinsic and n-type PbS QD films, there are few reports on controllably increasing the hole concentration in the PbS QD layer. To p-dope PbS QD films, existing reports typically rely on solid-state treatments to introduce chalcogens and/or the p-doping effect of oxygen.[13–15] For ultrasmall, 3 nm PbS QDs, the most commonly used material in QD photovoltaic devices, these approaches either are accompanied by aggressive chemistries that cause the QDs to fuse and/or that disturb other materials in the

device stack underneath the QD layer, which jeopardize the n-i-p device design as well as device performance.

Herein, we develop a solution-based, colloidal atomic layer deposition (cALD) method to manipulate the doping concentration of PbS QD thin films by altering their surface stoichiometry. The solution approach is advantageous for fine tuning the amount of sulfur added to the surface of PbS QDs while maintaining their dispersity. We study the effect of sulfur enrichment on charge transport and the doping concentration in PbS QD-EDT layers within the device platform of field-effect transistors (FETs) and by using photoconductivity measurements. Preliminary X-ray photoelectron spectroscopy (XPS) measurements suggest the oxidation state of sulfur, SO_3^{2-}, as the chemical origin of surface sulfur doping.

3.1 Sulfur-Enriched PbS QDs by Colloidal Atomic Layer Deposition

The cALD of sulfur on PbS QDs is modified from the half reaction of a process reported for growing CdS shells on PbS QD cores.[16] As depicted in Figure 3.1a, sulfur atoms are deposited onto PbS QDs by mixing non-polar and polar phases consisting of QDs dispersed in octane with Na_2S, the sulfur source, dissolved in formamide (FA). Typically, 100 μL of PbS QDs (20 mg/mL in octane), 1-30 μL of Na_2S (60 mM in FA), 100 μL of FA and 0.5 μL of OLAM are added to a centrifuge tube and vortexed for 1 min. After 1 min of centrifugation, the FA phase is extracted, replaced by fresh FA, and vortexed again with the QD dispersion for 10 s to remove excess and loosely bound S^{2-}. This FA washing step is repeated twice. S-enriched PbS (PbS/S) QDs are collected in their colloidal form in octane. Unlike the solution-ligand exchange process, where PbS QDs experience a phase transition if the organic surface ligand is successfully replaced by S^{2-}, QDs still remain dispersed in octane during the cALD process thanks to stabilization by oleylamine (OLAM) added in the beginning of the reaction. OLAM not only

coordinates surface Pb as L-type ligands, but also binds to the S^{2-} sites as RNH_3^+ after protonation.[17]

We observe the spectral evolution of PbS QD dispersions as the amount of S^{2-} applied in the cALD process varies [Figure 3.1b]. The first exciton absorption peak of 3 nm PbS QDs at 955 nm broadens as the volume of the Na_2S solution is increased from 1 to 3 μL [Figure 3.1b, black, red and green]. Upon treatment with 10 μL of the S^{2-} solution, the QD dispersion exhibits an increasingly broad absorption feature and consists of not only a peak at 955 nm, but also a shoulder between 1000 and 1100 nm. Further raising the volume of the Na_2S solution to 30 μL fully develops an absorption peak at 1040 nm, corresponding to a bandgap energy of 1.19 eV and particle size of 3.4 nm.[18] This evolution in the absorption peak at 1040 nm due to addition of S, distinct from the parent 955 nm absorption resonance, without showing intermediate wavelengths is consistent with similar observations reported in the CdS QD system.[18] Meanwhile, the stoichiometry of the QDs measured by energy dispersive X-ray spectroscopy (EDS) changes from Pb rich to S rich as the amount of S^{2-} increases [Table 3.1], in agreement with our expectation that more S atoms are added when the volume of the S-source is increased. TEM images taken for PbS QDs with Pb:S of 1.21:1 (pristine), 0.97:1 (10 μL Na_2S cALD) and 0.75:1 (30 μL Na_2S cALD), respectively [Figure 3.1d,e,f], show necking and fusion of QDs when the system becomes sulfur rich. The particle fusion process likely happens in the solid-state after the deposition of QD assemblies, suggested by the experimental and simulation results in the following section of the chapter. This structural instability of chalcogen-terminated PbS/Se QDs has been reported previously in our group, when their thin films are treatment by chalcogenide.[13]

To demonstrate the generality of the cALD process, we perform identical treatment on 4 nm PbS QDs. As anticipated, with increasing S^{2-} concentration the absorption peak, originally at 1170 nm, shows broadening and it red shifts [Figure 3.1c], and the Pb:S ratio decreases [Table 3.1].

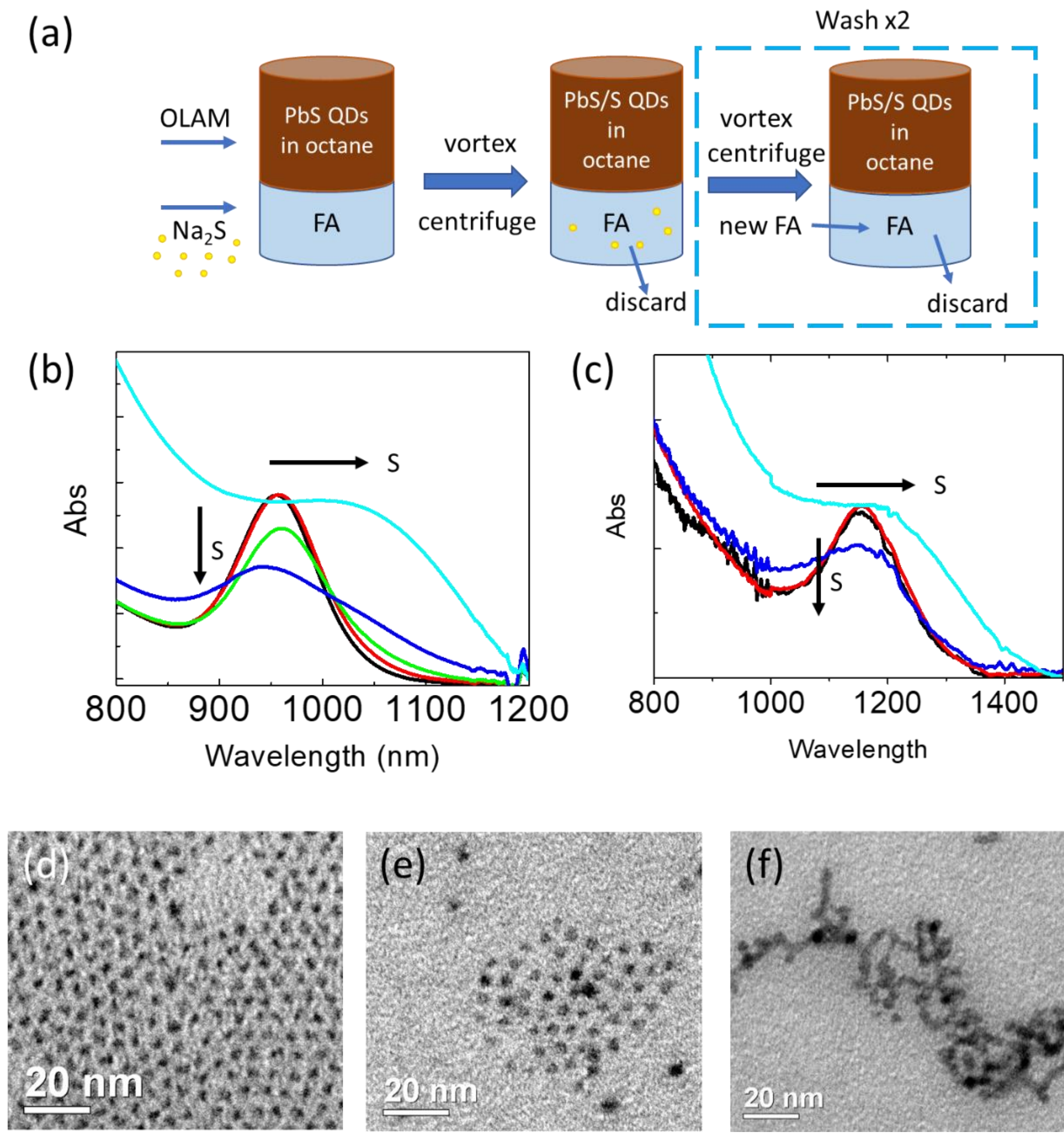

Figure 3.1 (a) Schematic of the cALD process. PbS QDs dispersed in octane are phase separated from the Na_2S solution in FA (left). Sulfur atoms are added to the PbS QD surface during mixing of the two phases (middle). The PbS/S QD dispersion is purified twice with fresh FA (right). UV-Vis absorption spectra of (b) 3 nm and (c) 4 nm PbS QD solution as made (black), treated by 1 (red), 3 (green), 10 (blue), and 30 (cyan) µL of Na_2S solution. TEM images of 3 nm PbS QDs (d) as synthesized and treated by (e) 10 and (f) 30 µL of Na_2S solution during the cALD process.

Table 3.1 Stoichiometry of 3 nm PbS QDs after different Na_2S cALD treatments

Pb:S	3 nm	4 nm
PbS-ref	1.21±0.05	1.11±0.03
1 μL Na_2S -0.5uL OLAM	1.18±0.05	1.05±0.04
3 μL Na_2S -0.5uL OLAM	1.10±0.06	
10 μL Na_2S -0.5uL OLAM	1.00±0.06	0.74±0.03
30 μL Na_2S -0.5uL OLAM	0.78±0.04	0.66±0.05

To study the role of FA and OLAM during the cALD reaction, we perform control experiments. First, we repeat the cALD process with only pristine FA, resulting in a blue shift of the absorption peak [Figure 3.2a] and a decrease in the Pb:S ratio as measured from EDS [Table 3.2]. The QDs become unstable and precipitate from solution after interacting with FA. It suggests that FA etches the QDs by stripping oleic acid and removing oleic-acid bound surface Pb atoms, similar to the stripping effect of dimethylformamide (DMF) found for the PbSe QD system.[19] Nevertheless, when the identical process is conducted in the presence of 0.5 μL of OLAM, the absorption peak is less blue shifted [Figure 3.2a] and the stoichiometry is almost unchanged, indicating that OLAM protects the QDs from etching by FA. Neither FA nor OLAM is responsible for the growth of QDs or the red-shift of the absorption peak in the presence of the Na_2S solution, hence the sulfur enrichment observed after the cALD process is a result of sulfur deposition on PbS QDs.

The role of OLAM is further revealed by performing the cALD process with fixed Na_2S concentration but varying the amount of OLAM. The absorption spectra show less broadening by the 10 μL Na_2S treatment when the concentration of OLAM is increased from 0.5 to 1 μL [Figure

3.2b]. This effect saturates when the amount of OLAM increases from 1 to 2 μL. The Pb:S ratio is higher but within the error when 1 μL of OLAM is used [Table 3.2], indicating fewer S atoms and more OLAM is bound to the QD surface. Therefore, besides stabilizing the colloidal system, the incorporation of OLAM also competes with S^{2-} for binding to surface Pb sites. A minimum amount of OLAM should be used if more effective S-enrichment is desired.

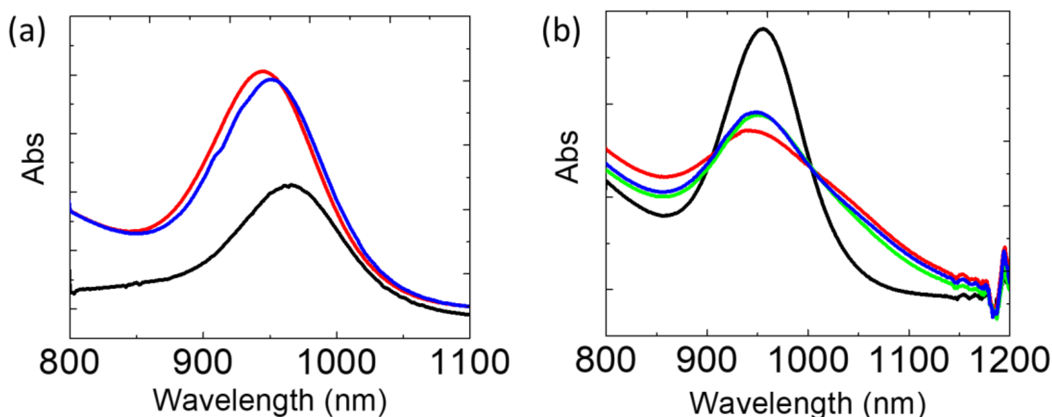

Figure 3.2 Absorption spectra of PbS QD solutions as synthesized (black), with (a) only FA (red) and FA and OLAM (blue) and (b) 10 μL of Na_2S and 0.5 (red), 1 (blue) and 2 (green) μL of OLAM.

Table 3.2 Stoichiometry of PbS QDs after different cALD treatments

	Pb:S
PbS-ref	1.21±0.05
PbS-FA	1.17±0.10
PbS-FA-OLAM	1.25±0.04
10 μL Na_2S -0.5 μL OLAM	1.00±0.06
10 μL Na_2S-1 μL OLAM	1.05±0.01

3.2 Facet-dependent Deposition of Sulfur Atoms

We investigate the mechanism of the sulfur atom addition during the cALD process. Powder X-ray diffraction (XRD) is employed to characterize the extend of orientation within the QD ensembles. If the sulfur enrichment changes the surface structure and chemistry and alters the preferential orientation direction, the relative intensities of diffraction peaks will be different. From the width of the diffraction peak, we can calculate the size of QDs to determine whether they fuse after the sulfur treatment and upon assembly. For this measurement, thick PbS QD films are drop cast on Si wafers. Consistent with the rock salt crystal structure of PbS, Figure 3.3a shows that the diffraction signal is primarily dominated by (111) reflections for the 4 nm PbS QD assembly, while it is more evenly distributed across (111), (200) and (220) in the 3 nm dots, suggesting that larger QDs tend to orient during film formation.

As reflections of underlying surface chemistry, the XRD pattern of films of 4 nm PbS QDs with various amount of Na_2S treatment is collected and shown in Figure 3.3b. Upon addition of OLAM, the relative intensity of (220) and (200) reflections increase significantly [Figure 3.3b red]. As Na_2S participates in the cALD, the intensity of (220) peak starts to decrease but the (200) reflection becomes increasingly stronger [Figure 3.3, green, blue and cyan]. The relative intensities of the (220) and (200) peaks are normalized to that of the (111) and plotted in Figure 3.3c. This change of diffraction intensity indicates that the preferential facets for QDs to assemble changes from {111} to {220} when only OLAM is introduced, consistent with the {220} facets providing stronger interdot interactions through the newly attached OLAM ligands that have replaced the original oleic acid ligands. However, the intensity of (220) decrease with increasing Na_2S concentration, suggesting that the QD orientation induced by OLAM ligands is altered by the introduction of S^{2-}. This is consistent with our observation in to the absorption spectra in Figure 3.2b that show S^{2-} competes with OLAM for surface Pb sites. The QD ensemble also obtains its ordering along the {200} facets, as the (200) reflection becomes more intense when

OLAM and more Na_2S is involved [Figure 3.3c, red]. We thus speculate the OLAM ligand exchange and S^{2-} deposition occur predominantly on the {220} and {200} facets. It is consistent with the lower binding energies of oleic acid on these facets in literature reports.[20] At high Na_2S concentrations, the width of the diffraction peaks narrows. We calculate the Scherrer grain size and correlate it with the S^{2-} concentration [Figure 3.3c, blue]. The grain size of PbS QD films is 3.9 nm prior to any treatment, in great alignment with the 4 nm particle size, and increases to 5.8 nm after 10 µL of Na_2S treatment. This is supportive to our hypothesis that as more S^{2-} is introduced, OLAM is further removed from {220} and {200} and QDs start to neck/partially fuse through S enriched {200} facets.

Likewise, the XRD pattern of 3 nm PbS QD films shows first an increase and then a decrease of the (220) peak intensity upon reacting separately with OLAM only and a mixture of OLAM and 1 µL Na_2S solution [Figure 3.3d, red and green]. However, possibly due to less well developed {111} facets in smaller PbS QDs,[21] there is no considerable difference between the diffraction intensity of (111) and (200) before any cALD treatment. The evolution of (200) during these chemical processes is therefore not as clearly demonstrated in this system as it is in the 4 nm QD films, although the underlying surface chemistry is common. The exchange of surface ligands during the cALD process can be described by Figure 3.3e, where both OLAM and S^{2-} replace the OA, but S^{2-} can also compete over OLAM for the surface Pb sites simultaneously.

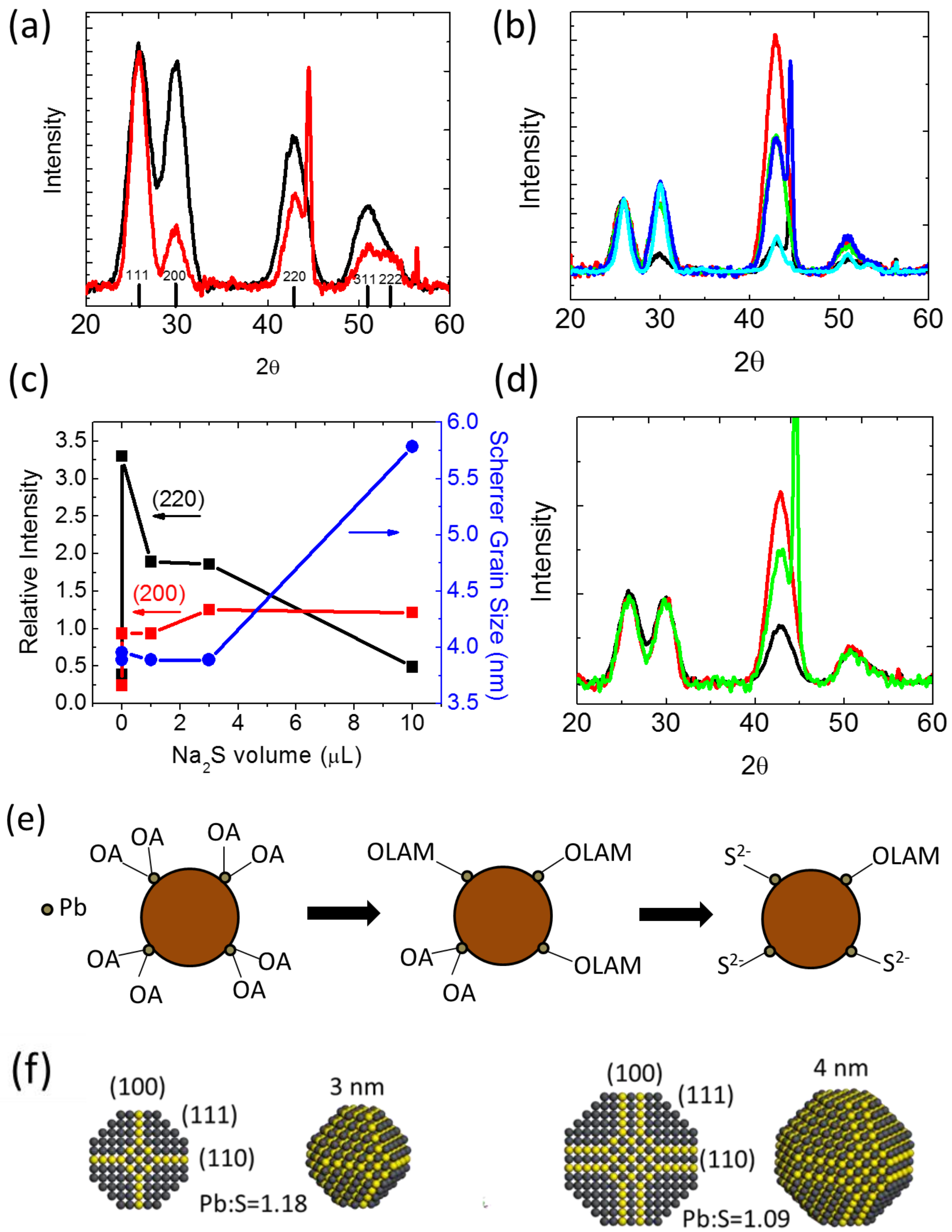
(a)
Intensity
111
200
220
311
222
20
30
40
50
60
2θ
(b)
Intensity
2θ
(c)
Relative Intensity
(220)
(200)
Scherrer Grain Size (nm)
Na_2S volume (μL)
(d)
Intensity
2θ
(e)
Pb
OA
OLAM
S^{2-}
(f)
(100)
(111)
(110)
3 nm
Pb:S=1.18
4 nm
Pb:S=1.09

Figure 3.3 XRD patterns of films of (a) 3 nm PbS QDs (black) and 4 nm PbS QDs (red), (b) 4 nm PbS QDs (black) treated by only OLAM (red), and OLAM mixed with 1 (green), 3 (blue), 10 (cyan) μL of Na_2S solution, and (c) Intensity of (220) (black) and (200) (red) relative to that of (111) and Scherrer grain size calculated from (220) (blue) for 4 nm PbS QD films as synthesized, with OLAM treated only and with increasing amount of Na_2S enrichment. (d) XRD patterns of 3 nm PbS QDs (black) treated by only OLAM (red) and OLAM mixed with 1 μL of Na2S solution (green). Note: the sharp features at 44 and 56 ° are from the Si substrate. (e) Schematics of the surface ligands changed from OA to OLAM and S^{2-} during the cALD process. (f) Simulated crystal structures of PbS QDs terminated by (100) (111) and (110) facets with 3 nm and 4 nm in size, respectively.

Based on the XRD result, we construct crystal structures for 3 and 4 nm PbS QDs terminated by (100), (111) and (110) facets [Figure 3.3f]. The stoichiometry calculated from the structure matches well with the EDS result. We simulate the Pb:S ratio as a S shell is added to each facet. For example, the Pb:S ratio of the 3 nm PbS QDs changes from 1.29 to 1.16 when all {110} facets are covered by S, and further decreases to 0.96 if {100} facets are also S enriched. Therefore, there are sufficient sites on these two facet groups to accommodate S atoms introduced by the cALD process with 1, 3 or 10 μL of Na_2S solution. When a larger S source is provided, {111} facets with additional Pb sites are required to participate even though this is energetically less favorable, so that the Pb:S ratio becomes as low as 0.68 when a complete S outer shell is formed. In the case of 30 μL of Na_2S treatment, the S atoms are expected to cover all sites on the {110} and {100} facets and partially of the {111} facets given the Pb:S ratio of 0.78. Simulating such crystal structures, we obtain a particle diameter about 3.5 nm, yielding an excellent match to the 1040 nm bandgap deduced from the absorption peak in Figure 3.1b. In comparison, there are more sites for S on the {110} and {100} facets of the 4 nm PbS QDs, making it more accessible to S incorporation when the same S source is presented.

Table 3.3 Simulated Pb:S ratios for 3 nm and 4 nm PbS QDs as each facet group is covered by S

Pb:S	3 nm	4 nm
pristine	1.29	1.09
{110} covered by S	1.16	0.91
{100} covered by S	0.99	0.94
both {110} and {100} covered by S	0.96	0.85
{111} covered by S	0.83	0.96
{110}, {100} and {111} covered by S	0.68	0.77

3.3 Charge Transport and Doping of PbS/S QD Films

We study the effect of S enrichment on the doping and transport properties of PbS QD films by fabricating FET devices. On heavily n-doped Si wafers with thermally grown 250 nm SiO_2, we spin coat PbS QDs after the solution cALD process using different concentrations of the Na_2S solution. A standard EDT solid-state ligand exchange is then applied on the QD film as commonly described in literature to remove remaining OLAM and oleic acid ligands on the QD surface,[2] and Au contacts are evaporated to complete the device.

All PbS QD FET devices show higher currents as the gate voltage is swept to negative values, characteristic of predominantly p-type semiconductor materials [Figure 3.4]. However, the overall current experiences a decrease when the QDs are treated by a 1 μL of Na_2S solution before increasing for all of the higher Na_2S concentrations. At a fixed gate voltage higher than the threshold voltage ($V_G>V_T$), current is proportional to the mobility and total carrier concentration of

the channel material. Since the device current in the linear regime is too small, we extract hole mobility μ and V_T from the I_D-V_G characteristics in the saturation regime to distinguish the effect of S enrichment on them. In the saturation regime, the current follows:

$$I_D = \mu C_{ox} \frac{W}{L} \frac{(V_G - V_T)^2}{2} \quad \text{or} \quad \sqrt{I_D} = \sqrt{\mu C_{ox} \frac{W}{2L}} (V_G - V_T)$$

where C_{ox} is the oxide capacitance per unit area, W and L are the channel width and length respectively, V_G is gate bias applied and V_T is threshold voltage. By linearly fitting the $I_D^{1/2}$ vs. V_G curve, we obtain μ from the slope and V_T from the intercept and plot them as a function of Pb:S stoichiometry in Figure 3.4b. Except for the data point at 1 μL Na_2S treatment, as the system is made more S-rich, the hole mobility increases and V_T shifts positively, indicating enhanced carrier transport and p-type doping. This trend is consistent with literature report, where the improved hole mobility with increasing S content is attributed to improved interdot electronic coupling in the PbS QD films, as the valence band density of states is increased by reduction of interparticle distance or densification of the QD film.[22] We further calculate the change of carrier concentration Δp induced by the S enrichment according to the relationship:[23]

$$\Delta p = \frac{\Delta V_T C_{ox}}{q T_{QD}}$$

where T_{QD} is the thickness of the active QD film which is the Debye length.[14] Based on T_{QD}= 20 nm, we obtain $\Delta p \sim 4 \times 10^{16}\ \Delta V_T$. Combining this relationship and the simulated crystal structures in Figure 3.3d, we can estimate the additional hole concentration and the number of sulfur atoms added to introduce it at a given Pb:S. For example, by adding 91 sulfur atoms on the surface of individual PbS QDs through cALD, we achieve Pb:S~1 in the QD dispersion, and ~2×10^{16} cm^{-3} extra holes generated after forming EDT capped QD thin films.

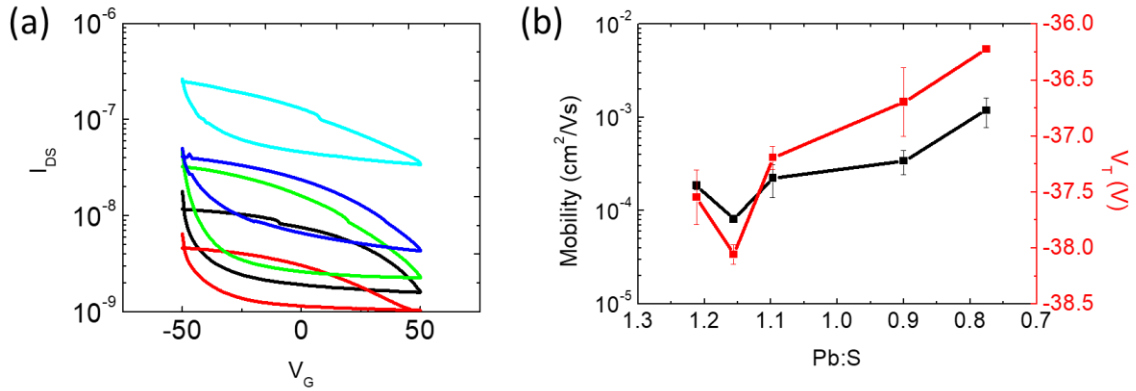

Figure 3.4 (a) I_D-V_G characteristics of EDT capped PbS QD thin-film FETs (black), after 1(red), 3 (green), 10 (blue) and 30 (cyan) μL of Na_2S treatments. (b) Hole mobility and threshold voltage extracted from the FET characteristics as a function of QD stoichiometry.

Motivated by improving the hole transport layer of PbS QD solar cells, we study how the photoresponse is influenced by the cALD process. We fabricate photoconductors on glass substrates using the same surface treatments to prepare the QDs before depositing their films, as used for FETs on Au bottom contacts. Current across the two terminals is collected at an electrical field of 500 V/cm both in the dark and under illumination by a 647-nm single-wavelength laser at 6.4 mW/m^2. The photoconductivity, or photocurrent at a constant electrical field, is directly proportional to the product of the lifetime τ and mobility μ of photogenerated majority carriers. And the τ·μ is proportional to the majority carrier diffusion length.

After the 1 μL Na_2S cALD treatment, both the dark current and photocurrents decrease [Figure 3.5, black and red]. The lower current in the dark is consistent with the FET measurement. Since the mobility is also reduced, it is not conclusive about the change in carrier lifetime from the decrease of photocurrent along in this case. However, the QD film treated by 3 μL of Na_2S solution shows higher photocurrents while maintaining similarly low dark current [Figure 3.5,

green]. Because the mobility is not altered significantly by this cALD condition confirmed by both the dark current here and FET measurements, the higher current under illumination is mainly attributed to extended carrier lifetime. After stored in ambient environment for 9 days, the samples are remeasured to be investigated for their air stability [Figure 3.5b]. The reference EDT-PbS QD film becomes apparently less conductive both in the dark and under illumination. Its absorption peak shifts from 990 to 890 nm [Figure 3.5c], indicating oxidation of QDs, which is responsible for poor carrier transport. The cALD treated QDs are yet less affected by the prolonged air exposure, showing higher dark and photocurrents than the reference. Their absorption peaks exhibit smaller blue shifts, from 990 to 920 nm, probably due to better passivation of surface Pb through the deposition of S atoms.

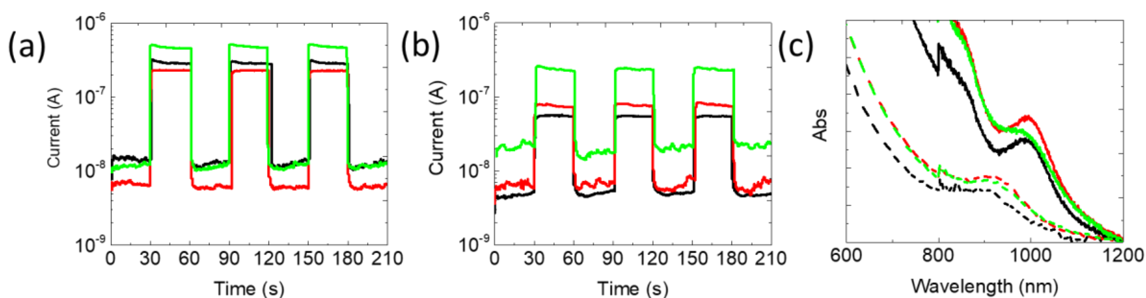

Figure 3.5 Photoconductivity measurements on (a) day 1 and (b) day 10 of EDT capped PbS QD films (black), with 1 (red) and 3 (green) μL of Na_2S cALD treatments. (c) Corresponding absorption spectra of the three samples on day 1 (solid) and 10 (dashed).

3.4 Chemical Origin of Surface Sulfur Doping in PbS QDs

The shift of threshold voltage in the FET measurement indicates a change of carrier concentration within the QD film after the cALD process. The sulfur enrichment mediates the

stoichiometry of PbS QDs, which is considered responsible for tuning the fermi level of the QD ensemble.[14,24] However, the decrease of doping concentration after 1 μL Na_2S cALD treatment even with compensated Pb:S ratios cannot be explained by this picture. In fact, there are reports claiming no net doping effect should be expected by adding doubly ionized sulfur, as the closed-shell S^{2-} should not alter the valence band filling.[22,25] Therefore, we suspect alternative chemical origins induced by the sulfur enrichment that essentially causes the doping phenomena, and employ XPS for preliminary studies.

We have examined two film samples of PbS QDs by XPS, one pristine as reference and the other with 1 μL Na_2S cALD treatment and plotted their Pb 4f and S 2s characteristics in Figure 3.6, respectively. By deconvoluting the XPS spectra, we identify spectral line of PbS and $PbSO_3$ from the both the Pb and S region, while there are also lines assigned to S-C and S-S originated from the EDT ligands.[26] No reasonable match is found for the additional peaks denoted as * and ** in the spectra in the NIST data base, and they are excluded for the concern of our study here. The atomic percentage of all composition is listed in Table 3.4.

After the 1 μL Na_2S cALD treatment, the relative percentage of $PbSO_3$ decreases in both the Pb and S spectra. It is known that $PbSO_3$ introduces shallow states close to the valence band edge,[27,28] which are possible to act as acceptors, so less $PbSO_3$ formation after the cALD process is consistent with lower doping observed in FET measurements. The PbS component detected in the S regime represents all Pb-S bonds including the ones in the nanocrystal lattice and those on the surface. A higher percentage of it relative to the $PbSO_3$ in the cALD treated sample suggests that the QD surface is enriched by sulfur but fewer sulfur atoms are transformed into $PbSO_3$. Hypothetically, when only a small number of S atoms are deposited onto the QD surface, the QDs are still surrounded by densely packed organic ligand shells, which block oxygen diffusion and prevent surface S atoms from oxidation. The remaining OLAM ligands from the cALD process as inferred from the XRD result can be barriers for carrier transport causing lower

mobility, if they are not fully exchanged by EDT. This assumption remains to be supported by further high resolution XPS and FTIR characterizations and other control experiments.

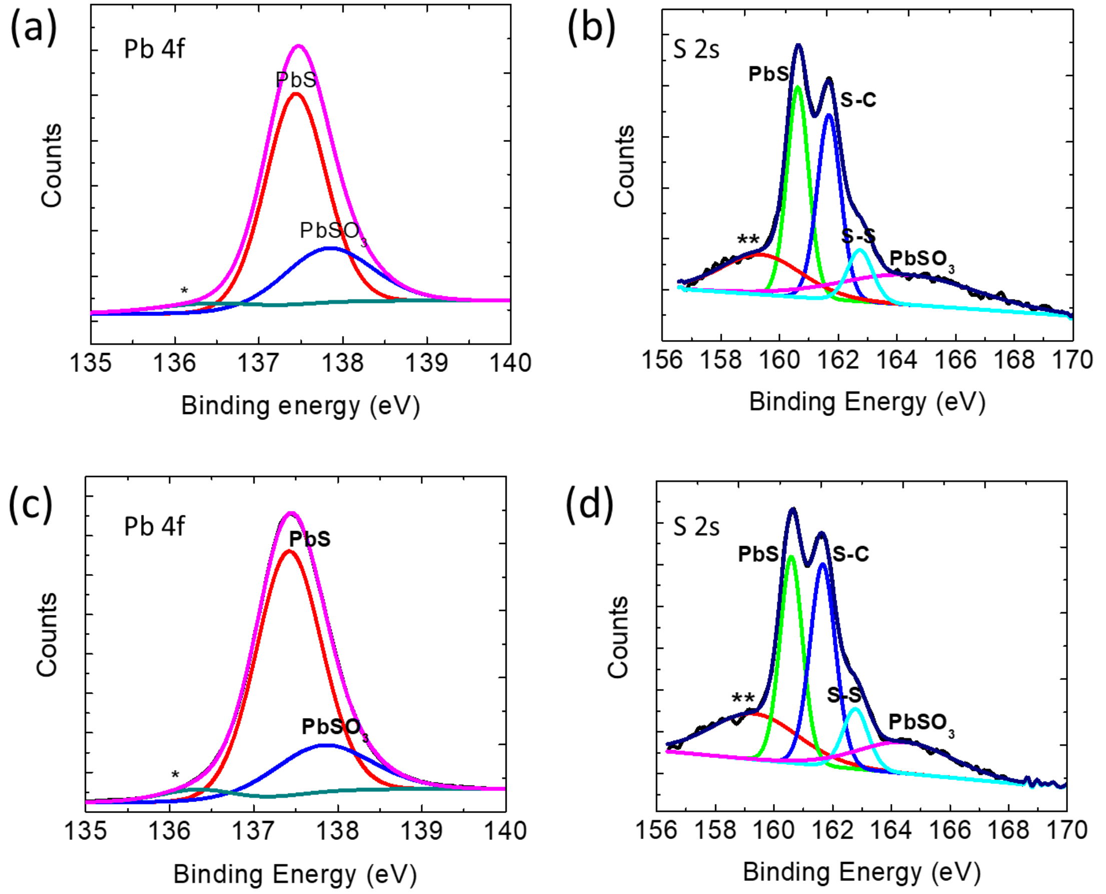

Figure 3.6 Pb 4f and S 2s XPS spectra of EDT-PbS QD films (a) (b) without cALD and (c) (d) after 1 μL Na_2S cALD treatment.

Table 3.4 Atomic percentage of components detected in XPS measurement

Atomic %	Pb		S			
	PbS	$PbSO_3$	PbS	$PbSO_3$	S-C	S-S
PbS-EDT	27.5	9.7	28.0	14.5	15.6	4.7
PbS/S-EDT	29.5	7.9	29.7	10.2	17.6	5.1

3.5 Conclusions

In this chapter, we describe a solution cALD approach utilizing Na_2S in FA to enrich the PbS QD surface with sulfur. This method is suitable for precisely tuning the stoichiometry of ultrasmall-sized PbS QDs from Pb rich till S rich while maintaining their colloidal stability by additional OLAM ligands. As the Pb:S ratio of QDs is decreased by the cALD process, we improve the hole mobility and concentration within the EDT capped PbS QD films and achieve enhanced photoconductivity from QDs treated by 3 µL of Na_2S solution. To investigate the doping mechanism and explain the opposite trend observed in FET characteristics with 1 µL Na_2S cALD treatment, we probe the surface composition of PbS QD films after EDT ligand exchange and speculate that the formation of $PbSO_3$ is the chemical origin of p-type doping. Moving forward, we will complete the correlation between oxidation states and doping concentration, study the effect of sulfur enrichment on PbS QD films as hole transport layers in the solar cell geometry. By increasing p-type doping of the EDT-PbS QD layer, we expect the Schottky barrier at the device back contact will be removed and band alignment will become more favorable for hole extraction, hence improving solar cell parameters including short-circuit current, open-circuit voltage and fill factor.

3.6 References

(1) Carey, G. H.; Abdelhady, A. L.; Ning, Z.; Thon, S. M.; Bakr, O. M.; Sargent, E. H. *Chem. Rev.* **2015**, *115* (23), 12732–12763.

(2) Chuang, C.-H. M.; Brown, P. R.; Bulović, V.; Bawendi, M. G. *Nat. Mater.* **2014**, *13* (8), 796–801.

(3) Pradhan, S.; Stavrinadis, A.; Gupta, S.; Christodoulou, S.; Konstantatos, G. *ACS Energy Lett.* **2017**, *2* (6), 1444–1449.

(4) Chuang, C.-H. M.; Maurano, A.; Brandt, R. E.; Hwang, G. W.; Jean, J.; Buonassisi, T.; Bulović, V.; Bawendi, M. G. *Nano Lett.* **2015**, *15* (5), 3286–3294.

(5) Xu, J.; Voznyy, O.; Liu, M.; Kirmani, A. R.; Walters, G.; Munir, R.; Abdelsamie, M.; Proppe, A. H.; Sarkar, A.; García de Arquer, F. P.; Wei, M.; Sun, B.; Liu, M.; Ouellette, O.; Quintero-Bermudez, R.; Li, J.; Fan, J.; Quan, L.; Todorovic, P.; Tan, H.; Hoogland, S.; Kelley, S. O.; Stefik, M.; Amassian, A.; Sargent, E. H. *Nat. Nanotechnol.* **2018**, *13* (6), 456–462.

(6) Liu, M.; Voznyy, O.; Sabatini, R.; García de Arquer, F. P.; Munir, R.; Balawi, A. H.; Lan, X.; Fan, F.; Walters, G.; Kirmani, A. R.; Hoogland, S.; Laquai, F.; Amassian, A.; Sargent, E. H. *Nat. Mater.* **2017**, *16* (2), 258–263.

(7) Pradhan, S.; Stavrinadis, A.; Gupta, S.; Konstantatos, G. *ACS Appl. Mater. Interfaces* **2017**, *9* (33), 27390–27395.

(8) Ren, Z.; Kuang, Z.; Zhang, L.; Sun, J.; Yi, X.; Pan, Z.; Zhong, X.; Hu, J.; Xia, A.; Wang, J. *Sol. RRL* **2017**, *1* (12), 1700176.

(9) Aqoma, H.; Mubarok, M. Al; Lee, W.; Hadmojo, W. T.; Park, C.; Ahn, T. K.; Ryu, D. Y.; Jang, S.-Y. *Adv. Energy Mater.* **2018**, *8* (23), 1800572.

(10) Kirmani, A. R.; García de Arquer, F. P.; Fan, J. Z.; Khan, J. I.; Walters, G.; Hoogland, S.; Wehbe, N.; Said, M. M.; Barlow, S.; Laquai, F.; Marder, S. R.; Sargent, E. H.; Amassian, A. *ACS Energy Lett.* **2017**, *2* (9), 1952–1959.

(11) Hu, L.; Mandelis, A.; Lan, X.; Melnikov, A.; Hoogland, S.; Sargent, E. H. *Sol. Energy Mater. Sol. Cells* **2016**, *155*, 155–165.

(12) Speirs, M. J.; Balazs, D. M.; Dirin, D. N.; Kovalenko, M. V.; Loi, M. A. *Appl. Phys. Lett.* **2017**, *110* (10), 103904.

(13) Oh, S. J.; Berry, N. E.; Choi, J.-H.; Gaulding, E. A.; Lin, H.; Paik, T.; Diroll, B. T.; Muramoto, S.; Murray, C. B.; Kagan, C. R. *Nano Lett.* **2014**, *14* (3), 1559–1566.

(14) Oh, S. J.; Berry, N. E.; Choi, J.-H.; Gaulding, E. A.; Paik, T.; Hong, S.-H.; Murray, C. B.; Kagan, C. R. *ACS Nano* **2013**, *7* (3), 2413–2421.

(15) Stavrinadis, A.; So, D.; Konstantatos, G. *J. Phys. Chem. C* **2016**, *120* (36), 20315–20322.

(16) Nasilowski, M.; Nienhaus, L.; Bertram, S. N.; Bawendi, M. G. *Chem. Commun.* **2017**, *53* (5), 869–872.

(17) Razgoniaeva, N.; Carrillo, L.; Burchfield, D.; Moroz, P.; Adhikari, P.; Yadav, P.; Khon, D.; Zamkov, M. *Chem. Mater.* **2016**, *28* (8), 2823–2833.

(18) Razgoniaeva, N.; Carrillo, L.; Burchfield, D.; Moroz, P.; Adhikari, P.; Yadav, P.; Khon, D.; Zamkov, M. *Chem. Mater.* **2016**, *28* (8), 2823–2833.

(19) Moreels, I.; Lambert, K.; Smeets, D.; De Muynck, D.; Nollet, T.; Martins, J. C.; Vanhaecke,

F.; Vantomme, A.; Delerue, C.; Allan, G.; Hens, Z. *ACS Nano* **2009**, *3* (10), 3023–3030.

(20) Bealing, C. R.; Baumgardner, W. J.; Choi, J. J.; Hanrath, T.; Hennig, R. G. *ACS Nano* **2012**, *6* (3), 2118–2127.

(21) Pradhan, S.; Stavrinadis, A.; Gupta, S.; Christodoulou, S.; Konstantatos, G. *ACS Energy Lett.* **2017**, *2* (6), 1444–1449.

(22) Balazs, D. M.; Bijlsma, K. I.; Fang, H.-H.; Dirin, D. N.; Döbeli, M.; Kovalenko, M. V.; Loi, M. A. *Sci. Adv.* **2017**, *3* (9), eaao1558.

(23) Zhao, Q.; Zhao, T.; Guo, J.; Chen, W.; Zhang, M.; Kagan, C. R. *ACS Nano* **2018**, *12* (2), 1313–1320.

(24) Kim, D.; Kim, D. H.; Lee, J. H.; Grossman, J. C. *Phys. Rev. Lett.* **2013**, *110* (19), 1–5.

(25) Voznyy, O.; Zhitomirsky, D.; Stadler, P.; Ning, Z.; Hoogland, S.; Sargent, E. H. *ACS Nano* **2012**, *6* (9), 8448–8455.

(26) Tang, J.; Brzozowski, L.; Barkhouse, D. A. R.; Wang, X.; Debnath, R.; Wolowiec, R.; Palmiano, E.; Levina, L.; Pattantyus-Abraham, A. G.; Jamakosmanovic, D.; Sargent, E. H. *ACS Nano* **2010**, *4* (2), 869–878.

(27) Konstantatos, G.; Levina, L.; Fischer, A.; Sargent, E. H. *Nano Lett.* **2008**, *8* (5), 1446–1450.

(28) Konstantatos, G.; Sargent, E. H. *Appl. Phys. Lett.* **2007**, *91* (17), 173505.

CHAPTER 4 The Effect of Dielectric Environment on Doping Efficiency in Colloidal PbSe Nanostructures

This work has been published as Zhao, Q.*; Zhao, T.*; Guo, J.; Chen, W.; Zhang, M.; Kagan, C. R. The Effect of Dielectric Environment on Doping Efficiency in Colloidal PbSe Nanostructures. *ACS Nano* **2018**, *12* (2), 1313–1320. (* equal contribution)

Colloidal lead chalcogenide nanostructures, including nanocrystals (NCs) and nanowires (NWs), are promising building blocks for solution-based deposition of high mobility and narrow bandgap semiconductor devices, such as electronic transistors and circuits, infrared photodetectors and photovoltaics, and thermoelectrics.[1–9] The design and operation of such devices requires control over the free carrier type and concentration in assemblies of the nanostructures.[10] The electron and hole concentrations in lead chalcogenide NC and NW assemblies have been manipulated through "remote doping," *i.e.*, by the addition of atoms, ions, or ligands at the surface of the nanostructures,[1,11–16] or charge transfer from adjacent molecules.[17] Although different methods have been developed to dope lead chalcogenide nanostructures, the doping efficiency is extremely low, such that only approximately 1% of dopants yield carriers.[11,18] Therefore high concentrations of dopants have been required to reach high conductances, at the anticipated expense of increasing carrier scattering, and hence reducing achievable carrier mobilities.

The low doping efficiency in these nanostructures can be attributed to dopants that are ineffectively bound,[11,19] and/or consumed by surface redox reactions, unidentified traps,[10] or self-compensation[10,20,21] and/or effectively bound but not ionized.[18] The concentration of inactive dopants may be increased in nanostructures, compared to their bulk analogues, as the dopant ionization energy can be enhanced by quantum and/or dielectric confinement effects.[22–24] For a

given size nanostructure, where quantum confinement effects are fixed, theoretical and experimental studies of silicon nanowires (SiNWs) have shown that the ionization energy of dopants increases as the dielectric mismatch between the NW and its surrounding increases.[25,26] Lead chalcogenides have larger Bohr radii for electrons and holes and a higher dielectric constant than Si, suggesting that lead chalcogenide nanostructures should experience more significant dielectric confinement effects that act to increase dopant ionization energies.

Here we study the doping efficiency in PbSe nanostructures and show that by tailoring the surrounding dielectric environment we can greatly increase doping efficiency. We choose to probe the doping efficiency of both NW arrays and single NWs integrated in the device platform of the field effect transistor (FET), as the wires span device electrodes and thus provide a simplified picture of carrier transport, in comparison to that for NC arrays, where there are a large number of interfaces created by intervening ligands at the NC surface in the transport pathway. The NW channel in the FET platform is also accessible, allowing us to modify the NW doping and dielectric environment of completed devices. Dopant atoms (Pb, In, Se) are introduced to remotely dope PbSe NW devices and different dielectric constant polymeric and oxide materials are deposited to encapsulate the FET devices. We measure the device characteristics to probe the majority carrier type and concentration in the NWs and to calculate the doping efficiency and ionization energy of dopants. As the dielectric constant of the surrounding medium increases, the doping efficiency increases significantly by 5-10 fold and the ionization energy approaches 0 eV, consistent with theoretical prediction.

4.1 Fabrication and Doping of PbSe Nanowire (NW) Array Field-Effect Transistors (FETs)

Highly n-doped, oxidized Si wafers are patterned with Au electrodes to serve as the gate electrode, gate oxide, and source and drain electrodes of the FET platform. In particular, the source and drain electrodes (2 nm Cr/18 nm Au) are defined by photolithography to form FET channels 10 μm in length and 150 μm in width. The substrate is treated by MPTS before use. All following fabrication steps are carried out inside a nitrogen filled glovebox, unless otherwise noted. To fabricate PbSe NW array FETs, 15 nm diameter, colloidal PbSe NWs capped with oleate and tri-n-octylphosphine are synthesized and dispersed in solvent. A drop of the NW dispersion is deposited and the NWs are directed to align across the 10 μm channel of bottom-contact FETs by applying a DC electric field of 10^5 V/cm between the pre-fabricated Au source and drain electrodes, as shown in Figure 4.1 A, B.[8] To remove the long organic ligands at the surface of as-aligned NWs and better passivate the NWs and improve their contact to devices electrodes, device substrates are immersed in a 10% NH_4SCN solution in acetone for 30 s.[27,28] NW devices are annealed at 180 ^oC for 20-40 s to desorb surface bound oxygen and water, which are known to act to p-dope PbSe NWs, following procedures previously developed by our group.[13,29] After annealing, the SCN-capped NW FETs show ambipolar behavior [Figure 1C, black curve].

Devices are doped remotely by modifying the NW stoichiometry *via* thermal evaporation of Pb (n-type) or Se (p-type) on the surface of NWs, following our group's previous work on lead chalcogenide NCs and NWs.[11,12] We also provide an example of n-type impurity doping by thermally evaporating In onto the PbSe NWs, consistent with reports of In serving as a donor in bulk PbSe.[30] A film of Pb, In or Se, varying from 3 Å to 15 Å is evaporated onto the NWs array channel. Pb- and Se- doped NW devices are used as is, however In-doped NW devices are annealed at 250 ^oC for approximately 5 min to "activate" the dopants.[31]

Representative source-drain current─gate voltage I_D─V_G characteristics for Pb-doped PbSe NW array FETs are shown in the linear and saturation regimes in Figure 4.1C and D. All the I_D─V_G measurements are carried out by sweeping forward from V_D=+50 V to -50 V (solid lines) and backward from V_D=-50 V to +50 V (dotted lines). As we increase the number of Pb atoms deposited on the channel, the device behavior changes from ambipolar to increasingly n-type and to eventually heavily n-type. Correspondingly, the threshold voltage (V_T) shifts in the negative direction and the on-state electron currents first increases and then decreases. From the shifts in the device threshold voltage (ΔV_T) of the linear characteristics, we calculate the concentrations of excess carriers (Δn) provided by added donors or acceptors as,

$$\Delta n = \frac{\Delta V_T C_{ox}}{q V_{NW}}$$

where V_{NW} is the volume of the active channel and C_{ox} is the unit capacitance of the gate oxide. The linear regime characteristics (V_{DS}=0.25 V) are used in calculations to avoid the non-uniform distribution of charges across the channel at high V_{DS} in the saturation regime. The thin film model is applied to find a C_{OX} of 13 nF/cm^2 in array FETs. We note that the NWs do not completely cover the channel area defined by the source and drain electrodes (*i.e.*, the NWs occupy ~10% of the area, as seen in Figure 4.1A), therefore simply treating the NW arrays as thin films may give rise to an underestimation of Δn. A comparison between the thin film and cylinder-on-a-plate models is discussed below:

The capacitance and the change of carrier concentration calculated by thin film model is,

$$C_{ox,1} = \frac{\epsilon_0 \epsilon_{r,ox} A}{t_{ox}}, \Delta n_1 = \frac{\Delta V_T C_{ox,1}}{2RAq}$$

by the cylinder-on-plate is,[32]

$$C_{ox,2} = \frac{2\pi\epsilon_0\epsilon_{r,ox}L}{\ln[\frac{2(t_{ox}+R)}{R}]}, \Delta n_2 = \frac{\Delta V_T C_{ox,2}}{LR^2\pi q}$$

where $C_{OX,1}$ and $C_{OX,2}$ are the gate oxide capacitance by thin film model and cylinder-on-plate model, respectively, $\epsilon_{r,ox}$ is the dielectric constant of gate oxide, A and L is the channel area and length, respectively, R is the radius of NW, and t_{ox} is the thickness of the gate oxide layer. The ratio of Δn between the two models is, $\frac{\Delta n_1}{\Delta n_2} = \ln\left(\frac{2t_{ox}}{R}\right)\frac{R}{2t_{ox}} = 0.06$. If NWs sparsely span the channel such that there is no coupling between any two of the NWs, as is the case for the single NW FET, the cylinder-on-plate model is suitable. However, if the channel is entirely filled by NWs with interactions among them, then the thin film model is more appropriate. Our NW array FETs are in between the two cases, as they are not dense films, but they are also not arrays of isolated NWs. We choose the thin film model to capture the presence of bundles and overlap of NWs across the channel. We use this model consistently for NW array FETs to make comparisons in Δn as a function of doping and as a function of dielectric environment.

For Pb-doped NW array channels, as the amount of Pb increases upon evaporation of 3 Å to 10 Å thick films, the carrier concentration change calculated from the linear (Δn) regime characteristics increases from 10^{17} cm^{-3} to $3x10^{17}$ cm^{-3} [inset of Figure 4.1C]. At higher doping levels of 15 Å of deposited Pb, Δn reaches ~10^{18} cm^{-3} and the gate modulation of the current is weak.[33] Given the ~10^{14} cm^{-3} intrinsic carrier concentration of PbSe NWs with a 0.4 eV bandgap is negligible[12] compared to Δn (>10^{17} cm^{-3}), the free electron concentration (n) is approximately equal to Δn.

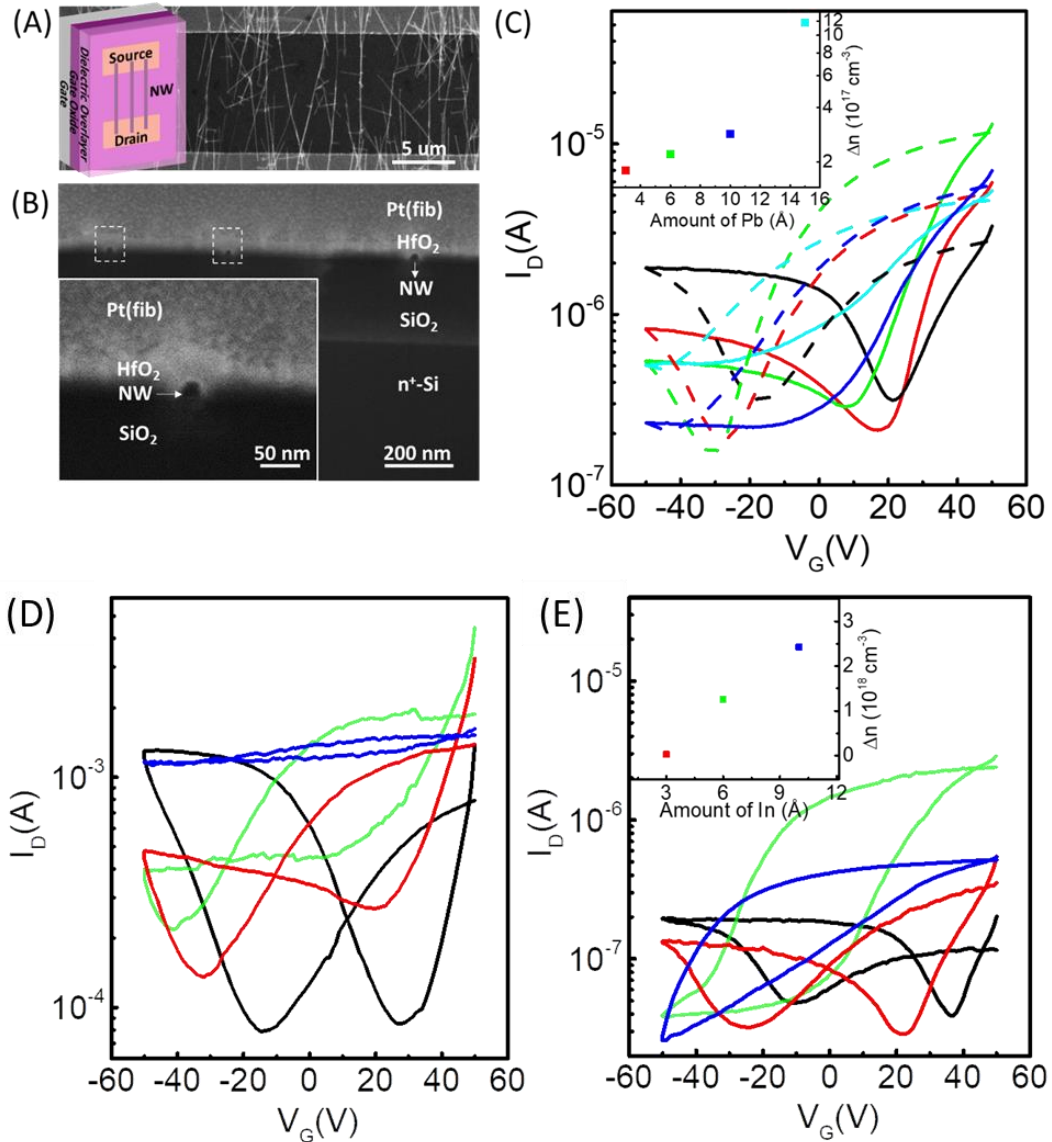

Figure 4.1 (A) Top-view SEM image of a NW array FET and inset, schematic of the device geometry. (B) Cross-sectional SEM image of a NW array FET encapsulated by HfO_2 at low and (inset) high magnification. Representative I_D–V_G characteristics at (C) V_{DS}=0.25 V and (D) V_{DS}=20 V of a NW array FET with 0 Å (black), 3 Å (red), 6 Å (green), 10 Å (blue), and 15 Å (cyan) of thermally-deposited Pb. (E) Representative I_D–V_G characteristics of PbSe NW array FETs doped by 0 Å (black), 3 Å (red), 6 Å (green), 10 Å (blue) of indium deposited by thermal evaporation in the linear regime (V_{DS}=0.25 V). Inset C and E: calculated change in carrier concentration as a function of the amount of thermally-deposited Pb or In.

Similar behavior is also observed in In-doped devices [Figure 4.1E]. V_T shifts in the negative direction, consistent with n increasing from 10^{16} cm^{-3} to $2.5x10^{18}$ cm^{-3} as the amount of In increases upon evaporation of 3 Å to 10 Å films. We also demonstrate an example of p-type doping on PbSe NWs by evaporating 10 Å of Se. The resulting V_T of the I_D–V_G curve shifts positively and the hole concentration increases by $7x10^{17}$ cm^{-3} [Figure 4.2].

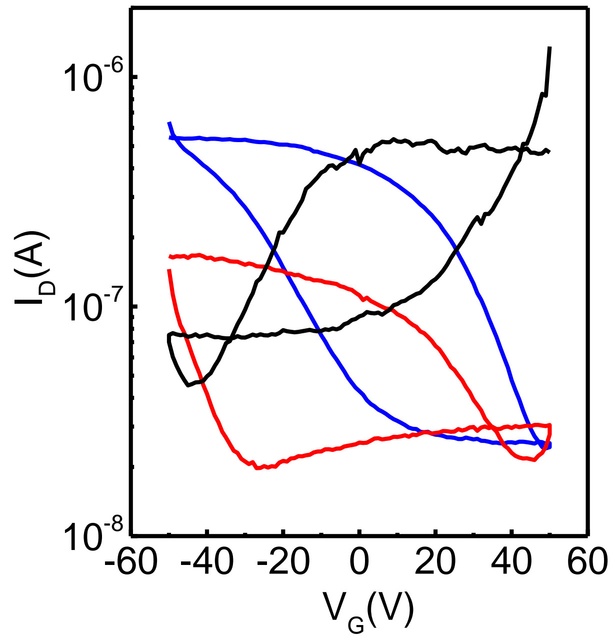

Figure 4.2 I_D–V_G characteristics of PbSe NW array FETs as made (black), doped by 10 Å of Se (red), and encapsulated by PMMA (blue) at V_{DS}=-20 V.

4.2 Encapsulation of PbSe NW Array FETs with Different Dielectric Overlayer

We investigate the effect of dielectric environment on the doping efficiency of PbSe NWs. Doping efficiency is defined as the percentage of ionized impurities, N_D^+/N_D or N_A^-/N_A, where N_D^+ or N_A^- is the concentration of ionized donors or acceptors and N_D or N_A is the concentration of total impurities. Unencapsulated PbSe NW array FETs are first doped with Pb, In, or Se and then are coated with either Poly(methyl methacrylate) (PMMA), Polyvinylidene fluoride (PVDF) or HfO_2 [Figure 4.1B]. 180 nm PMMA or 2 μm PVDF is spin-cast on top of the Pb- or In-doped devices and annealed at 200 ^oC for 2 min to evaporate the solvent. For Se-doped samples, evacuation at -0.1 MPa is used to remove residual solvent to avoid possible Se loss during annealing. 50 nm HfO_2 is deposited on top of NW array FETs *via* atomic layer deposition (ALD) at 200 ^oC for 3 hours. The relative dielectric constants ϵ_r for PMMA, PVDF and HfO_2 insulators are found to be 3.0±0.2, 9.0±0.5 and 20±4, respectively, by fabricating and characterizing their metal/insulator/metal capacitors.

For example, Figure 4.3A shows the I_D—V_G characteristics of unencapsulated, PbSe NW array FETs before (black) and after (red) n-doping by 3 Å of Pb, to yield n~10^{17} cm^{-3}, as described above. The FET is then coated with PVDF (blue). Embedding the NW array channel in the high-ϵ PVDF matrix increases the source-drain current and shifts V_T to more negative voltages, consistent with an increase in the accumulated electron concentration at the same gate voltage. As V_T shifts to more negative voltages with an increase in NW carrier concentration, the I_D—V_G curves of the covered NW array FETs show lower gate modulation in the scanned voltage range. Likewise shown in Supporting Information Figure 4.4A, B, both the PMMA and HfO_2 coatings enhance the current and negatively shift the V_T, suggesting more electrons are introduced from the 3 Å of Pb deposited. It is worth mentioning that the n-type NW array device covered with 50 nm of HfO_2 maintains its I_D—V_G characteristics after being exposed to air for 24 hours with only a small change of its performance [Figure 4.4B].

PbSe NW array FETs n-doped by 5 Å of In deposited show similar effects of PMMA [Figure 4.4C], PVDF [Figure 4.3B] and HfO_2 [Figure 4.4D] encapsulation on the device characteristics, as described above for Pb doping, leading to an increase in current and a negative shift of V_T. PbSe NW array FETs p-doped by evaporation of 10 Å Se, show a positive shift of V_T after PMMA coating [Figure 4.2]. The doping efficiency for both n-and p-type dopants increases for NW arrays embedded in high-ϵ media.

We calculate the Δn in the n-type NW array devices before and after encapsulation of the Pb- and In-doped devices by PMMA, PVDF and HfO_2 media. Δn is equal to the free electron concentration (n), as discussed above. The initial doping state of the NWs varies, as NW synthesis yields Pb-rich unintentionally n-doped NWs, and trace (<1 ppm) amounts of oxygen in the nitrogen glovebox p-dope the NWs. Therefore, we collect data from 3 different samples for each type of dopant and encapsulating layer. For devices doped by 3Å of Pb, the average n increases by 3.3, 9.4 and 11 fold with PMMA, PVDF and HfO_2 coating, respectively [Figure 4.3C, black]. In-doped devices show a similar trend [Figure 4.3C, purple] as the average n increases by 1.9 fold after PMMA coating, but saturates at ~8 fold for PVDF and HfO_2 encapsulation. In the case of Se-doped p-type devices, the hole concentration increases by 3 fold for NWs embedded in a PMMA matrix.

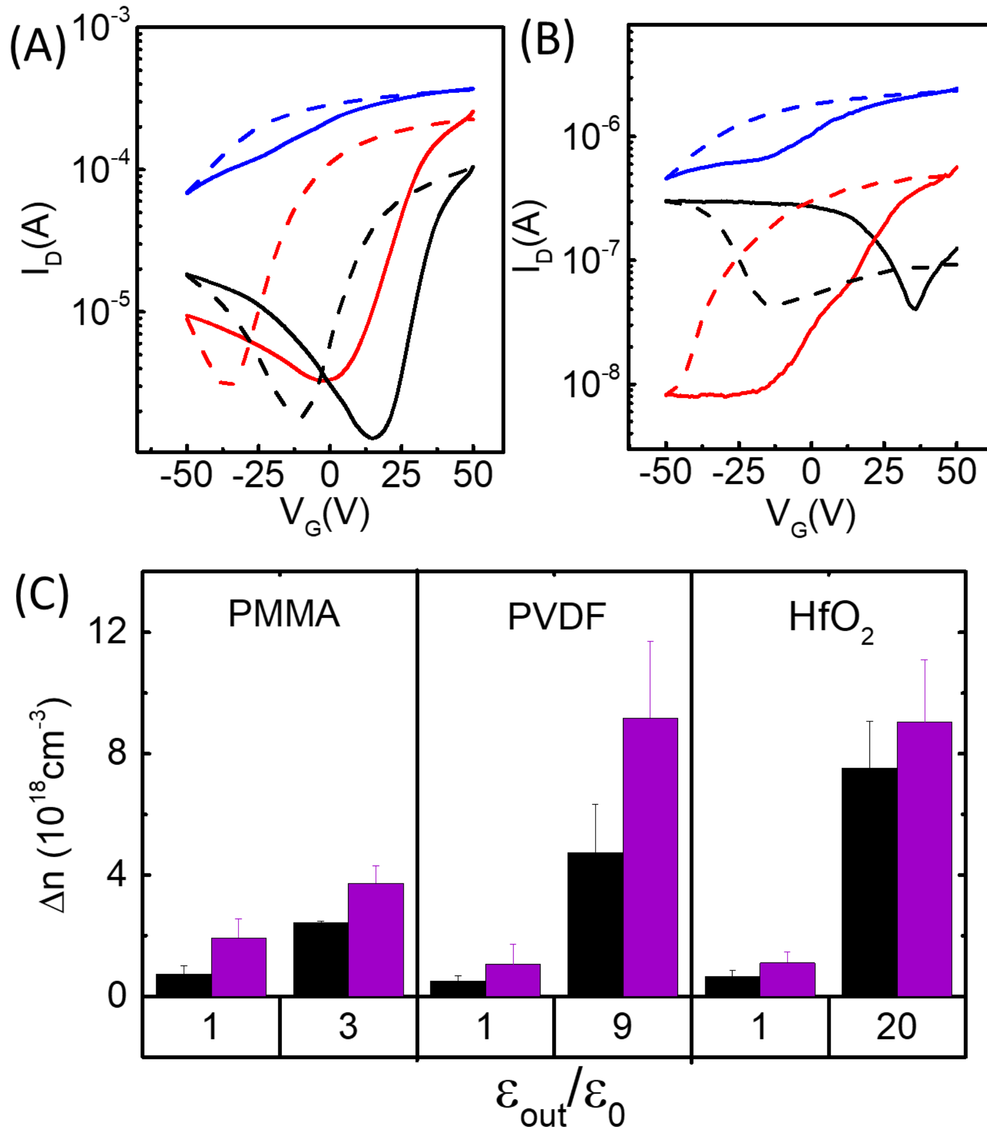

Figure 4.3 Representative I_D–V_G characteristics of (A) Pb-doped and (B) In-doped NW array FETs as aligned (black), with 3 Å of Pb or with 5 Å of In deposited (red), and further covered by PVDF (blue). (C) Change in carrier concentration (Δn) in the NW arrays created by either 3 Å of Pb (black) or 5 Å of In (purple) before ($\frac{\epsilon_{out}}{\epsilon_0} = 1$) and after encapsulation by PMMA ($\frac{\epsilon_{out}}{\epsilon_0} = 3$) , PVDF ($\frac{\epsilon_{out}}{\epsilon_0} = 9$) and HfO_2 ($\frac{\epsilon_{out}}{\epsilon_0} = 20$) , respectively.

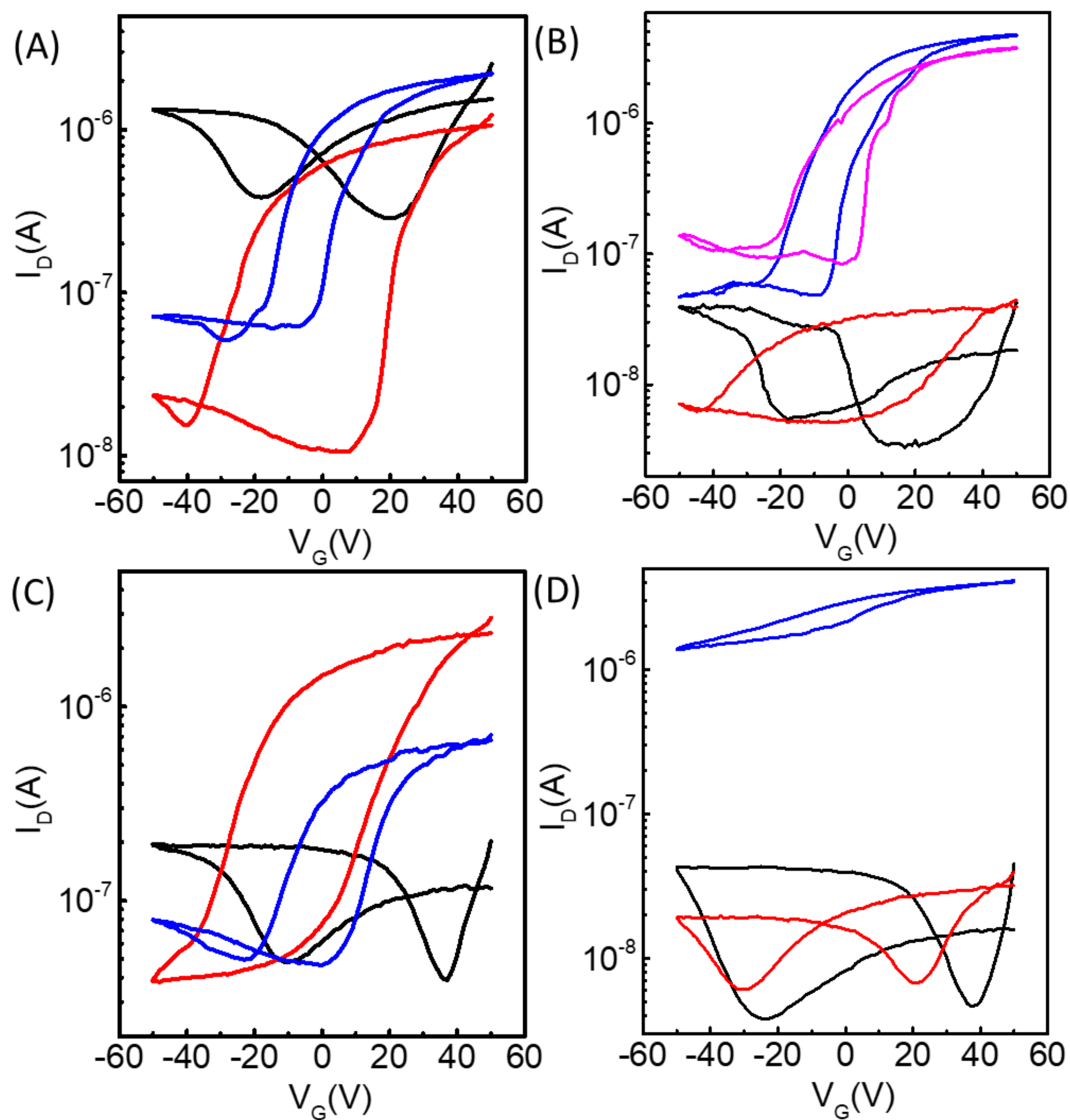

Figure 4.4 I_D–V_G characteristics of PbSe NW array FETs as made (black), doped by 3 Å of Pb (red), and embedded in (a) PMMA (blue) and (b) HfO_2 (blue) and after air exposure overnight (magenta). I_D–V_G characteristics of PbSe NW array FETs as made (black), doped by 5 Å of In (red), and embedded in (c) PMMA (blue) and (d) HfO_2 (blue).

4.3 Theorical Model for Ionization Energy and Doping Efficiency of Dopants in PbSe NWs Embedded in Different Dielectric Environment

In n-type semiconductors, the free electron concentration equals the ionized donor concentration (N_D^+), *i.e.*, n= N_D^+. However, for the same concentration of donors (N_D) introduced by Pb- or In-deposition, n= N_D^+ increases as the dielectric constant of surrounding environment increases. In other words, the same amount of thermal energy can promote more electrons into the conduction band from the same concentration of donor states, suggesting the ionization energy (E_I) for donors decreases when NWs are encapsulated in a higher-ϵ matrix [Figure 4.5A]. The stronger screening effect of charge in the NWs embedded in a higher-ϵ environment results in a weaker Coulomb interaction between free carriers and ionized impurities [Figure 4.5B]. [34]

For a mathematical description of the ionization energy of dopants for high-ϵ dielectric environments in our PbSe nanostructures, we modify the equation used to describe that for impurities in Si NWs,[26]

$$E_I - E_I^0 = \alpha \times F_{Si}\left(\frac{\epsilon_{in}}{\epsilon_{out}}\right)\frac{2(\epsilon_{in}-\epsilon_{out})}{\epsilon_{in}R(\epsilon_{in}+\epsilon_{out})}$$

where $E_I - E_I^0$ is the difference in the ionization energies of the donor in the NWs with and without dielectric confinement effects, respectively, α is a scaling factor to capture the broader extension of the electron Bohr radius of PbSe (a_{PbSe}) relative to that for Si (a_{Si}). The broader the wavefunction extension, the more significant dielectric confinement effects such that $\alpha = a_{PbSe}/a_{Si} = m^*_{SiNW}/m^*_{PbSeNW} \sim 3$.[35,36] R is the NW radius, ϵ_{in} and ϵ_{out} are the dielectric constants of the NW and its surrounding environment respectively, and $F(\frac{\epsilon_{in}}{\epsilon_{out}})$ is a positive-

valued function of $\frac{\epsilon_{in}}{\epsilon_{out}}$.[26] Based on this model, Calculated ionization energy enhancements as a function of medium dielectric constant are listed in Table 4.1.

Table 4.1 Theoretical Prediction of Ionization Energy

$\epsilon_{out,r}$	1	3	6	9	15	20
$E_I - E_I^0$ (eV)	0.24	0.105	0.054	0.033	0.012	0.004

Theoretically, doping efficiency can be derived from the ionization energy and density of states.[26,36] A supercell with a length twice larger than the Bohr radius is used to meet the 'lightly-doping' condition mentioned above.[36] In addition, the band structure (and density of states) can be different when the free electron concentration is above the Mott criterion. Above the Mott criterion, the NW is metallic and the doping efficiency can be treated as unity. Here we only calculate the doping efficiency and Fermi level when the free electron concentration is below the Mott criterion. The Fermi energy and doping efficiency can be determined from

$$n = \frac{1}{1 + 2\exp\left(\frac{E_F - E_D}{kT}\right)} N_D = \frac{1}{1 + 2\exp\left(\frac{E_F - E_C + E_I}{kT}\right)} N_D$$

$$n = \int_{E_c}^{\infty} g(E) f(E)\, dE = \int_0^{\infty} g(E) \frac{kT}{1 + \exp\left(\frac{E_F - E_C}{kT} - x\right)} dx \qquad x = \frac{E - E_c}{kT}$$

$$g(E) = \frac{1}{\hbar\pi} \sqrt{\frac{m^*}{2(E - E_c)}}$$

where N_D is the concentration of dopants, which remains constant for the same sample regardless of the dielectric environment, $f(E)$ is the Fermi-Dirac distribution of electrons, E_F is the Fermi energy, E_C is the conduction band edge, *g(E)* is the one-dimensional density of states. Using the ionization energy obtained above, we are able calculate the doping efficiency according to the change of ϵ_{out} and normalize it to the highest doping efficiency achieved when encapsulated by HfO_2. There is predicted to be a polaron shift of ~10 meV in HfO_2-coated NWs due to the response of the ions in HfO_2. [37] Ignoring the polaronic effect introduces a 3-10% error in calculating doping efficiency. Given the relative variations in the doping efficiency for experimental HfO_2-coated NWs are ~20%, the polaronic effect is not significant enough to be observed.

From Table 4.1, the ionization energy decreases as ϵ_{out} increases and approaches a constant value E_I^0 when ϵ_{out} is higher than 20 (closer to or higher than $\epsilon_{\text{in}} \sim 23$). To make a clear comparison between our theoretical model and experimental results, the calculated doping efficiencies for each E_I^0 (E_I^0 from 0.01 to 0.07 eV) are normalized by its value at $\epsilon_{out} = 20$ [Figure 4.5C, yellow]. The experimental n of NW array FETs before encapsulation and after encapsulation by PMMA and PVDF are normalized by n for the device covered by HfO_2, for each of the 3 devices [Figure 4.5C, black and green]. Normalization also cancels out variations in Δn (or n) from device-to-device differences in channel coverage and in the number of unbound dopants introduced in the fabrication process. As shown in Figure 4.5C, the carrier concentration increases in both Pb- and In-doped PbSe NWs as ε_{out} increases, indicating the doping efficiency is improved by reducing the dielectric mismatch between the NWs and their surroundings. The experimental results lie in the range of our theoretical prediction.

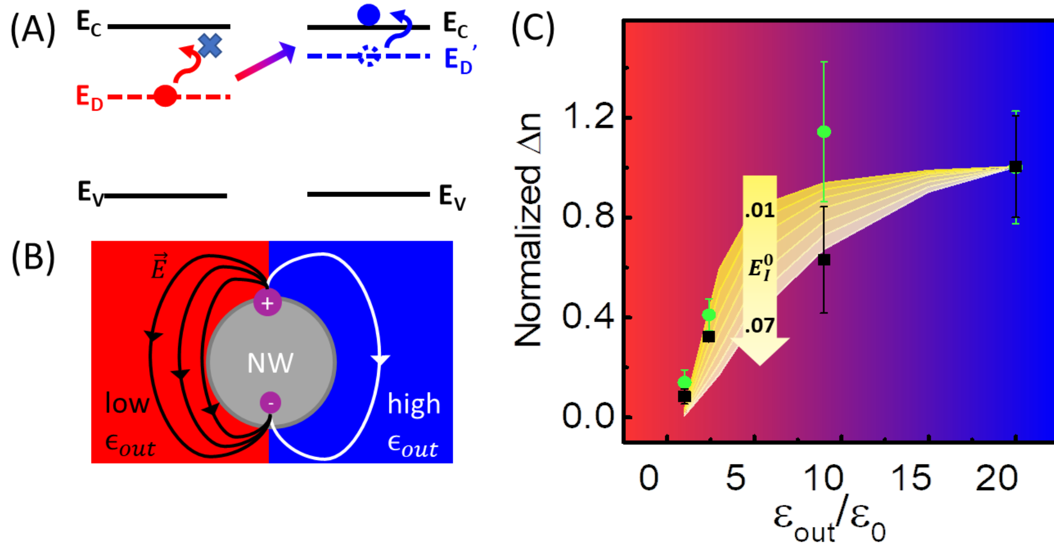

Figure 4.5 (A) Schematics showing the larger ionization energy ($E_I = E_C - E_D$) and therefore lower probability of promoting electrons from the donor state to conduction band at room temperature (low doping efficiency) in a low (red) dielectric constant medium in comparison to that for a high (blue) dielectric medium. (B) Coulomb interactions, depicted by the density of electric field lines, are not as readily screened between the ionized dopant and free electrons in a low, relative to a high-ϵ medium. (C) Theoretical doping efficiency (yellow) and measured doping efficiency (normalized Δn) of Pb (black squares) or In (green circles) in PbSe NWs as a function of the dielectric constant of the surrounding medium. From bright yellow to light yellow, the E_I^0 used in theoretical calculation change from 0.01 to 0.07 eV.

4.4 Fabrication and Doping Efficiency of PbSe single NW FETs

The study of doping efficiency in NW arrays is instructive for device engineering and the bottom-contact device geometry allows us to explore dielectric confinement effects on different dopants in PbSe nanostructures. However, the number and orientation of NWs that span the channel cannot be precisely controlled or counted. Therefore, we fabricate and measure single PbSe NW FETs with Pb as the dopant to gain a more quantitative understanding of dielectric confinement effects on carrier concentration and transport. The fabrication of PbSe single NW FET is similar to the literature reports. [38] A dilute NW dispersion is dropcast on heavily n-doped, oxidized Si wafers, with the same thickness as array FETs, and the same NH_4SCN ligand exchange process is performed as described above for the array devices. PMMA e-beam resist is spincast on the sample and the location of single wires within the contact pairs is recorded by an optical microscope. E-beam lithography is used to define source and drain electrodes and are customized for each single NW to connect them with the pre-patterned, large contact pads. The channel dimensions are designed as 1 μm: 4 μm (W: L). Different from the bottom contacts used in array FETs, 2 nm of Pb along with 18 nm of Au is evaporated onto the e-beam defined electrodes to form source and drain top contacts. Here the layer of Pb at the contact area is introduced to compensate unintentional oxygen p-doping that is inevitable during the e-beam lithography process, and yield devices displaying ambipolar behavior [Figure 4.6A, black line]. SEM images are taken to confirm single NW channel FETs [Figure 4.6A, inset].

We deposit Pb on the single NW channel. I_D–V_G characteristics at V_{DS}=2 V in linear regime are collected for PbSe ingle NW FETs as a function of the amount of thermally-deposited, elemental Pb [Figure 4.6A]. Unsurprisingly, the evolution of I_D–V_G characteristics observed for single NW FETs is similar to that for NW array FETs. The I_D–V_G characteristic of the single NW FET doped by 1 Å of elemental Pb is still ambipolar, but with a more negative V_T. The characteristics become increasingly n-type with V_T monotonically shifting to negative voltages as

more than 2 Å of elemental Pb is added. The cylinder-on-a-plate model, rather than thin film model, is applied to find the gate capacitance when deriving Δn, as discussed previously.

Pb-doped single NW FETs are then coated by PMMA, PVDF, and HfO_2 and tested similarly as the array devices described above. Figure 4B shows representative I_D—V_G characteristics of a PbSe single NW FET as made (black), doped by 5 Å of Pb (red) and covered by PVDF (blue). The high-ϵ surrounding PVDF increases the on-state electron currents and shifts the V_T negatively, consistent with the trends exhibited by the NW array examples. As shown in Figure 4.7, PMMA and HfO_2 coating both enhance the current and negatively shift the V_T, yielding more electrons in the channel. Based on the relation between n and V_T, the n introduced upon doping with Pb and coating with PMMA are $2.7 \times 10^{19}\ \mathrm{cm}^{-3}$ and $6 \times 10^{19}\ \mathrm{cm}^{-3}$, doping with Pb and coating with PVDF are $2.3 \times 10^{19}\ \mathrm{cm}^{-3}$ and $1.1 \times 10^{20}\ \mathrm{cm}^{-3}$, and doping with Pb and coating with HfO_2 are $3 \times 10^{19}\ \mathrm{cm}^{-3}$ and $1.2 \times 10^{20}\ \mathrm{cm}^{-3}$. Akin to the behavior of array devices, in increasingly high-ϵ media, the number of electrons generated by a given amount of Pb increases and gradually saturates, suggesting the E_I in single NWs approaches E_I^0 [Figure 4.6B inset]. When n of single NW FETs in different dielectric surroundings are normalized by the n of the HfO_2-covered-FET, they match well with the normalized theoretical doping efficiency for E_I^0 of 0.03 eV. Considering the closed-packed structure of Pb, thermally-deposited, 5 Å films of Pb introduce $4.7 \times 10^{20}\ \mathrm{Pb\ atoms/cm^3}$ to the NW. Therefore, on average, the doping efficiency of Pb is 6% in uncoated single NWs, 13% in PMMA-coated single NWs, 23% in PVDF-coated single NWs and 25% in HfO_2-coated single NWs, respectively. While the doping efficiency of the NWs increases in high-ε environments, it is well-below 100% as would be expected for the low

ionization energy. We attribute the loss in doping efficiency to ineffectively bound Pb atoms as discussed above.

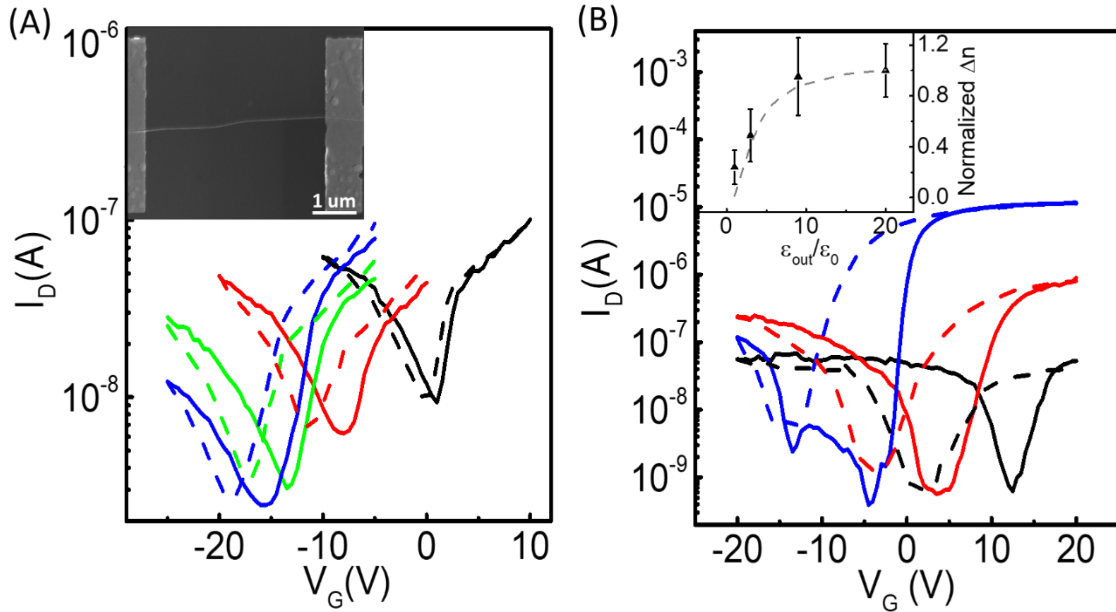

Figure 4.6 (A) Representative I_D–V_G characteristics of a single PbSe NW FET as made (black) and with 1 Å (red), 2 Å (green), and 3 Å (blue) of evaporated Pb. (B) Representative I_D–V_G characteristics of a single PbSe NW FET as made (black), with 5 Å of Pb (red), and PVDF encapsulation (blue). Inset: normalized doping efficiency and electron concentration change calculated based on theoretical model (dash line) and single PbSe NW FET data (dots).

Figure 4.7 shows the device characteristics of 9 individual Pb-doped single NW FETs before and after encapsulation by different dielectric media. After coating the NW channel with dielectric layers, the device hysteresis is reduced, while the current on-off ratio is improved. More specifically, for PMMA-covered FETs, the on-currents only slightly increase, but off-currents dropped from ~10^{-6} A to ~10^{-7} A. We also extract electron mobilities from the slope of I_D–V_G curves in the high gate voltage region to minimize contact resistance effects. For the set of samples we measure, electron mobilities of single PbSe NW FETs after being coated by PMMA and PVDF mostly decrease, while the mobility for all FETs encapsulated by HfO_2 increases. However the variation in mobilities among individual single NW samples [Figure 4.8], as well as in NW array devices, is too large and we are unable to draw a conclusion regarding the effect of dielectric media on carrier mobilities in the PbSe NW devices. Based on Figure 4.7, we also calculate the trap density of single NW FET devices with different dielectric environment to exclude the effect of surface trap density change on doping. The subthreshold slope $S^{-1} = \frac{dlogI_D}{dV_G}$ is related to trap density in the depletion layer,

$$S = ln10\frac{kT}{q}\ (1 + \frac{e^2}{C_{ox}}N_{trap})$$

where the C_{ox} is the gate oxide capacitance and N_{trap} is trap density per area per unit energy. As the NW is only 15-nm thick and fully depleted, S is measurement of all the traps at the NW surface, not only at the gate-NW interface. The calculated trap densities (N_{trap}/d where d is the NW diameter) are listed in Table 4.2. Within the error of the measurement, there is no significant changes in trap density upon encapsulating the NW devices in polymer or HfO_2 matrices.

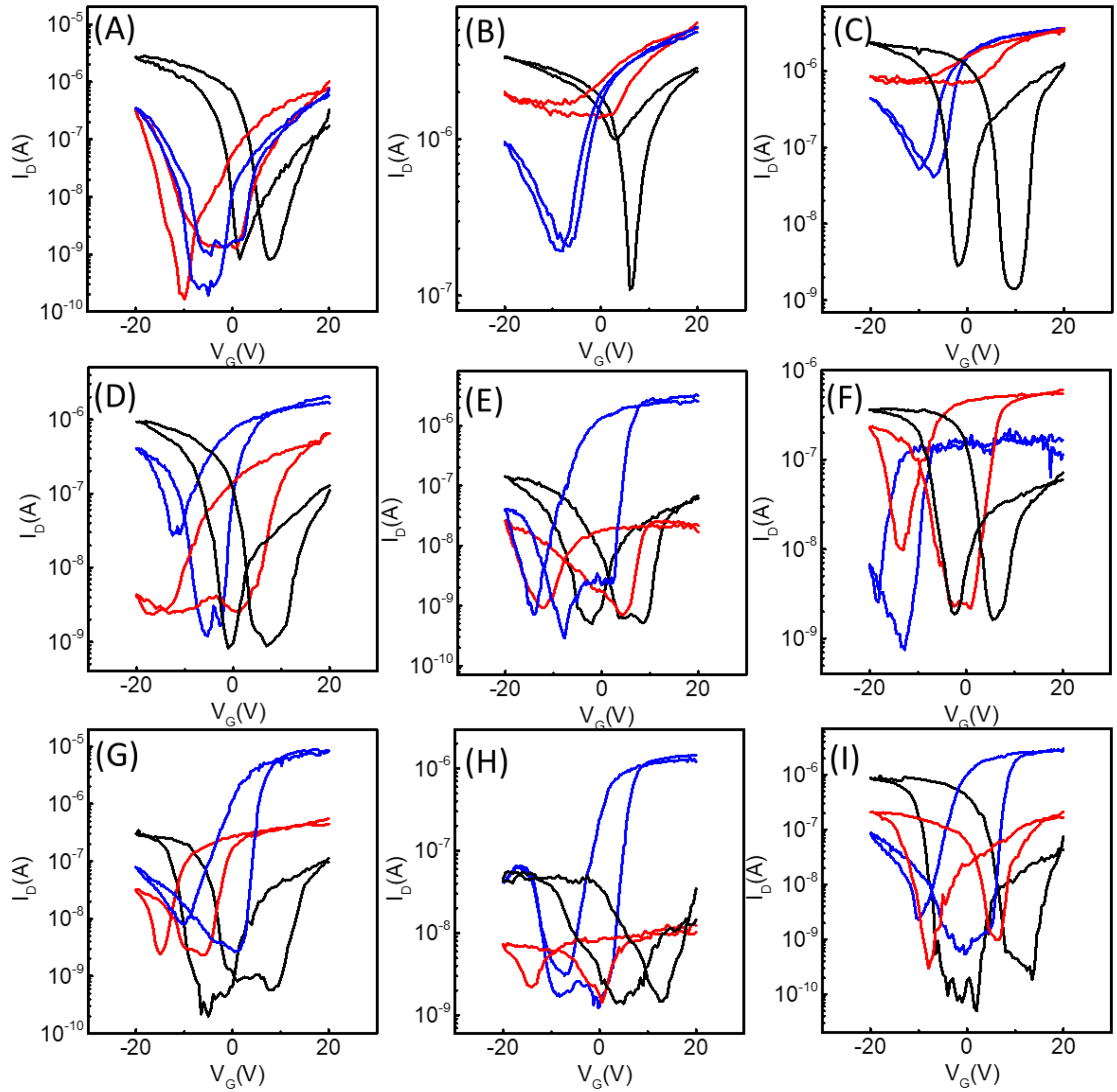

Figure 4.7 I_D–V_G characteristics of individual PbSe single NW FETs as made (black), doped by 3 Å of Pb (red), and embedded in (a)-(c) PMMA, (d)-(f) PVDF, and (g) –(i) HfO_2 (blue).

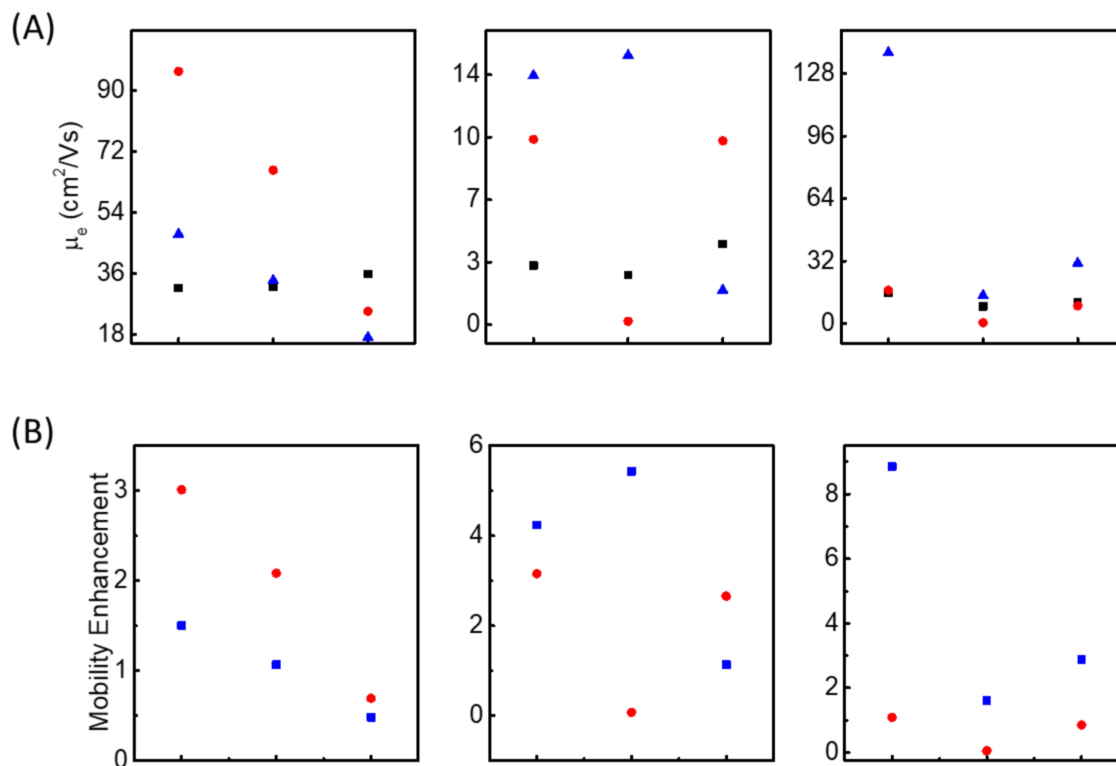

Figure 4.8 (a) Electron mobility extracted from PbSe single NW FETs in Figure S4 as made (black), with 3 Å of Pb (red), and embedded in left: PMMA, middle: PVDF, right: HfO_2 (blue). (b) Mobility enhancement of samples in (a) after doped by Pb (red) and encapsulated by the corresponding dielectric matrix (blue).

Table 4.2 Trap Density in PbSe NW

$cm^{-3}eV^{-1}$	PMMA	PVDF	HfO_2
Before encapsulation	$(6 \pm 2) \times 10^{18}$	$(4 \pm 1) \times 10^{18}$	$(7 \pm 2) \times 10^{18}$
After encapsulation	$(7 \pm 4) \times 10^{18}$	$(4 \pm 2) \times 10^{18}$	$(4 \pm 2) \times 10^{18}$

4.5 Ionization Energy Measured from PbSe single NW FET devices

The relative air-stability of HfO_2-coated n-type NW devices provides us with a platform to quantitatively study the ionization energy of Pb in PbSe NWs and investigate the electron barrier at the metal-NW contact. Representative temperature-dependent I_D—V_G characteristics between 230 and 320 K for Pb-doped-single NW FETs with HfO_2 encapsulation are shown for a subset [Figure 4.9A] of measured temperatures. The Schottky barrier (SB) for electrons at the metal-NW contact is extracted from temperature dependent I_D—V_G characteristics using the thermionic emission equation:[39]

$$I = A^{*}T^{2}\exp[-\frac{q\phi_{MS} - \left(\frac{qE}{4\pi\epsilon_{PbSe}}\right)^{0.5}}{k_{B}T}]$$

where A* is the effective Richardson's constant, k_B is Boltzmann's constant, ϕ_{MS} is the SB height, and E is the electric field at metal semiconductor interface. $\left(\frac{qE}{4\pi\epsilon_{PbSe}}\right)^{0.5}$ describes the image-force lowering effect and is proportional to $V_{DS}^{1/2}$. From Figure 4.9 C, the barrier height is extracted as 0.196 eV, which is about half of the bandgap energy of PbS NW despite its n-type doping, it suggests the Fermi level at the NW/metal contact interface is largely pinned, consistent with our group's previous report.[38]

The electron concentrations at various temperatures are extracted from V_T and plotted in Figure 4.9B. The electron concentration (n) is exponentially proportional to the ionization energy of donors (E_I) and temperature (*T*) according to the following relation:[25,39]

$$n \propto exp(-\frac{E_I}{2k_B T})$$

Thus, the ionization energy of Pb atoms in HfO_2-covered PbSe NWs is extracted by fitting ln(n) against 1/T and found to be 0.04 ± 0.01 eV, consistent with our theoretical calculation results [Table 4.1]. The E_I obtained by measurement and fitting over a larger temperature range (80-300 K) is 0.02-0.04 eV [Figure 4.10]. We hypothesize that this slightly smaller E_I is due to the temperature-dependent band structure of PbSe NWs and the dominance of the Schottky barrier at lower temperatures. Nevertheless, we observe a shallow ionization energy of Pb for HfO_2-coated NWs, which can be attributed to the considerable reduction in dielectric mismatch. Given the ionization energy of impurities in bulk lead chalcogenides is less than 0.01 eV,[40] quantum confinement effects are anticipated to cause a further increase in E_I of around 30 meV in our 15 nm-diameter NW system.

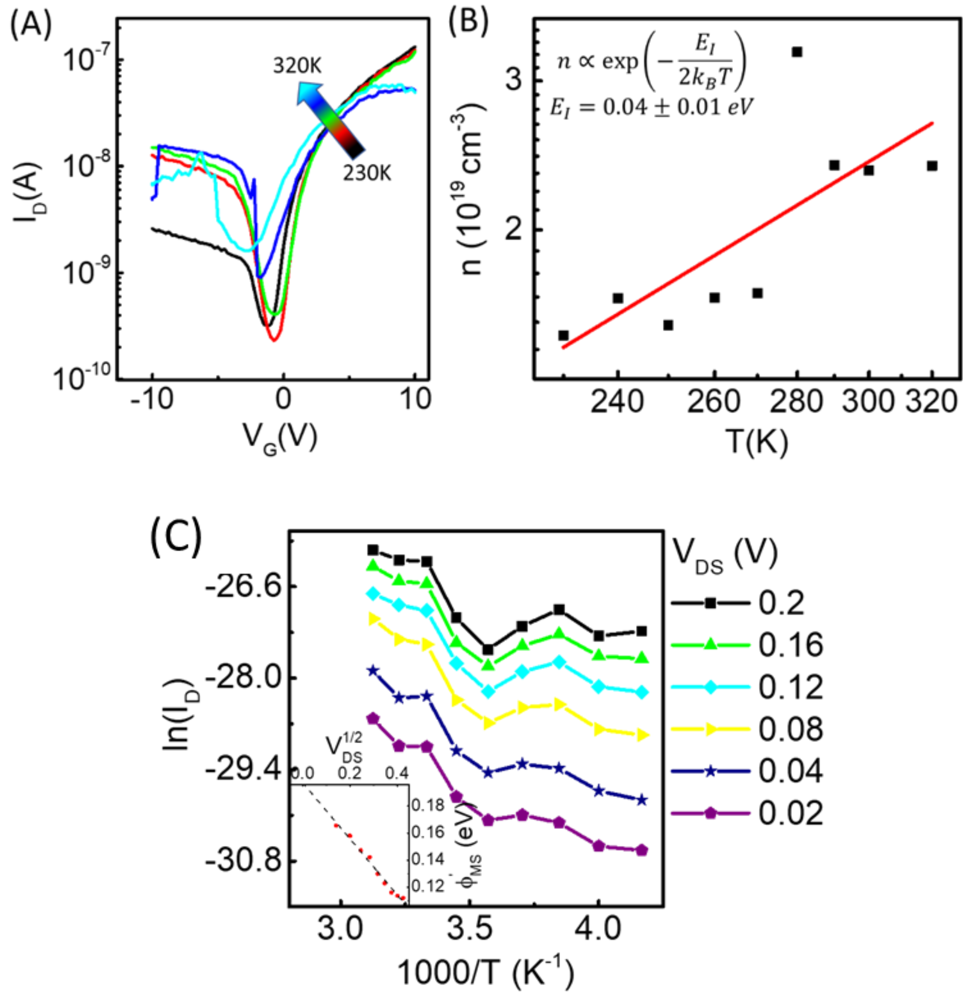

Figure 4.9 (A) I_D–V_G characteristics of a HfO_2-covered, 5 Å Pb-doped single NW FET at V_D=2 V at 230 K (black), 250 K (red), 270 K (green), 300 K (blue), and 320 K (cyan). (B) Calculated free electron concentration (black symbols) as a function of temperature (T) and (red line) fit to ln(n) *versus* T. (c) $\ln(I_D) - 1000/T$ plots at different V_{DS} and the electron barrier at metal semiconductor interface as a function of $V_{DS}^{1/2}$. ϕ'_{MS} represents $\frac{q\phi_{MS}-\left(\frac{qE}{4\pi\epsilon_{PbSe}}\right)^{0.5}}{q}$. The extrapolation of the inset plot gives the SB height (0.196 eV)

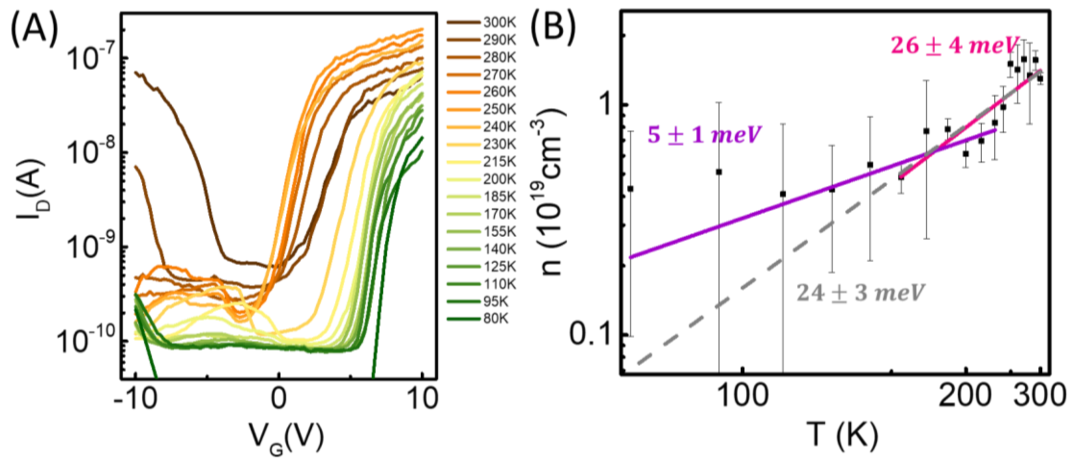

Figure 4.10 (A) I_D–V_G characteristics of a HfO_2-covered, 5 Å Pb-doped single NW FET at V_D=2 V from 80 K to 300 K. (B) Calculated free electron concentration (black symbols) as a function of temperature (T) and fit to ln(n) *versus* T over a lower T range (80 – 240 K, purple), a higher T range (155 -300 K, pink) and over the whole range (80-300 K, dashed grey line). The E_I calculated from fitted slopes are labeled with corresponding colors. The errors of *n* and E_I are measurement uncertainty.

4.6 Conclusions

This study showcases a strategy to study the ionization energy and efficiency of doping fundamentally and provides a simple approach technologically to enhance doping efficiency in nanostructures. We find both experimentally and theoretically that as the dielectric constant of the surrounding medium increases, the proportion of ionized dopants in PbSe NWs increases, both for n-type (Pb/In) and p-type (Se) dopants, which agrees with Law's observation of a higher electron concentration measured after Al_2O_3 coating of PbSe NC solids.[41] More generally, the dielectric environment influences excitonic[42–45] and impurity states in other low dimensional materials, such as zero-dimensional Si nanocrystals[21] and two-dimensional graphene.[22] Engineering the dielectric environment of low-dimensional materials integrated in the platform of the FET, as shown here, may provide a route to study dielectric confinement effects on the electronic properties in a broader range of low dimensional material systems, such as nanocrystals, 2D perovskites and 2D semiconducting transition-metal dichalcogenides.[44,45]

4.7 References

(1) Talapin, D. V.; Murray, C. B. PbSe Nanocrystal Solids for N- and p-Channel Thin Film Field-Effect Transistors. *Science.* **2005**, *310* (5745), 86–89.

(2) Kovalenko, M. V.; Manna, L.; Cabot, A.; Hens, Z.; Talapin, D. V.; Kagan, C. R.; Klimov, V. I.; Rogach, A. L.; Reiss, P.; Milliron, D. J.; et al. Prospects of Nanoscience with Nanocrystals. *ACS Nano* **2015**, *9* (2), 1012–1057.

(3) Liang, W.; Hochbaum, A. I.; Fardy, M.; Rabin, O.; Zhang, M.; Yang, P. Field-Effect Modulation of Seebeck Coefficient in Single PbSe Nanowires. *Nano Lett.* **2009**, *9* (4), 1689–1693.

(4) Padilha, L. A.; Stewart, J. T.; Sandberg, R. L.; Bae, W. K.; Koh, W.-K.; Pietryga, J. M.; Klimov, V. I. Aspect Ratio Dependence of Auger Recombination and Carrier Multiplication in PbSe Nanorods. *Nano Lett.* **2013**, *13* (3), 1092–1099.

(5) Pietryga, J. M.; Werder, D. J.; Williams, D. J.; Casson, J. L.; Schaller, R. D.; Klimov, V. I.; Hollingsworth, J. A. Utilizing the Lability of Lead Selenide to Produce Heterostructured Nanocrystals with Bright, Stable Infrared Emission. *J. Am. Chem. Soc.* **2008**, *130* (14), 4879–4885.

(6) Zhang, J.; Gao, J.; Church, C. P.; Miller, E. M.; Luther, J. M.; Klimov, V. I.; Beard, M. C. PbSe Quantum Dot Solar Cells with More than 6% Efficiency Fabricated in Ambient Atmosphere. *Nano Lett.* **2014**, *14* (10), 6010–6015.

(7) Kagan, C. R.; Lifshitz, E.; Sargent, E. H.; Talapin, D. V. Building Devices from Colloidal Quantum Dots. *Science (80-.).* **2016**, *353* (6302), aac5523.

(8) Talapin, D. V.; Black, C. T.; Kagan, C. R.; Shevchenko, E. V.; Afzali, A.; Murray, C. B. Alignment, Electronic Properties, Doping, and on-Chip Growth of Colloidal PbSe Nanowires. *J. Phys. Chem. C* **2007**, *111* (35), 13244–13249.

(9) Ko, D.-K.; Murray, C. B. Probing the Fermi Energy Level and the Density of States Distribution in PbTe Nanocrystal (Quantum Dot) Solids by Temperature-Dependent Thermopower Measurements. *ACS Nano* **2011**, *5* (6), 4810–4817.

(10) Norris, D. J.; Efros, A. L.; Erwin, S. C. Doped Nanocrystals. *Science.* **2008**, *319* (5871), 1776–1779.

(11) Oh, S. J.; Berry, N. E.; Choi, J.-H.; Gaulding, E. A.; Paik, T.; Hong, S.-H.; Murray, C. B.; Kagan, C. R. Stoichiometric Control of Lead Chalcogenide Nanocrystal Solids to Enhance Their Electronic and Optoelectronic Device Performance. *ACS Nano* **2013**, *7* (3), 2413–2421.

(12) Oh, S. J.; Uswachoke, C.; Zhao, T.; Choi, J.-H.; Diroll, B. T.; Murray, C. B.; Kagan, C. R. Selective P- and n-Doping of Colloidal PbSe Nanowires To Construct Electronic and Optoelectronic Devices. *ACS Nano* **2015**, *9* (7), 7536–7544.

(13) Leschkies, K. S.; Kang, M. S.; Aydil, E. S.; Norris, D. J. Influence of Atmospheric Gases on the Electrical Properties of PbSe Quantum-Dot Films. *J. Phys. Chem. C* **2010**, *114* (21), 9988–9996.

(14) Crisp, R. W.; Kroupa, D. M.; Marshall, A. R.; Miller, E. M.; Zhang, J.; Beard, M. C.; Luther, J. M. Metal Halide Solid-State Surface Treatment for High Efficiency PbS and PbSe QD Solar Cells. *Sci. Rep.* **2015**, *5*, 9945.

(15) Ning, Z.; Voznyy, O.; Pan, J.; Hoogland, S.; Adinolfi, V.; Xu, J.; Li, M.; Kirmani, A. R.; Sun, J.-P.; Minor, J.; et al. Air-Stable n-Type Colloidal Quantum Dot Solids. *Nat. Mater.* **2014**, *13* (8), 822–828.

(16) Voznyy, O.; Zhitomirsky, D.; Stadler, P.; Ning, Z.; Hoogland, S.; Sargent, E. H. A Charge-Orbital Balance Picture of Doping in Colloidal Quantum Dot Solids. *ACS Nano* **2012**, *6* (9), 8448–8455.

(17) Koh, W.; Koposov, A. Y.; Stewart, J. T.; Pal, B. N.; Robel, I.; Pietryga, J. M.; Klimov, V. I. Heavily Doped N-Type PbSe and PbS Nanocrystals Using Ground-State Charge Transfer from Cobaltocene. *Sci. Rep.* **2013**, *3*, 2004.

(18) Kroupa, D. M.; Hughes, B. K.; Miller, E. M.; Moore, D. T.; Anderson, N. C.; Chernomordik, B. D.; Nozik, A. J.; Beard, M. C. Synthesis and Spectroscopy of Silver-Doped PbSe Quantum Dots. *J. Am. Chem. Soc.* **2017**, *139* (30), 10382–10394.

(19) Erwin, S. C.; Zu, L.; Haftel, M. I.; Efros, A. L.; Kennedy, T. A.; Norris, D. J. Doping Semiconductor Nanocrystals. *Nature* **2005**, *436* (7047), 91–94.

(20) Nemov, S. A.; Gavrikova, T. A.; Zykov, V. A.; Osipov, P. A.; Proshin, V. I. Features of the Electrical Compensation of Bismuth Impurities in PbSe. *Semiconductors* **1998**, *32* (7), 689–691.

(21) Kashiwaba, Y.; Kanno, I.; Ikeda, T. P-Type Characteristics of Cu-Doped CdS Thin Films. *Jpn. J. Appl. Phys.* **1992**, *31* (Part 1, No. 4), 1170–1175.

(22) Keldysh, L. V. Coulomb Interaction in Thin Semiconductor and Semimetal Films. *Sov. J. Exp. Theor. Phys. Lett.* **1979**, *29*, 658.

(23) Pereira, R. N.; Stegner, A. R.; Andlauer, T.; Klein, K.; Wiggers, H.; Brandt, M. S.; Stutzmann, M. Dielectric Screening versus Quantum Confinement of Phosphorus Donors in Silicon Nanocrystals Investigated by Magnetic Resonance. *Phys. Rev. B* **2009**, *79* (16), 161304.

(24) Cudazzo, P.; Tokatly, I. V.; Rubio, A. Dielectric Screening in Two-Dimensional Insulators: Implications for Excitonic and Impurity States in Graphane. *Phys. Rev. B* **2011**, *84* (8), 085406.

(25) Björk, M. T.; Schmid, H.; Knoch, J.; Riel, H.; Riess, W. Donor Deactivation in Silicon Nanostructures. *Nat. Nanotechnol.* **2009**, *4* (2), 103–107.

(26) Diarra, M.; Niquet, Y.-M.; Delerue, C.; Allan, G. Ionization Energy of Donor and Acceptor Impurities in Semiconductor Nanowires: Importance of Dielectric Confinement. *Phys. Rev.*

B **2007**, *75* (4).

(27) Fafarman, A. T.; Koh, W.; Diroll, B. T.; Kim, D. K.; Ko, D.-K.; Oh, S. J.; Ye, X.; Doan-Nguyen, V.; Crump, M. R.; Reifsnyder, D. C.; et al. Thiocyanate-Capped Nanocrystal Colloids: Vibrational Reporter of Surface Chemistry and Solution-Based Route to Enhanced Coupling in Nanocrystal Solids. *J. Am. Chem. Soc.* **2011**, *133* (39), 15753–15761.

(28) Graham, R.; Yu, D. High Carrier Mobility in Single Ultrathin Colloidal Lead Selenide Nanowire Field Effect Transistors. *Nano Lett.* **2012**, *12* (8), 4360–4365.

(29) Kim, D. K.; Lai, Y.; Vemulkar, T. R.; Kagan, C. R. Flexible, Low-Voltage, and Low-Hysteresis PbSe Nanowire Field-Effect Transistors. *ACS Nano* **2011**, *5* (12), 10074–10083.

(30) Androulakis, J.; Lee, Y.; Todorov, I.; Chung, D.-Y.; Kanatzidis, M. High-Temperature Thermoelectric Properties of n -Type PbSe Doped with Ga, In, and Pb. *Phys. Rev. B* **2011**, *83* (19).

(31) Kim, D. K.; Fafarman, A. T.; Diroll, B. T.; Chan, S. H.; Gordon, T. R.; Murray, C. B.; Kagan, C. R. Solution-Based Stoichiometric Control over Charge Transport in Nanocrystalline CdSe Devices. *ACS Nano* **2013**, *7* (10), 8760–8770.

(32) Wunnicke, O. Gate Capacitance of Back-Gated Nanowire Field-Effect Transistors. *Appl. Phys. Lett.* **2006**, *89* (8), 083102.

(33) Kim, D. K.; Vemulkar, T. R.; Oh, S. J.; Koh, W.-K.; Murray, C. B.; Kagan, C. R. Ambipolar and Unipolar PbSe Nanowire Field-Effect Transistors. *ACS Nano* **2011**, *5* (4), 3230–3236.

(34) Shklovskii, B. I.; Efros, A. L. *Electronic Properties of Doped Semiconductors*; Springer Science & Business Media, 2013.

(35) Niquet, Y. M.; Lherbier, A.; Quang, N. H.; Fernández-Serra, M. V.; Blase, X.; Delerue, C. Electronic Structure of Semiconductor Nanowires. *Phys. Rev. B* **2006**, *73* (16), 165319.

(36) Bartnik, A. C.; Efros, A. L.; Koh, W.-K.; Murray, C. B.; Wise, F. W. Electronic States and Optical Properties of PbSe Nanorods and Nanowires. *Phys. Rev. B* **2010**, *82* (19), 195313.

(37) Diarra, M.; Delerue, C.; Niquet, Y.-M.; Allan, G. Screening and Polaronic Effects Induced by a Metallic Gate and a Surrounding Oxide on Donor and Acceptor Impurities in Silicon Nanowires. *J. Appl. Phys.* **2008**, *103* (7), 073703.

(38) Oh, S. J.; Kim, D. K.; Kagan, C. R. Remote Doping and Schottky Barrier Formation in Strongly Quantum Confined Single PbSe Nanowire Field-Effect Transistors. *ACS Nano* **2012**, *6* (5), 4328–4334.

(39) Sze, S. M.; Ng, K. K. *Physics of Semiconductor Devices*, 3rd ed.; Wiley-Interscience: Hoboken, N.J, 2007.

(40) Smith, R. *Semiconductors*; Cambridge University Press, 1961.

(41) Liu, Y.; Tolentino, J.; Gibbs, M.; Ihly, R.; Perkins, C. L.; Liu, Y.; Crawford, N.; Hemminger, J.

C.; Law, M. PbSe Quantum Dot Field-Effect Transistors with Air-Stable Electron Mobilities above 7 Cm2 V(-1) s(-1). *Nano Lett.* **2013**, *13* (4), 1578–1587

(42) Berkelbach, T. C.; Hybertsen, M. S.; Reichman, D. R. Theory of Neutral and Charged Excitons in Monolayer Transition Metal Dichalcogenides. *Phys. Rev. B* **2013**, *88* (4), 045318.

(43) Hong, X.; Ishihara, T.; Nurmikko, A. V. Dielectric Confinement Effect on Excitons in PbI 4-Based Layered Semiconductors. *Phys. Rev. B* **1992**, *45* (12), 6961.

(44) Lin, Y.; Ling, X.; Yu, L.; Huang, S.; Hsu, A. L.; Lee, Y.-H.; Kong, J.; Dresselhaus, M. S.; Palacios, T. Dielectric Screening of Excitons and Trions in Single-Layer MoS_2. *Nano Lett.* **2014**, *14* (10), 5569–5576.

(45) Raja, A.; Chaves, A.; Yu, J.; Arefe, G.; Hill, H. M.; Rigosi, A. F.; Berkelbach, T. C.; Nagler, P.; Schüller, C.; Korn, T.; et al. Coulomb Engineering of the Bandgap and Excitons in Two-Dimensional Materials. *Nat. Commun.* **2017**, *8*, 15251.

CHAPTER 5 General Synthesis Route to High Quality Colloidal III-V Semiconductor Quantum Dots Based on Pnictogen Chlorides

III-V semiconductors are an attractive material family with excellent electrical and optical properties including high carrier mobilities and a direct band gap.[1,2] Ternary and quaternary alloys formed in this material system offer wide-range tunability and exquisite control over stoichiometry, which allow continuous tuning of band gap energies.[3] III-V based thin film heterostructures enable these semiconductors in the use of high-speed electronics and highly efficient optoelectronics.[4] However, the strong covalent nature of atomic bonding requires highly reactive precursors, high reaction temperature and high-quality vacuum system for gas-phase synthesis processes.[5] Efforts to develop large scale, low-temperature synthesis and easily accessible fabrication techniques for utilizing these materials are highly motivated, considering increasing demands for ubiquitous electronics such as Internet of Things.

Developing colloidal III-V semiconductor quantum dots (QDs) can realize opto/electronic devices with low cost, large area, solution-based fabrication techniques.[6] Taking advantage of the quantum confinement effect, we can achieve size-dependent bandgap energies of III-V QDs due to the extremely large exciton Bohr radius, in order to obtain broadband optical response in optoelectronics.[7] However, the difficulties aforementioned in the growth of bulk III-V materials still haunt the solution-phase reactions, impeding the preparation of colloidal III-V QDs.[8] These challenges have mainly been tackled with the development of group V precursors. Dehalosilylation reaction is firstly employed and relatively well-established to synthesize InP QDs with tris(trimethylsilyl)phosphine, $(TMS)_3P$, as precursors.[9] Nevertheless, this reaction is difficult to extend to the synthesis of InAs and InSb QDs, because $(TMS)_3As$ and $(TMS)_3Sb$ are unstable, pyrophoric and highly toxic.[10,11] Recently, aminopnictogen precursors have been introduced to synthesize InAs and InSb QDs in the presence of reducing agents.[12–15] Still, some of these

precursors suffer from tedious preparation and chemical instability. The size of the III-V QDs made by these reported methods is typically less than 6 nm in diameter.

Here, we develop a general route to synthesize III-V NCs based on the heat-up and co-reduction of indium and pnictogen chloride precursors. By dissolving $InCl_3$ and pnictogen chloride ($PnCl_3$, Pn = P, As and Sb) in olyelamine (OLAM), we greatly simplify the preparation and improve the stability of both group III and V precursors. Colloidal InP, InAs and InSb QDs tailored in size are realized by controlling the precursor concentration, reaction temperature and time, which allows the preparation of QD samples with bandgaps tunable from the visible to short-wavelength infrared. We develop a solution- and solid-state hybrid ligand exchange for III-V QDs and achieve field-effect transistor (FET) carrier mobilities (>5 cm^2/Vs) from InAs QD channel materials. The generality of this synthesis approach also enables the formation of ternary alloy III-V NCs. By changing the molar ratio between As and Sb precursors, we successfully prepare $InAs_xSb_{1-x}$ QDs with various compositions and band gap energies. The carrier concentration also changes with the QD composition.

5.1 Synthesis of III-V Colloidal Quantum Dots (QDs) via Co-reduction

In a typical synthesis reaction [Scheme 1], $InCl_3$ (0.05 M) and $AsCl_3$ (or PCl_3 or $SbCl_3$) (0.25 M) stock solutions are separately prepared by stirring the halide salts in oleylamine (OLAM) at ~50 °C overnight inside a nitrogen glovebox. To form InAs and InSb QDs, 10 mL of $InCl_3$- and 1 mL of $AsCl_3$- or $SbCl_3$-OLAM precursors are mixed in a reaction flask at room temperature and then 2.2 mmol lithium triethylborohydride or also known as superhydride (SH) is injected, so that the molar ratio In:As:SH=2:1:9. The successful synthesis of InP QDs, unlike InAs and InSb, requires a In:P precursor molar ratio of 1:4, therefore 2.5 mL of $InCl_3$, 2 mL of PCl_3 are used instead in addition to 1.9 mmol of SH, possibly due to lower reactivity of PCl_3-OLAM precursors.

The mixture is then heated up to the reaction temperature at 3 °C/min under nitrogen flow and held at that temperature for 15 min before being cooled. In a nitrogen filled glovebox, the QDs are isolated from the growth medium and purified through a "size selection process" of precipitation and redispersion using acetonitrile and toluene, respectively. While the InP and InAs QDs are capped by OLAM as synthesized, 1 mL of oleic acid is typically added before the purification step to stabilize the InSb QDs in toluene. The precipitation and redispersion steps are carried out two more times to improve the size distribution of the final QD product.

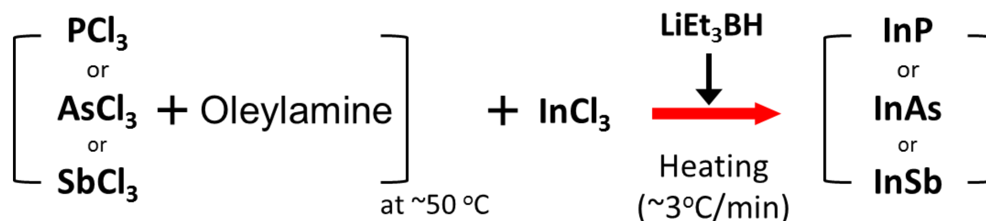

Scheme 1. Schematic diagram of co-reduction reaction for Indium based III-V semiconductor NC formation

Size tunable InP, InAs and InSb QDs are prepared based on this general synthesis route. The size of the QD samples can be controlled by the reaction temperature and precursor concentration. For example, InAs QD samples are prepared with diameters ranging from 3.1 ± 0.2 nm to 6.3 ± 0.5 nm as the reaction temperature is increased from 240 °C to 340 °C, while maintaining the same reaction time of 15 min. Similarly, InSb QD samples with diameter ranging from 4.2 ± 0.45 to 7.5 ± 0.62 nm in size are achieved by varying the reaction temperature from 280 to 320 °C. We also prepare InP QDs with diameters of 3.1 ± 0.60 and 4.7 ± 0.57 nm. To increase the size of InP QDs, we increase the total precursor concentration by 1.5 times, which can facilitate the formation of monomers from the relatively less reactive phosphorus precursors. Representative TEM images of III-V NCs with different sizes are shown in Figure 1a to f. The electron diffraction patterns and high-resolution TEM images of InAs and InSb QDs are consistent

with zinc blend crystal structures. Given the Bohr radius of InP, InAs and InSb as large as ~10, 34 and 65 nm, QDs synthesized with these sizes experience strong quantum confinement, leading to size-dependent optical properties. The first exciton absorption peak spans the visible to near-infrared regions of the electromagnetic spectrum for the InP, InAs and InSb QDs as the particle size increases [Figure 5.1g].

To study the effect of reaction time on the size of InAs QDs, we grow QDs at 320 °C for times varying between 15 min to 60 min. As shown in Figure 5.2, the red shift of absorption peaks, suggesting bandgap narrowing and particle growth, stops at 1350 nm after a 45 min reaction time, hypothetically due to complete consumption of the precursors. The absorption peak also broadens with reaction time, indicating that the Ostwald ripening process is reducing the monodispersity of the QD sample.

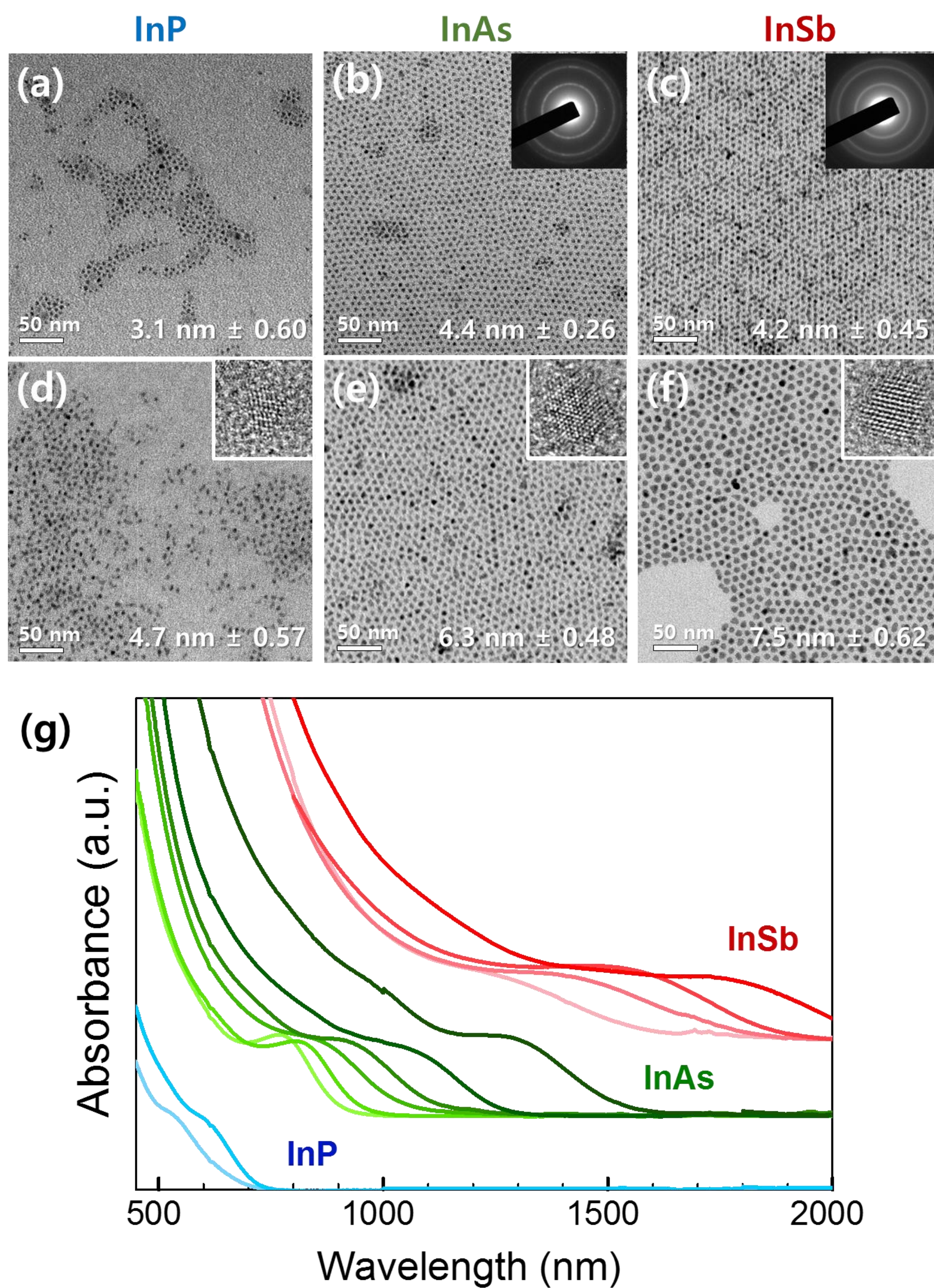

Figure 5.1 (a) to (f) low magnification TEM images, selected area electron diffraction pattern (b to c insets) and high resolution TEM images (d to f insets) and (g) UV-Vis-NIR absorption spectra of different-sized InP, InAs and InSb QDs.

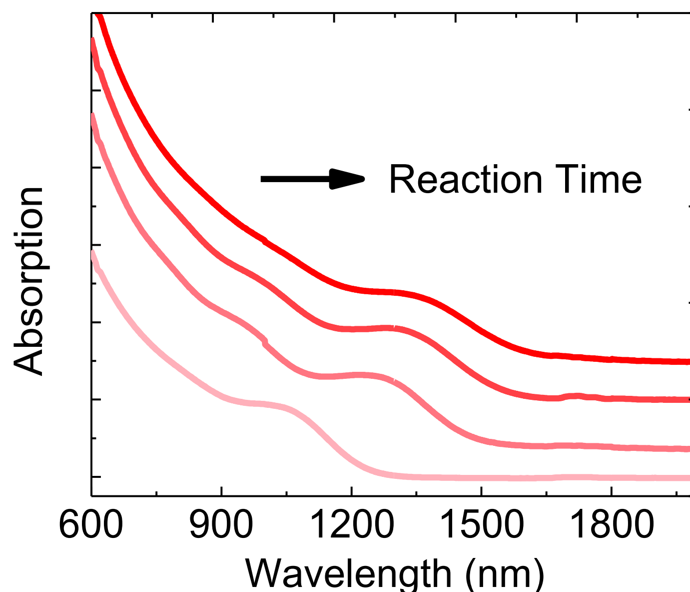

Figure 5.2 UV-Vis-NIR absorption spectra of InAs NCs synthesized at a reaction temperature of 320 °C for 15, 30, 45 and 60 min (from left to right).

5.2 Pnictogen Chloride ($PnCl_3$)-Oleylamine Precursors

The development of $PnCl_3$-OLAM as a group V precursor is advantageous for both its chemical stability and commercial availability. Figure 5.3a shows stock solutions of PCl_3, $AsCl_3$ and $SbCl_3$ in OLAM (from left to right). After being stirred overnight at ~50 °C, all three pnictogen halides are fully dissolved to form clear solutions. The solutions solidify when cooled to room temperature. Upon the addition of anti-solvents (e.g., hexane, acetone, methanol, isopropanol, or ethanol), the $PnCl_3$-OLAM solutions become turbid [Figure 5.3b], and white powders are precipitated and can be collected. The stable powder form of the precursors makes them easy to handle and store for a long term.

To further investigate the chemical reaction taking place in the formation of precursor solutions, room temperature H-nuclear magnetic resonance (NMR) measurements are performed. Figure 5.3c shows the resonance energy of the hydrogen atom in OLAM closest to the NH_2 group, denoted as "f", shifts to a significant higher value once $AsCl_3$ is added into the OLAM, consistent with chemical bonds between $AsCl_3$ and NH_2R. The shift is independent of the presence of $InCl_3$, indicating the reaction between $AsCl_3$ and OLAM is faster and predominant over that between $InCl_3$ and OLAM. The NMR results of $SbCl_3$- and PCl_3-oleylamine solutions all follow the same trend.

The variation in $PnCl_3$ precursor reactivity results in different kinetics, which affect QD nucleation and growth. After weeks of heating, the $SbCl_3$-OLAM solution eventually turns dark and starts to precipitate, while the PCl_3 and $AsCl_3$ solution remains clear. This experimental observation is consistent with the trend in precursor chemical reactivity where Sb>As>P. The relatively low reactivity of PCl_3-OLAM prevents P (+III) from being effectively reduced to P (0). The same precursor ratio of In:P=2:1 only yields large amorphous particles, presumably elemental In. To balance precursor reactivity, we increase the amount of the phosphorus precursor such that In:P=1:4 and succeed in making InP QDs. The particle size of InP QDs are still less uniform than that of InAs and InSb QDs prepared by the same method, possibly limited by the slow nucleation kinetics under the current synthesis conditions. Although the colloidal synthesis of InP QDs is relatively better established in the III-V family, we apply this pnictogen chloride-based approach here as a way to show the generality of the method and study the reaction mechanism.

(a)

(b)

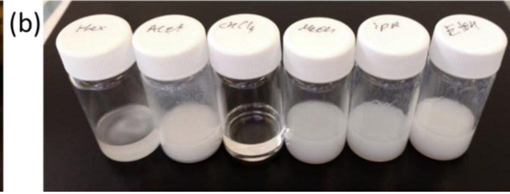

(c)

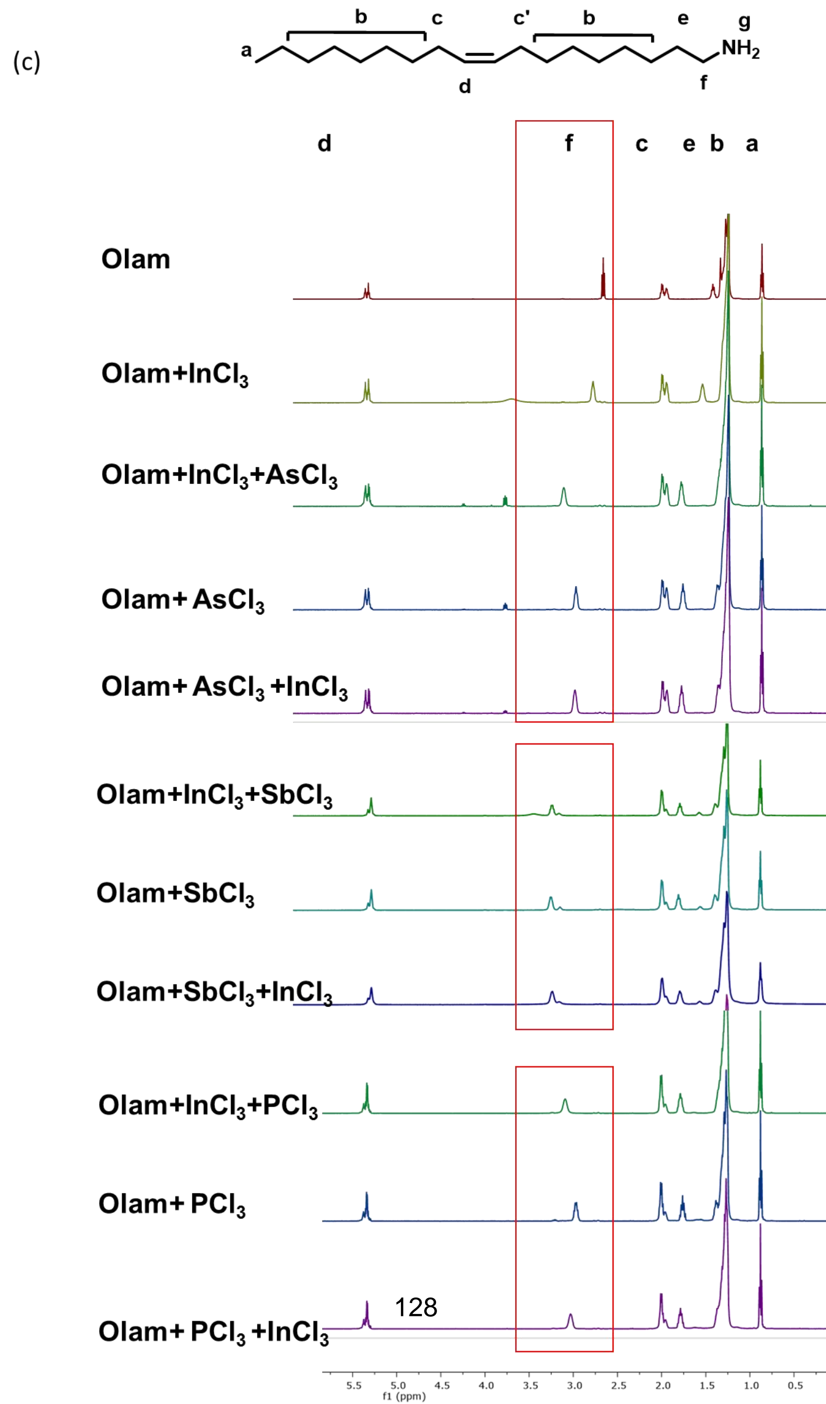

Figure 5.3 Photos of (a) PCl_3-, $AsCl_3$- and $SbCl_3$-oleylamine solutions (from left to right) at 50 °C, and (b) $PnCl_3$-OLAM solution with addition of hexane, acetone, chloroform, methanol, isopropanol, or ethanol from left to right. (c) H-NMR spectra of OLAM (red), OLAM mixed with $InCl_3$ (light green), OLAM mixed with $InCl_3$ then $PnCl_3$ ($AsCl_3$, $SbCl_3$ and PCl_3) (dark green) and OLAM mixed with $PnCl_3$ (blue), OLAM mixed with PnCl3 then $InCl_3$ (purple).

5.3 Optical, Structural and Electrical Characterization of III-V QDs

5.3.1 InAs QD Characterization, Ligand Exchange and Devices

The characterization of one representative batch of InAs QDs synthesized at 320 °C for 15 min is shown in Figure 5.4. A size and size distribution of 4.0±0.36 nm is obtained from TEM images [Figure 5.4a], and high-resolution TEM images [Figure 5.4a inset] indicate the QD surface is terminated by (111) facets. These InAs QDs have a well-defined absorption peak at 1020 nm, corresponding to a bandgap energy of 1.22 eV [Figure 5.4b, black]. In the same plot, we also include room temperature photoluminescence (PL) observed from these QDs without any additional surface passivation or core/shell formation.

It has been shown in the InP QD system, that HF etching removes surface dangling P bonds as fluorine reacts with unpassivated P atoms to form PF_3 complexes. HF treatment renders InP QDs with In-rich surfaces and improved PL.[16] Consistent with HF treatment of InP QDs, we treated InAs NC dispersions with $NOBF_4$. The $NOBF_4$ is dissolved in acetonitrile and used to wash the QD dispersion. After redispersing the QDs in toluene, the InAs QD dispersion shows enhanced PL with the peak position slightly blue shifted with increasing concentrations of $NOBF_4$ [Figure 5.4b, lighter blue and cyan], suggesting the removal of excess surface As atoms. The In:As ratio measured from x-ray photoelectron spectroscopy (XPS) shows indeed an increase in In:As composition from 48.7:51.3 to 50.6:49.4 after the $NOBF_4$ treatment.

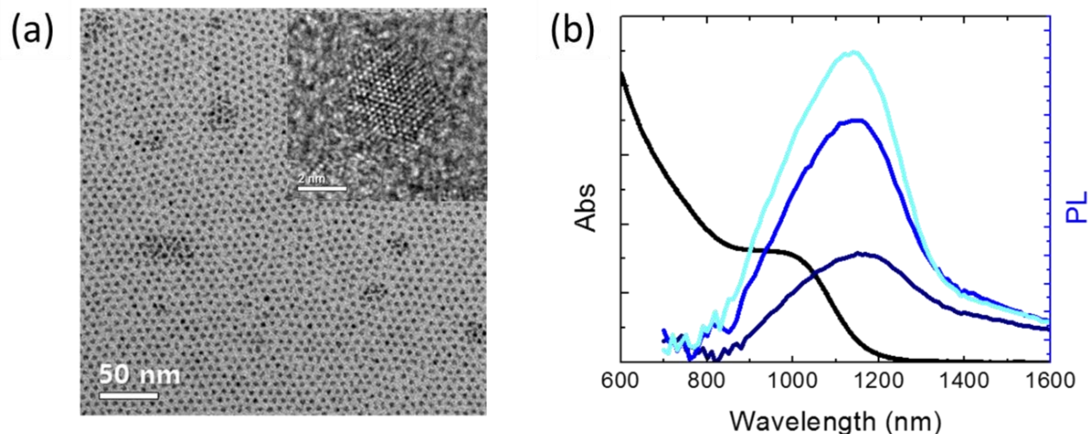

Figure 5.4 (a) Low-resolution and (inset) high-resolution TEM images of InAs QDs synthesized at 320 °C for 15 min. (b) Absorption (black) and photoluminescence spectra of InAs QDs as-synthesized (dark blue) and upon treatment with 1 mg/mL (light blue) and 2 mg/mL (cyan) $NOBF_4$ in acetonitrile.

To prepare electronically-conductive III-V QD thin films for integration in devices, effective ligand exchange and doping strategies are developed to enhance interdot coupling and control carrier concentration. Solution ligand exchange of InAs QDs is modified from a reported method,[17] where Na_2S is selected as the ligand exchange agent to replace OLAM ligands introduced during synthesis. Illustrated in Figure 5.5a, the transfer of QDs from the non-polar toluene to polar formamide (FA) after vortexing marks the altered surface chemistry. After washing the sample twice with fresh toluene and precipitating the QDs using acetonitrile, the S^{2-} capped InAs QDs are finally dispersed in N,N-Dimethylformamide (DMF), a solvent suitable for spin coating thin films. The absorption spectrum of the InAs QD film after the solution ligand exchange preserves the first exciton peak [Figure 5.5b, red], indicating the QDs remain quantum confined and well separated by S^{2-} ligands. The area we calculate under the C-H stretch in the Fourier transform infrared (FTIR) spectra [Figure 5.5c, red] shows that 91.2% of OLAM is

removed after the solution exchange. We fabricate thin film field-effect transistors (FETs) by spin-coating the S^{2-} solution exchanged InAs QDs on n++ Si device grade wafers and evaporating 40 nm In 40 nm/40 nm Au through shadow masks to define source and drain contacts. The device exhibits n-type characteristics, consistent with sulfur serving as a low-lying donor in bulk InAs. An electron field-effect mobility of 0.25±0.04 cm^2/Vs is measured in the saturation regime [Figure 5.5d, black], comparable to reported values with similar ligand exchange processes.[18]

To further improve carrier transport, we introduce an additional ligand exchange step in the solid state following each deposition of the solution-exchanged QD layer [Figure 5.5a], i.e., the QD films are treated with a "hybrid" ligand exchange consisting of both a solution- and solid-state ligand exchange step. A dilute, 5 mM methanolic solution of Na_2S or NaN_3 is used to treat the QD films for a short reaction time of 10s. The InAs QD film shows a broadened absorption peak [Figure 5.5b, green], and more complete removal of OLAM (as indicated by the 94.8% reduction of the C-H stretch) [Figure 5.5c, green], indicating enhanced electronic coupling due to reduced interparticle distance. Further annealing of the QD film at 300 °C for 5 min, experimentally a necessary step to yield high mobility, gives rise to a further red shift as well as continued broadening of the absorption peak [Figure 5.5c, blue]. Consistently, FET devices based on the hybrid-exchanged InAs NC film, with an additional Na_2S solid-state treatment, show higher currents and electron mobility (4.03±0.26 cm^2 /Vs) compared to solution-exchanged only devices [Figure 5.5d, red]. However, due to the double role of S^{2-}, both as a ligand and a donor in the system, the excessive incorporation of sulfur during the hybrid ligand exchange also tends to over-dope the QD film, reducing gate modulation and carrier mobility. Using NaN_3 as the solid-state ligand exchange reagent, reduces interparticle distance upon decomposition of the azide at annealing temperatures without introducing excess dopants to the system. InAs QD FET devices with such a hybrid ligand exchange show higher electron mobility (5.46±0.37 cm^2/Vs) and on/off ratios (10^4) in the saturation regime. I_D-V_G characteristics of a representative device with mobility of 5.24 cm^2/Vs is shown in Figure 5.5e. To our knowledge, high mobility III-V QD devices have

only been realized based on ligand chemistries involving hydrazine, which is highly toxic and corrosive. The hybrid ligand exchange developed here, as an alternative approach, is compatible with flexible NC electronics fabrication and applicable to the general III-V NC family.

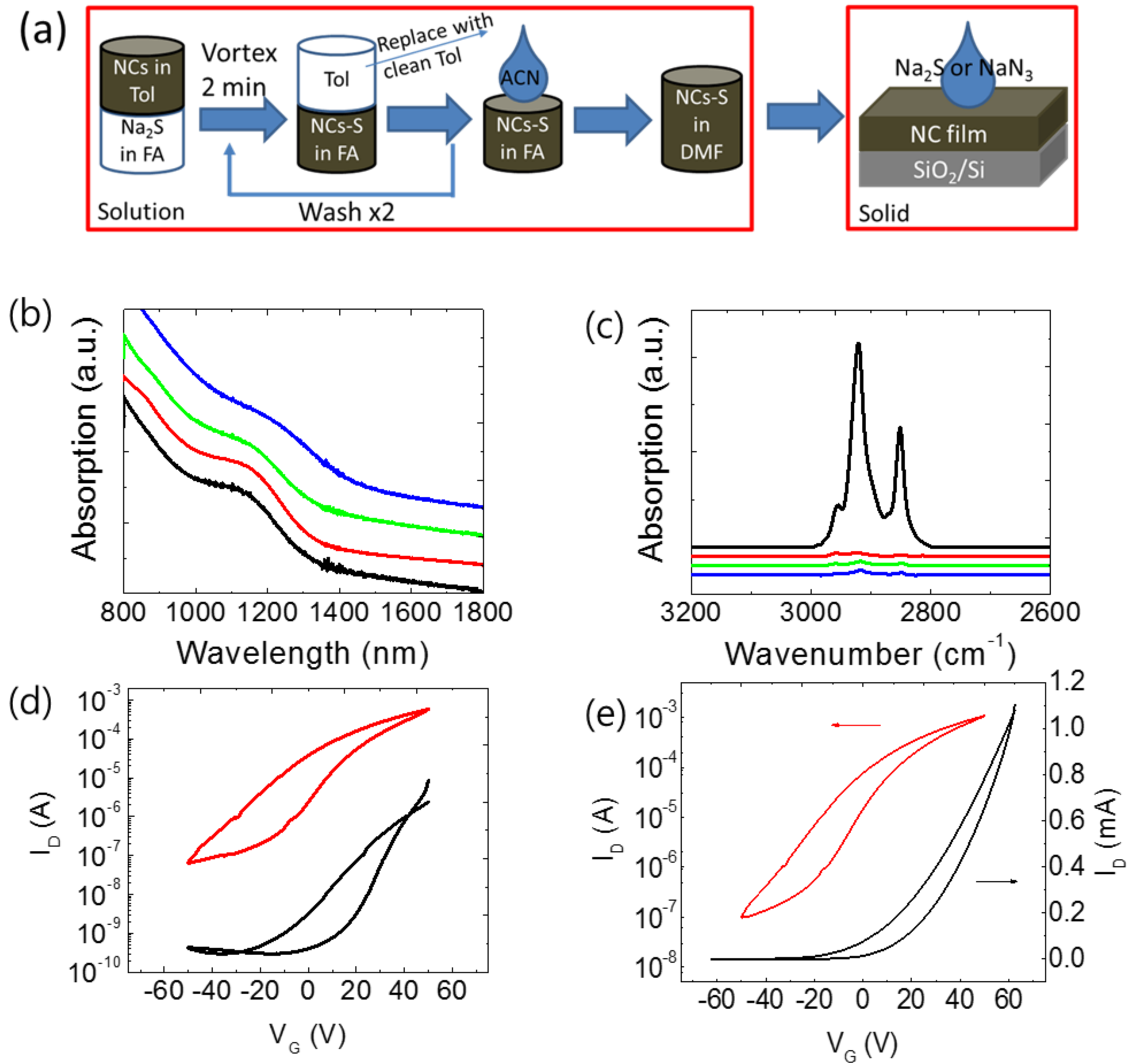

Figure 5.5 (a) Schematics of solution and solid hybrid ligand exchange process. (b) UV-Vis absorption and (c) FTIR spectra of InAs QD films before (black) and after only solution exchange (red), with hybrid exchange (green), and with hybrid exchange and annealing at 300 °C for 5 min (blue). I_D-V_G characteristics (saturation regime, V_D=50 V) of InAs QD FETs (d) with Na_2S solution exchange only (black) and hybrid

ligand exchange with Na_2S (red), and (e) with Na_2S solution exchange and NaN_3 solid-state ligand exchange in linear (black) and log (red) scale.

5.3.2 Surface Oxidation of InSb NCs

In contrast to the high performance InAs QD FETs, the InSb QD device characteristics are less consist and more prone to oxidation during QD synthesis and storage, device fabrication and measurement.

We use XPS to study the evolution of surface oxidation in the InSb QD systems. Figure 5.6 shows the XPS spectra of InSb QDs synthesized by a typical reaction. By scanning the In 3d 5/2 region [Figure 5.6a], we identify a feature at 444.4 eV in additional to a predominant peak at 443.4 eV, and assign them as indium-oxygen and indium-antimony bonds, respectively. In the Sb 3d 5/2 spectra, the peak represents Sb-In binding energy is found to be 527.0 eV while another peak detected at 530.0 eV characterizes the oxidation state of Sb, such as Sb_2O_5. XPS measurements are consistent with unintentional oxidation of both In and Sb even though every synthesis step is handled using air-free techniques. The effect of oxidation on particle size, doping, carrier transport and other physical properties of III-V NCs are under further investigation.

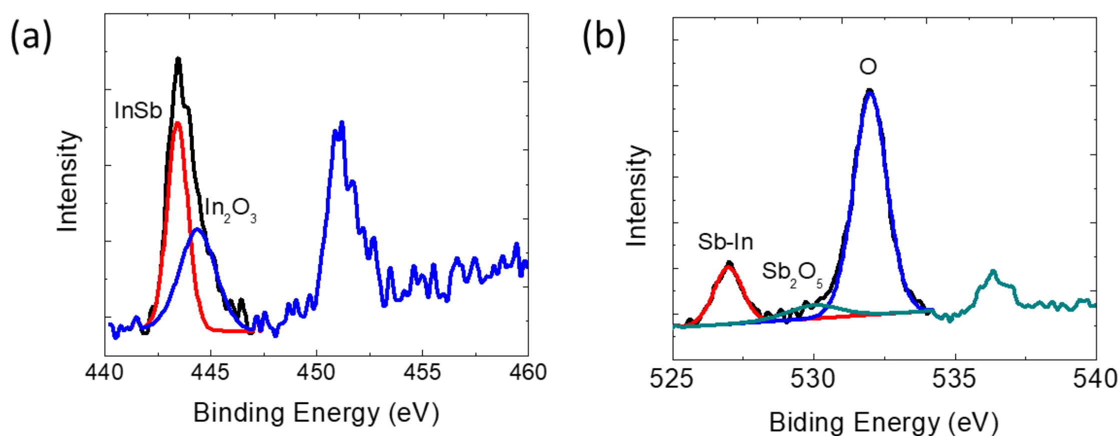

Figure 5.6 XPS spectra of (a) In 3d and (b) Sb 3d lines. Experiment data (black) and fitting of InSb (black), In_2O_3 (blue), and Sb_2O_5 (green).

To avoid unintentional oxidation introduced during the QD synthesis, we degas the $InCl_3$-OLAM precursor at 120 °C for 2 h before its use to remove trace amounts of oxygen and water contained in the commercial anhydrous precursors. From XPS measurements [Figure 5.7, top row], the In_2O_3 peak is reduced significantly after the degassing process. The In_2O_3:InSb peak area ratio decreases from 0.83 to 0.20 after degassing the In precursor. Meanwhile, the intensity of oxidized Sb peak is also weaker. This suggests that dry chemicals are helpful in suppressing oxidation during QD synthesis.

Surface oxidation of InSb NCs does, however, evolve with sample storage. The same batch of QDs made with the degassed precursors is dispersed in anhydrous toluene and stored in a nitrogen filled glovebox with O_2 level less than 10 ppm. After one week, the In_2O_3 peak grows to nearly the same intensity as the InSb peak, and the Sb_2O_5 bonds increase at the expense of Sb-In bonds [Figure 5.7, middle row]. More extremely, if the QD sample is exposed to air for 10 min before the XPS measurement, the In_2O_3 signal outgrows the InSb peak, consistent with this trend.

The Sb-In intensity further decreases, indicating more Sb is oxidized [Figure 5.7, bottom row]. It is worth mentioning that Sb oxidation states, including Sb_2O_5, which has a binding energy that overlaps that of free oxygen, and therefore may lead to an underestimation of the amount of antinomy oxide. The extreme oxygen sensitivity and surface instability of InSb NCs limit the device application of this material unless more efficient surface etching and/or passivation processes are developed.

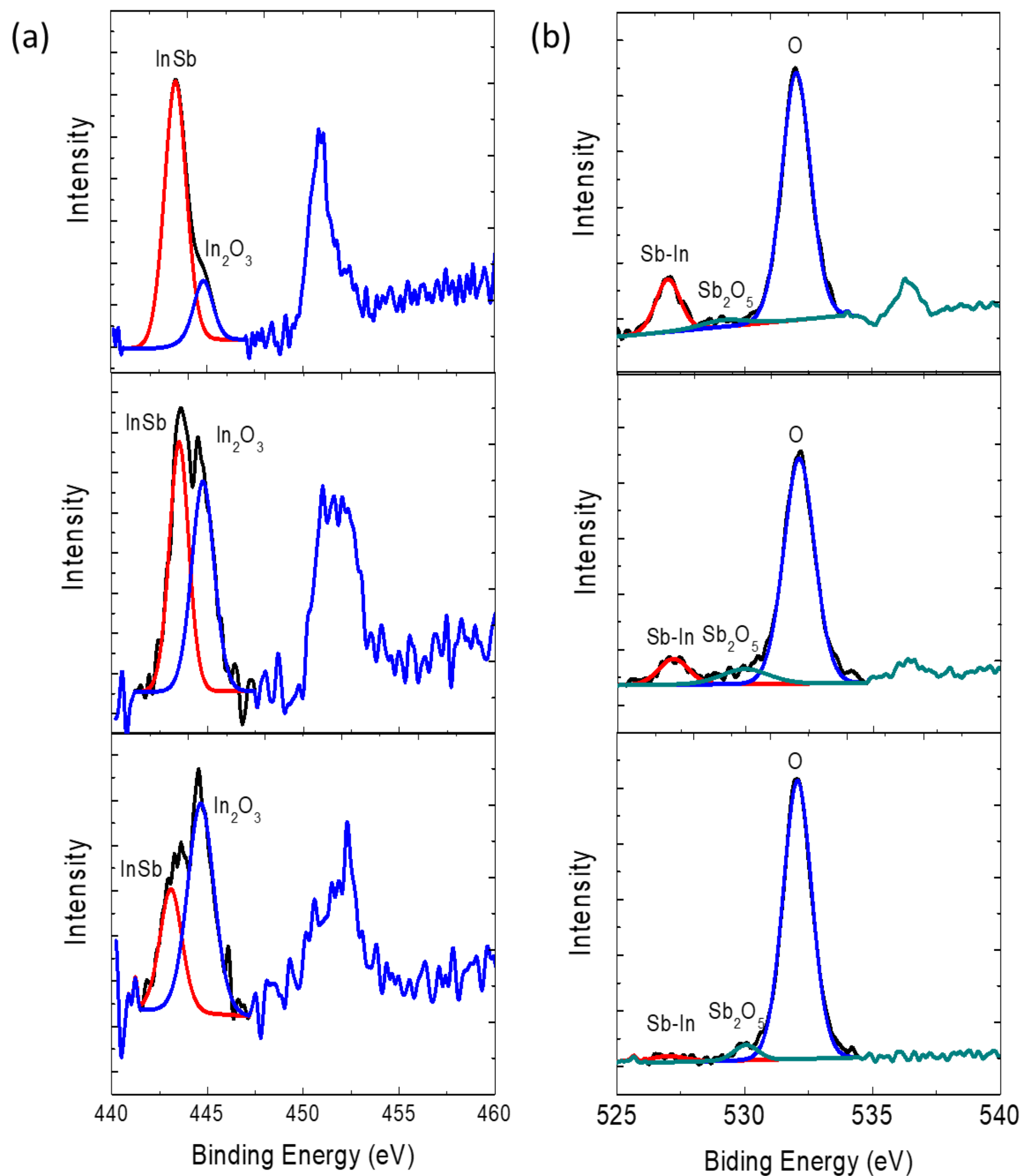

Figure 5.7 XPS spectra of (a) In 3d and (b) Sb 3d lines. Experimental data (black) and fitting (red, blue, green). From top to bottom rows: InSb QDs as synthesized, stored in glovebox for one week and exposed to air for 10 min.

5.4 Synthesis and Characterization of $InAs_xSb_{1-x}$ Alloy NCs

The versatility of this synthesis approach allows the formation of ternary $InAs_xSb_{1-x}$ alloy QDs through addition of both As and Sb precursors in the beginning of the reaction. By increasing the ratio of Sb precursors, we obtain a series of $InAs_xSb_{1-x}$ QDs at 320 °C for 15 min. The elemental composition of these alloy QDs is confirmed by energy-dispersive X-ray spectroscopy (EDS) and inductively coupled plasma mass spectrometry (ICP-MS), and the As:Sb results are listed in Table 5.1 in close agreement with the initial ratio of their precursors. The alloy QDs are imaged by high resolution TEM and show uniform crystallization without phase separation [Figure 5.8a]. Powder X-ray diffraction (XRD) measurements on the binary and ternary III-V NCs show the single (111) diffraction peak shifts from 2θ = 25 ° (InAs phase) to 23 ° (InSb phase) as the stoichiometry changes from As rich to Sb rich, consistent with alloying and not the co-existence of the two pure binary phases [Figure 5.8b]. The lattice constants analyzed both from the XRD and TEM results are in excellent agreement, increasing from InAs to InSb as the Sb content increases [Table 1]. Figure 5.8c shows that the first excitonic peaks of the alloy QDs shift to longer wavelength with the Sb ratio.

Another evidence to prove that the $InAs_xSb_{1-x}$ QDs are not phase separated into InAs and InSb is provided by the photoluminescence (PL) measurements. Figure 5.8d presents the PL spectra of InAs, $InAs_{0.5}Sb_{0.5}$ and InSb QDs synthesized at 300 °C for 15 min. All three QD dispersions show well-defined single PL peaks, indicating the absence of secondary phase. As the Sb content increases, the PL peak red shifts, consistent with the trend of in excitonic absorption in Figure 5.8c. The PL peak intensity decreases with increasing Sb ratio, suggesting lower PL quantum yield as more Sb is introduced.

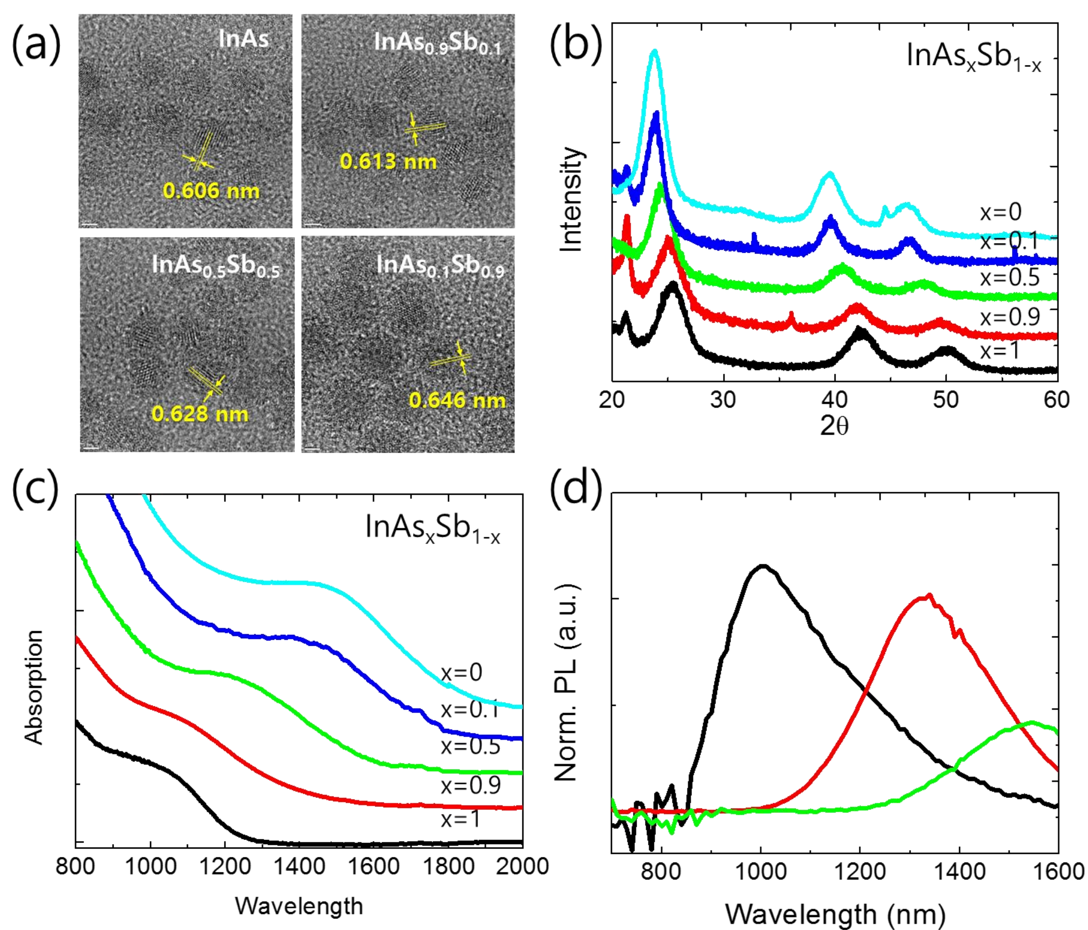

Figure 5.8 (a) Absorption spectra and (b) Powder XRD patterns of InAs, $InAs_xSb_{1-x}$ and InSb QD dispersions and films with an As:Sb precursor ratio from 1:0 to 0.9:0.1, 0.5:0.5, 0.1:0.9 and 0:1, respectively. (c) High resolution TEM images of $InAs_xSb_{1-x}$ QDs with x=0, 0.9, 0.5 and 0.1. (d) PL spectra of InAs (black), $InAs_{0.5}$-$Sb_{0.5}$ (red), and InSb (green) synthesized at 300 °C for 15 min.

Table 5.1 Elemental composition and lattice constant of $InAs_xSb_{1-x}$ NCs

Initial As to Sb precursor ratio	Elemental composition by EDS (%)			Elemental composition by ICP-MS (%)			Lattice constant (nm)	
	In	As	Sb	In	As	Sb	by XRD	by TEM
InAs	45	55	-	51	49	-	0.606	0.606
$InAs_{0.9}Sb_{0.1}$	41	52	7				0.612	0.613
$InAs_{0.5}Sb_{0.5}$	45	31	24	49	27	24	0.630	0.628
$InAs_{0.1}Sb_{0.9}$	48	6	46				0.646	0.646
InSb	50	-	50	50	-	50	0.652	0.650

Formation of alloys determines the bandgap energies of QDs both by changing their sizes and compositions. The diameter of alloy QDs is extracted from the TEM images [Figure 5.9 a to e] as 3.0 ± 0.3, 3.1 ± 0.3, 5.0 ± 0.4, 5.7 ± 0.5 and 6.4 ± 0.6 nm as the composition is tailored from InAs to $InAs_{0.9}Sb_{0.1}$, $InAs_{0.5}Sb_{0.5}$, $InAs_{0.1}Sb_{0.9}$ and InSb. Since all QDs are synthesized under the same temperature and reaction time, the particle growth increases with the addition of Sb precursor. At the same composition, the enhancement of bandgap energy due to quantum confinement effect weakens as the particle size increases.

The composition of QDs also plays a role in directly determining the bandgap energies. Figure 5.10 shows the correlation between bandgap energy and particle diameter of InAs, InSb and their alloy NCs. Even at the same particle dimension, the bandgap energy of InAs QDs is larger than that of the InSb NCs, originating from the difference in their bulk bandgap energies and carrier effective masses. As expected, equally-sized $InAs_xSb_{1-x}$ NCs have intermediate bandgap energies, suggesting their band structure tailored by the relative amount of In-As and In-Sb bonds.

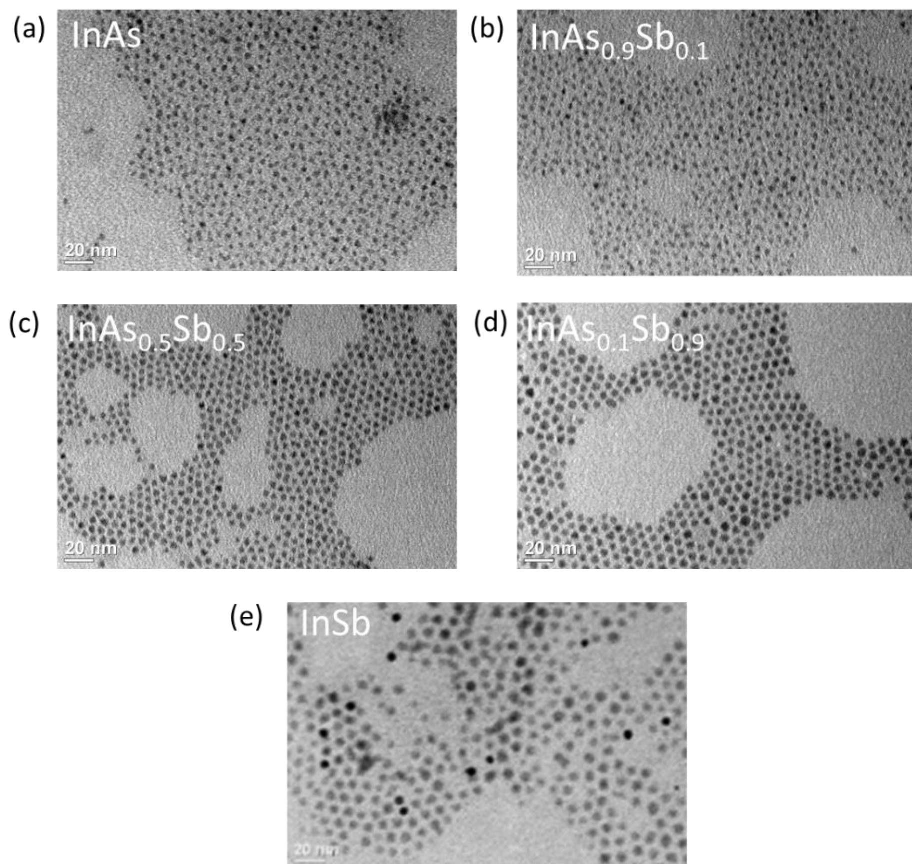

Figure 5.9 TEM images of $InAs_xSb_{1-x}$ QDs with As:Sb precursor ratio of (a) 10:0, (b) 9:1, (c) 5:5, (d) 1:9 and (e) 0:10.

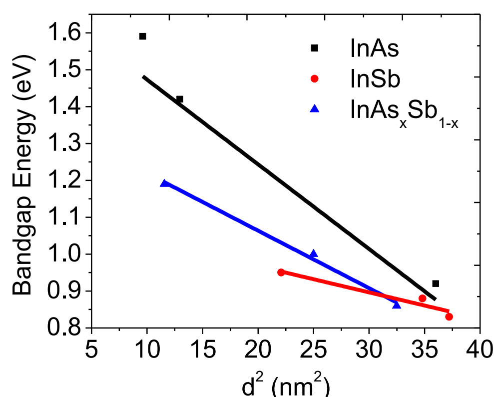

Figure 5.10 Bandgap energies of InAs (black squares), $InAs_xSb_{1-x}$ (blue triangles) and InSb (red dots) as a function of NC diameter square d^2.

In addition to tuning the bandgap energy, the chemical composition of the alloy also affects the carrier concentration of the material. We fabricate FET devices of InAs and $InAs_xSb_{1-x}$ NC thin films using a Na_2S solid-state ligand exchange. In a nitrogen filled glovebox, a QD dispersion (15 mg/mL) is spin cast on device grade Si wafers and treated by Na_2S (15 mM in methanol) for 10 s followed by three times of methanol washing. Two to three such NC layers are usually deposited sequentially to ensure deposition of a continuous channel. 40 nm of Au is thermally deposited as the top contact for the FET device.

As the Sb ratio increases, the I_D-V_G characteristics of the devices transform from predominantly n-type to p-type as the device on-state switches from positive gate voltages to negative gate voltages [Figure 5.11a]. Holes have become the majority carriers instead of electrons correspondingly. In those p-type devices, the threshold voltage continuously positively shifts with Sb ratio, indicating that holes can be accumulated in the channel material at lower gate voltages, or in other words, the Fermi level of the alloy NC layer moves towards the valence band when there is more Sb included. This p-doping effect of Sb alloying also induces higher hole

mobility and currents. Annealing the FETs at 200 °C further decreases interparticle distance and increases current levels. The high temperature activates surface S atoms introduced during ligand exchange that serve as donors as well, giving rise to an increase in the electron currents [Figure 5.11b]. Nevertheless, with increasing Sb content, the electron current still decreases, which is presumably due to compensation of Sb. The increase in off-current is expected because of the narrowed bandgap energies of the alloy QDs. The growing p-type doping, however, seems contradictory to the trend of becoming In-rich as the alloy QDs include more Sb [Table 5.1]. We speculate that In-on-Sb antisite defects to be a possible cause. Antisite defects are known in bulk III-V systems to serve as acceptors and dominate at surfaces. Also, the formation of an oxide may create surface dead layers, such as In_2O_3, that have no contribution to the carrier concentration and transport.

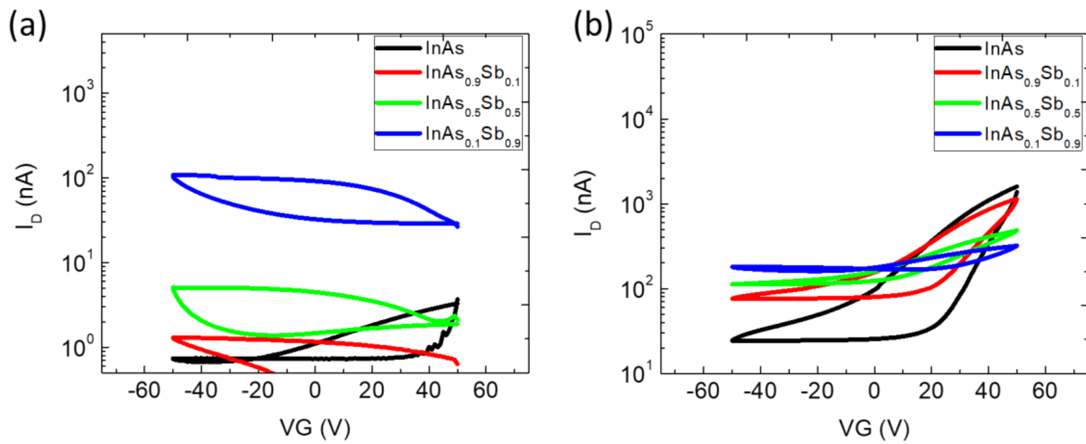

Figure 5.11 I_D-V_G FET device characteristics of $InAs_xSb_{1-x}$ alloy QDs (saturation regime, V_D=50 V) (a) as fabricated with Na_2S solid-state ligand exchange and (b) after being annealed at 200 °C for 10 min

5.5 Conclusions

In conclusion, we report the successful synthesis of InP, InAs, InSb and ternary $InAs_xSb_{1-x}$ colloidal QDs through a general and facile approach. Commercially available and chemically stable $InCl_3$ and pnictogen chlorides-OLAM are exploited as precursors to form QDs in the presence of reducing agents. We study the size and composition tunability of these QDs. The alloying of Sb facilitates particle growth and narrows the band gap. More pronounced p-type characteristics are observed in Sb-rich $InAs_xSb_{1-x}$ QD films. We also explore the surface chemistry of III-V NCs and develop a solution- and solid-state hybrid ligand exchange to build InAs QD FETs with high electron mobility. This versatile synthesis reaction is possibly expandable to wider range of colloidal NC systems such as Ga-based III-V semiconductors. The tunable bandgap energy and promising transport characteristics make this class of III-V NCs appealing for electronic and optoelectronic devices, including photovoltaics and IR photodectors.

5.6 References

(1) Mokkapati, S.; Jagadish, C. III-V Compound SC for Optoelectronic Devices. *Mater. Today* **2009**, *12* (4), 22–32.

(2) del Alamo, J. A. Nanometre-Scale Electronics with III–V Compound Semiconductors. *Nature* **2011**, *479* (7373), 317–323.

(3) Vurgaftman, I.; Meyer, J. R.; Ram-Mohan, L. R. Band Parameters for III–V Compound Semiconductors and Their Alloys. *J. Appl. Phys.* **2001**, *89* (11), 5815–5875.

(4) Dupuis, R. D. III-V Semiconductor Heterojunction Devices Grown by Metalorganic Chemical Vapor Deposition. *IEEE J. Sel. Top. Quantum Electron.* **2000**, *6* (6), 1040–1050.

(5) Stringfellow, G. B. VPE Growth of III/V Semiconductors. *Annu. Rev. Mater. Sci.* **1978**, *8* (1), 73–98.

(6) Kagan, C. R.; Lifshitz, E.; Sargent, E. H.; Talapin, D. V. Building Devices from Colloidal Quantum Dots. *Science (80-.).* **2016**, *353* (6302), 5523.

(7) Krauss, T. D.; Peterson, J. J. Electronic Structure and Optical Transitions in Colloidal Semiconductor Nanocrystals. In *Colloidal Quantum Dot Optoelectronics and Photovoltaics*; Konstantatos, G., Sargent, E. H., Eds.; Cambridge University Press: Cambridge, 2013; pp 59–86.

(8) Reiss, P.; Carrière, M.; Lincheneau, C.; Vaure, L.; Tamang, S. Synthesis of Semiconductor Nanocrystals, Focusing on Nontoxic and Earth-Abundant Materials. *Chem. Rev.* **2016**, *116* (18), 10731–10819.

(9) A. A. Guzelian; J. E. B. Katari; A. V. Kadavanich; U. Banin; K. Hamad; E. Juban, and; Alivisatos, A. P.; R. H. Wolters; C. C. Arnold, and; Heath, J. R. Synthesis of Size-Selected, Surface-Passivated InP Nanocrystals. *J. Phys. Chem.* **1996**, *100* (17), 7212–7219.

(10) Guzelian, A. A.; Banin, U.; Kadavanich, A. V.; Peng, X.; Alivisatos, A. P. Colloidal Chemical Synthesis and Characterization of InAs Nanocrystal Quantum Dots. *Appl. Phys. Lett.* **1996**, *69* (10), 1432–1434.

(11) Harris, D. K.; Bawendi, M. G. Improved Precursor Chemistry for the Synthesis of III–V Quantum Dots. *J. Am. Chem. Soc.* **2012**, *134* (50), 20211–20213.

(12) Tessier, M. D.; De Nolf, K.; Dupont, D.; Sinnaeve, D.; De Roo, J.; Hens, Z. Aminophosphines: A Double Role in the Synthesis of Colloidal Indium Phosphide Quantum Dots. *J. Am. Chem. Soc.* **2016**, *138* (18), 5923–5929.

(13) Grigel, V.; Dupont, D.; De Nolf, K.; Hens, Z.; Tessier, M. D. InAs Colloidal Quantum Dots Synthesis via Aminopnictogen Precursor Chemistry. *J. Am. Chem. Soc.* **2016**, *138* (41), 13485–13488.

(14) Liu, W.; Chang, A. Y.; Schaller, R. D.; Talapin, D. V. Colloidal InSb Nanocrystals. *J. Am.*

Chem. Soc. **2012**, *134* (50), 20258–20261.

(15) Srivastava, V.; Dunietz, E.; Kamysbayev, V.; Anderson, J. S.; Talapin, D. V. Monodisperse InAs Quantum Dots from Aminoarsine Precursors: Understanding the Role of Reducing Agent. *Chem. Mater.* **2018**, *30* (11), 3623–3627.

(16) Adam, S.; Talapin, D. V.; Borchert, H.; Lobo, A.; McGinley, C.; de Castro, A. R. B.; Haase, M.; Weller, H.; Möller, T. The Effect of Nanocrystal Surface Structure on the Luminescence Properties: Photoemission Study of HF-Etched InP Nanocrystals. *J. Chem. Phys.* **2005**, *123* (8), 084706.

(17) Zhang, H.; Jang, J.; Liu, W.; Talapin, D. V. Colloidal Nanocrystals with Inorganic Halide, Pseudohalide, and Halometallate Ligands. *ACS Nano* **2014**, *8* (7), 7359–7369.

(18) Liu, W.; Lee, J.-S.; Talapin, D. V. III–V Nanocrystals Capped with Molecular Metal Chalcogenide Ligands: High Electron Mobility and Ambipolar Photoresponse. *J. Am. Chem. Soc.* **2013**, *135* (4), 1349–1357.

CHAPTER 6 III-V Colloidal Quantum Dots Based Electronic and Optoelectronic Devices

The III-V QD family is considered as one of the promising candidates for replacing Cd and Pb containing materials in the application of electronic and optoelectronic devices.[1,2] InP has comparable bulk properties, including a bandgap energy of 1.34 eV, electron mobility ≤5400 cm^2/Vs and hole mobility ≤200 cm^2/Vs, to that of CdSe (bandgap energy of 1.74 eV, electron mobility ≤650 cm^2/Vs), and thus InP QDs hold great potentials for constructing high performance electronic devices. Bulk InSb have excellent transport properties (electron mobility ≤77000 cm^2/Vs and hole mobility ≤850 cm^2/Vs). Its smaller bandgap (0.17 eV) makes this material suitable for IR light detection, and especially when designed to have bandgap energy of 1550 nm, InSb QDs create new opportunities in the area of telecommunication.[3]The enhanced bandgap energy of InSb QDs due to quantum confinement is advantageous for reducing the device dark current by having smaller intrinsic carrier concentration n_i compared to its bulk counterpart.

However, III-V QD based electronic and optoelectronic devices are rarely reported, as their synthesis is less-established and their surface chemistry is relatively unexplored. To our knowledge, the best InP QD FET mobility reported in the literature is <0.1 cm^2/Vs and requires the use of corrosive and hazardous chemicals, such as hydrazine, and high annealing temperature (>350 °C), which is incompatible with flexible substrates.[2] While the large-scale synthesis of uniform InSb QDs is still a bottleneck,[4] more effort is needed to tailor the doping, carrier mobility and lifetime through surface modification.

In this chapter, the synthesis of tetrahedral InP QDs is described, which is expected to favor carrier transport as the facets create a larger interparticle contact area.[5] We develop solution and solid-state hybrid ligand exchange to enhance electronic coupling and manipulate doping of the QD solids. After In and Se doping and passivation processes, we achieve electron mobility~0.5 cm^2/Vs from the tetrahedral InP QD FETs. Meanwhile, we study the effect of post-

synthesis surface modification on the doping and transport properties of InSb QD solids and preliminarily explore their photoresponse at 1550 nm.

6.1 Synthesis of Tetrahedral InP QDs

There have been a number of approaches to synthesize InP QDs since the discovery of the dehalosilylation reaction between indium halide and tris(trimethylsilyl)-phosphine ($P(SiMe_3)_3$ or $(TMS)_3P$) in the 1990s.[6] An important leap forward was made by the Peng group, when 1-octadecene (ODE) was first used as the non-coordinating solvent and fatty acids were introduced as stabilizing ligands.[7] Following this work, the same group further reduced the reaction temperature by introducing short chain primary amines, such as octylamine, together with the injection of the phosphine precursor. They found the oxide formation is thus greatly avoided during particle growth without using elevated temperatures >250 °C. Another benefit of this approach is it yields larger QDs with the first excitonic absorption peak at >700 nm; without amine addition the absorption resonance only reaches ~600 nm.[8] Several subsequent studies revealed the role of the primary amine in destabilizing and preventing the formation of magic-sized clusters, allowing the homogeneous growth of InP QDs at lower temperatures.[9,10] We adopt this recipe to synthesize large-sized InP QDs in order to reduce the number of interfaces along the transport path and achieve superior carrier transport across the QD film.

In a typical synthesis [Figure 6.1a], indium acetate (0.8 mmol), myristic acid (MA) (3.08 mmol) and ODE (10 mL) are loaded in a three-neck flask and quickly heated up under nitrogen flow. Upon reaching the reaction temperature, $(TMS)_3P$ (130-160 μL), 1-octylamine (0.5 mL) and ODE (1 mL), pre-mixed in a glovebox, are swiftly injected into the flask. The reaction temperature drops by ~10 °C and the color of the reaction changes immediately. After grow the QDs for 30 min at 200 °C, the solution is quenched using a water bath and transferred into a glovebox without air exposure for purification. 4 mL of acetone is slowly added to the crude reaction to

precipitate the QDs and it is centrifuged at 8000 r.p.m. for 5 min. After discarding the supernatant, we add toluene to redisperse the QDs at a concentration of 15 mg/mL.

Based on the same route described above but with different reaction temperatures, we obtain InP QDs with three different shapes as shown in the TEM images in Figure 6.1b to d. When the reaction temperature is lower than 190 °C, large particles are formed with branched morphology [Figure 6.1b] and the dispersion of these “flower”-like particles lacks long-term stability. However, if the reaction temperature is higher than 210 °C, the particles are smaller and their shape becomes spherical [Figure 6.1d]. In between these two cases, at a reaction temperature as high as 200 °C, tetrahedral-shaped InP QDs are generated. A similar trend in particle size and shape with growth temperature has been reported in the zinc blende CdSe QD systems as well.[11] Due to the different activation energies of atom adsorption/ligand desorption on distinct crystal facets, there exists a preferential direction for particle growth at different temperatures. If the temperature is high enough such that the thermal energy provided is higher than the activation energy of all facets, then the QDs grow isotropically into spheres. Intermediate reaction temperatures, however, are only sufficient to activate the atom growth on {100} facets, leading to the disappearance of these facets and formation of tetrahedral InP QDs terminated by the {111} facets in the final product. At even lower temperature, growth is dominated by kinetics with branch and arm growth only along certain directions that has less steric hindrance.

Besides the evolution in particle morphology, the particle size also decreases as reaction temperature increases. This is explained by the LaMer model as high precursor-to-monomer conversion rate at increased temperatures provides more nuclei initially and gives rise to smaller QD diameters.[12]

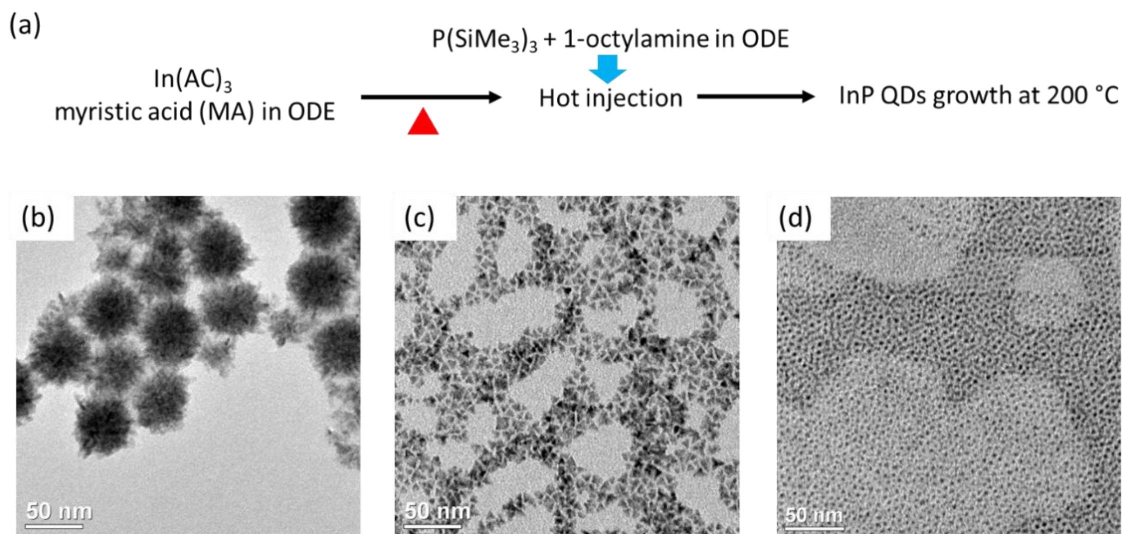

Figure 6.1 (a) Reaction scheme of InP QD synthesis. TEM images of (b) branched (c) tetrahedral and (d) spherical InP QDs achieved at 190 °C, 200 °C and 210 °C, respectively.

The size and shape dispersity of the final QD products is also affected by the concentration of $(TMS)_3P$ and growth time. We keep the reaction temperature at 200 °C and other parameters constant but only vary the amount of $(TMS)_3P$ from 130 to 140, 150 and 160 μL. The QD products all have tetrahedral shape but become more clearly defined and decrease in size as the amount of $(TMS)_3P$ increases based on TEM images shown in Figure 6.2a to d. The extracted edge length is 14.6±0.8, 12.3±0.8, 9.9±0.6 and 7.9±0.3 nm corresponding to 120, 130, 140, 150 and 160 μL of $(TMS)_3P$, respectively. The UV-Vis absorption spectra develop an excitonic peak at around 710 nm as higher $(TMS)_3P$ concentrations are used [Figure 6.2e]. Quantum confinement effects increase as the particle size decreases to approach the exciton Bohr radius of InP (10 nm). The size distribution also decreases and is reflected in the narrower width of the absorption peak. This correlation between P precursor concentration and particle size is consistent with the LaMer model, as high concentrations of precursors creates more monomers and results in smaller and more uniform particles.[12]

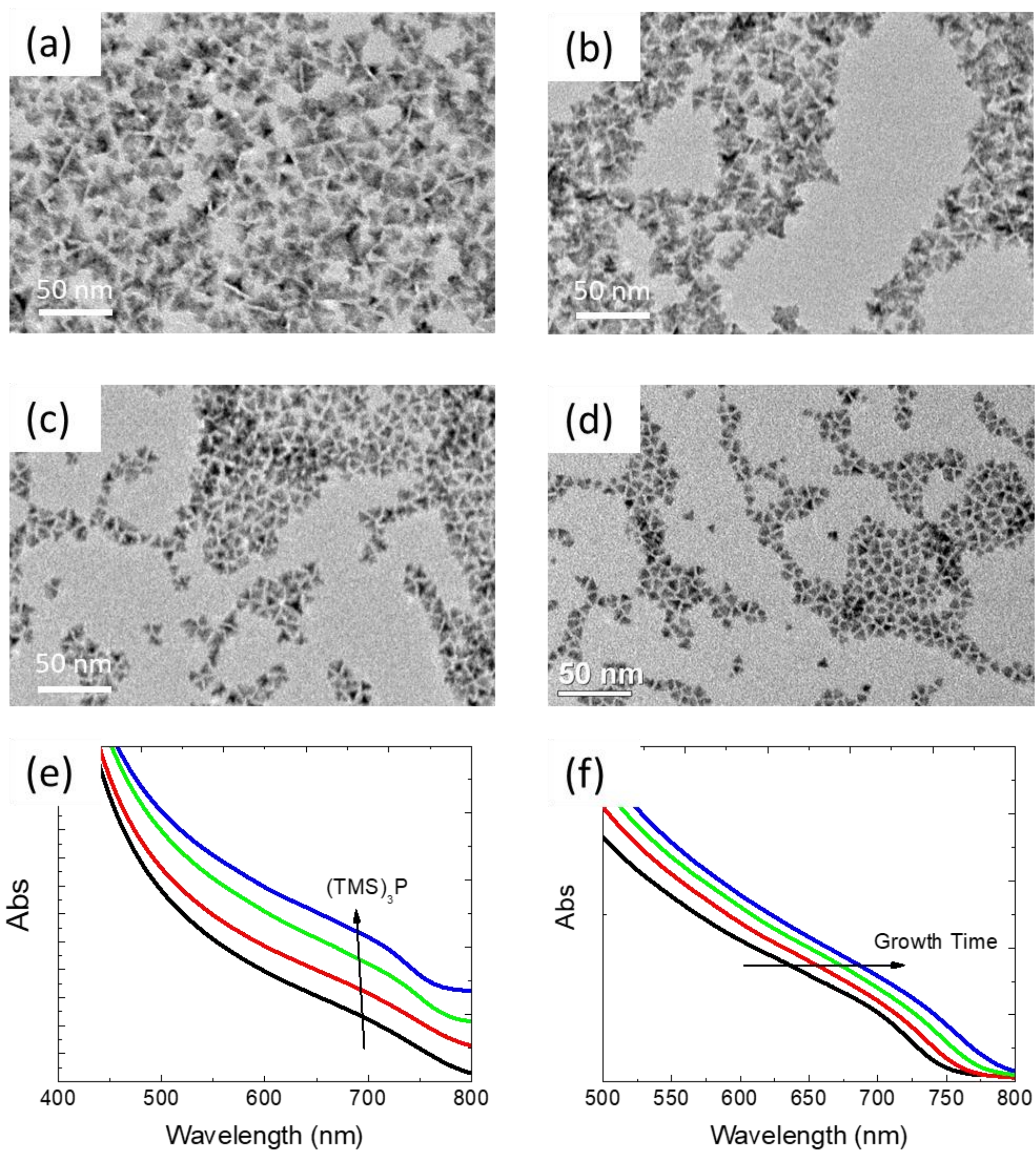

Figure 6.2 (a) to (d) TEM images and (e) absorption spectra of InP QDs made with 130 (black), 140 (red), 150 (green), and 160 μL (blue) of $(TMS)_3P$, respectively. (f) UV-Vis absorption of InP QDs synthesized at 200 °C with 160 μL of $(TMS)_3P$, but different growth times ranging from 10 (black) to 20 (red), 30 (green) and 60 (blue) min.

Figure 6.2f shows that the absorption peak of InP QDs made using 160 μL of $(TMS)_3P$ red shifts with growth time from 10 min to 60 min. The peak broadens with growth time, which may be indicative of reduction in QD dispersity owing to the Ostwald ripening process. The yield of the product is also reduced after longer reaction time. Based on above results, we choose to inject 160 μL of $(TMS)_3P$ at 200 °C and grow for 30 min as the standard parameters used to synthesize tetrahedral InP QDs.

Photoluminescence (PL) spectra of tetrahedral InP QD dispersions are measured and shown in Figure 6.3. Straight out of a standard synthesis pot, the InP QDs are stabilized by MA and are weak emitters [Figure 6.3a], indicating non-radiative recombination prevails due to poor surface passivation. With the same batch of material, we add a 0.1 mL of oleic acid (OA) and observe a significant increase in PL [Figure 6.3b], suggesting that OA ligands more efficiently passivate dangling bonds and suppresses non-radiative recombination. Nevertheless, the PL almost vanishes after 30 min of air exposure even with OA [Figure 6.3b dashed curve]. We also test the effect of introducing trioctylphosphine (TOP) into the QD dispersion [Figure 6.3c]. It shows enhanced PL, but lower than that for OA ligands, and higher air-stability than both MA and OA. For the purpose of carrier transport, devices made with QDs originally capped by these three organic ligands show no significant difference.

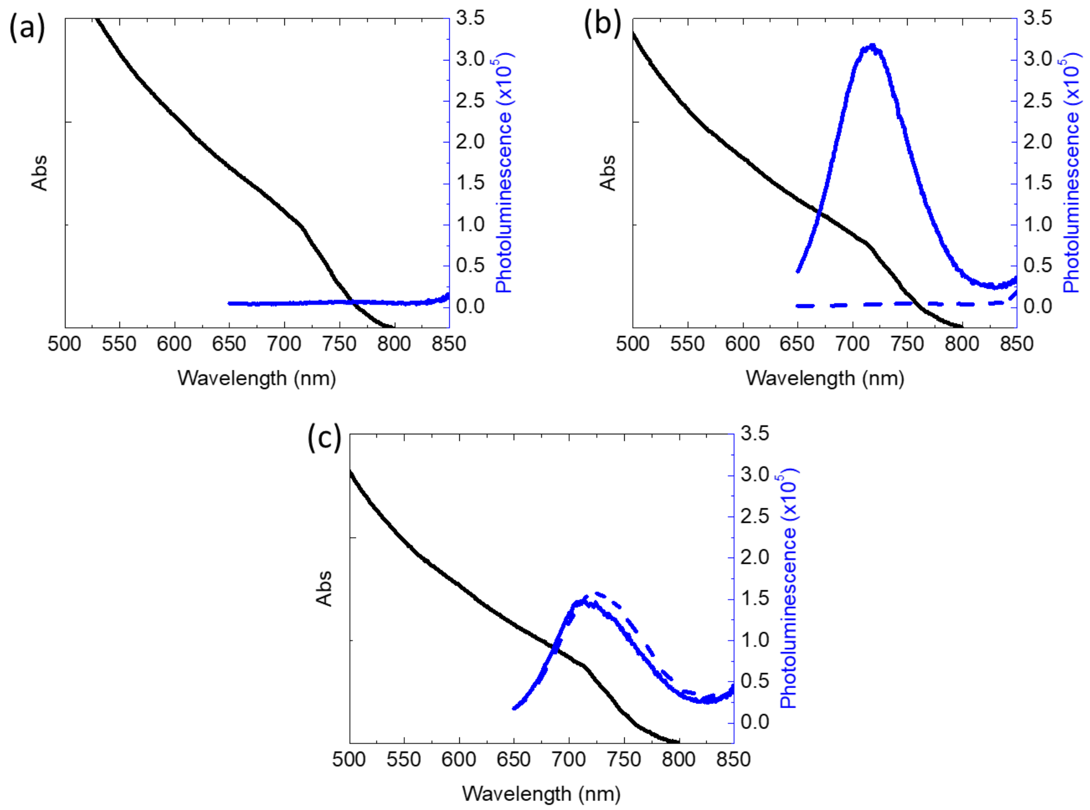

Figure 6.3 Absorption (black) and PL (blue) spectra of tetrahedral InP QD dispersions with (a) MA, (b) OA and (c) TOP as ligands. Dashed line: same sample remeasured after air exposure for 30 min.

6.2 Solid-State and Solution Ligand Exchange of InP QDs

To enhance the electronic coupling between neighboring InP QDs and promote carrier transport across the QD thin films, a ligand exchange process is necessary to replace the insulating organic ligands with more compact molecules. We screen a variety of ligands commonly employed in solid-state ligand exchange process used to construct II-V and IV-VI QD devices. The following procedures are all done in a nitrogen filled glovebox unless otherwise noted. Briefly, the InP QD dispersion (15 mg/mL in toluene) is spin cast onto device-grade Si wafers and immersed in the following ligand solutions: Na_2S (50 mM in methanol), NaHS (50 mM in methanol), NH_4SCN (50 mM in methanol), tetrabutylammonium iodide (TBAI, 30 M in methanol), NH_4Cl (50 mM in methanol), NaN_3 (50 mM in methanol), and 3-mercaptopropionic acid (MPA, 1% vol% in methanol) for 10s followed by three times of pristine methanol flushing. Two or three such QD layers are usually built to form a continuous QD film of thickness ~50 nm. In/Au (40 nm/40 nm) is thermally evaporated to define the source of drain electrodes of FETs with 100 μm channel lengths and a channel width to channel length ratio of 15. All devices are annealed at 300 °C for 10 min before current-voltage measurements.

Figure 6.4a stacks all the I_D-V_G characteristics of InP QD FETs after different solid-state ligand treatments. Among them, Na_2S and NaHS treatment yield the highest currents and electron mobility, although all devices except the TBAI treated one show n-type behavior. Three ligands, Na_2S, NH_4Cl and NaN_3, are selected for further FTIR study. By calculating the remaining area under the C-H stretch in Figure 6.4b, we conclude that Na_2S is the most effective in removing the organic ligands used in synthesis, which is consistent with the high currents in their FET device characteristics. Figure 6.4c shows the absorption peak slightly red shifts and broadens after the Na_2S ligand exchange and further annealing at 300 °C, also indicating improved interdot coupling. From TEM images [Figure 6.4d], we indeed observe touching and even partial fusion of the tetrahedral InP QDs. There are two possible reasons for the n-type

behavior: 1) non-stoichiometry, as excess In serves as n-dopants, similar to the report of n-type doping in lead chalcogenide QDs via metal enrichment,[13,14] and 2) doping by sulfur, a low lying donor in bulk InP. Energy-dispersive X-ray spectroscopy (EDS) measurement is performed and listed in Table 6.1. We notice the In to P ratio decreases after the ligand exchange and speculate that some surface In atoms are removed by free S^{2-} with the assistance of the protic methanol solvent environment, which has been reported in CdSe QD systems previously in our group.[12] Since the In ratio does not increase after the solid-state Na_2S treatment, the n-type doping is more likely a result of sulfur incorporation, which is also detected by the EDS measurement. Therefore, S^{2-} serves two roles, both as a ligand and a dopant.

Akin to solution-phase Na_2S ligand exchange of InAs QDs, described in Chapter 5, this same solution-exchange is achievable for the InP QD system as well. As described in Chapter 5 Figure 5.4a, the successful ligand exchange switches the polarity of the InP QD surface resulting in the dispersion of S^{2-}-capped InP QDs in polar solvents such as DMF. EDS results indicate that less In is lost and more S is attached to the QD surface using solution ligand exchange in comparison to its solid-state counterpart [Table 6.1]. Therefore, we expect a higher doping concentration in the solution-exchanged InP QD film. Figure 6.5a compares the I_D-V_G characteristics of InP QD FETs processed using the solid and solution phase ligand exchange. The solution-exchanged sample shows higher currents and negatively shifted threshold voltage from 34.1 to 14.1 V. This observation is consistent with higher electron concentration in the channel layer after the solution ligand exchange. Both the on- and off-state currents increase, giving rise to higher saturation electron mobility (from 0.04 to 0.27 cm^2/Vs), but less gate-modulation of the device. This is due to over-doping of sulfur introduced during the solution ligand exchange, undesirable for switching function of FETs. To solve this problem, an additional treatment that can bring down the doping level without hindering carrier transport needs to be introduced.

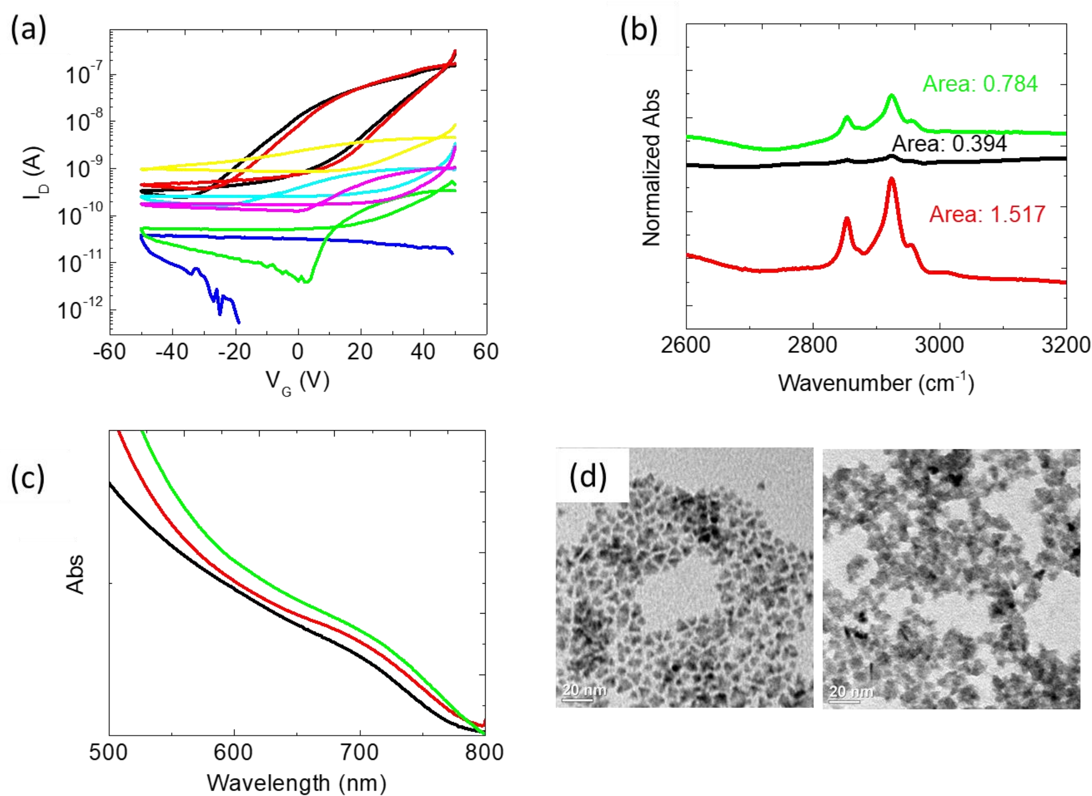

Figure 6.4 Solid-state ligand exchange of InP QDs. (a) I_D-V_G characteristics (V_D=50 V) of InP QD FETs with Na_2S (black), NaHS (red), NH_4SCN (green), TBAI (blue), NH_4Cl (cyan), NaN_3 (purple) and MPA (yellow) solid-state ligand exchange. (b) FTIR spectra of InP QDs with Na_2S (black), NaN_3 (red) and NH_4Cl (green) treatment normalized to the film thickness. The area under C-H stretch is integrated for every treatment. (c) UV-Vis absorption spectra of InP QD film as made (black), after Na_2S ligand exchange (red) and after Na_2S ligand exchange and being annealed at 300 °C for 10 min (green). (d) TEM images of InP QDs before (left) and after (right) the solid-state Na_2S ligand exchange.

Table 6.1 EDS result of InP QDs as synthesized, with Na_2S treatment in the solid-state or solution phase

	In	P	S
InP-MA	1	1.11±0.05	
InP-Na_2S (solid)	1	1.17±0.01	0.37±0.01
InP-Na_2S (solution)	1	1.11±0.04	0.41±0.03

Following the idea of hybrid ligand exchange described in Chapter 5, we perform a solid-state ligand exchange treatment on the solution-exchanged InP QD film. In the example of NH_4Cl hybrid-exchanged device, the off-state current increases leading to even lower on/off ratios and carrier mobilities [Figure 6.5b, green and Table 6.2]. However, after the extra Na_2S or NaN_3 treatment, both the on- and off-state currents decrease, but the on/off ratio increases [Figure 6.5b, red and blue and Table 6.2], indicating reduced doping concentrations. Meanwhile, the mobility also slightly decreases compared to the Na_2S solution-exchanged only case. This trend is predictable from the effect of solid-state ligand exchange on the stoichiometry of the QD films [Table 6.1]. The lower In and S content detected in the solid-exchanged InP QD films suggests that the solid-state Na_2S treatment tends to remove surface In atoms and is unlikely to add more S compared to the solution exchange process. Therefore, a subsequent solid-state ligand treatment can reduce the doping effect introduced by the solution ligand exchange.

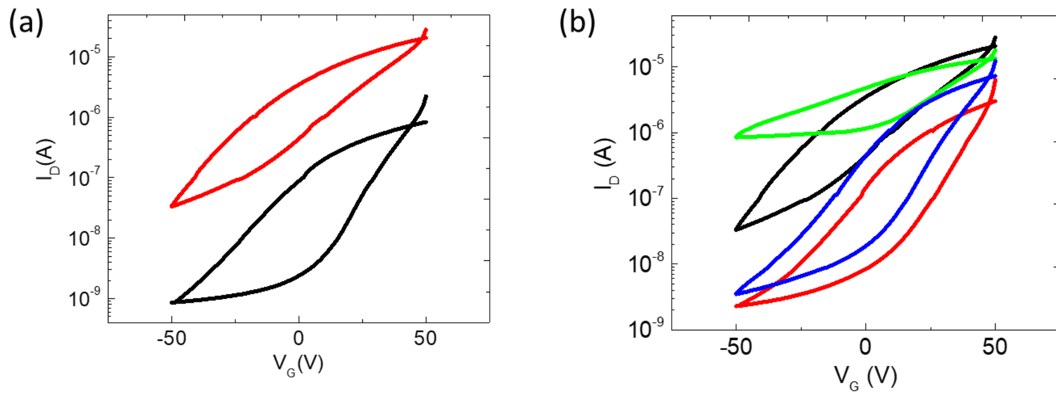

Figure 6.5 I_D-V_G characteristics of InP QD FETs (V_D=50 V) (a) with Na_2S solid-state (black) and solution (red) ligand exchange, (b) with Na_2S solution exchange only (black), and solution and solid-state Na_2S (red), NaN_3 (blue) and NH_4Cl (green) ligand treatment.

Table 6.2 Electron mobility and on/off ratio of the FET devices operated in the saturation regime

	Solution ex only	**Na_2S solid ex**	**NH_4Cl solid ex**	**NaN_3 solid ex**
μ (cm^2/V s)	0.27 ±0.01	0.16 ±0.06	0.11±0.01	0.22±0.02
on/off	$<10^3$	$\sim10^3$	~10	$\sim10^3$

6.3 Doping of InP QD Films for FETs

Doping of InP QD films can also be realized through thermal evaporation and diffusion of elemental metals, such as In, Sn and Se.

A facile and effective way of introducing In is developed by our group for doping CdSe QD thin film FETs.[15] Similarly, we deposit In/Au as the top contact of the InP QD device. As the device is being annealed at elevated temperatures, In diffuses into channel from the contact,

possibly forming shell-like structures around QD arrays and donating electrons. To compare the effect of different metal contacts, we fabricate identical InP QD devices with Au, Ag, Al and In/Au electrodes, respectively. The QD thin film shows the highest currents and mobility and the smallest threshold voltage when in contact with In/Au electrodes. This is owing to the diffusion doping of In as well as improved carrier injection by reducing/removing the Schottky contact barrier at the InP QD/In interface.

In bulk InP, Sn and Se are found to be donors. Here, we introduce Sn and Se atoms by direct thermal evaporation on the device channel and study their doping effects. Upon deposition of 5 Å of Sn, the InP QD FET shows high currents and little gate modulation (~10) with electron mobility increased from 0.03 to 0.14 cm^2/Vs, indicating heavy n-doping [Figure 6.6b, red]. After annealing at 150 °C for 10 min, the device characteristics, instead show a lowering of the currents as well as electron mobility (0.05 cm^2/Vs). Therefore, thermally deposited Sn is able to n-dope the InP QD films, but the doping concentration is hard to control, and annealing reduces the doping effect.

We also deposit a thin film of Se (2 nm) onto the channel of InP QD FETs. Unlike the Sn doping discussed above, the device with a thin Se overlayer needs to be "activated" at 300 °C first to enable carrier transport. There are two different trends observed after the Se doping depending on the metal contact. Figure 6.6c and d show the device characteristics with Au and In/Au as source and drain electrodes, respectively. When Au alone is used, after the Se doping, the off-state current further decreases while the on-state current almost stays constant, leading to higher on/off ratio and slight increase of electron mobility (from 0.03 to 0.04 cm^2/Vs) [Figure 6.6c]. However, both currents are increased and on/off ratio is maintained by the Se doping in the device that has In/Au top contacts [Figure 6.6d]. The mobility has a more prominent improvement in this case from 0.04 to 0.11 cm^2/Vs. The only difference between the two device structures is the additional In source in the In/Au electrode, which provides In atoms to the InP QDs in the

channel region through thermal diffusion. Hypothetically, the more In-rich the QD, the more available surface sites for Se atoms to attach to. Thus, the same amount of Se deposited possibly forms a larger number of effective In-Se bonds when In/Au is used as electrodes, giving rise to higher electron concentration.

Based on the above findings, we develop the optimal condition for fabrication of high performance InP QD FETs. Firstly, the tetrahedral InP QDs (15 mg/ mL in toluene) are ligand exchanged with Na_2S (15 mg/mL in FA) in the solution phase with a volume ratio of 1:0.3 and spin coated on device-grade wafers (see Chapter 5 for detailed description). We apply a solid-state chemical treatment with Na_2S or NaN_3 (5 mM in methanol for 10 s) on the InP QD thin film with three times of methanol washing. Two of such layers are fabricated prior to deposition of In/Au (40 nm/40 nm) as the top source and drain electrode. Lastly, 2 nm of Se is thermally deposited onto the InP QD FET channel followed by an annealing process at 300 °C for 10 min. The mobility of five FET devices with either the Na_2S or NaN_3 treatment before and after the Se doping as well as the champion performance among them are summarized in Figure 6.7a. Both ligand exchange approaches render similar high electron mobility reaching ~0.5 cm^2/Vs, which exceeds the literature reported values of InP QD FETs to date.[2] The I_D-V_G characteristics of two champion devices are shown in Figure 6.7b, where NaN_3 treated device shows not only high mobility but also favorable gate modulation.

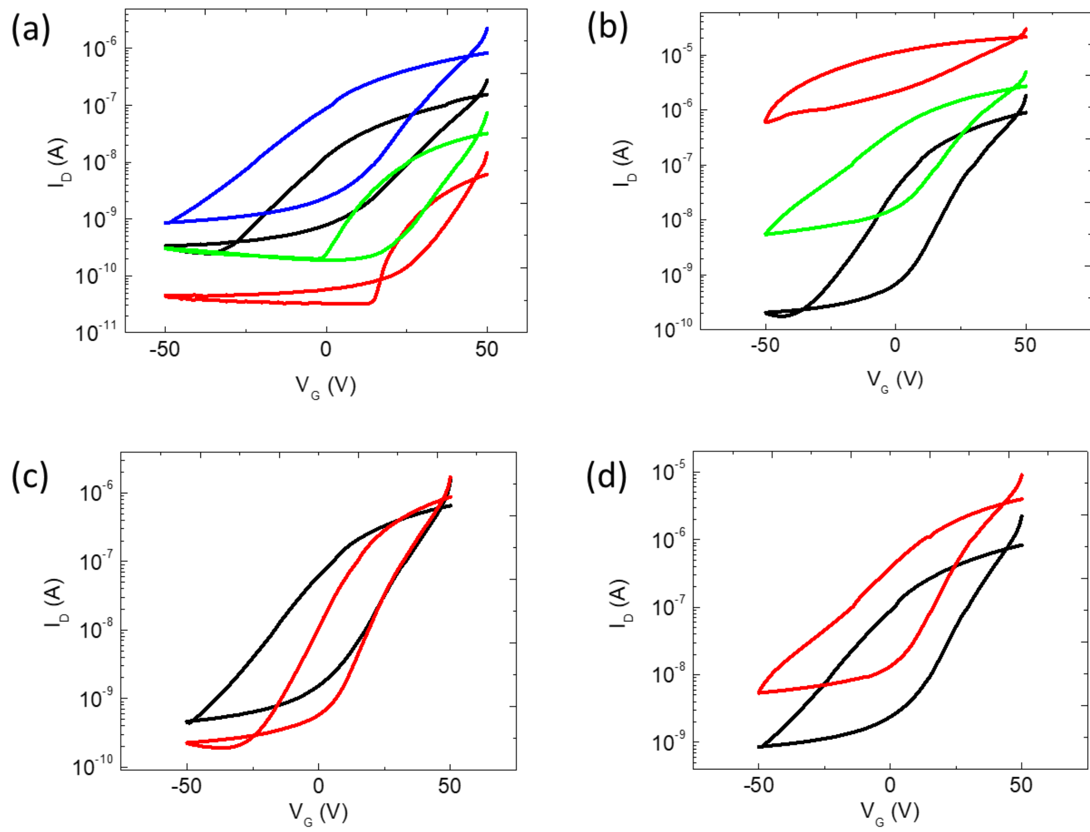

Figure 6.6 I_D-V_G characteristics of InP QD FETs (V_D=50 V) (a) with Au (black), Al (red), Ag (green) and In/Au (blue) top contacts, (b) without (black) and with (red) 5 Å of Sn deposited and annealed at 150 °C for 10 min (green), (c) with Au (d) with In/Au electrodes before (black) and after (red) 2-nm Se doping and annealing at 300 °C for 10 min.

(a)

μ ($cm^2/V\ s$)	Na_2S solution ex. Na_2S solid ex.	Na_2S solution ex. NaN_3 solid ex
No Se	0.16±0.06	0.21±0.02
2 nm of Se	0.45±0.07	0.42±0.06
Champion device	0.55 (sat) 0.22 (lin) I_{on}/I_{off}~10^3	0.49(sat) 0.21(lin) I_{on}/I_{off}~10^3-10^4

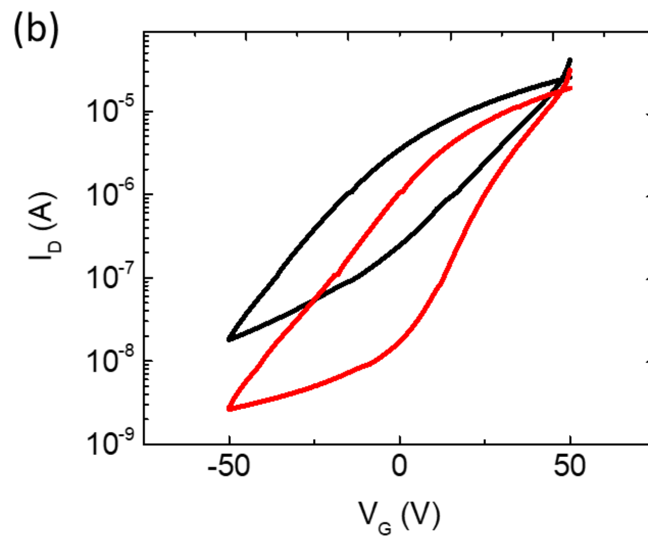

Figure 6.7 (a) Statistics and champion performance of InP QD FETs with Na_2S solution exchange and Na_2S or NaN_3 solid-state ligand treatments. (b) I_D-V_G characteristics (V_D=50 V) of champion FETs with Na_2S solution exchange and Na_2S (black) or NaN_3 (red) solid-state treatment.

6.4 Surface Modification and Optoelectronic Properties of InSb and $InAs_xSb_{1-x}$ QD films

Narrow bandgap III-V semiconductors, such as InSb and $InAs_xSb_{1-x}$, are potential candidate materials for IR photodetection. We exploit different surface modification processes to tailor the carrier transport and doping concentration of InSb QDs. InSb QDs are synthesized by modifying an existing recipe.[3] $InCl_3$ and $Sb[N(Si(Me)_3)_2]_3$ are dissolved in oleylamine instead of TOP used in the literature. The mixture is then heated up to 260 °C at 3 °C/min under nitrogen flow in the presence of superhydride. After being kept at 260 °C for 30 min, the reaction is cooled by air. During the cooling down, TOP:$InCl_3$ (1 M) solution prepared in a glovebox beforehand is injected to restore the stoichiometry and stabilize the QD surface. For the application in telecommunication, the 1st exciton absorption peak of InSb QDs is designed to be at 1550 nm by tuning the QD size.

We study the effect of different ligand exchange treatments, including Na_2S, MPA, TBAI, NH_4SCN, on carrier transport properties of InSb QD films. Based on the FET results [Figure 6.8a], all above ligand chemistries lead to p-type device behavior. Na_2S or NH_4SCN give rise to higher hole mobility (~10^{-3} cm^2/Vs) than that of MPA or TBAI treated devices (~10^{-4} cm^2/Vs). NH_4SCN exchange has a larger >10^2 current modulation, than the <10 on-off ratio after the Na_2S treatment, suggesting a lower level of p-doping. We measure the stoichiometry of InSb QDs altered by the ligand exchange. Consistent with their FET characteristics, TBAI treated films have the highest In to Sb ratio (47:53) or lowest free hole concentration, while MPA or Na_2S treated ones have slightly lower (46:54) In content and show more p-type characteristics, indicating that less In is removed during the TBAI ligand exchange process.

The doping concentration of InSb QD films is further controlled by post-synthesis surface modification, which simultaneously affects the surface stoichiometry and introduces dopants. Due to the Sb-terminated surface (In:Sb=47:53), the as synthesized InSb QDs tend to exhibit p-type characteristics when forming thin films. Indium salts enrich the system with In and sulfide

containing molecules offer donors to the QDs, so that both treatments are expected to compensate p-doping. We utilize InI_3, $InCl_3$, EDT, Na_2S and their combinations during the solid-state ligand exchange step to modify the doping concentration of InSb QD films [Figure 6.8b]. For example, when InI_3 instead of TBAI is used to treat the QD film, a negatively-shifted threshold voltage (V_T) is observed. For a predominantly p-type device, this means it becomes more difficult to induce holes in the channel by applying gate bias as the fermi level is further away from the valence band edge before any gate voltage is applied, i.e. the material is intrinsically less p-type. Following the trend, when we further apply an EDT treatment on the InI_3-treated film, a more negative V_T is measured, indicating the thiol groups are attached to the In sites and donate additional electrons to reduce free hole concentration in the system. The sequential treatment of Na_2S and InI_3 is proven to be more effective in n-doping the InSb QD films, as the V_T continuously shifts towards negative, and its FET device I_D-V_G curve starts to show the on-state current when electrons can be accumulated in the channel under positive gate bias. Hypothetically, since the QD surface is covered by Sb and S^{2-} after the Na_2S ligand exchange, more anion sites are available for In^{3+} during the following InI_3 treatment, resulting in a higher In:Sb ratio. We also demonstrate an example of n-type InSb QD FET by soaking the Na_2S treated film into a TOP:$InCl_3$ solution at 100 °C for overnight. Owing to the weaker bonds between TOP and In^{3+} than In-S and In-Sb, it is more thermodynamically favorable to grow shells of In atoms outside the InSb-S^{2-} QDs during the TOP:$InCl_3$ treatment. The mobility and V_T yielded by different surface treatments are summarized in Figure 6.8c assorted from p-type to n-type (left to right). We successfully switch the majority carrier of InSb QD films from holes with mobility ~10^{-3} cm^2/Vs to electrons with mobility ~10^{-4} cm^2/Vs, providing more freedom for designing complicated device architectures.

(c)

	Na_2S (10 mM)	TBAI	InI_3	InI_3-EDT	Na_2S-InI_3	Na_2S-TOP:In
μ_{FET} (cm^2/V s)	1.6×10^{-3}	1.3×10^{-3}	2.9×10^{-3}	2.5×10^{-4}	1.0×10^{-3}	4.4×10^{-4}
V_T (V)	-8.5	-16	-23.5	-24.0	-27.3	14.4

p-type → n-type

(d)

(e)

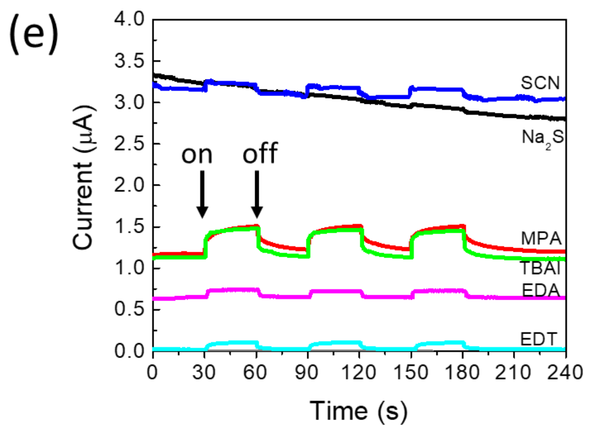

Figure 6.8 I_D-V_G characteristics of InSb QD FETs (a) with Na_2S (black), MPA (red), TBAI (green) and NH_4SCN (blue) solid-state ligand exchange, (b) with InI_3 (dark blue), InI_3-EDT (light blue), Na_2S-InI_3 (light purple) and Na_2S-TOP:$InCl_3$ (dark purple). (c) Electron mobility and V_T of InSb QD FET devices after different solid-state treatments with p-type to n-type doping from left to right. (d) Photos and schematics and (e) photoconductivity measurements (V=10 V) of InSb QD photoconductors with varying ligands.

To study the optoelectronic property at 1550 nm, we fabricate InSb QD photoconductors with a variety of commonly used ligands, including Na_2S, TBAI, NH_4SCN, MPA, EDT, and ethylenediamine (EDA) on the interdigitated Au electrodes prepared by photolithography with a 10-μm spacing [Figure 6.8d]. The I-V characteristics are obtained with and without 1550 nm laser illumination under an electrical filed of 10^6 V/m [Figure 6.8e]. InSb QD films treated by Na_2S shows the highest currents both in the dark and under illumination, consistent with its higher hole mobility in FETs, but the photoresponse of the device is low as seen by the low photo gain (I_{light}/I_{dark}). NH_4SCN treated films show a similar current level and a better photoresponse than Na_2S treated devices, also consistent with the lower p-doping level suggested by the FET characteristics. Compared to EDT and EDA treated samples that have low dark and light currents, the ones treated by TBAI and MPA have relatively high currents under illumination but low dark current. Notably, TBAI treated films show faster response time than the MPA samples, which is more promising as a candidate photodetector material. Based on the photocurrent, we calculate the responsivity of the TBAI treated photoconductor to be $R_{1.55\ \mu m}=3.4\times10^{-3}$ A/W and an external quantum efficiency to be $EQE_{1.55\ \mu m}=2.7\times10^{-3}$.

We build InSb QD heterojunction photodiodes with the structure shown in Figure 6.9a. The 25-nm ZnO layer is made on ITO/glass substrates using a sol-gel method described in the literature.[16] $AlCl_3$ is added during preparation of the sol to ensure high carrier concentration and high mobility of ZnO by Al doping and Cl passivation, respectively. InSb QD layers are fabricated by repeatedly (x8) depositing QDs (15 mg/mL) with different solid-state ligand exchange reagents, including Na_2S, EDT and NH_4Cl. We thermally evaporate 12 nm of MoO_3 and 65 nm of Au on top of the InSb QD layer to form the hole transporting layer and top contact, respectively. To measure the photoresponse of these diode devices, we couple 1550 nm wavelength laser light into a probe station mounted inside a nitrogen filled glovebox to illuminate the sample from the bottom ITO side with a mirror [Figure 6.9b].

The photoresponse of these diodes to 1550 nm illumination is measured at 0 V bias [Figure 6.9c]. For devices made of the same batch of InSb QDs, the current level follows NH_4Cl>EDT>Na_2S both in the dark and under illumination, while the EDT treated device shows the highest on/off ratio of 4.2. We also preliminarily explore the photoresponse of $InAs_{0.5}Sb_{0.5}$ QDs. Treated by Na_2S, the film possesses photocurrent above μA and on/off ratio of 4.4. The I-V characteristics of the EDT treated $InAs_{0.5}Sb_{0.5}$ QD device is shown in Figure 6.9d. Due to the large leakage current, it is difficult to distinguish photocurrent from dark current at any other bias than 0 V. The responsivity as a function of reverse bias is calculated based on the illumination intensity of 3.5 mW [Figure 6.9d inset].

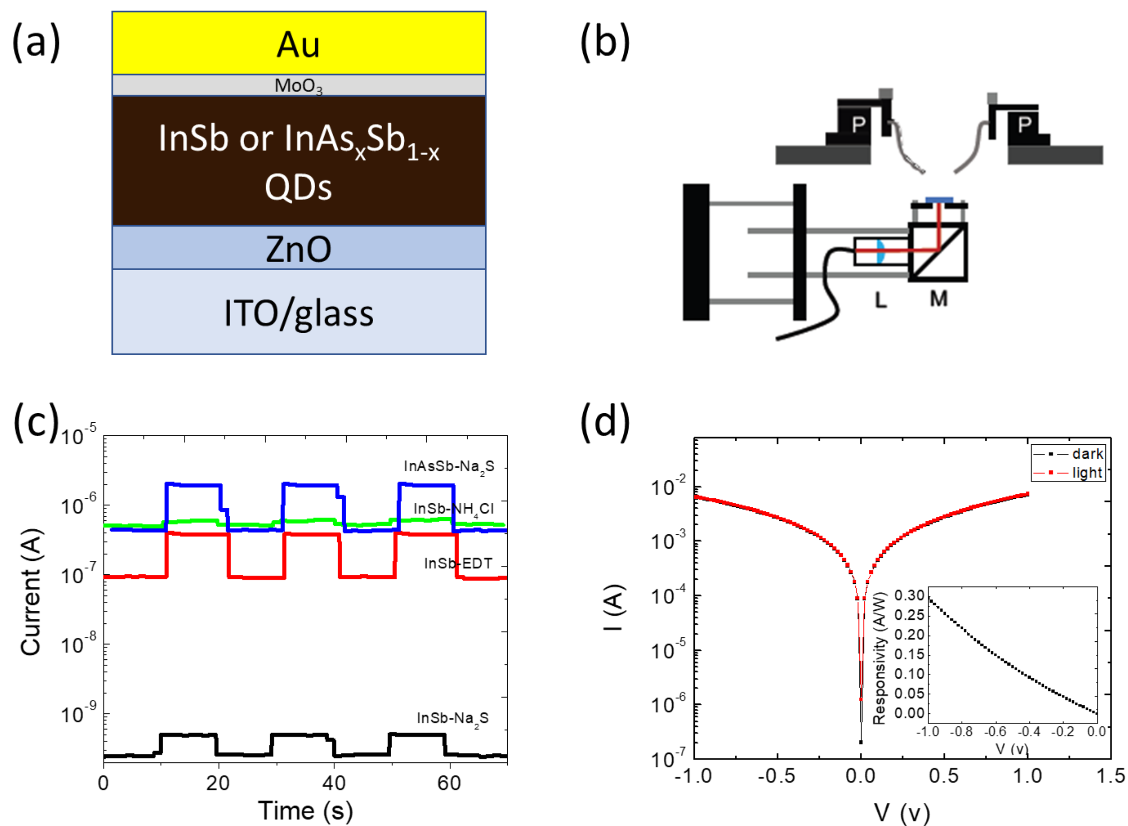

Figure 6.9 Schematics of (a) device structure and (b) I-V measurement setup for InSb and $InAs_xSb_{1-x}$ QD photodiodes. (c) Photoresponse at 1550 nm illumination of InSb and $InAs_xSb_{1-x}$ QD photodiodes with different ligand treatments at 0 V. (d) Representative I-V characteristics of Na_2S treated $InAs_xSb_{1-x}$ QD photodiodes in the dark (black) and under 1550 nm illumination (red). Inset: responsivity calculated based on the photocurrent.

6.5 Conclusions

III-V QDs hold promise for constructing high performance electronic and optoelectronic devices. We study InP QDs, as a wider bandgap semiconductor, from synthesis to ligand exchange chemistry for FET applications. By carefully controlling the reaction temperature, precursor concentration and reaction time, we synthesize large-sized InP QDs in tetrahedral shape, advantageous for carrier transport. Na_2S solution ligand exchange hybridized with Na_2S or NaN_3 solid-state treatment is developed for InP QDs to enhance electronic coupling and provide dopants. The In contact diffusion and Se doping process are discovered to further improve carrier mobility to ~0.5 cm^2/Vs without sacrificing the on/off ratio (>10^3). Since there is no corrosive chemicals or high temperature steps involved, this process is applicable for plastic substrates in making InP QD based flexible circuits. On the other hand, we explore the feasibility of III-V QD based IR photodetectors using InSb and its alloy QDs with absorption peak near 1550 nm. Through different ligand exchange and post-synthesis surface treatments, the carrier type, concentration and mobility of InSb QD solids can be manipulated. We demonstrate the transition from p-type to n-type on the InSb QD FET platform. To study the photoresponse at 1550 nm, we fabricate photoconductors and photodiodes based on InSb and $InAs_xSb_{1-x}$ QDs. Moving forward, more investigation is needed to correlate the defects/impurities in the III-V QD systems and material properties in order to further improve device performance.

6.6 References

(1) Song, J. H.; Choi, H.; Pham, H. T.; Jeong, S. *Nat. Commun.* **2018**, *9* (1), 4267.

(2) Liu, W.; Lee, J.-S.; Talapin, D. V. *J. Am. Chem. Soc.* **2013**, *135* (4), 1349–1357.

(3) Liu, W.; Chang, A. Y.; Schaller, R. D.; Talapin, D. V. *J. Am. Chem. Soc.* **2012**, *134* (50), 20258–20261.

(4) Yarema, M.; Kovalenko, M. V. *Chem. Mater.* **2013**, *25* (9), 1788–1792.

(5) Koh, W.; Saudari, S. R.; Fafarman, A. T.; Kagan, C. R.; Murray, C. B. *Nano Lett.* **2011**, *11* (11), 4764–4767.

(6) Tamang, S.; Lincheneau, C.; Hermans, Y.; Jeong, S.; Reiss, P. *Chem. Mater.* **2016**, *28* (8), 2491–2506.

(7) Battaglia, D.; Peng, X. *Nano Lett.* **2002**, *2* (9), 1027–1030.

(8) Xie, R.; Battaglia, D.; Peng, X. *J. AM. CHEM. SOC* **2007**, *129*, 39.

(9) Gary, D. C.; Terban, M. W.; Billinge, S. J. L.; Cossairt, B. M. *Chem. Mater.* **2015**, *27* (4), 1432–1441.

(10) Allen, P. M.; Walker, B. J.; Bawendi, M. G. *Angew. Chemie Int. Ed.* **2010**, *49* (4), 760–762.

(11) Liu, L.; Zhuang, Z.; Xie, T.; Wang, Y.-G.; Li, J.; Peng, Q.; Li, Y. *J. Am. Chem. Soc.* **2009**, *131* (45), 16423–16429.

(12) LaMer, V. K.; Dinegar, R. H. *J. Am. Chem. Soc.* **1950**, *72* (11), 4847–4854.

(13) Kim, D.; Kim, D. H.; Lee, J. H.; Grossman, J. C. *Phys. Rev. Lett.* **2013**, *110* (19), 1–5.

(14) Oh, S. J.; Berry, N. E.; Choi, J.-H.; Gaulding, E. A.; Paik, T.; Hong, S.-H.; Murray, C. B.; Kagan, C. R. *ACS Nano* **2013**, *7* (3), 2413–2421.

(15) Choi, J. H.; Oh, S. J.; Lai, Y.; Kim, D. K.; Zhao, T.; Fafarman, A. T.; Diroll, B. T.; Murray, C. B.; Kagan, C. R. *ACS Nano* **2013**, *7* (9), 8275–8283.

(16) Choi, J.; Jo, J. W.; de Arquer, F. P. G.; Zhao, Y.-B.; Sun, B.; Kim, J.; Choi, M.-J.; Baek, S.-W.; Proppe, A. H.; Seifitokaldani, A.; Nam, D.-H.; Li, P.; Ouellette, O.; Kim, Y.; Voznyy, O.; Hoogland, S.; Kelley, S. O.; Lu, Z.-H.; Sargent, E. H. *Adv. Mater.* **2018**, *30* (29), 1801720.

CHAPTER 7 Conclusions

7.1 Future Work

III-V QDs are less established members of the colloidal QD family compared to II-VI and IV-VI QDs. Their unique structural and physical properties as well as surface chemistry are not yet well understood. Therefore, more systematic investigation to correlate defects with the physical properties of InSb QDs is of significance for improving the InSb QD device performance. Air-stability of III-V QD devices should also be evaluated and effective encapsulation should be developed. Based on more comprehensive knowledge about this material system, we propose to design all III-V QD based solar cells.

7.1.1 Correlation Between Defects and Physical Properties of InSb QDs

Bulk InSb is a well-known material for IR detectors with electron and hole mobility as high as 77,000 and 850 cm^2/Vs, respectively.[1] However only mobility of ~10^{-4} cm^2/Vs is measured in InSb QD solids after Na_2S ligand exchange.[2] To identify the culprit for poor carrier transport, more defect characterization will be needed for this system. Upon correlating the defects with their physical properties, we will develop post-synthesis treatments to reduce defects.

In Chapter 5, we have observed oxidation states of both In and Sb from XPS measurement of pristine InSb QD dispersion, which may form potential energy barriers for carrier transport. The evolution of oxides with storage time probed by XPS will be further studied in combination with absorption and XRD measurements. As the oxidation happens from surface to core of the QD, blue shifts of the absorption peak will be expected due to shrinkage of the effective QD size. Meanwhile, the oxide crystal phase will become apparent under XRD characterization. The identical measurement will also be conducted on the film of InSb QDs after

ligand exchange to examine the effect of ligands on chemical oxidation states and correlate them with doping concentration and carrier transport properties obtained from the FET geometry.

Photoluminescence (PL) is another informative characterization reflecting the band structure of the material. Figure 7.1 shows the preliminary PL spectra of InSb QDs both at room and low temperatures. First of all, the InSb QDs synthesized by the method described in Chapter 5 emit weakly at room temperature, indicating non-radiative recombination occurs due to the existence of trap states. Although the low room temperature PL can be picked up by the photo-multiplier tube (PMT) detector, only part of the spectra is collected due to the spectral cut-off at 1650 nm of the PMT detector. The InGaAs detector has a wider range of IR spectral response but lower sensitivity, therefore it's used to measure PL of InSb QDs at 11 K. At low temperature, carriers are slowed down or frozen, so that non-radiative recombination is suppressed and exciton-phonon interaction is reduced,[3] giving rise to increased PL intensity and more detailed feature of the PL spectrum. Besides the major peak at 1650 nm, there is another feature at ~1800 nm detected, which may be attributed to emission from the in-gap states located 0.06 eV away from the band edge. To further investigate the band structure and photogenerated carrier dynamics, we will perform temperature-dependent PL decay measurements to characterize PL lifetimes.

In sum, we will combine XPS, XRD, absorption and temperature-dependent PL measurements to characterize defects and associated trap states. By applying post-synthesis treatments proven successful in other material systems, such as fluoride etching,[4] metal halide passivation,[5] high temperature annealing,[6] etc., we will monitor the change of defects and its effects on transport properties.

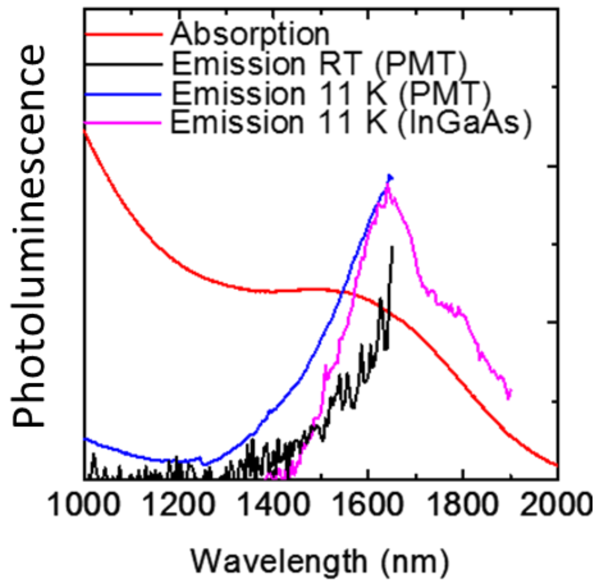

Figure 7.1 Room and low temperature PL spectra of InSb QDs.

7.1.2 Encapsulation and Passivation of III-V QD Devices

In Chapter 5 and 6, we have demonstrated promising device performance from III-V QD based devices. Air-stability of these devices, however, is still under investigation. Figure 7.2a shows the evolution of I_D-V_G characteristics of a Na_2S treated InAs QD FET after being stored in glovebox for four days (red), exposed to air for 5 min (green) and re-annealed in glovebox at 300 °C for 5 min (blue). The device current degrades with exposure time, more rapidly in air than in the glovebox. It is hypothetically because the oxidation of In and As, as seen by XPS in InSb QDs, or mid-gap states caused by adsorbed oxygen and moisture reported in the CdSe QD system previously.[7] Also akin to the recovery phenomenon in the CdSe QD FETs, thermal annealing of air-exposed InAs QD FETs with In/Au contacts in the glovebox enhances the device current to even higher than that of the as fabricated devices. Thermal diffusion of In from the contact is assumed to remove adsorbed oxygen and water and passivate mid-gap states.[7]

To investigate the recovery mechanism, we will use EDS and XPS measurements to track the ratio and oxidation states of the components in InAs QDs during the oxidation and recovery process. Cyclic-voltammetry measurement will be employed to probe if there is any observable mid-gap state induced by oxygen. We will optimize the re-annealing procedure, such as the recovery agent and annealing conditions, as the preliminary result shows reduced gate modulation due to over-doping by the annealing treatment.

The recovery effect in the InAs QD devices allows for possible further processing in air. In both the CdSe and PbSe QD systems, atomic layer deposition (ALD) has been used to encapsulate their devices with thin metal oxide layers to passivate surface traps and improve air-stability.[7,8] Preliminarily, we deposit a 3 nm Al_2O_3 layer through ALD at 250 °C to cover the InAs QD FET as shown in the inset of Figure 7.2b. The device then experiences a decrease of current levels, especially the on-current, leading to a decrease of electron mobility as well. Nevertheless, the reduced hysteresis is consistent with the passivation of traps by the ALD layer. And the current is stable after the sample being re-annealing at 300 °C, suggesting the ALD matrix prevents QDs from further fusion. We will perform absorption and XPS measurements to seek for the reason that causes device currents to decrease after the ALD process. The encapsulation process will be thus optimized to yield air-stable high performance InAs QD based FETs.

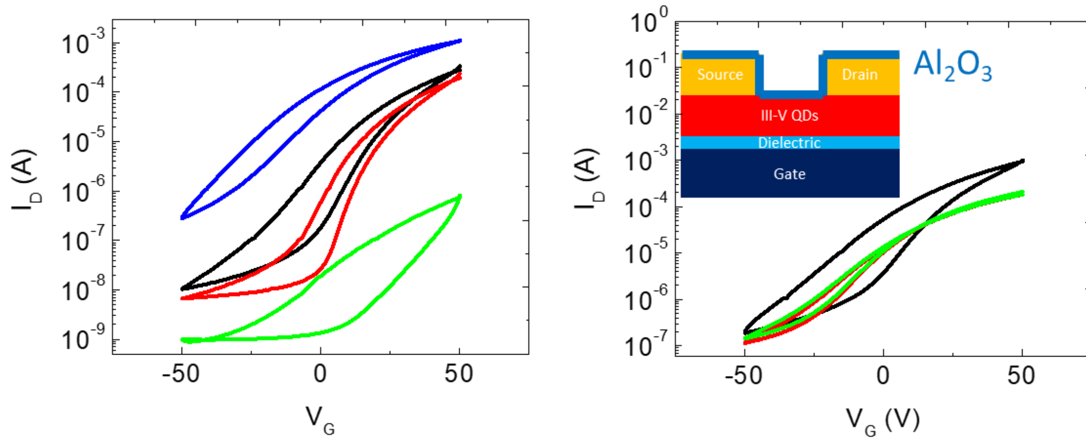

Figure 7.2 I_D-V_G characteristics of representative InAs QD FETs (a) as fabricated (black), stored in a glovebox for 4 dyas (red), with air exposure for 5 min (green) and after being re-annealed at 300 °C for 5 min in a glovebox, and (b) before (black) and after (red) ALD encapsulation and further being annealed at 300 °C for 2 min in inert glovebox atmosphere (green).

7.1.3 Designing All III-V QD Based Solar Cells

PbS QD solar cells have been active studied and achieved significant progress, however Pb as a heavy metal is restricted in commercial products in many countries. The facile and large-scale synthesis of III-V QDs developed in Chapter 5 raises the opportunity for Pb free QD based photovoltaics. Recently, there is an encouraging study about incorporating InAs QDs into solar cell design for the first time, however, still relying on p-type PbS QD layers to form the heterojunction.[9] Here, we propose an all III-V QD based solar cell device design shown in Figure 7.3, where a pn junction composed of III-V QD layers is sandwiched between ITO and Au electrodes with MoO_3 and ZnO as hole and electron transport layers, respectively.

The key to realize this design is having the capability to independently prepare n-type and p-type III-V QD layers. InAs QDs with bandgap energy of 1.2 eV, ~4 nm in size, can be

prepared by controlling the reaction temperature, suitable for solar cell applications. We have also shown the hybrid ligand exchange method to yield high electron mobility in n-type InAs and InP QD devices. By controlling the concentration of Na_2S during the ligand exchange, we can tune the electron concentration in the n-type layer. P-type III-V QDs have not been well established yet. The Bawendi group has provided one possible approach to p-dope InAs QDs through cation exchange with Cd.[10] We will therefore examine other metals that are acceptors for bulk InAs, such as Zn, Sn and Ag, using the same post-synthesis cation exchange idea and observe the change of carrier concentration within the InAs QD films in the FET geometry.

In Chapter 5 and 6, we have developed the synthesis of $InAs_xSb_{1-x}$ QDs and shown that their bandgap and carrier concentration is tunable through controlling the chemical composition. As the ratio between Sb and As precursor increases during synthesis, resulting in higher Sb content in the final product, the bandgap decreases and the alloy QDs become increasingly more p-type. We will carefully tailor the As:Sb ratio and reaction temperature to obtain appropriate bandgap and p-type doping in the $InAs_xSb_{1-x}$ QDs to act as the p-type layer in the device stack. The doping concentration and energy levels will be characterized by capacitance-voltage and cyclic voltammetry measurements to ensure favorable band alignment across the pn junction.

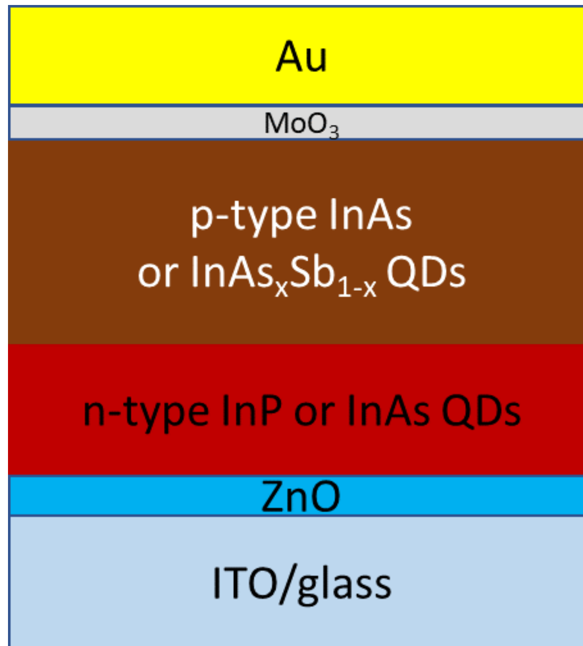

Figure 7.3 The proposed device structure for all III-V QD based solar cells.

7.2 Concluding Remarks

In conclusion, we have manipulated physical properties including carrier mobility and lifetime, doping concentration and energy levels of QDs through surface modification. By ligand exchange, remote doping and surface stoichiometry control, we have designed II-VI, IV-VI and III-V QDs for various electronic and optoelectronic device applications and successfully improved their device performance.

In Chapter 2, we exploit the size and surface dependent properties of CdSe QDs to design a thin buffer layer for the ZnO NP/PbS QD heterojunction interface. We apply CdI_2 ligand exchange treatment on the CdSe QD films to achieve n-type transport. Size tunable bandgap energy is utilized to study and optimize band alignment of the CdSe QD buffer layer with the rest of the junction. By improving the device design, we have improved the PCE by 25%, which is

attributed to reduced interface recombination and additional photogenerated carriers by the buffer layer.

Chapter 3 introduces a solution cALD approach to controllably enrich the PbS QD surface with sulfur. By utilizing Na_2S in FA in this method, we can precisely tune the stoichiometry of ultrasmall-sized PbS QDs during the solution phase. As the Pb:S ratio of QDs is decreased by the cALD process, we observe higher hole mobility and concentration within the EDT capped PbS QD films and achieve enhanced photoconductivity from QDs treated by 3 μL of Na_2S solution. We probe the surface composition of EDT-PbS QD films and speculate that the formation of $PbSO_3$ is the chemical origin of p-type doping. By increasing p-type doping of the EDT-PbS QD layer, we expect the Schottky barrier at the device back contact will be removed and band alignment will become more favorable for hole extraction.

In Chapter4, we study the effect of dielectric environment on doping efficiency in PbSe nanostructures based on PbSe NW FETs. PbSe NWs are remotely doped by Pb, In or Se. Through the shifting of threshold voltage in the FET characteristics, we correlate the doing concentration and further doping efficiency with the dielectric constant of the surrounding environment. When embedded in high dielectric material, the doping efficiency in PbSe NW increases>10 fold. We have also established a theoretical model to predict doping efficiency change within the dielectric media.

In Chapter 5, a general chemical synthesis for III-V QDs is described. Based on the co-reduction of indium and pnictogen halides, this approach greatly simples the preparation of V precursor. By tuning the size and composition of the QDs, we can tune the absorption peak from visible to infrared. Hybrid ligand exchange with Na_2S and NaN_3 give rise to promising carrier transport from InAs QD FETs.

Chapter 6 describes the synthesis of tetrahedral InP QDs and fabrication of InP QD FETs with electron mobility >0.5 cm^2/Vs. The reaction temperature and P precursor concentration are key parameters to yield uniform tetrahedral shape, and hybrid ligand exchange along with Se post passivation ensure n-doping and high mobility. The rest of the Chapter shows that the surface indium treatment can n-dope the InSb QDs, and the $InAs_{0.5}Sb_{0.5}$ alloy QDs demonstrates higher photoresponse than InSb QDs under 1550 nm illumination.

In the last Chapter of this thesis, we propose to carry on the research about III-V QDs and their devices by gaining a deeper scientific understanding about this material family such as correlating defects with physical properties of the material, and then designing air-stable and high performance electronic and optoelectronic devices.

7.3 References

(1) Avery, D. G.; Goodwin, D. W.; Rennie, M. A. E. New Infra-Red Detectors Using Indium Antimonide. *J. Sci. Instrum.* **1957**, *34* (10), 394–395.

(2) Liu, W.; Chang, A. Y.; Schaller, R. D.; Talapin, D. V. Colloidal InSb Nanocrystals. *J. Am. Chem. Soc.* **2012**, *134* (50), 20258–20261.

(3) Gaponenko, M. S.; Lutich, A. A.; Tolstik, N. A.; Onushchenko, A. A.; Malyarevich, A. M.; Petrov, E. P.; Yumashev, K. V. Temperature-Dependent Photoluminescence of PbS Quantum Dots in Glass: Evidence of Exciton State Splitting and Carrier Trapping. *Phys. Rev. B* **2010**, *82* (12), 125320.

(4) Adam, S.; Talapin, D. V.; Borchert, H.; Lobo, A.; McGinley, C.; de Castro, A. R. B.; Haase, M.; Weller, H.; Möller, T. The Effect of Nanocrystal Surface Structure on the Luminescence Properties: Photoemission Study of HF-Etched InP Nanocrystals. *J. Chem. Phys.* **2005**, *123* (8), 084706.

(5) Thon, S. M.; Ip, A. H.; Voznyy, O.; Levina, L.; Kemp, K. W.; Carey, G. H.; Masala, S.; Sargent, E. H. Role of Bond Adaptability in the Passivation of Colloidal Quantum Dot Solids. *ACS Nano* **2013**, *7* (9), 7680–7688.

(6) Srivastava, V.; Liu, W.; Janke, E. M.; Kamysbayev, V.; Filatov, A. S.; Sun, C.-J.; Lee, B.; Rajh, T.; Schaller, R. D.; Talapin, D. V. Understanding and Curing Structural Defects in Colloidal GaAs Nanocrystals. *Nano Lett.* **2017**, *17* (3), 2094–2101.

(7) Choi, J. H.; Oh, S. J.; Lai, Y.; Kim, D. K.; Zhao, T.; Fafarman, A. T.; Diroll, B. T.; Murray, C. B.; Kagan, C. R. In Situ Repair of High-Performance, Flexible Nanocrystal Electronics for Large-Area Fabrication and Operation in Air. *ACS Nano* **2013**, *7* (9), 8275–8283.

(8) Liu, Y.; Gibbs, M.; Perkins, C. L.; Tolentino, J.; Zarghami, M. H.; Bustamante, J.; Law, M. Robust, Functional Nanocrystal Solids by Infilling with Atomic Layer Deposition. *Nano Lett.* **2011**, *11* (12), 5349–5355.

(9) Song, J. H.; Choi, H.; Pham, H. T.; Jeong, S. Energy Level Tuned Indium Arsenide Colloidal Quantum Dot Films for Efficient Photovoltaics. *Nat. Commun.* **2018**, *9* (1), 4267.

(10) Geyer, S. M.; Allen, P. M.; Chang, L.-Y.; Wong, C. R.; Osedach, T. P.; Zhao, N.; Bulovic, V.; Bawendi, M. G. Control of the Carrier Type in InAs Nanocrystal Films by Predeposition Incorporation of Cd. *ACS Nano* **2010**, *4* (12), 7373–7378.